MANCHESTER 1824

The University of Manchester

Ultrafast charge dynamics in novel colloidal quantum dots

A thesis submitted to The University of Manchester for the degree of Doctor of Philosophy in the Faculty of Engineering and Physical Sciences

2014

MUSA CADIRCI

The Photon Science Institute

School of Physics and Astronomy

Contents

Word count: 47,890

List of figures

List of tables

List of abbreviations

AM1.5G	Air mass 1.5 global
AOM	Acousto-optic modulator
BBO	β-barium borate
CB	Conduction band
CBM	Conduction band minimum
ESA	Excited state absorption
FWHM	Full width at half maximum
I.I	Impact ionization
LBO	Lithium triborate
LED	Light-emitting diodes
IR	Infrared
MCP	Multi-channel plate
MEG	Multiple exciton generation
ML	Monolayer
Nd:YVO_4	Neodymium-doped yttrium orthovanadete
Nd:YLF	Neodymium-doped yttrium lithium fluoride
NC	Nanocrystal
ND	Neutral density
NIR	Near infrared
OPA	Optical parametric amplifier
PA	Photo-induced absorption
PD	Photodiode
PL	Photoluminescence
PMT	Photomultiplier tube

PV	Photovoltaic
QD	Quantum dot
QY	Quantum yield
SFP	Self-focussing process
SHG	Second harmonic generation
SPM	Self-phase modulation
TA	Transient absorption
TCSPC	Time correlated single photon counting
THG	Third harmonic generation
TRPL	Time-resolved photoluminescence
UV	Ultraviolet
VB	Valance Band
VBM	Valance band maximum
WLC	White light continuum
X-X	Exciton-Exciton
Δ_{XX}	Exciton-exciton interaction energy

Abstract

The work presented in this thesis was submitted to The University of Manchester for the degree of Doctor of Philosophy in March 2014 by MUSA CADIRCI and is entitled "Ultrafast charge dynamics in novel colloidal quantum dots".

In this thesis ultrafast exciton dynamics of several colloidal quantum dots have been studied using visible transient absorption spectroscopy. The resultant transient decays and differential transmission spectra were analysed to determine the ultrafast relaxation channels, multiple exciton generation (MEG) efficiency and multi-exciton interactions in the observed materials. All QDs were preliminarily optically characterized using steady state absorption and photoluminescence spectroscopies. In addition, a high repetition infrared femtosecond pump probe experiment was designed and built to detect the picosecond intraband carrier relaxations in quantum dots.

Picosecond carrier dynamics of type-II ZnTe/ZnSe and of $CuInSe_2$ and $CuInS_2$ type-I quantum dots were investigated. The common feature of these materials is that they are eco-friendly materials, being alternatives to the toxic Cd- and Pb- based materials. It was found that surface trapping occurred in both cases for electrons in the hot states, and in the minimum of the conduction band for ZnTe/ZnSe core/shell materials. Trion formation was observed in ZnTe/ZnSe core/shell dots at high power and unstirred conditions. The hot and cold electron trapping processes in type-II dots and $CuInS_2$ and $CuInSe_2$ dots shifted, distorted and moderately cancelled the bleach features. In addition, intra-gap hole trapping was observed in $CuInS_2$ and $CuInSe_2$ dots which results in a long decay feature in the recorded transients.

MEG competes with Auger cooling, surface mediated relaxation and phonon emission. To enhance the MEG quantum yield, the rival mechanisms were suppressed in well-engineered CdSe/CdTe/CdS and CdTe/CdSe/CdS core/shell/shell and CdTe/CdS core/shell type-II quantum dots. The MEG slope efficiency and threshold for a range of different core size and shell thickness were found to be $(142\pm9)\%/E_g$ and $(2.59\pm0.16)E_g$, respectively. The observed threshold was consistent with the literature, whereas, the obtained slope efficiency was about three times higher than the previously reported values.

The biexciton interaction energy of the dots stated in the previous paragraph was also studied. To date, time-resolved photoluminescence (TRPL) has been employed to study exciton interactions in type-II quantum dots and large repulsive biexciton interaction energy values between 50-100 meV have been reported. However, unlike the TRPL method, the TA experiment ensures that only two excitons remain in the band edge of the dot. Using this method, large attractive biexciton interaction energies up to ~-60 meV was observed. These results have promising implications regarding enhancing the MEG quantum yield.

Declaration

No portion of the work referred to in the thesis has been submitted in support of an application for another degree or qualification of this or any other university or other institute of learning.

Copyright Statement

i. The author of this thesis (including any appendices and/or schedules to this thesis) owns certain copyright or related rights in it (the "Copyright") and he has given The University of Manchester certain rights to use such Copyright, including for administrative purposes.

ii. Copies of this thesis, either in full or in extracts and whether in hard or electronic copy, may be made only in accordance with the Copyright, Designs and Patents Act 1988 (as amended) and regulations issued under it or, where appropriate, in accordance with licensing agreements which the University has from time to time. This page must form part of any such copies made.

iii. The ownership of certain Copyright, patents, designs, trade marks and other intellectual property (the "Intellectual Property") and any reproductions of copyright works in the thesis, for example graphs and tables ("Reproductions"), which may be described in this thesis, may not be owned by the author and may be owned by third parties. Such Intellectual Property and Reproductions cannot and must not be made available for use without the prior written permission of the owner(s) of the relevant Intellectual Property and/or Reproductions.

iv. Further information on the conditions under which disclosure, publication and commercialisation of this thesis, the Copyright and any Intellectual Property and/or Reproductions described in it may take place is available in the University IP Policy (see http://www.campus.manchester.ac.uk/medialibrary/policies/ intellectual-property.pdf), in any relevant Thesis restriction declarations deposited in the University Library, The University Library's regulations (see http://www.manchester.ac.uk/library/aboutus/ regulations) and in The University's policy on presentation of Theses

List of publications and presentations

Journal articles

M. Cadirci , S. K. Stubbs , S. M. Fairclough , E. J. Tyrrell , A. A. R. Watt , J. M. Smith and D. J. Binks, "Ultrafast exciton dynamics in Type II ZnTe–ZnSe colloidal quantum dots", Phys. Chem. Chem. Phys., 2012, **14**, 13638-13645

Musa Cadirci , Stuart K. Stubbs , Samantha J. O. Hardman , Ombretta Masala , Guy Allan , Christophe Delerue , Nigel Pickettand David J. Binks "Ultrafast exciton dynamics in InAs/ZnSe nanocrystal quantum dots", Phys. Chem. Chem. Phys., 2012, **14**, 15166-15172

Musa Cadirci, Ombretta Masala, Nigel Pickett, and David Binks, "Ultrafast charge dynamics in $CuInS_2$ nanocrystal quantum dots", Chemical Physics, 2014, **438**, 60-65

Musa Cadirci, Robert Page, Daniel Espinbarro-Valesquez, Stanko Tomic, Paul O'Brien and David Binks, "Tripled multiple exciton generation efficiency by reduced electron cooling" (*In preparation*)

Musa Cadirci, Daniel Espinbarro-Valesquez, Robert Page, Jacek Miloszewski, Stanko Tomic, Paul O'Brien, Edward Lewis, Sarah Haigh, David Binks, "Attractive biexciton interaction energies in Type II colloidal quantum dots" (*In preparation*)

Conference presentations

Musa Cadirci, Robert Page, Daniel Espinbarro-Valesquez, In-Sik Kim, Paul O'Brien & David Binks, "Attractive Biexciton Interaction Energies in CdSe/CdTe/CdS Type II Colloidal Dots", Photon12, Durham, UK, (3 - 6 September 2012)

Musa Cadirci, Daniel Espinbarro-Valesquez, Robert Page, Paul O'Brien, David Binks, "Attractive Exciton-Exciton Interaction Energies in Type II Colloidal Nanocrystals", NanoTR-9, Erzurum, Turkey (24-28 Jun 2013)

Conference posters

M. Cadirci, S. K. Stubbs, D. J. Binks, S. M. Fairclough, J. M. Smith, "Investigation of Ultrafast Charge Dynamics of Type II ZnTe/ZnSe Colloidal Quantum Dots" IOP One-Day Quantum Dot Meeting, London, UK (5th January 2012)

Musa Cadirci, Robert Page, Paul O'Brien, David Binks, "Doubled Multiple Exciton Generation Efficiency in Type II Colloidal Quantum Dots", E-MRS 2013 Spring Meeting, Strasbourg, France, (28- 30 May)

Musa Cadirci, Daniel Espinbarro-Valesquez, Robert Page, Paul O'Brien, Edward Lewis,

Sarah Haigh, David Binks, "Attractive Biexciton Interaction Energies in CdSe/CdTe/CdS and CdTe/CdSe/CdS Type II Colloidal Dots" E-MRS 2013 Spring Meeting, Strasbourg, France, (28-30 May)

Musa Cadirci, Robert Page, Paul O'Brien, David Binks, "Improved Multiple Exciton Generation Efficiency in Type II CdSe/CdTe/CdS and CdTe/CdSe/CdS Colloidal Quantum Dots", NanoTR-9, Erzurum, Turkey (24-28 June 2013)

Book contribution

N. McElroy, **M. Cadirci**, A. Al-Otaify, R. Page, and D. J. Binks, "Chapter 9: Increasing Efficiency with Multiple Exciton Generation" In "Quantum Dot Solar Cells" Wu, Jiang; Wang, Zhiming M. (Eds.) (Springer, New York)

Acknowledgements

First and foremost, I would like to thank my supervisor, Dr. David Binks, for all his supervision, encouragement, advice and support during these years of PhD studies and of course for his feedback to the thesis. His guidance regarding both the understanding of the theory and interpretation of the results was priceless to me.

I also thank Dr. Darren Graham and Dr. Ben Spencer for their support regarding the ultrafast TA experiment.

I would like to express my sincere gratitude to all my group members especially Ali Al-Otaify, Daniel Espinbarro-Valesquez, and Dr. Marina Leontiadou for their help and constructive discussions. Chris Page also deserves my thanks for making excellent quantum dots.

I would like to thank the Ministry of National Education of Turkey for supporting my PhD studies.

All of my friends deserve my sincere gratitude particularly, my house mates for their support and invaluable friendship.

Finally, I would like to give a special warm thank to my parents and all of my siblings. Without their encouragement, prayers and great patience at all times, none of this would have been possible.

This work is dedicated to my parents and my little brother, Yusuf, who passed away at the very young age of 17.

Chapter 1: Introduction

1.1 Introduction

At present, humanity is in need of clean energy sources due to rapid growing of population, global warming and depleted sources. It has been estimated that the annual world energy consumption is about 14 TW which is predicted to increase to about 30 TW by 2050 [1]. However, the clean solar energy received by Earth in one hour is sufficient enough for the yearly world energy demand. To put it another way, if a little portion of sun light is converted to electricity by photovoltaics (PV), then there would be no concerns regarding energy resources and global warming [2]. Despite the recent rapid expansion of solar cell industry, still only less than 5 % of the energy consumption is met by solar cell power worldwide [3]. Clearly, much research remains to be carried out to develop new economically-competitive technologies to exploit more solar energy.

PV is a direct way of generating electricity from the sunlight which employs a semiconductor material whose band gap lies in the spectrum of solar radiation. Conventional PVs essentially consist of a p-n junction. When the cell absorbs photons with energy greater than the material band gap, free carriers are photo-generated and subsequently separated, resulting in current flow. For conventional silicon based solar cells, the theoretical maximum photon-to-light conversion efficiency is about 31 % under standard air mass 1.5 global (AM1.5G) radiation [4]. This is termed as Shockley-Queisser limit or detailed balanced limit. The highest conversion efficiency of PV devices has been observed to be ~22 % in industry and 24.7% in laboratory [5]. The rest of the energy is wasted as heat, transmission and emission. The second disadvantage of this type of solar

cells is that they are too expensive to be fabricated compared with other energy sources [6]. Hence, "thin film" technology and dye sensitized solar cells [7], which are so called "second generation" solar cells, were suggested to be an alternative to the first generation solar cells as the new technology reduces the material cost significantly by eliminating the silicon wafer [8]. However, this technology offers less power conversion efficiency in comparison with silicon based PVs [8]. Therefore, third generation solar cells have been proposed as an alternative way to overcome the high cost and low-efficiency issues of PV devices. This technology includes a variety of materials including polymer cells [9], tandem or multi-junction cells [10], hot carrier cells [11], and quantum dot (QD) solar cells [12]. Figure 1.1 compares the three types of solar cells in terms of cost and conversion efficiency.

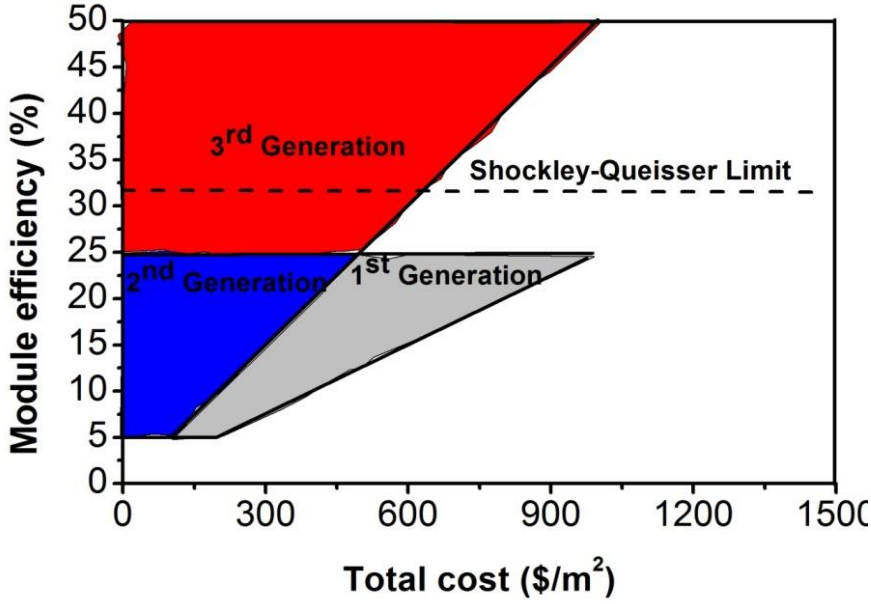

Figure 1.1. The comparison of the efficiency and cost for 1st (grey), 2nd (blue) and 3rd (red) generation PVs. [Modulated from [6]].

QDs are a nano-crystal form of semiconducting materials that have size-dependant spectral response. An electron and hole pair (exciton) is confined in three dimensions in

these structures. QDs stand between molecules and bulk materials and hence are called artificial atoms due to their quasi-discrete energy states. Moreover, they are grown by wet chemistry and are cheap to produce in industrial scale applications. These nano-materials have drawn significant research interest due to their unique structures and properties. In this work, I will focus on the ultrafast exciton dynamics of QDs, including the multiple exciton generation (MEG) process in QDs. MEG occurs when a nanoparticle absorbs an energetic photon whose excess energy creates extra excitons. Unlike bulk materials, the separation of energy states in QDs is wide enough to suppress phonon relaxation which competes with MEG, increasing MEG rate in QDs. It has been calculated that MEG has potential to increase the theoretical efficiency of PV devices up to 44 % [13]. This value is expected to increase further to about 50 % by well- engineering the structure of QDs [14].

1.2 Thesis outline

Chapter 2 outlines the optical and electronic structure of QDs explained by the particle-in-a-sphere model. Next, different types of colloidal QDs are discussed before a detailed explanation of MEG and exciton-exciton (X-X) interaction energies in QDs. In the last section of the chapter a brief history of MEG and exciton-exciton interactions in QDs are presented. Chapter 3 describes the techniques that are used in this study to characterize basic optical properties and to measure the ultrafast exciton dynamics of QDs. Firstly, linear absorption and photoluminescence (PL) spectroscopy are described in detail. Then the principles of the time correlated single photon counting (TCSPC) is presented. Next the non-linear generation of ultrafast light used in the transient absorption (TA) experiment is outlined before a description of the instrumentation of the TA experiment itself. Finally, a newly developed high-repetition rate infrared TA experiment is explained.

Chapters 4 and 5 discuss a study of the ultrafast exciton dynamics of ZnTe/ZnSe type-II QDs and that of $CuInSe_2$ and $CuInS_2$ QDs, respectively. The absorption and PL spectra of these materials are initially investigated. Then a complete study of exciton cooling of the specified samples is highlighted using an ultrafast TA experiment. The effect of the direct surface-mediated trapping and trion formation on the ultrafast dynamics of the materials is observed. MEG efficiency in CdSe/CdTe/CdS and CdTe/CdSe/CdTe type-II QDs is reported in Chapter 6 using the TA experiment. A depiction of the steady-state absorption and PL characterization of the samples is outlined before the description of the life time measurements. Then the MEG quantum yield (QY) is measured for a few excitation wavelengths.

Chapter 7 details the X-X interaction energy measurements in a set of both CdSe/CdTe/CdS and CdTe/CdSe/CdS core/shell/shell QDs using TA experiment. Initially the basic optical properties of the samples are determined using the steady-state absorption and PL spectroscopies. A comprehensive measurement of X-X interactions in the QDs is explained following the presentation of the effects of surface trapping and of the early rise time. The multi-exciton interaction in the employed QDs is measured using the time-resolved PL (TRPL) method. Finally, the main findings in this thesis are summarised in the conclusion chapter. Suggestions are provided for possible future activities to expand upon these results.

1.3 References

1. Tsao, J., Lewis, N. and G. Crabtree, *Solar FAQs.* US Department of Energy, 2006.
2. Morton, O. *Solar energy: A new day dawning?: Silicon Valley sunrise.* Nature 2006. **443**(7107): p. 19-22.
3. *Worldwide electricity production from renewable energy sources* 2013 [cited 2014; 2013:[Fifteenth Inventory - Edition 2013]. Available from: http://www.energies-renouvelables.org/observ-er/html/inventaire/Eng/conclusion.asp.
4. Shockley, W. and H.J. Queisser, *Detailed Balance Limit of Efficiency of p-n Junction Solar Cells.* Journal of Applied Physics, 1961. **32**(3): p. 510-519.
5. Beard, M.C. and R.J. Ellingson, *Multiple exciton generation in semiconductor nanocrystals: Toward efficient solar energy conversion.* Laser & Photonics Reviews, 2008. **2**(5): p. 377-399.
6. Hillhouse, H.W. and M.C. Beard, *Solar cells from colloidal nanocrystals: Fundamentals, materials, devices, and economics.* Current Opinion in Colloid & Interface Science, 2009. **14**(4): p. 245-259.
7. Grätzel, M., *Dye-sensitized solar cells.* Journal of Photochemistry and Photobiology C: Photochemistry Reviews, 2003. **4**(2): p. 145-153.
8. Green, M.A., *Third generation photovoltaics: solar cells for 2020 and beyond.* Physica E: Low-dimensional Systems and Nanostructures, 2002. **14**(1–2): p. 65-70.
9. Gang Li, R.Z., Yang Yang, *Polymer solar cells.* Nature Photonics, 2012. **6**: p. 153-156.
10. Conibeer, G., *Third-generation photovoltaics.* Materials Today, 2007. **10**(11): p. 42-50.
11. Hanna, M.C., Z. Lu, and A.J. Nozik, *Hot carrier solar cells.* AIP Conference Proceedings, 1997. **404**(1): p. 309-316.
12. Nozik, A.J., *Quantum dot solar cells.* Physica E: Low-dimensional Systems and Nanostructures, 2002. **14**(1–2): p. 115-120.
13. Hanna, M.C. and A.J. Nozik, *Solar conversion efficiency of photovoltaic and photoelectrolysis cells with carrier multiplication absorbers.* Journal of Applied Physics, 2006. **100**(7): p. 074510.
14. McElroy, N., et al., *Quantum Dot Solar Cells*. Lecture Notes in Nanoscale, ed. J.W.a.Z.M. Wang. 2013, New York: Springer Science+Business Media.

Chapter 2: Theory and background

2.1 Colloidal semiconductor quantum dots

Colloidal QDs are spherical semiconductor nanoparticles whose size is about or smaller than the Bohr radius of an exciton in its bulk counterpart and they contain 1000s of atoms. Electron and hole pairs (excitons) are confined in three dimensions in these nanostructures and thus they are also called zero-dimensional nanocrystals (NC). The properties of QDs can be manipulated straightforwardly to enhance the properties of the material. Their electronic structure lies somewhere between molecules and bulk materials making them one of the key systems for nanotechnology. These structures can absorb light and either re-emit it at the desired wavelengths or allow it to be converted to electricity. Colloidal QDs are produced by wet chemistry which is a straightforward way to produce QDs in large scale. The synthesising method of producing QDs also allows scientists to have accurate control on the size, shape and optical properties of the materials. QDs grown by this method can have high PL QY, which is a key metric for evaluating the materials' quality. QDs are size tunable materials so that the material size is inversely proportional to the band edge and to the separation between quasi-discrete energy levels. This feature is particularly useful for applications where the emission wavelength is important *i.e.* light-emitting diodes (LEDs) [1], biological applications [2], lasing [3]. The ability of tuning the materials' band gap is also important for solar cell applications. That is because the band gaps in the near infrared (NIR) region where solar spectrum harvesting is optimum can be easily accessed by controlling the dot size [4].

2.1.1 Electronic structure of QDs

Unlike bulk materials, the conduction and valance bands in QDs have quasi-discrete energy levels due to strong electronic confinement in the QDs and thus these materials are known as "artificial atoms". Figure 2.1 compares the electronic structures of QDs and of bulk materials. The separation between each energy level and the band gap change depends on the nanocrystals' size so that as the diameter increases the energy level separation and band gap decrease. For a typical material, the energy difference between two energy states in the conduction band is about 100 meV, whereas this value is about 30 meV in the valance band [4]. The energy states in the conduction and valance bands are respectively denoted as nq and nQ, where n is the number of level with a given symmetry, q (Q)= s,p,d…(S,P,D….) is the lowest value of envelope angular momentum (the valance band energy states are denoted with upper case notation, whereas, the conduction band energy levels are denoted with lower case notations). The band gap of QDs is larger than that of their bulk counterparts and the relationship between them is described by [5];

$$E_g(QD) = E_g(bulk) + \frac{\pi^2\hbar^2(m_e+m_h)}{2D^2} - E_C\ , \quad (2.1)$$

where, D is the diameter of the ideal spherical QD, E_C is Coulomb energy and m_e and m_h are the effective masses of electron and hole, respectively. This equation clearly shows that QDs with larger diameter have narrower band gap.

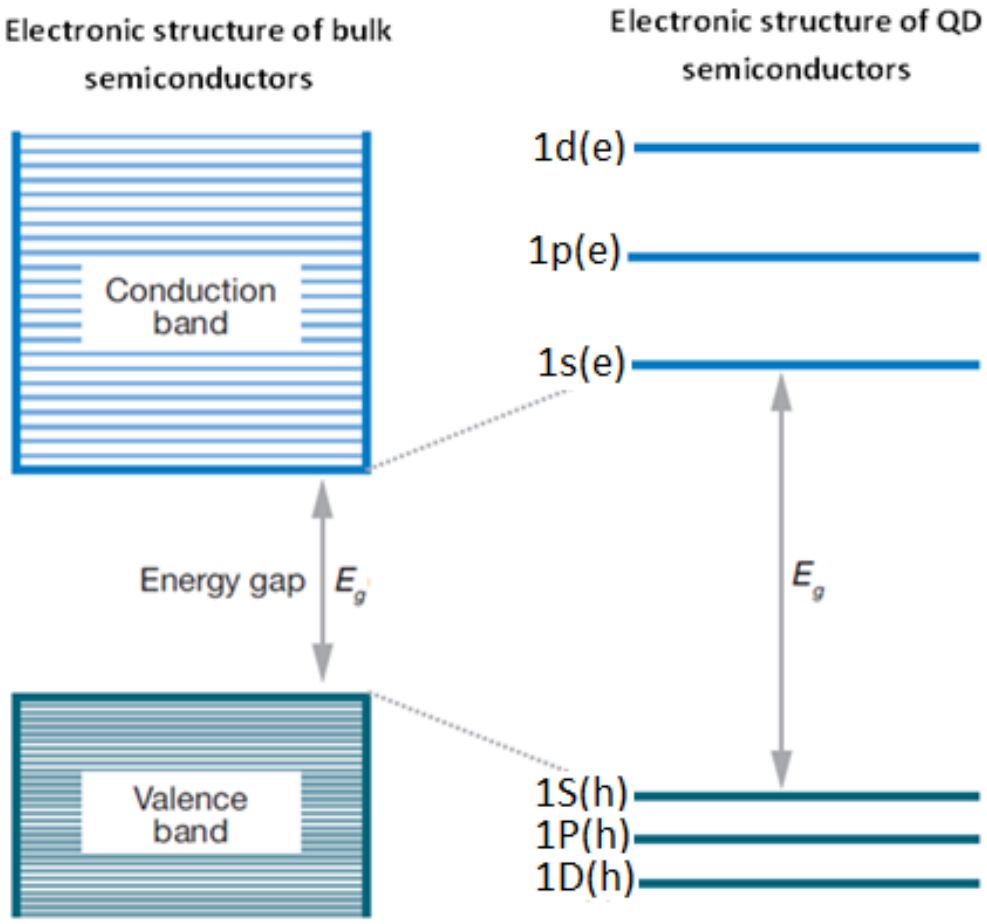

Figure 2.1. The comparison of energy band structure of bulk and QD semiconductor materials [Modified from [5]].

2.1.2 Strong confinement regimes

As stated above when the quantum dot size approaches the Bohr radius or less a blue shift appears in the absorption spectra of quantum dots, indicating that every motion of electron and holes are quantized. Therefore, the energy band structure of QDs become "atomic like" and carriers are confined in three dimensions. In this regime, the energy levels of QDs are easily tailored to modify the optical properties as the permitted energy states of electrons are more limited and size dependant. In the strong confinement regime, the reduced mass of carriers is dominant and the Coulomb energy is too small and thus it is treated as a perturbation [6]. Since the exciton Bohr radius depends on the dielectric

constant and the carriers' effective masses, then the confinement regime varies from material to material. For instance, InAs QDs always experience the strong confinement regime as the exciton Bohr radius in this material is 36 nm. In contrast, CuCl quantum dots are commonly in the weak confinement regime as the exciton Bohr radius for this material is 0.7 nm [7].

Several theoretical models have been developed to describe the structures of QDs. The simplest model that predicts the carriers' behaviour and the relationship between dot size and confinement energy in QDs is the "particle-in-a-sphere" model. According to this approach electrons and holes are predicted to stay inside the dot boundary i.e. material's surface. The potential inside and outside of the quantum well with a diameter of D becomes [8];

$$V(r) = \begin{cases} 0, & if\ 0 \le r \le D/2 \\ \infty, & otherwise \end{cases}, \qquad (2.2)$$

This means that the carriers are free within the dot, except at the boundaries (r=0, D/2) where the high dielectric constant of the ligands acts as a barrier to prevent the escaping of the carrier from the sphere and hence the wavefunction is zero outside of the box. A three dimensional Schrödinger equation solution will result in the wavefunction form which is divided into angular and radial parts and formed as [9];

$$\Psi_{n,l,m}(r,\theta,\emptyset) = C\,\frac{j_l(k_{n,l}r)\,Y_l^m(\theta,\emptyset)}{r}, \qquad (2.3)$$

where, C is a normalization factor, $j_l(k_{n,l}r)$ is the lth order spherical Bessel function and $Y_l^m(\theta,\emptyset)$ is a spherical harmonic which is applied to the hydrogen atom. Due to boundary conditions, wavevector, $k_{n,l} = {}^{2\alpha_{n,l}}/_{D}$, is quantized and thus does not take any value

where $\alpha_{n,l}$ is the *n*th zero of $j_{l.}$ The energy of these states are given by [9];

$$E_{n,l} = \frac{\hbar^2 k_{n,l}^2}{2m} = \frac{2\hbar^2 \alpha_{n,l}^2}{mD^2}, \quad (2.4)$$

Similarly, Eq. (2.1) is derived based on this model which claims that the energy difference in the band gap due to size dependance is proportional to $1/D^2$. The strong confinement leads to an increase in the band gap and hence discrete energy levels are formed [7].

2.1.3 Type-II QDs

Depending on the localization of the carriers, QDs have different characteristics and hence they are classified in different groups. In type-I QDs, the electron and hole are confined in the same volume of the material, and their wavefunctions overlap strongly. However, in type-II structures electrons and holes reside in a different section of the material *i.e.* if an electron resides in the core, then a hole is confined in the shell section. Type-II QDs have an effective band gap which is lower than that of its type-I counterparts [10]. Carrier wavefunction overlap is also reduced in these hetero-structured materials. A final structure of QDs is the quasi type-II where one carrier confines in the core volume and the other resides in the whole structure or vice-versa. The Auger recombination rate is related to the Coulomb interaction and hence to the spatial separation between carriers [11]. Therefore, a reduced wavefunction overlap in type-II QDs leads to a decrease in both single [12] and multi [11, 13, 14] exciton recombination rates. In particular, this feature results in large exciton-exciton (X-X) interaction energies (Δ_{XX}) [15]; a desirable feature for numerous applications [16, 17]. For example, if the magnitude of Δ_{XX} is greater than the emission line width and its sign is positive (repulsive, $\Delta_{XX}>0$), then the band gap of the QD is increased by Δ_{XX} and absorption at the emission wavelength is decreased [14]. And if the

average number of excitons per dot is greater than unity, then population inversion can be realized and optical gain in QDs might occur [3]. Figure 2.2 compares the typical electronic band alignments for type-I and type-II structures.

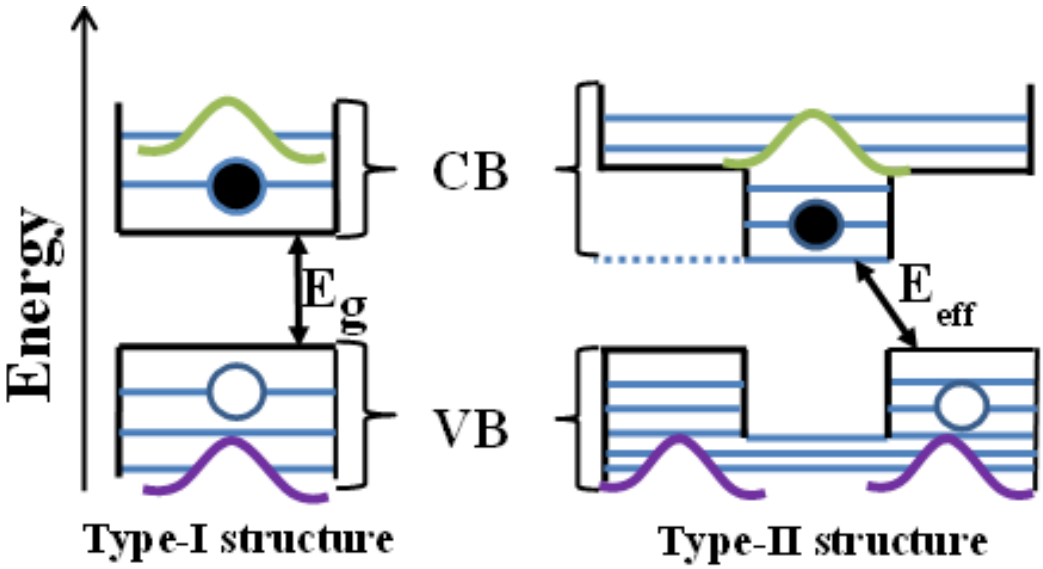

Figure 2.2. Typical band alignment of type-I and type-II QDs. (CB= Conduction Band, VB= Valance Band, E_{eff}= effective band gap. The green and purple curves show the wavefunctions of electron and hole, respectively.)

The localization of charges are determined based on the energy criterion in type-II nanostructures [18]. It dictates that the electron occupies the core volume if its energy is less than the conduction band of the shell and the hole occupies the shell if its energy is less than the valance band off-set. Due to the segregation of carriers in type-II QDs, the electron and hole wavefunction overlap is reduced and can be controlled by the core diameter and shell thicknesses grown during the synthesis [18]. This feature allows scientists to engineer the material structure to enhance the optical properties upon need. Since the effective band gap in type-II QDs can be controlled, then the narrow band gaps, corresponding to the region where the solar spectrum harvesting is maximum, can be easily achieved. Therefore type-II hetero-nanostructures have a promising future for photovoltaic

devices [19]. They are also considered as new NIR light sources since their band gap can easily tuned to the corresponding regime. The second most distinctive advantage of these structures is that as a result of electron and hole segregation the Auger relaxation rate is decreased. As will be described in detail (section 2.4), the decline of Auger relaxation rate will increase the MEG yield, which is a promising feature for next generation solar cells [4].

2.2 Auger recombination

Auger recombination is an ultrafast process that occurs in QDs wherein an electron-hole pair non-radiatively recombines and transfers its energy to a nearby carrier, exciting it to a hot state [5]. Figure 2.3 depicts the process of Auger recombination in a QD with two electron-hole pairs (biexcitons). Because of the strong carrier-carrier interaction in QDs, Auger recombination is significantly more efficient in these nanostructures compared with their bulk counterparts. Depending on the QD size, Auger recombination occurs on a ps timescale and has a linear relationship with QD volume [20, 21]. Multiple carriers at the band edge of QDs undergo Auger recombination until one exciton remains in the system which recombines radiatively on a ns time scale. Thus, Auger lifetimes are quantized in nanocrystals. In a femtosecond pump-probe experiment, decay features of transient transmittance dynamics reveal the Auger recombination life time of charges. Spatial separation of electrons and holes will decrease the efficiency of Auger recombination in QDs and hence in type-II QDs Auger recombination is not as efficient as it is in type-I QDs [11].

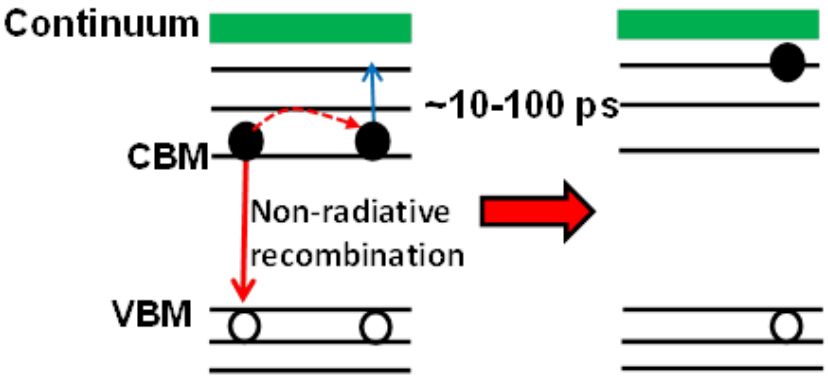

Figure 2.3. Illustration of Auger recombination of biexcitons in QDs. (CBM= Conduction band minimum, VBM= Valance band maximum.)

2.3 Multiple exciton generation

MEG is a process that occurs in quantum dots following the excitation of dots with photon energies of at least twice band gap energy. In this process the absorbed single energetic photon creates more than one exciton in the QD system. This effect has potential to significantly enhance solar cell performance as it utilizes the excess energy of the photon instead of wasting it as heat. In conventional silicon based solar cells the extra energy of the absorbed photon is lost as heat due to continuous energy levels in the structure of bulk semiconductors. Hence the maximum theoretical exploitation of the solar spectrum in the conventional solar cells is calculated to be about 31% [22]. However, the converted photocurrent efficiency is potentially improved to about 44 % [23] in QDs due to the MEG effect. Figure 2.4 compares the thermalization of hot electrons in bulk and QD structures and illustrates the MEG process in QDs. In the MEG process, the excited electron in the conduction band interacts with the electron in the valance band and dissipates its excess energy to the valance band electron via a Coulomb interaction. In that case the MEG channel dominates the relaxation and hence depending on the photon energy new excitons are produced [5] in the nanostructure. MEG can occur in bulk semiconductors and is

known as impact ionization (I.I) [24]. However, this process is inefficient in bulk semiconductors as the threshold photon energy is in the ultraviolet which is far from the spectral region where the solar exploitation is maximum. Therefore this methodology is not an effective way to improve the traditional silicon based solar cells' efficiency.

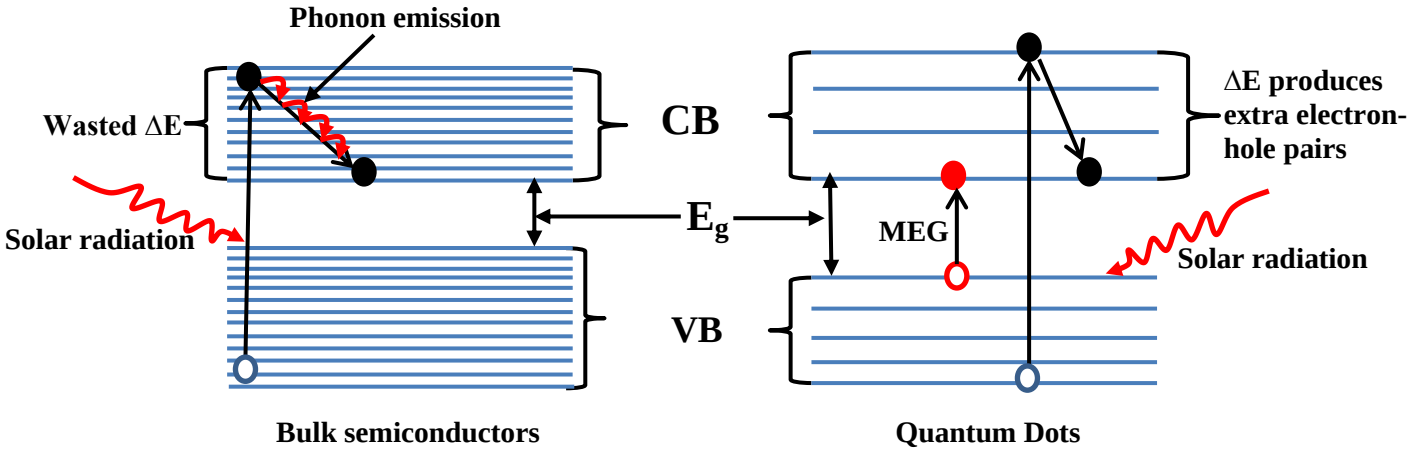

Figure 2.4. Hot electron relaxation in bulk and MEG mechanism in QD semiconductors. The excess photon energy in bulk materials is wasted, while, this energy produces new electron hole pairs (red carriers) in QDs.

The "Detailed balance model" proposed by Shockley and Queisser explains the power conversion efficiency of solar cells [5]. As described above, about 69% of photon energy in conventional solar cells is wasted as heat through phonon emission, sub-band gap transmission and radiative relaxation [25]. Because of the continuous energy levels in bulk materials, the relaxation of the hot electrons by phonon emission is completed within about 1 ps time scale [26] which is too fast for I.I rate to compete [27]. Thus only one exciton is produced per absorbed photon in bulk semiconductors and the excess energy is lost as heat. However, in QDs the energy difference between two states in the conduction band is about 100 meV which is much more than the phonon energy (~30 meV) and thus phonon emission is reduced [4]. In that case the relaxation rate of electrons decreases and hence "phonon bottleneck" could occur in the conduction band of QDs [28], which is a

situation of hot electron accumulation in the excited states.

In the case of MEG, the photon-to-exciton conversion efficiency is associated with both material band gap and the photon energy [19]. In the ideal case, QY has a step-like spectral dependence and is expressed as [19];

$$QY(hv, Eg) = \sum_{n=1}^{\infty} \theta\left(hv, nE_g\right), \qquad (2.5)$$

where θ is the unit step function and n is an integer where the maximum energy of the photon $hv_{max} \geq nE_g$. The created electron and holes share the extra energy of the photon depending on their effective masses in inverse proportion [4]. The electron energy is given by [29];

$$E_e = \frac{(hv - E_g)m_h}{m_e + m_h}, \qquad (2.6)$$

According to the energy conservation rule MEG can occur if E_e is greater than E_g, and hence the threshold energy for MEG becomes [30];

$$hv_{th} = E_g(2 + \frac{m_e}{m_h}). \qquad (2.7)$$

In materials, where $m_e \approx m_h$, the MEG effect starts at $3E_g$ and in materials where $m_h \gg m_e$, the MEG effect theoretically should start at $2E_g$ point. As of yet, no one has reported the MEG threshold reached down to the energy conservation limit in any material. Figure 2.5 a) illustrates the step-like QY as a function of (hv/E_g) for different (m_e/m_h) values and no MEG case. The corresponding conversion efficiency as function of band gap energy is shown in Figure 2.5 b). The MEG photo-generated current density, J_{pg}, is shown as [19];

$$J_{pg} = e\int_0^{\infty} QY(hv, nE_g)\emptyset(hv)d(hv), \quad (2.8)$$

where, $\emptyset(hv)$ and e are the density of solar photon flux and electron charge, respectively. As it is clear that in the case of no MEG, the maximum QY is 1, indicating that only one exciton is produced and the corresponding photo-current conversion efficiency is in the theoretical Shockley–Queisser limit which is about 31%. However, in the case of MEG the QY increases to the maximum energy limit depending on the effective masses of carriers and the corresponding photocurrent conversion efficiency increases up to 44%.

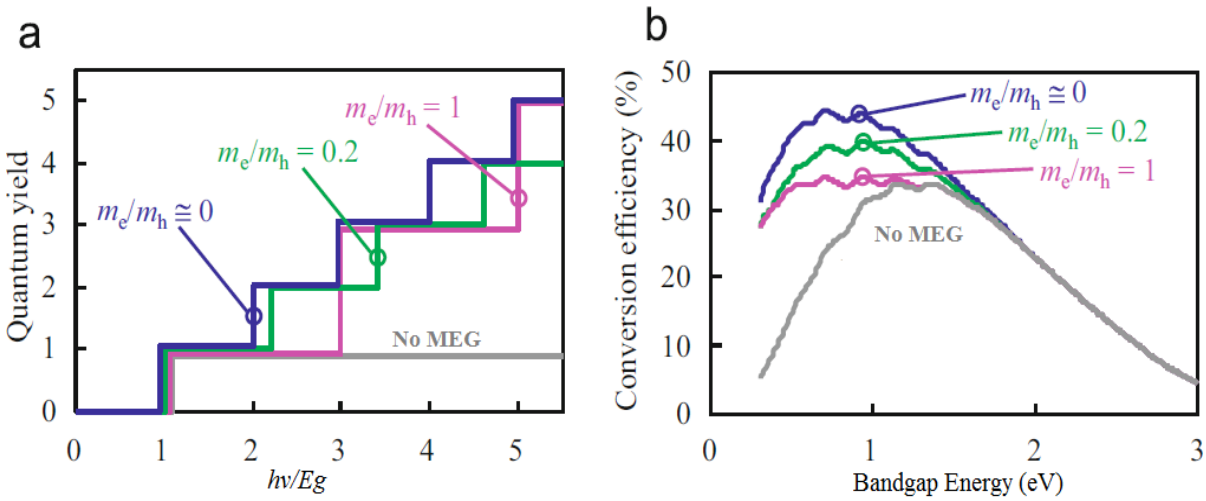

Figure 2.5. a) Step-like QY increase as a function of (hv/E_g) for three different m_e/m_h values and for the absence of MEG. b) Comparison of photon-to-current conversion efficiency in the case of no MEG and MEG with different m_e/m_h values. [Modified from [29]].

2.4 Possible ultrafast processes in QDs

2.4.1 Auger relaxation

Phonon emission by electrons in QDs is reduced compared to the bulk as the energy level spacing (~100 meV) in the conduction band of these nanostructures is larger than the phonon energy (~30 meV). In contrast, Auger relaxation becomes more efficient than in the bulk. Here, an excited electron transfers energy to its hole partner via a strong Coulomb

interaction to cool to the CBM, exciting the hole to a hot state in the valance band. Because of the relatively larger effective mass of hole, the energy level density in the valance band is relatively higher, resulting in a lower energy level spacing compared with the conduction band. Therefore, the excited hole rapidly cools to the VBM via phonon emission, removing the phonon bottleneck [7, 31]. This process of Auger relaxation is illustrated in Figure 2.6. This mechanism is very efficient in small size QDs as the electron-hole Coulomb interaction is significant. Auger relaxation occurs on a time scale of ~1 ps [32]. It competes with the MEG rate and thus decreases the MEG yield in QDs. A well-engineered carrier wavefuntion will decrease the rate of Auger cooling and hence increase MEG efficiency.

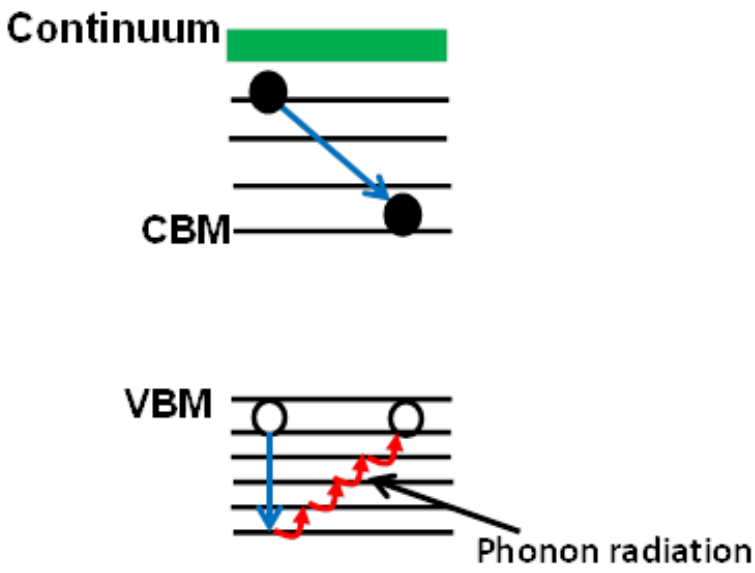

Figure 2.6. Schematic representation of Auger relaxation process in semiconductor QDs.

2.4.2 Trion recombination

Trion recombination occurs via an Auger interaction in QDs that do not have a well-controlled surface. Thus an ultrafast decay feature arises in a TA kinetic signal in the case

of trion recombination and can be confused with a MEG signal. A trion forms when a charge is trapped on the sample surface for a time period longer than that between two consecutive laser pulses in a TA experiment. The second pulse excites the pre-charged QD and creates an extra exciton, leaving three charges in the dot and one charge on the surface, as shown in Figure 2.7. The trapped carrier can stay on the surface for as long as 30 s [33]. The paired electron and hole recombines by Auger recombination and only the un-paired charge resides inside the dot and its geminate partner is still trapped on the surface. The un-paired exciton is not detected by our TA experiment, which includes a lock-in amplifier, as it does not affect pump transmittance at the reference frequency of the experiment. Therefore, trion recombination decays to zero instead of to a plateau as in the process of Auger recombination of biexcitons in QDs. In addition, the trion formation does not modulate the state filling spectra [4]. An electron is trapped in the case of positive trion formation, whereas a hole is trapped in the case of negative trion formation. The effect of this type of photocharging can be eliminated by carefully stirring [34] or flowing [35] the QD solution in a TA experiment. By doing so, the accumulated pre-charged QDs are swept out of the active volume and fresh QDs are pumped by the second pulse.

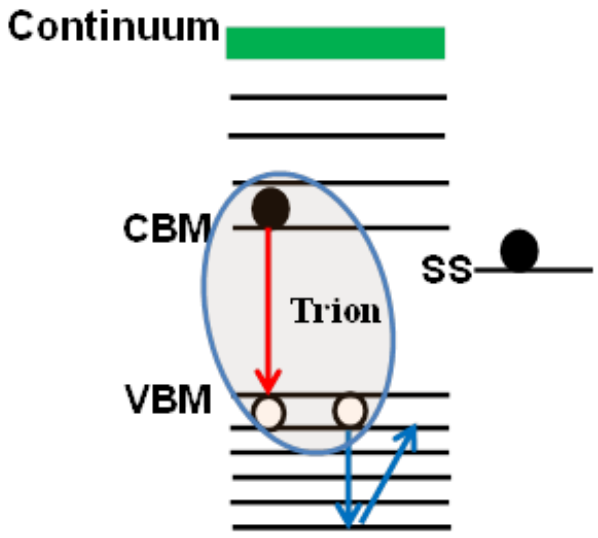

Figure 2.7. Schematic depiction of positive trion recombination in QDs. (SS= surface state.)

2.4.3 Direct surface trapping

Direct surface trapping is a sub-ns process that can be mistaken for the true MEG signal in QDs. In this mechanism, excited carriers are trapped on the sample surface for a period less than the time between pump pulses [36]. There are two types of direct surface trapping: cold and hot electron trappings. Figure 2.8 a) and b) show the cartoon representations of cold and hot electron trapping, respectively. Cold electron trapping is the rapid electron depopulation from the CBM to the sample surface. It reduces, distorts and sometimes reverses the TA spectrum taken near the band edge region by both removing the relaxed electrons and causing photo-induced absorption [36]. Therefore, the effect of cold electron trapping can be determined from the bleach (state filling) decay signal. On the other hand, hot electron trapping occurs when an excited electron directly moves to the sample surface from a hot state [36]. This process can be detected from the initial part of the TA transient as this is determined by electron relaxation processes. If the electron cools to the CBM from a hot state to fill available band-edge states, then the initial rise is monotonic, starting from zero to the bleach maximum. However, if the excited electron moves to the surface directly from the hot state, where it causes photo-induced absorption, then the initial part of the TA transient may be below zero before rising to the bleach maximum. Direct surface trapping issues can be eliminated by growing a shell with a wider band gap around the QD to act as a barrier to break the carrier-surface interaction [37].

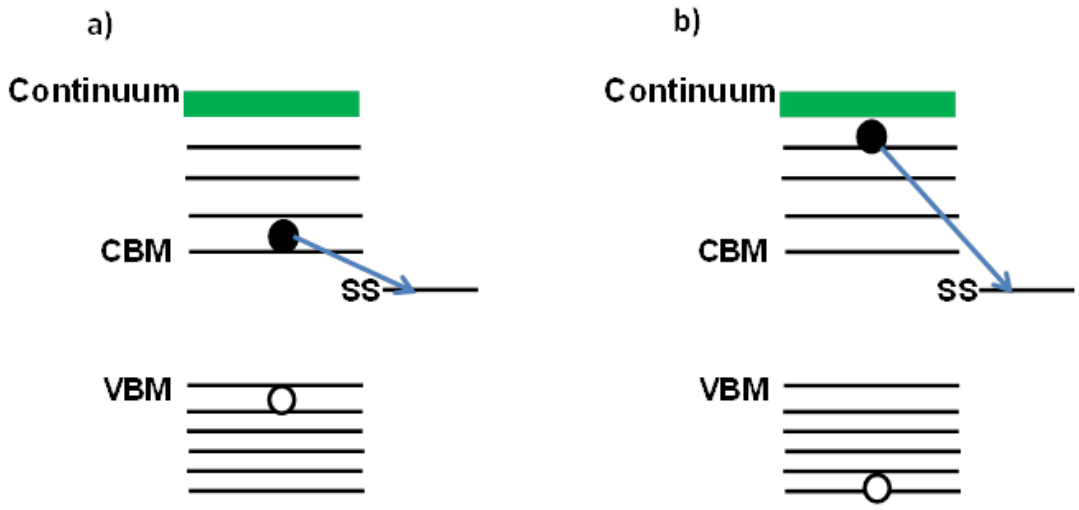

Figure 2.8. Schematic illustration of a) cold and b) hot electron trappings.

2.5 Exciton-exciton interaction

Due to quantum confinement in QDs, the Coulomb interaction energy between carriers is increased. This effect has the potential to shift the energy level of multi-excitons and to modify the selection rules [38]. The effect of multi-exciton interaction energy in QD is complicated to fully analyse and thus biexciton (exciton-exciton (X-X)) interaction energy, Δ_{XX}, is usually investigated for the sake of simplicity. Δ_{XX} is observed as a spectral shift in the materials' band gap using a TA experiment. This spectral shift can also be observed by TRPL experiments but this method collects data straight after excitation and hence includes contributions from hot excitons, which emit at energy levels higher than the conduction band minimum (CBM). Therefore the TA method is the most reliable tool to detect cooled biexciton interaction energy in QDs.

In order to observe the pure biexciton interaction effect, the probe beam is delayed with respect to the pump beam so that the fractional transmittance spectra is observed after carrier cooling to the band edge and the recombination of pump-created multi-excitons are

complete. In these circumstances, the biexcitons studied in this way comprise a pump-created exciton cooled to the band edge and a probe-created exciton formed at the band edge. In order to extract the Δ_{XX} magnitude the following equation is fitted to the recorded fractional differential transmission spectra in the TA experiment [5];

$$\frac{\Delta T}{T} = A_0\left[\frac{1}{x^2+1} - \frac{0.5}{(x-\delta_{xx})^2+1}\right], \qquad (2.9)$$

where, A_0 is the 1S absorption amplitude, $x = (\hbar\omega - E_{1S})/\Gamma_{1S}$ is the normalized detuning from the optical band gap (E_{1S}), and where Γ_{1S} is the transition line width, and $\delta_{xx} = \frac{\Delta_{xx}}{\Gamma_{1S}}$ is the normalized biexciton interaction energy. A slightly different equation is used to extract the magnitude of the Δ_{XX} in QDs straight after excitation when the photogenerated excitons are in the hot states which is expressed as [5];

$$\frac{\Delta T}{T} = A_0\left[\frac{1}{x^2+1} - \frac{1}{(x-\delta_{xx})^2+1}\right]. \qquad (2.10)$$

Because of the relatively large Δ_{XX} in QDs, the absorption cross-section in QDs changes in the case of exciting the dots. Therefore, when the exciton that is produced relaxes to the band-edge state and one of the 1S transitions is blocked, then the probability of absorbing one more exciton decreases by a half. This leads to a factor of 0.5 difference between Eq. (2.9) and (2.10).

The magnitude and the sign of Δ_{XX} depend on the structure of the QD and thus three different scenarios arise in these nanostructures. The first scenario is when the Δ_{XX} value is negligible. The strength of Δ_{XX} is correlated with local carrier density, $\rho_x(r)$. Since the electron and hole wavefunctions, ($\Psi_e(r)$ and $\Psi_h(r)$, respectively) are overlapped in type-I structures, then $\rho_X(r)$ becomes [39];

$$\rho_X(\mathrm{r}) = \mathrm{e}\,(|\Psi_e(r)|^2 - |\Psi_h(r)|^2) \approx 0, \qquad (2.11)$$

where r is the spatial coordinate. Hence the Coulomb interaction between opposite and same sign charges is almost equal [40], resulting in an attractive Δ_{XX} with a magnitude of about 10 meV [5, 41, 42], as demonstrated in Figure 2.9 a). This value is significantly greater than the bulk binding energies [15] but negligible compared to the linewidths of QDs' band gap spectra. The magnitude of Δ_{XX} is correlated with the degree of the confinement so that as the confinement increases the magnitude increases [43].

The second scenario is the large repulsive X-X interaction. This type of interaction energy can occur in type-II QDs as they have a reduced wavefunction overlap, as shown in Figure 2.9 b). In this case, a substantial imbalance occurs between the opposite charges and thus a strong local electric field is produced which makes the magnitude of Δ_{XX} greater than the transition linewidth [14]. The magnitude of this energy is inversely related to materials size and the dielectric constant difference between core and shell [15]. The magnitude can be increased by using thicker shells without losing the confinement quality wherein the Coulomb repulsion between same charges in the core becomes significant [40]. The enhanced repulsive X-X interaction energy is beneficial for optical gain in QDs, which is crucial for semiconductor laser technology [3]. If the energy of the absorption edge is increased more than the transition linewidth of the 1S absorption then the absorption losses become insignificant at the emission wavelength and thus optical gain can occur in the single-exciton regime [39]. This situation requires the absorption of more than one exciton where the population inversion, a condition in which the population of excited electrons is greater than that of the ground state, occurs [39]. Large repulsive Δ_{XX} in type-II QDs is supported by theoretical calculations based on an effective-mass model [18]. However, this treatment neglects configuration interactions between electrons which

might cause the opposite sign of Δ_{XX}.

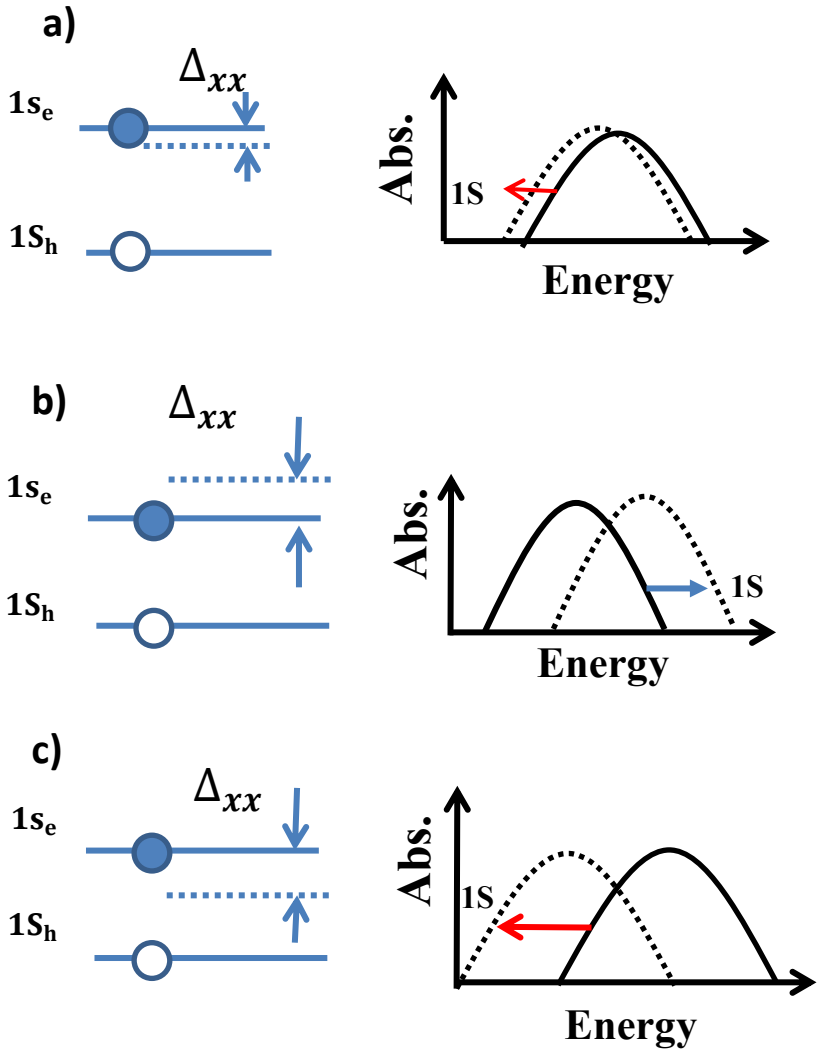

Figure 2.9. A schematic illustration of change in band-edge as a result of biexciton interaction and the corresponding shifts in near band-edge absorption transition 1S for a) Δ_{xx} negligible, b) Δ_{xx} large and repulsive, and c) Δ_{xx} large and attractive. The bold and dotted lines represent transitions and the CBM in unexcited and excited cases, respectively.

The third scenario is the large attractive Δ_{XX} in type-II structures, as shown in Figure 2.9 c). A recent study showed that different geometry of core-shell structures of type-II QDs results in different sign of Δ_{XX} [44]. This indicates that the effective mass-model does not consider entire parameters that have effect on X-X interactions. Therefore, more experimental and theoretical studies that include the interfacial layer geometry and

the effects of band bending and electron correlation are needed. Large attractive Δ_{XX} will decrease the MEG threshold and hence enhances the MEG yield in QDs [45]. In the case of type-I QDs where the sign of Δ_{XX} is negative and the magnitude is about 10 meV, the maximum calculated solar cell efficiency is about 44% [23]. However, in type-II QDs which shows attractive Δ_{XX} with a magnitude greater than the linewidth of the 1S absorption feature, the solar cell efficiency could reach about 50% [26]. Figure 2.10 compares the maximum photocurrent conversion efficiency of solar cells in the case of no MEG, MEG in type-I QDs and MEG in type-II QDs for a range of band gaps.

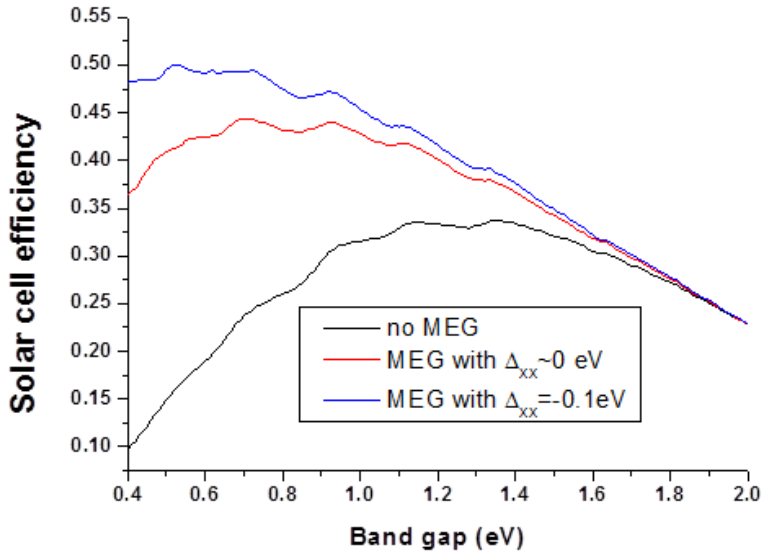

Figure 2.10. The Comparison of solar cell efficiency as a function of band gap for bulk materials (black), QDs with Δ_{XX} negligiable and attractive (red) and with Δxx large and attractive (blue) [Taken from[19]].

2.6 Brief history of MEG and controversy

The idea of MEG in QDs was suggested for the first time in 2001 by Nozik *et al*. [46]. Soon after, Schaller *et al*. demonstrated MEG for the first time via I.I in PbSe QDs using TA spectroscopy [21]. The PbSe QDs were pumped with photon energies above (~$3.3E_g$) and below ($1.54E_g$) MEG threshold at low fluences. In the case of below MEG pumping,

there was only a long-lived single exciton signature, whereas, at high photon energies, a fast decay of biexciton to single exciton was observed which is attributed to the signature of MEG. The authors repeated the process for several different pump wavelengths and sample sizes and found that the MEG threshold for PbSe QDs was about $3E_g$, as shown in Figure 2.11 a) and b).

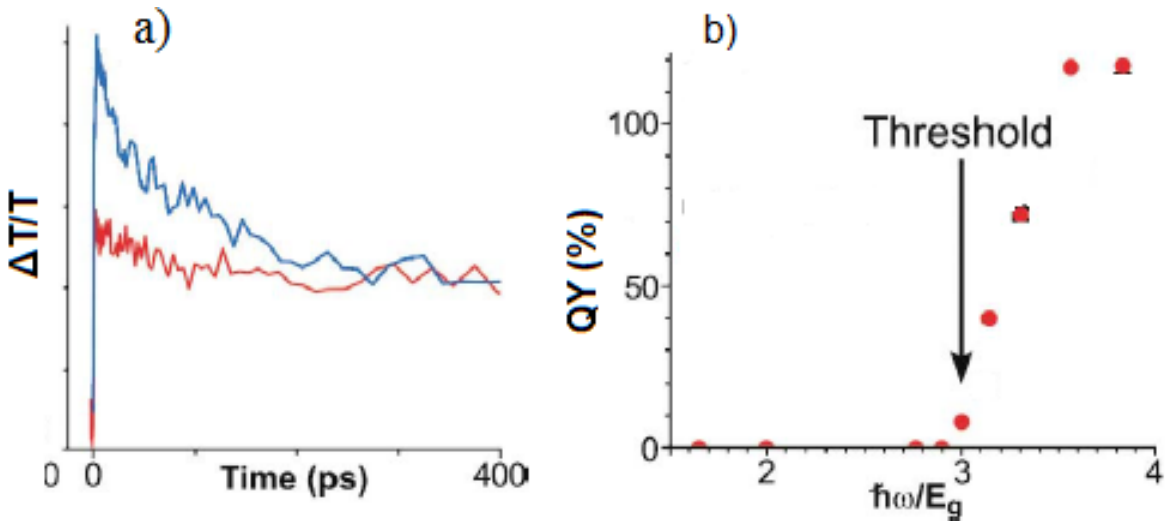

Figure 2.11. MEG measurements for PbSe QDs. a) TA dynamics of a PbSe QDs at above (blue) and below (red) MEG threshold. b) MEG QY as function of $\hbar\omega/E_g$ which clearly shows that MEG threshold is about $3E_g$. [Modified from [21]].

Shortly after that Ellingston *et al.* reported extremely efficient MEG (average 3 excitons per absorbed photon at $4E_g$) in PbSe and PbS colloids using both an intraband and an interband TA experiment [47]. Furthermore, they observed a MEG threshold of $2E_g$ for these materials, which was significantly less than the previously reported value. The reason for probing intraband dynamics was that the observed TA traces are linearly proportional to the exciton multiplicity and thus a clear MEG signal would be recorded [47]. Soon after this confirmative study, in an extended study, Schaller's group focused on the degree of energy conservation in the MEG process [48]. Herein, they attained up to seven excitons

per absorbed photon with energy of $7.8E_g$ in PbSe(E_g= 0.636 eV) and PbS QDs. The MEG threshold for those colloids was found to be about $3E_g$, confirming the results presented in reference [21].

These impressive initial MEG results motivated significant interest in this research field. Before long, Schaller and co-workers [49] reported efficient MEG in a comparative examination of PbSe and CdSe QDs using ultrafast TA spectroscopy. The MEG onsets for PbSe (E_g=0.86 eV) and CdSe (E_g=2.0 eV) were observed as $2.9E_g$ and $2.5E_g$, respectively, as shown in Figure 2.12. This work demonstrated the generality of MEG in QDs because, despite the different electronic structure of PbSe and CdS nanostructures, they both showed efficient MEG.

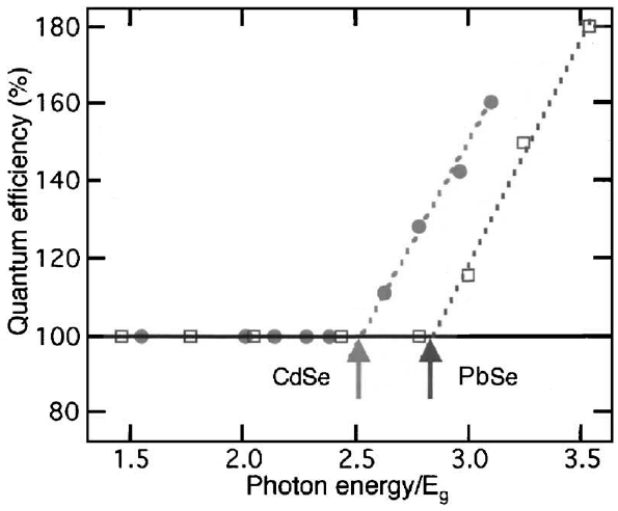

Figure 2.12. MEG efficiency as a function of excitation photon energy normalized by bandgap energy for CdSe (circles) and PbSe (squares) [Modified from [49]].

In a different study, Beard *et al.*[25] studied MEG in indirect-band gap Si QDs (E_g=1.2 eV) using intraband TA spectroscopy. The reason for monitoring the intraband dynamics of the samples was that due to indirect band gap Si nanoparticles, they have a weak linear band gap absorption feature and thus a weak bleach (state filling) signal. The MEG threshold and the maximum attained QY were $2.4E_g \pm 0.1$ and 2.6 ± 0.2 exciton per

absorbed photon at $3.4E_g$, respectively. In this work the MEG QY value was calculated using a new method. The QY value is found from the ratio, R_{pop}, of the average number of excitons generated per excited QD immediately after excitation and cooling to the band edge to the number remaining after the recombination of pump-created multi-excitons is complete. The QY value corresponds to the ratio between the R_{pop} value in the limit of low fluences where the possibility of absorbing more than one photon is negligible. Figure 2.13 illustrates the extraction of QY values with the proposed method for two different sizes of Si QDs.

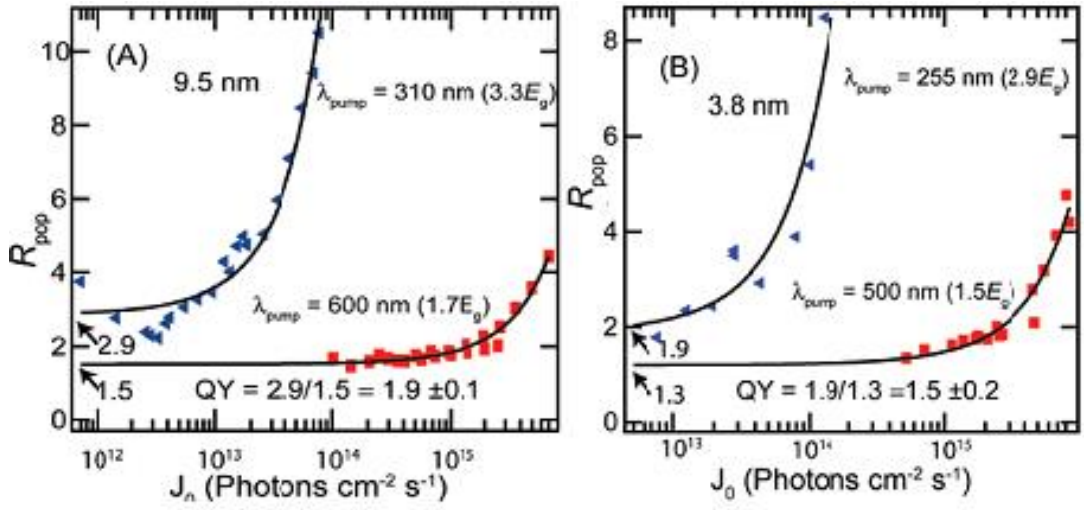

Figure 2.13. Average number of excitons produced for each QD as a function of pump fluence for samples with diameter of: A) 9.5 nm pumped with photon energies of $3.3E_g$ (blue) and $1.7E_g$ (red), B) 3.8 nm pumped with photon energies of $2.9E_g$ (blue) and $1.5E_g$ (red). [Modified from [25]].

As explained in the theory section, the MEG threshold in some QDs, wherein $m_e << m_h$, is as low as $2E_g$ being limited only by the energy conservation criterion. This feature encouraged Schaller *et al.*[45] to investigate MEG onset in InAs nanoparticles using TA spectroscopy. In the experiment InAs core and InAs/CdSe core/shell NCs were pumped under both high ($4.28E_g$) and low ($1.53E_g$) excitations, as illustrated in Figure 2.14 a) and b), respectively. As was predicted, MEG threshold for InAs samples were slightly

over $2E_g$ which is significantly less than that of lead salts reported previously. Another interesting feature observed here was that as the sample size increased the MEG onset increased beyond the $2E_g$ point. In addition, the authors also performed measurements of X-X interaction to investigate the change in the MEG threshold. However, they observed attractive Δ_{XX} of 16 meV which corresponds to only 1% of the band gap. Thus, the small fraction of X-X interaction energy does not have a significant effect on MEG threshold value in InAs NCs.

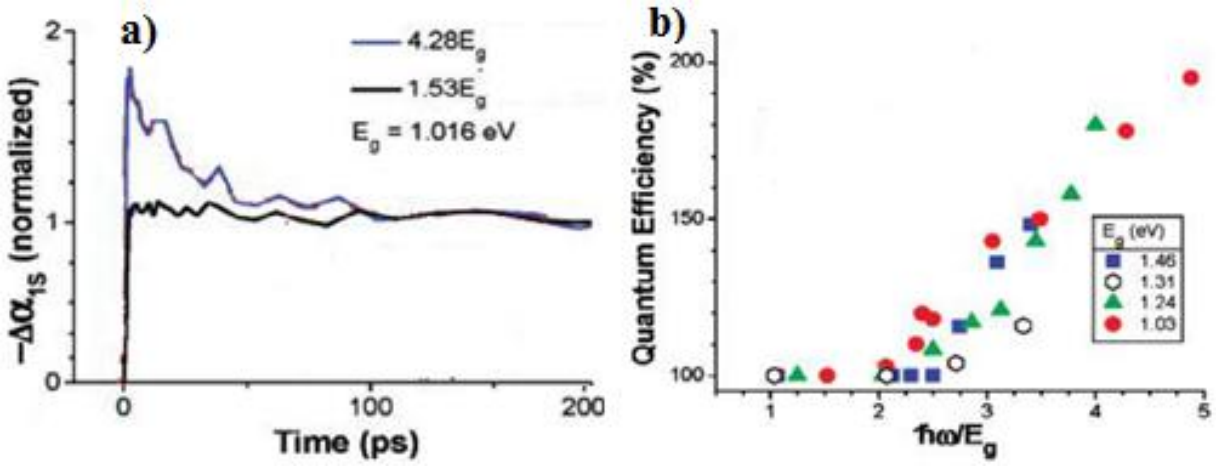

Figure 2.14. MEG measurements of InAs samples. a) TA dynamics of InAs/CdSe core/shell structures pumped at high (blue) and low (black) excitations. b) MEG quantum efficiency as a function of pump photon energy per band gap for three different in size InAS/CdSe core/shell QDs and one InAs core QDs. [Modified from [45]].

In contrast to the above efficient MEG reports, Nair and co-worker found no MEG in CdSe and CdTe QDs for excitation at least three times above band gap energy using the TRPL method [50]. Unlike the above MEG papers, they observed no difference between transients taken at high and low pump energies, as shown in Figure 2.15 a) and b).

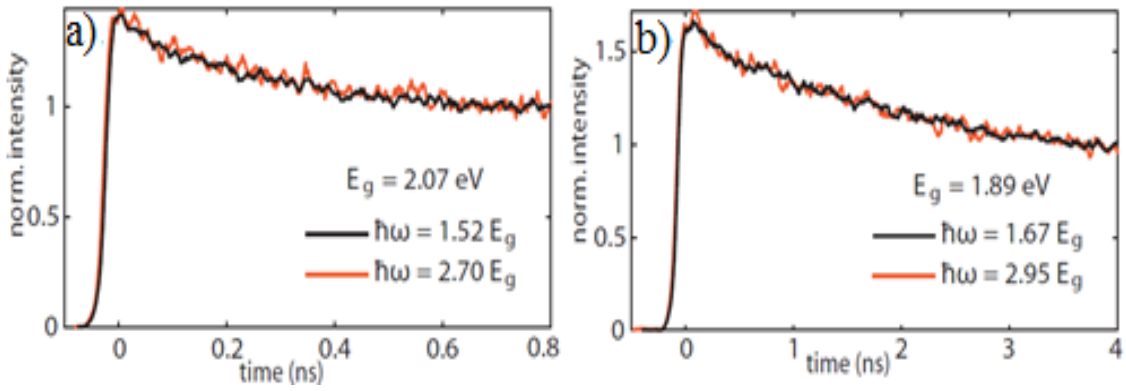

Figure 2.15. Comparison of the transient PL dynamics taken under high (red) and low (black) pump energy pulses for two samples with band gaps of a) E_g= 2.07 eV and b) E_g=1.89 eV. [Modified from [50]].

In an extended study, Pijpers and co-workers could not reproduce their previously reported efficient MEG results [51] in InAs QDs using both TA and Terahertz TA experiments [52]. They attributed these discrepancies to a number of factors including different batches, uncertainty in the absorption cross-section and inhomogeneity in the pump beam. Moreover, Ben-Lulu *et al*. in a new study could not find the evidence of MEG in InAs/CdSe/ZnSe core/shell/shell semiconductor nanoparticles [53]. These contradictory results casted doubt about the efficiency and generality of MEG in semiconductor QDs.

A period of disagreement followed after the discrepancies between the early MEG reports until a few studies emerged which resolved the reasons for the differing results. Mcguire *et al.*'s work [34] was one of these studies wherein they observed that MEG efficiency is affected by the sample synthesising conditions and photoionization of the samples. Firstly, the group observed that about 30% MEG QY difference was found in two sets of PbSe QDs which were identical in size but differ in growing batches. Secondly, to emphasize the influence of photocharging on MEG QY of PbSe QDs, the authors performed the TRPL and TA experiments under stirred and static circumstances, as shown in Figure 2.16 a) and b), respectively. The results showed that the apparent MEG QY taken under the static case is about 3 times more than that of the stirred case. Based on these

results, the authors claimed that the earlier overestimated MEG QYs were due to the uncontrolled photocharging which can be avoided by stirring the sample solutions vigorously [34].

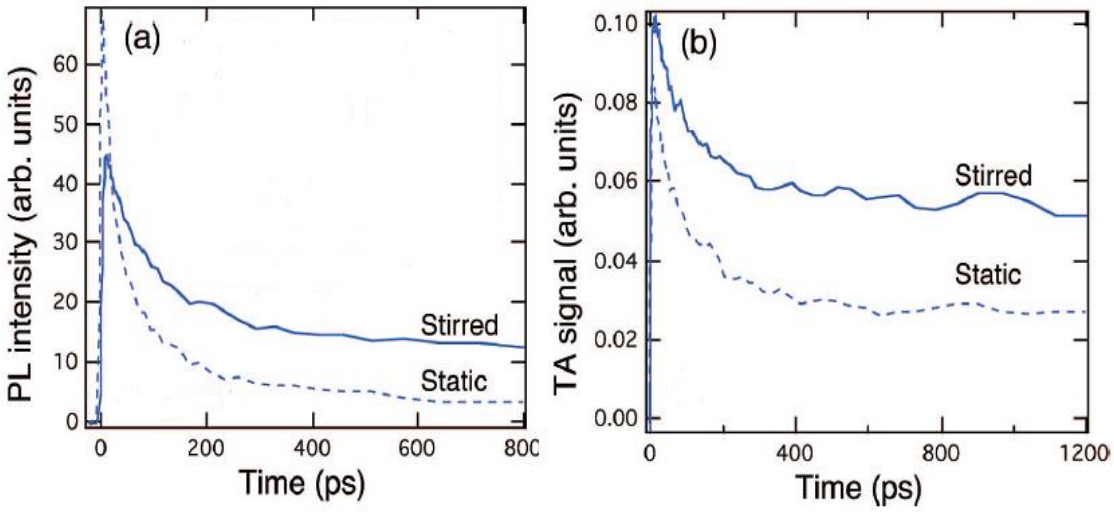

Figure 2.16. Ultrafast PL (a) and TA (b) dynamics recorded under stirred (solid lines) and static (dashed lines) conditions. [Modified from [34]].

The same group in a different study [35] announced that the effect of photocharging significantly diverges the measured MEG QY in PbSe nanoparticles from its actual value. Results are illustrated in Figure 2.17 a) and b). They found a significant difference (about a factor of 3) between PL dynamics of stirred and static cases. Thus the average number of excitons in each QD, A/B, at low pump fluence exhibits MEG QY where still there is a remarkable difference between the stirring and static circumstances. All these findings indicate that the early seemingly high MEG values were owing to the photocharging of the sample which occurs by sequential ultrafast pump pulses [35]. The same group confirmed their studies by conducting new MEG measurements in PbSe QDs under flowing and static conditions [33]. Here they observed that there was a clear MEG QY deviation between static and flowing conditions proving that excited charges are

trapped on the surface of QDs. In the same study the authors studied the effect of surface treatment on MEG efficiency in the PbSe QDs using Cd-oleate treatment.

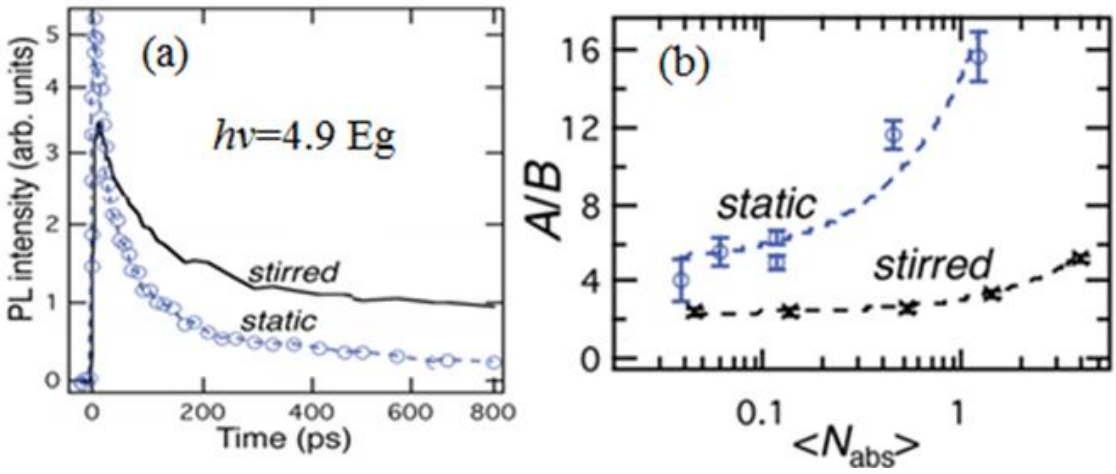

Figure 2.17. Comparison of; a) PL dynamics taken under stirred (black line) and static (circles) and b) the corresponding average number of excitons per QD as a function of average number of photons (<N_{abs}>). [Modified from [35]].

They observed that MEG efficiency in the treated samples was reduced by a factor of 10 in comparison with untreated samples. Finally the authors concluded that preliminary seemingly high MEG efficiencies were due to the effect of photocharging which can be avoided by flowing and by a better sample engineering [33]. Nevertheless, some groups reported efficient MEG in QDs after realizing the effect of photocharging which was suppressed by flowing or stirring the sample. For example, Stubbs *et al*. [37] detected efficient MEG in InP nanoparticles (1.18 exciton per absorbed photon at $2.6E_g$) with supressing the impact of photocharging by stirring the sample vigorously. Likewise, Hardman *et al.* and Gachet *et al.* reported efficient MEG in PbS [54] (1.6 exciton per absorbed photon at $4E_g$) and in type II CdTe/CdSe [55] (1.6 exciton per absorbed photon at $3.75E_g$) QDs, respectively, after carefully taking the effect of photocharging into consideration.

2.7 Brief history of X-X interaction in type-II QDs

The staggered band alignment of type-II QDs enables their optical properties to be manipulated by control of the core diameter and shell thickness; consequently, they have been the subject of interest in many studies. The investigations were mainly about the multi-exciton interactions and emission lifetime as a function of shell thickness. In this regard, Klimov *et al*. [39] has reported a giant (~106 meV) repulsive Δ_{XX} in CdS/ZnSe type-II NCs, using TRPL spectroscopy, as shown in Figure 2.18

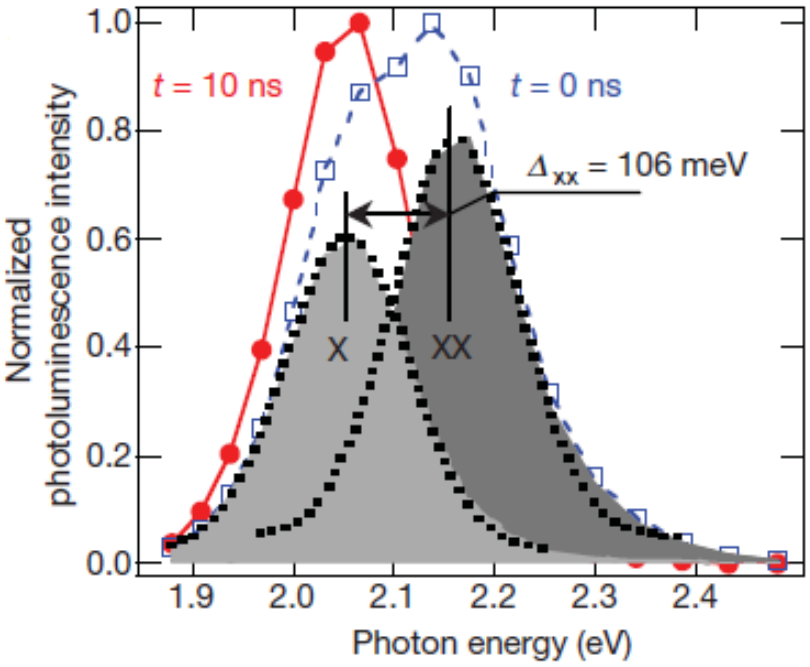

Figure 2.18. The TRPL spectra of CdS/ZnSe QDs at t=0 ns (red) (single exciton) and t= 10 ns (biexciton) (blue). [Modified from [39]].

They also theoretically calculated the Δ_{XX} and found about 91 meV which is consistent with the experimental results. The authors` motivation was that if the repulsive Δ_{XX} is greater than the transition line width then the balance between absorption and the stimulated emission varies, enabling increased optical gain. Immediately after this paper, the same group demonstrated large blue shifted Δ_{XX} (80 meV) and optical gain in the

single exciton regime of ZnTe/CdSe NCs. The X-X interaction results were supported with theoretical calculations conducted in the same study [14]. In another study, Sachin and co-workers [56] studied ultrafast charge dynamics of CdTe/CdS type-II QDs using TRPL and femtosecond TA spectroscopy. They observed an increase in the average emission lifetime of carriers as the shell thickness increased in the studied QDs, indicating that as the CdS shell thickness increases the overlap of the electron and hole wavefunction decreases. Additionally, a direct relationship between the rise time and shell thickness was observed. In a later study, the same group investigated the charge transfer dynamics of CdTe/CdSe core-shell heterostructures and found that the carrier average emission lifetime was linearly proportional to the CdSe shell thickness [57].

Piryantski *et al*. [18] theoretically calculated Δ_{XX} in type-II core-shell QDs. They separately calculated the contribution to the Δ_{XX} from direct Coulomb coupling, always large and positive, and from core-shell interface polarization, either large and positive or small and negative. Energy criteria were used to determine the carrier localization regimes that define the type of QDs. For instance, the electron resides in the core if its energy is less than the conduction band of the shell and the hole resides in the shell if its energy is less than the valance band off-set, as shown in Figure 2.19. The group also quantitatively measured the spatial separation between electrons and holes. The authors concluded that the biexciton interaction energy in type-II heterostructures is generally repulsive and larger than the transition line width (on the order of 100 meV) enabling increased optical gain [18].

In another study, Ivanov *et al*. [40] studied carrier dynamics of type II CdS/ZnSe core/ shell heterostructures, in which electrons and holes reside in turn in the core and shell using the TRPL experiment. The group managed to increase the average emission lifetime

from 23 ns to 45 ns by increasing the ZnSe shell thickness in the single exciton regime, showing that as the shell becomes thicker the spatial separation between the electron and hole increases. In the high excitation densities, the ultrafast decay rate of biexcitons was found to be slower as the ZnSe shell thickness increased. They observed ~70 meV repulsive X-X binding energy in CdS/ZnSe core/shell heterostructures. The resultant reconstructed TRPL spectra was sliced in times t=0 and t=2 ns, as shown in Figure 2.20. At t=0 ns the recorded signal was attributed to biexciton emission whereas, at t= 2 ns the signal is due to long-lived single excitons.

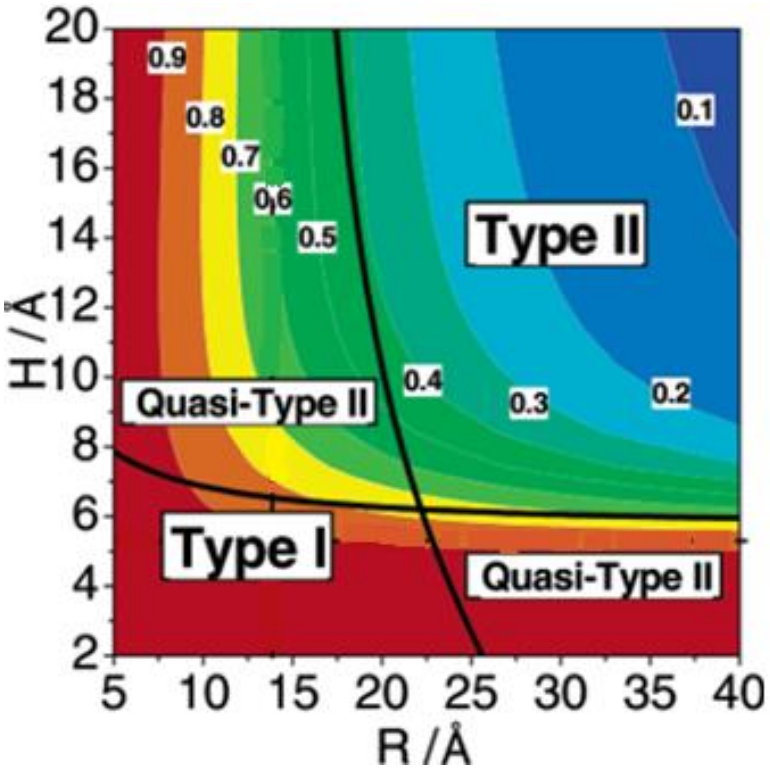

Figure 2.19. Theoretically calculated constant-electron-hole overlap integral contours (decimal numbers) and localization phase diagram based on the carrier energy criteria. R and H represent the core radius and shell thickness, respectively. The electron is delocalized over the whole core-shell structure in the left hand side quasi-Type II regime, while, the hole is delocalized over the entire structure in the right hand side quasi type II regime. Å represents Angstrom unit. [Modified from [18]].

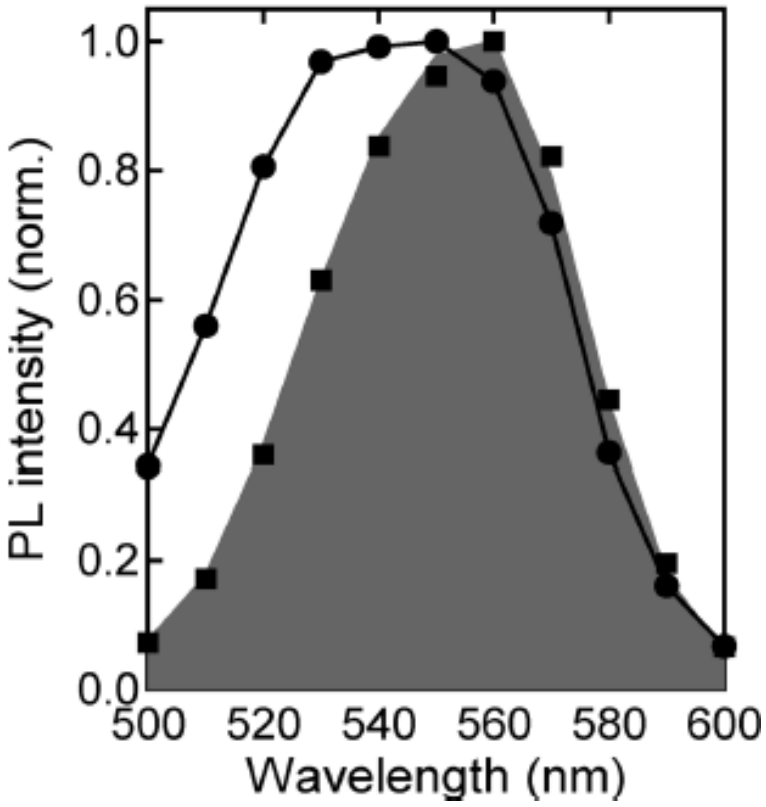

Figure 2.20. Comparison of t=0 ns PL component (circles) and t=2 ns PL component (squares) of CdS/ZnSe core/shell heterostructures.[Modified from [40]].

The reported repulsive Δ_{XX} was found to be directly proportional with the ZnSe shell thickness. This characteristic feature was attributed to the fact that as the overlap integral decreases, the attractive Coulomb interaction between electrons and holes drops and the repulsive Coulomb interaction between electrons in the core increases [40].

Oron *et al*. [13] studied dynamics of type-II CdTe/CdSe heterostructures using the quasi-continuous-wave excitation technique. They observed a volume dependant emission life time which altered from 20 ns for a CdTe core to 240 ns for the thickest CdSe shell. Investigating the X-X interaction in CdTe/CdSe core-shell structures with a set of shell thicknesses, they observed a maximum blue shift of ~30 meV in the thickest CdSe shell [13].

2.8 Summary

Colloidal QDs are semiconductor nanostructures in which electrons and holes are confined in three dimensions due to strong quantum confinement. They have quasi-discrete energy levels and their electronic and optical properties are size-dependant, which makes them attractive for a number of applications. Depending on the material composition and charge localization in QDs, they are categorized into two types: type-I and type-II. In the former the electron and hole wavefuntion overlap is increased, whereas it is decreased in the latter. Multiple exciton generation is efficient in colloidal QDs due to separated energy levels. Therefore, these nanocrystals have a promising future regarding 3rd generation PVs. Due to enhanced Coulomb interaction between carriers in QDs, Δ_{XX} in these nanostructures is significant, compared with bulk materials. Depending on the sign of Δ_{XX}, the band gap of the dot can either increase or decrease by the magnitude of Δ_{XX}. Due to the spatial separation of electrons and holes, the magnitude of Δ_{XX} in type-II QDs is significantly larger than in type-I QDs.

2.9 References

1. Qingjiang Sun, Y.A.W., Lin Song Li, Daoyuan Wang, Ting Zhu, Jian Xu, Chunhe Yang, Yongfang Li, , *Bright, multicoloured light-emitting diodes based on quantum dots.* Nat Photon, 2007. **1**(12): p. 717.
2. Jamieson, T., et al., *Biological applications of quantum dots.* Biomaterials, 2007. **28**(31): p. 4717-4732.
3. Klimov, V.I., et al., *Optical Gain and Stimulated Emission in Nanocrystal Quantum Dots.* Science, 2000. **290**(5490): p. 314-317.
4. Binks, D.J., *Multiple exciton generation in nanocrystal quantum dots - controversy, current status and future prospects.* Physical Chemistry Chemical Physics. **13**(28): p. 12693-12704.
5. Klimov, V., *Spectral and Dynamical Properties of Multiexcitons in Semiconductor Nanocrystals.* Annu. Rev. Phys. Chem., 2006. **58**: p. 635–73.
6. Barbagiovanni, E.G., et al., *Quantum confinement in Si and Ge nanostructures.* Journal of Applied Physics, 2012. **111**(3): p. 034307.
7. Klimov, V.I., *Semiconductor and Metal Nanocrystals*, ed. V.I. Klimov. Vol. 484. 2004, New York.
8. Griffiths, D.J., *Introduction to Quantum Mechanics*. 1995, Prentice Hall: Englewood Cliffs.
9. Klimov, E.V.I., *Nanocrystal quantum dots*. 2nd ed. 2004, New York: CRC Press.
10. Bang, J., et al., *ZnTe/ZnSe (Core/Shell) Type-II Quantum Dots: Their Optical and Photovoltaic Properties.* Chemistry of Materials, 2009. **22**(1): p. 233-240.
11. Nanda, J., et al., *Absorption cross sections and Auger recombination lifetimes in inverted core-shell nanocrystals: Implications for lasing performance.* Journal of Applied Physics, 2006. **99**(3): p. 034309-7.
12. Jack Li, J., et al., *Wavefunction engineering: From quantum wells to near-infrared type-II colloidal quantum dots synthesized by layer-by-layer colloidal epitaxy.* Chemical Physics, 2005. **318**(1–2): p. 82-90.
13. Oron, D., M. Kazes, and U. Banin, *Multiexcitons in type-II colloidal semiconductor quantum dots.* Physical Review B, 2007. **75**(3): p. 035330.
14. Nanda, J., et al., *Light Amplification in the Single-Exciton Regime Using Excitonâ^'Exciton Repulsion in Type-II Nanocrystal Quantum Dots.* The Journal of Physical Chemistry C, 2007. **111**(42): p. 15382-15390.
15. Deutsch, Z., et al., *Energetics and dynamics of exciton-exciton interactions in compound colloidal semiconductor quantum dots.* Physical Chemistry Chemical Physics. **13**(8): p. 3210-3219.
16. Ivanov, S.A., et al., *Light Amplification Using Inverted Core/Shell Nanocrystals: Towards Lasing in the Single-Exciton Regime.* The Journal of Physical Chemistry B, 2004. **108**(30): p. 10625-10630.
17. Schaller, R.D., V.M. Agranovich, and V.I. Klimov, *High-efficiency carrier multiplication through direct photogeneration of multi-excitons via virtual single-exciton states.* Nat Phys, 2005. **1**(3): p. 189-194.
18. Piryatinski, A., et al., *Effect of Quantum and Dielectric Confinement on the Exciton−Exciton Interaction Energy in Type II Core/Shell Semiconductor Nanocrystals.* Nano Letters, 2006. **7**(1): p. 108-115.
19. N. McElroy, M.C., A. Al-Otaify, R. Page, D.J. Binks, *Quantum Dot Solar Cells*. Lecture Notes in Nanoscale, ed. J.W.a.Z.M. Wang. 2013, New York: Springer Science+Business Media.
20. Klimov, V.I., et al., *Quantization of Multiparticle Auger Rates in Semiconductor Quantum Dots.* Science, 2000. **287**(5455): p. 1011-1013.
21. Schaller, R.D. and V.I. Klimov, *High Efficiency Carrier Multiplication in PbSe*

Nanocrystals: Implications for Solar Energy Conversion. Physical Review Letters, 2004. **92**(18): p. 186601.
22. Shockley, W. and H.J. Queisser, *Detailed Balance Limit of Efficiency of p-n Junction Solar Cells.* Journal of Applied Physics, 1961. **32**(3): p. 510-519.
23. Hanna, M.C. and A.J. Nozik, *Solar conversion efficiency of photovoltaic and photoelectrolysis cells with carrier multiplication absorbers.* Journal of Applied Physics, 2006. **100**(7): p. 074510.
24. KOC, S., *The quantum efficiency of the photo-electric effect in germanium for the 0.3 2 μ wavelength region.* Czechoslovak Journal of Physics, 1957. **7**(1): p. 91-95.
25. Beard, M.C., et al., *Multiple Exciton Generation in Colloidal Silicon Nanocrystals.* Nano Letters, 2007. **7**(8): p. 2506-2512.
26. Beard, M.C. and R.J. Ellingson, *Multiple exciton generation in semiconductor nanocrystals: Toward efficient solar energy conversion.* Laser & Photonics Reviews, 2008. **2**(5): p. 377-399.
27. Nozik, A.J., *Multiple exciton generation in semiconductor quantum dots.* Chemical Physics Letters, 2008. **457**(1-3): p. 3-11.
28. Benisty, H., C.M. Sotomayor-Torrès, and C. Weisbuch, *Intrinsic mechanism for the poor luminescence properties of quantum-box systems.* Physical Review B, 1991. **44**(19): p. 10945-10948.
29. Takeda, Y. and T. Motohiro, *Requisites to realize high conversion efficiency of solar cells utilizing carrier multiplication.* Solar Energy Materials and Solar Cells, 2010. **94**(8): p. 1399-1405.
30. Richard, D.S., A.P. Melissa, and I.K. Victor, *Effect of electronic structure on carrier multiplication efficiency: Comparative study of PbSe and CdSe nanocrystals.* Applied Physics Letters, 2005. **87**(25): p. 253102.
31. Efros, A.L., V.A. Kharchenko, and M. Rosen, *Breaking the phonon bottleneck in nanometer quantum dots: Role of Auger-like processes.* Solid State Communications, 1995. **93**(4): p. 281-284.
32. Hendry, E., et al., *Direct Observation of Electron-to-Hole Energy Transfer in CdSe Quantum Dots.* Physical Review Letters, 2006. **96**(5): p. 057408.
33. Midgett, A.G., et al., *Flowing versus Static Conditions for Measuring Multiple Exciton Generation in PbSe Quantum Dots.* The Journal of Physical Chemistry C. **114**(41): p. 17486-17500.
34. McGuire, J.A., et al., *New Aspects of Carrier Multiplication in Semiconductor Nanocrystals.* Accounts of Chemical Research, 2008. **41**(12): p. 1810-1819.
35. McGuire, J.A., et al., *Apparent Versus True Carrier Multiplication Yields in Semiconductor Nanocrystals.* Nano Letters. **10**(6): p. 2049-2057.
36. Pooja, T. and K. Patanjali, *False multiple exciton recombination and multiple exciton generation signals in semiconductor quantum dots arise from surface charge trapping.* J. Chem. Phys., 2011. **134**(9): p. 094706.
37. Stubbs, S.K., et al., *Efficient carrier multiplication in InP nanoparticles.* Physical Review B, 2010. **81**(8): p. 081303.
38. Klimov, V., S. Hunsche, and H. Kurz, *Biexciton effects in femtosecond nonlinear transmission of semiconductor quantum dots.* Physical Review B, 1994. **50**(11): p. 8110-8113.
39. Klimov, V.I., et al., *Single-exciton optical gain in semiconductor nanocrystals.* Nature, 2007. **447**(7143): p. 441-446.
40. Ivanov, S.A. and M. Achermann, *Spectral and Dynamic Properties of Excitons and Biexcitons in Type-II Semiconductor Nanocrystals.* ACS Nano. **4**(10): p. 5994-6000.
41. Kang, K.I., et al., *Confinement-enhanced biexciton binding energy in semiconductor quantum dots.* Physical Review B, 1993. **48**(20): p. 15449-15452.
42. Achermann, M., J.A. Hollingsworth, and V.I. Klimov, *Multiexcitons confined within a subexcitonic volume: Spectroscopic and dynamical signatures of neutral and charged biexcitons in ultrasmall semiconductor nanocrystals.* Physical Review B, 2003. **68**(24): p.

245302.
43. Woggon, U., et al., *Confined biexcitons in CuBr quantum dots.* Journal of Luminescence, 1994. **59**(3): p. 135-145.
44. Sitt, A., et al., *Multiexciton Engineering in Seeded Core/Shell Nanorods: Transfer from Type-I to Quasi-type-II Regimes.* Nano Letters, 2009. **9**(10): p. 3470-3476.
45. Schaller, R.D., J.M. Pietryga, and V.I. Klimov, *Carrier Multiplication in InAs Nanocrystal Quantum Dots with an Onset Defined by the Energy Conservation Limit.* Nano Letters, 2007. **7**(11): p. 3469-3476.
46. Nozik, A.J., *Spectroscopy and hot electron relaxation dynamics in semiconductor quantum wells and quantum dots.* Annual Review of Physical Chemistry, 2001. **52**(1): p. 193-231.
47. Ellingson, R.J., et al., *Highly Efficient Multiple Exciton Generation in Colloidal PbSe and PbS Quantum Dots.* Nano Letters, 2005. **5**(5): p. 865-871.
48. Schaller, R.D., et al., *Seven Excitons at a Cost of One:â€‰ Redefining the Limits for Conversion Efficiency of Photons into Charge Carriers.* Nano Letters, 2006. **6**(3): p. 424-429.
49. Schaller, R.D., M.A. Petruska, and V.I. Klimov, *Effect of electronic structure on carrier multiplication efficiency: Comparative study of PbSe and CdSe nanocrystals.* Applied Physics Letters, 2005. **87**(25): p. 253102.
50. Nair, G. and M.G. Bawendi, *Carrier multiplication yields of CdSe and CdTe nanocrystals by transient photoluminescence spectroscopy.* Physical Review B, 2007. **76**(8): p. 081304.
51. Pijpers, J.J.H., et al., *Carrier Multiplication and Its Reduction by Photodoping in Colloidal InAs Quantum Dots.* The Journal of Physical Chemistry C, 2007. **111**(11): p. 4146-4152.
52. Pijpers, J.J.H., et al., *Carrier Multiplication and Its Reduction by Photodoping in Colloidal InAs Quantum Dots.* The Journal of Physical Chemistry C, 2008. **112**(12): p. 4783-4784.
53. Ben-Lulu, M., et al., *On the Absence of Detectable Carrier Multiplication in a Transient Absorption Study of InAs/CdSe/ZnSe Core/Shell1/Shell2 Quantum Dots.* Nano Letters, 2008. **8**(4): p. 1207-1211.
54. Hardman, S.J.O., et al., *Electronic and surface properties of PbS nanoparticles exhibiting efficient multiple exciton generation.* Physical Chemistry Chemical Physics. **13**(45): p. 20275-20283.
55. Gachet, D., et al., *An Upper Bound to Carrier Multiplication Efficiency in Type II Colloidal Quantum Dots*, in *Nano Letters*2009, American Chemical Society. p. 164-170.
56. Rawalekar, S., et al., *Ultrafast Charge Carrier Relaxation and Charge Transfer Dynamics of CdTe/CdS Coreâ^'Shell Quantum Dots as Studied by Femtosecond Transient Absorption Spectroscopy.* The Journal of Physical Chemistry C, 2009. **114**(3): p. 1460-1466.
57. Rawalekar, S., et al., *Surface-State-Mediated Charge-Transfer Dynamics in CdTe/CdSe Core–Shell Quantum Dots.* ChemPhysChem, 2011. **12**(9): p. 1729-1735.

Chapter 3: Experimental techniques

3.1 Introduction

Optical spectroscopy utilises the interactions between matter and light such as the absorption and emission processes. Steady-state absorption and PL spectroscopy allow one to characterise the basic optical transitions in materials and thus evaluate the quality of the sample. These methods are widely used by scientist from a variety of disciplines as these techniques offer direct access to the sample`s electronic structures. Moreover, ultrafast optical spectroscopy is a prevailing tool that sheds light on ultrafast carrier dynamics of materials since it can be non-destructive and its spectrum range is covered by the solar spectrum. Further, the recent technological developments in the field of optical instruments (i.e. ultrafast lasers and detectors) have opened doors to measure exciton dynamics more accurately. For example, the major challenge in determining a correct MEG output in QDs is the fast decay of multiple excitons due to Auger recombination in 10s to 100s of picosecond [2]. In order to be able to measure the exciton dynamics before they nonradiatively recombine, ultrafast lasers are employed as they provide short pulse durations on the scale of sub-100 fs offering more than sufficient time-resolution. Ultrafast TA spectroscopy directly measures the MEG signature in QDs and distinguishes between Auger recombination of multi-excitons and radiative recombination of single excitons (occurs on the time scale of 10s ns [3]). Likewise, a TRPL experiment is also commonly used to detect ultrafast charge dynamics of materials as it also utilizes the remarkable sensitivity of multichannel plates, which is a detector that amplifies incident electron signal by creating an avalanche of the secondary electrons. Optical spectroscopy reveals the electronic structures of semiconductors and answers how the properties of these materials

change with size and shape. This chapter will examine the instruments and experiments that are used in this project in detail.

3.2 Photoluminescence (PL) spectroscopy

PL in QDs is produced by the radiative recombination of excited electron and hole pairs, radiating randomly polarised spontaneous light [4], following the excitation of the system by absorbed photons, as illustrated in Figure 3.1. This process is the reverse of absorption, where PL spectroscopy measures the emitted light intensity as function of wavelength and absorption spectroscopy measures the light transmitted through the sample as a function of wavelength. PL lifetimes in QDs occur on the time-scale of nanoseconds and the resultant light is informative about the semiconductors' electronic structure, in particular about the band edge. The PL linewidth allow access to the materials' size dispersion where a broad linewidth is an indicator of large size dispersion. It is a powerful tool to determine the electronic structures of materials following optical excitation and is a flexible and non-damaging technique. In this study, the PL spectroscopy is primarily used to determine the sample band edge and thus calculate the MEG threshold.

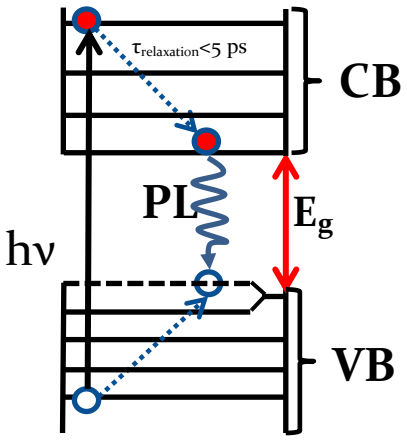

Figure 3.1. PL process in semiconductor QDs.

The design of a common PL experiment basically consists of a light source (laser or lamp), monochromator and photo detector and its data recording is straightforward. In this study, a Horiba Jobin Yvon Fluorolog-3 model FL3-22iHR spectrofluorometer is used to characterize the optical properties of QDs. A 450 W Xenon lamp is used to produce continous pump wavelengths between 240 nm and 600 nm. Two double grating excitation and emission monochromators are used to obtain high resolution and to reject the maximum stray-light, as shown in Figure 3.2. A room temperature R928P photomultiplier tube (PMT) from Hamamatsu Corp. is used to detect the emission spectra from 240 nm to 850 nm region which covers the emission spectrum of QDs used here. The sample compartment is T-shaped, allowing access to a second emission detector if necessary.[5]

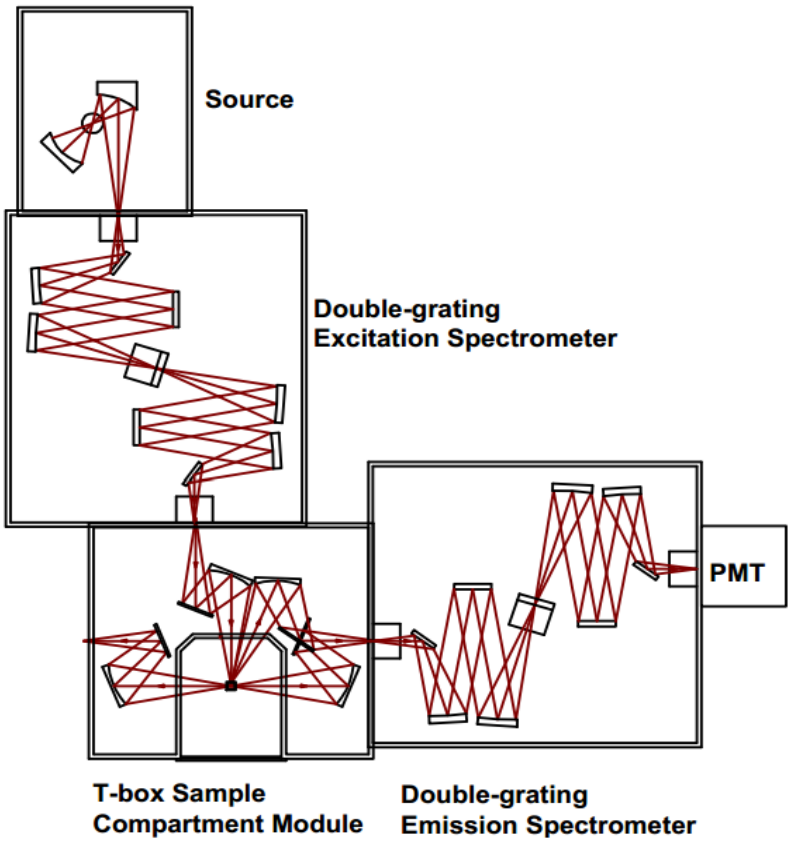

Figure 3.2. The configuration of the Horiba Jobin Yvon Fluorolog-3 model FL3-22iHR spectrofluorometer.[Taken from [5]]

3.3 Absorption spectroscopy

Absorption is an outcome of the interaction between matter and light which is measured in this work across the ultraviolet (UV), visible and NIR part of the spectrum. When a photon is absorbed by a material, depending on the photon's energy, an electron can be transferred from the ground state to a higher energy level (from valance band to the conduction band for semiconductors). The absorption spectrum allows direct access to the materials' electronic levels where each level absorbs a particular amount of energy to reveal the absorption transitions. That is to say, the wavelength corresponding to any transition shows the position of the energy state in the material. In steady state absorption spectroscopy of the QDs, the lowest absorption feature corresponds to the band gap which decreases as the QDs size increases. Since carriers in a QD structure are confined in three dimensions, the resultant absorption feature is an excitonic absorption transition. Steady state absorption spectroscopy is the measurement of the intensity of the incident and transmitted light through an absorbing medium for a desired spectrum range. Absorbance, A, is measured from the transmission (T) where the relationship between them is expressed as [6];

$$A = -\log(T). \qquad (3.1)$$

The amount of transmitted light through the sample is determined from [6];

$$T = \frac{P}{P_0} = e^{-\beta l}, \qquad (3.2)$$

where P and P_0 are, respectively, the transmitted and incident amount of light. β and l are the wavelength dependent absorption coefficient with unit of cm^{-1} and the path length of the sample in unit of cm, respectively. Absorption is described by the Beer Lambert law which states that each section of sample absorbs the same fraction of light and the

absorbance is directly proportional to the sample concentration. This is expressed as [6];

$$A = \varepsilon lc\ , \qquad (3.3)$$

where, ε and c are the molar absorptivity coefficient in the unit of $M^{-1}cm^{-1}$ varying with wavelength, and the molar concentration of the absorbing material in unit of M, respectively.

In this study a Perkin Elmer Lambda 1050 UV/Vis/NIR spectrophotometer is used to characterize the QDs. The device measures the amount of light passes through the sample and hence absorbed by the sample. It consists of three fundamental features: a double holographic grating spectrometer, a double beam and ratio-sensitive optical detection scheme. The spectrometer is capable of measuring the absorption spectra of materials from 175 nm to 3300 nm range by using three unique detectors: a Photomultiplier R6872 (175-860 nm), Peltier-cooled InGaAs (860-2500 nm), and PbS (1800-3300) detectors[7]. As the source, a pre-aligned deuterium lamp and a halogen lamp are placed in the lamp compartment to excite the sample with cw light. The absorption machine has a large, dual sample compartment wherein sample and reference beams travel parallel to each other and two 10 mm cuvette holders are located. By using two beams, the ratio between those beams are recorded which removes signal variation due to any change in the intensity of the source. The absorbance of the sample is proportional to the logarithm of this ratio. Here the sample solution and the blank solvent are, respectively, placed in the sample and reference cuvette holders and the ratio between the transmitted light is recorded. The spectrometer is capable of characterizing both liquid and solid samples and features detector optics that can compensate for the material's width [7].

3.4 Time correlated single photon counting (TCSPC)

TCSPC method is a widely used optical method of measuring the ultrafast carrier dynamics of semiconductors. It directly records the PL intensity following excitation by ultrafast pulses with high repetition rate where the PL intensity is proportional to the number of created excitons. The delay time between the pump pulse and the recorded PL is measured and the process is repeated for a substantial number of laser pulses. Hence the PL decay curve results from the accumulated delayed photon distribution. This method can provide MEG data with low pulse energy [8] where the probability of absorbing more than one photon per dot is negligible. To detect the low excitation rates, a sensitive multi-channel plate (MCP) is employed.

The common optical scheme of a TCSPC experiment consists of an ultrafast laser source, a collection lens, a monochromator, an MCP and electronics, as shown in Figure 3.3. The sample is pumped with the high repetition ultrafast pulses and the resultant PL signals are collected and then directed onto the MCP after passing through the monochromator. A small fraction of the output from the excitation source is directed to the photodiode (PD) to be used as the reference beam which determines the delay time by means of electronics [9]. The time resolution in this method strongly depends on the response of the MCP.

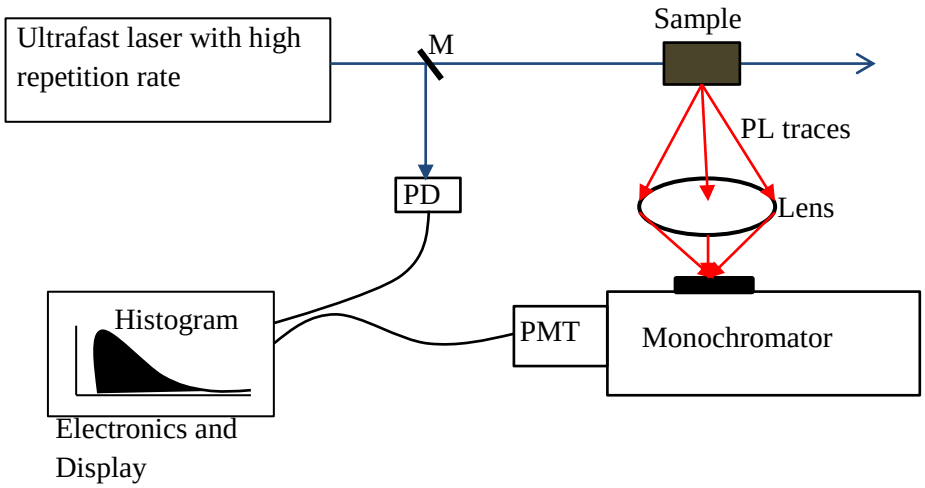

Figure 3.3. Experimental set-up for a typical TCSPC experiment.

Femtosecond mode-locked lasers are widely used as the excitation source for the TCSPC method as they offer unique characteristics *i.e.* low pulse energy, high repetition rate, etc. In this study a Spectra Physics Mai Tai HP mode-locked Ti:sapphire femtosecond laser is used as the main source. It offers sub-100 fs pulses between 720-850 nm with 80 MHz repetition rate which is ideal for collecting fast data. The high repetition rate of this type of laser may cause the optical "pile-up" which results from the detection of more than one photon in the same signal period and misrepresents the signal shape [9] and so is often combined with a pulse selector. Another advantage of the mode-locked Ti:sapphire laser is that its pulse duration is far less than the 10 ps which corresponds to the time spread of the best detectors [9]. The TCSPC experimental set up used in this project was built by Stuart Stubbs and Daniel Espinabarro-Valesquez. The oscillator is pumped by a CW diode-pumped laser producing output at 532 nm with 12 W power. 800 nm peak emission of the Ti:sapphire laser is directed to a Coherent Harmonic generator to produce 400 nm pump pulses via a nonlinear second harmonic generation (SHG) process which is described in the next section. One of the major limitations of a high repetition rate oscillator is that the time period between two consecutive pulses is shorter than the exciton radiative recombination

life time. For example, the radiative recombination life time of the excitons in the sample is 10s of ns [3] in most of QDs. However, the time period between the two sequential pulses of the Mai Tai HP Ti:Sapphire laser is about 12.5 ns which does not give a true value of PL as the recombination process of PL has not completed yet. In order to overcome this problem the oscillator repetition rate was decreased from 80 MHz to 8 MHz using an APE Pulse Select device. This device consists of an acousto-optic modulator (AOM) where a sound wave applied to its transparent crystal creates diffraction for some of the laser pulse at the desired repetition rate, allowing it to be transmitted. The resultant pump pulse at 400 nm with 8 MHz repetition rate can be focused on the sample using a microscope objective lens to increase the pump fluence on the sample. The average power at the sample position is measured to be around 3 mW corresponding to about 0.4 nJ per pulse. The resultant PL trace is collected throughout a Spex monochromator before being directed onto a MCP PMT (Hamamatsu R3809U-50) using a collector lens. The PMT has a large detection area and low dark count rate. A small fraction of the output from the APE Pulse Select is diverted to a silicon photodiode which is then amplified and sent to electronics to determine the delay time between the laser pulse and the PL photon.

3.5 Femtosecond pump probe experiment

An ultrafast pump probe experiment, also known as TA, is an optical spectroscopic technique that has the ability to measure the ultrafast carrier dynamics of materials accurately since it uses laser pulses with sub-picosecond duration. Figure 3.9 illustrates a detailed schematic representation of a typical femtosecond TA experiment. The energy of the pump beam is high enough to excite the system and create hot electrons in QDs. The subsequent probe pulse energy is tuned to a specific energy level to monitor the charge

carrier population. Usually the probe beam energy is tuned to the band edge of the QDs. The resultant spectroscopy shows the charge dynamics as a function of delay time corresponding to the time between pump and probe beams which emerge from the same source. With the development of the femtosecond laser, the ultrafast TA experiment has replaced the flash-photolysis technique which was limited by poor time resolution, sample damage due to long excitation time and the slow response of the detection instruments [9]. Since the ultrafast processes in QDs such as Auger recombination and MEG occur in time scales of 10s of ps or less [10], they require a powerful tool with a better resolution. Hence femtosecond lasers with pulses about 10s of fs are the best candidate to be used for measuring MEG in QDs.

For a typical TA experiment a mode locked-femtosecond Ti:Sapphire laser is used as the main source. However, the pulse energy of femtosecond laser output is in the nJ scale which is not sufficient for the subsequent nonlinear processes *i.e.* white light continuum (WLC) generation and frequency mixing. Therefore an amplifier is required to increase the energy per pulse, though simultaneously decreasing the repetition rate. A substantial amount of output from the amplifier is directed into an optical parametric amplifier (OPA) and the output from this is then directed onto nonlinear crystals to generate second and third harmonic wavelengths. The output from the OPA is used as the pump beam and directed onto the sample to be excited following a chopping process which is phase-locked to a lock-in amplifier and blocks every other pump pulse. The remaining amount of the output from the amplifier is used as the probe beam and focused on to a sapphire window to generate a WLC after passing through a delay stage. Two perpendicular mirrors are placed on the delay line which moves backward and onward to control the delay time between the pump and probe pulses. The delay time (Δt) is calculated from the relationship

between the speed of light (c) and the delayed distance of the translation stage (Δl) which is expressed as;

$$\Delta t = 2\Delta l/c, \qquad (3.4)$$

where the factor of 2 emerges from the back reflection of the light from the delay stage. Here the key concern is that the beam path must be parallel to the delay line to avoid any unexpected spatial movement of the probe beam when the delay line moves backward and forward. In order to obtain a stable WLC from the sapphire plate, the beam power should exceed a critical point which will be explained in the next section. The resultant WLC is directed onto the sample. The pump and probe optical paths (starting from the beam splitter placed just after the amplifier to the sample position) must be equal for some position of the delay stage. The other important requirement is that the spot size of the probe beam must be about 5 times smaller than that of the pump beam so that it experiences a uniform level of excitation transversely [11]. In addition the angle between both beams should be narrow enough so that walk-off does not significantly reduce the pumped volume that can be probed. The intensity-attenuated probe beam is then directed on to the detector after passing through the monochromator to separate the probe wavelength from the WLC. The TA experiment principally measures the transmission change (ΔT) between when the pump beam is on ($T_{pumping}$) and off ($T_{no\ pumping}$). In order to cancel out the contributions from the instruments the ΔT values are divided by the normal transmission value ($T_{no\ pumping}$) which is related to the absorption difference as [6];

$$\frac{\Delta T}{T} = -\Delta\propto l, \qquad (3.5)$$

where $\Delta\propto$ is the absorption difference when pump is on and off, and l is the length of the

sample.

3.5.1 Mode-locked Ti:sapphire laser pulse generation

In a TA experiment the source laser is the heart of the system since its characteristics play a key role from the amplification to the detection process. Four key characterizations of a laser source need to be considered in details before building the experiment; pulse width, pulse energy, the dominant wavelength and the repetition rate [9]. However these parameters can be modulated as required by introducing some external optics except the pulse duration, which can only be modulated inside the cavity. Mode-locking arises when controlling the gain or the loss of the laser cavity periodically at a frequency corresponding to the laser repetition rate [1]. With recent rapid developments in optics technology, modern mode-locked Ti:sapphire femtosecond lasers have become the favourite candidate for the source laser in an ultrafast TA system [10, 11]. This is because, as well as being tunable over a broad wavelength range, these lasers also can produce pulse widths of as low as 10s of fs due to the fact that Ti^{3+} ion offers a wide gain band. These lasers are pumped with high intensity CW lasers since the saturation power of the absorber in Ti:sapphire is relatively high [12]. A typical femtosecond mode-locked Ti:sapphire laser produces wavelengths between 700 nm to 950 nm with a few nJ pulse energy and the repetition rate of around 85 MHz. One of the most common method of generating Ti:sapphire femtosecond pulses is active mode locking which usually employs an AOM inside the optical cavity near to the end mirror, as shown in Figure 3.4. When the AOM is driven with an electrical signal then the acoustic grating produced by the standing wave will turn on and off to scatter light off of the optical path of the laser [13]. In that case the AOM frequency must be equal to the laser repetition rate.

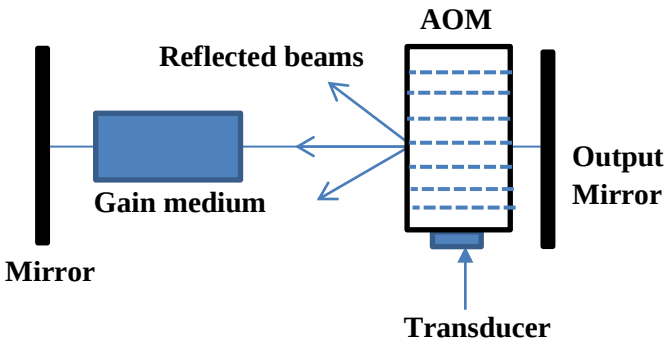

Figure 3.4. A typical active mode-locking system to generate ultra-short pulses. [Modified from [1]].

Ti:sapphire femtosecond lasers can also be based on the Kerr lens mode-locking technique, which is a passive mode-locking method. In that case, the intense beam in the gain medium undergoes self-focusing wherein each spatial point of the beam experiences different refractive index in the amplifying medium. This effect occurs only when the intensity of the beam is high enough and the resultant fast self-mode locking modes are focused through a narrow slit that blocks the low intensity beams and CW modes, as shown in Figure 3.5 [12].

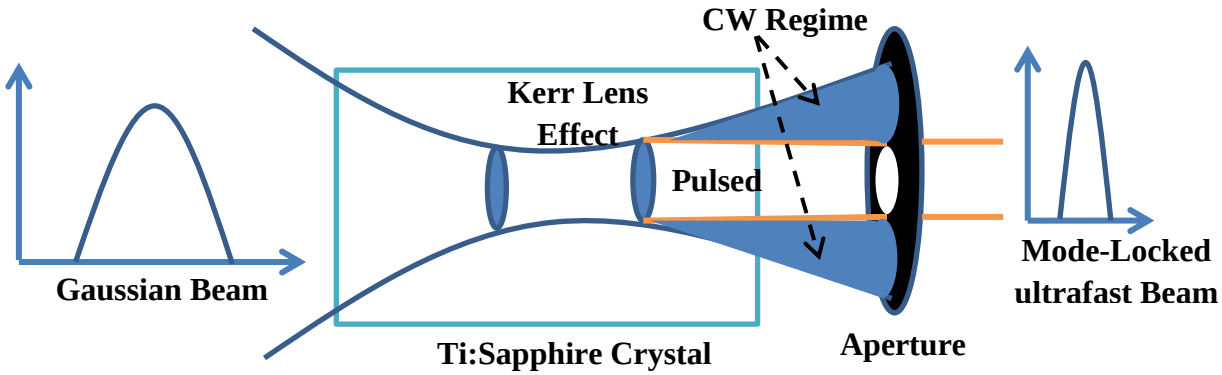

Figure 3.5. The schematic representation of mode-locked femtosecond Ti:Sapphire pulse generation.

As explained earlier for a pump probe experiment, pulses with energy in the scale of nJ is not sufficient to excite enough electrons across the band gap of the QDs for

our experiments or undergo the nonlinear conversion to produce a WLC. Hence amplifiers are used to increase the pulse energy of the Ti:sapphire mode-locked seed lasers.

3.5.2 Amplification of short pulses

Ultra short pulses from a mode locked Ti:sapphire seed laser are typically amplified using an optically pumped Ti:sapphire amplifier. In this process, the low energy pulses from the oscillator are multiply passed through an optically pumped Ti:sapphire crystal placed in a resonator wherein an electro-optical switch is also located to regulate the number of round trips and hence pulse gain. Usually two Pockel cells are used as the electro-optic switch; one of which acts as a pulse picker which accepts the low energy seed pulses into the resonator to be amplified and reduces repetition rate and the other lets the amplified pulse out of the resonator to be compressed, as outlined in Figure 3.6. However, some issues arise during the amplification process. Firstly, the femtosecond pulses' width is broaded as they pass through the gain medium for amplification. Secondly, due to high intensity of the seed laser the Ti:sapphire crystal and other optics can be damaged. To overcome these problems the pulses are initially stretched in time and then recompressed to its initial duration. This method is called chirped pulse amplification which temporarily decreases the pulse intensity by increasing its width using a pair of gratings [12].

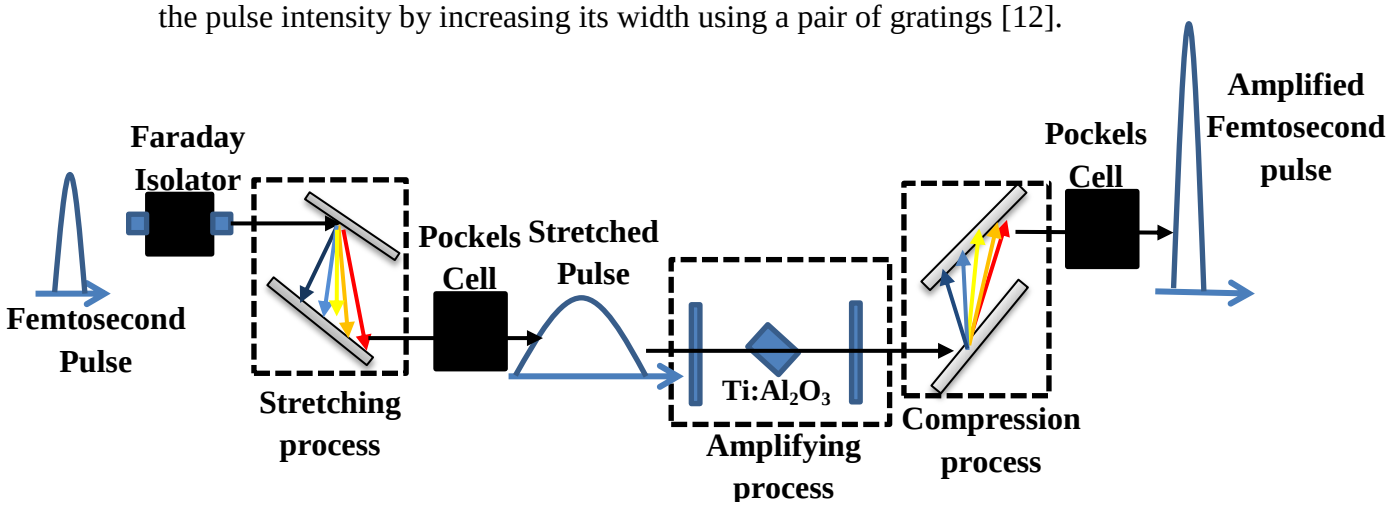

Figure 3.6. A typical layout of a Ti:Sapphire regenerative amplifier.

3.5.3 Nonlinear optics

In principle, nonlinear optics is about the behavior of light in a nonlinear medium where the relationship between electric polarization ($\vec{P}$) and electric field ($\vec{E}$) is nonlinear rather than being linear and expressed as [14];

$$\vec{P} = \varepsilon_0 \chi \vec{E} + \varepsilon_0 \chi_2 \vec{E}^2 + \ldots\ldots\ldots \quad (3.6)$$

where χ and χ_2 denote the linear and 2nd order nonlinear electric susceptibility, respectively, and ε_0 is the electric permittivity. Since the linear coefficient is typically much greater than the nonlinear coefficients, a strong and coherent light source is needed to produce a significant nonlinear response. Therefore a laser beam is used to investigate the nonlinear phenomena rather than a normal light source.

3.5.4 Second harmonic generation

As explained earlier for a TA experiment the main source is a femtosecond Ti:sapphire laser whose maximum efficiency occurs when the lasing wavelength is about 800 nm. However, the band gap energy of most QDs lies above the energy level of the fundamental wavelength of 800 nm and thus more energetic photons are needed to excite the QDs. In addition to generate MEG in QDs, a photon energy greater than at least twice the band gap is required. Therefore, energetic photons are needed. In this regard, a nonlinear medium is used and new coherent light is generated from the 800 nm fundamental beam. When strong laser light with a frequency of (ω) propagates in a nonlinear medium new coherent beams at double the frequency of the incident beam (2ω) emerges, which is called SHG, as seen in Figure 3.7. If the fundamental incident beam and the generated beam are out of phase then destructive interference occurs and the intensity of the SHG beam decreases

which is expressed as:

$$I \propto \left(\frac{sin\left(\frac{\Delta kL}{2}\right)}{\frac{\Delta kL}{2}} \right)^2, \quad (3.7)$$

where Δk is the degree of the phase mismatch between the fundamental beam and the SHG and expressed as $\Delta k = 2k_\omega - k_{2\omega}$ and L is the thickness of the nonlinear medium. It is clear that the maximum conversion efficiency occurs when both beams are in phase. Third harmonic generation (THG) occurs when the fundamental beam (ω) and SHG (2ω) interact in a nonlinear medium providing that both interacted beams are phase matched, as shown in Figure 3.7. Optical parametric amplification is another nonlinear phenomena occurring as a result of two laser beams interacting. In this process two perfectly phase matched beams (pump and signal) combine together to amplify the intensity of the signal beam wherein a third beam (idler) also emerges, as shown in Figure 3.8. By rotating the orientation of the nonlinear crystal in an OPA device, a wide tunability of the output beam is achieved. Therefore, this phenomenon is particularly important for TA experiment wherein the band gap of QDs vary.

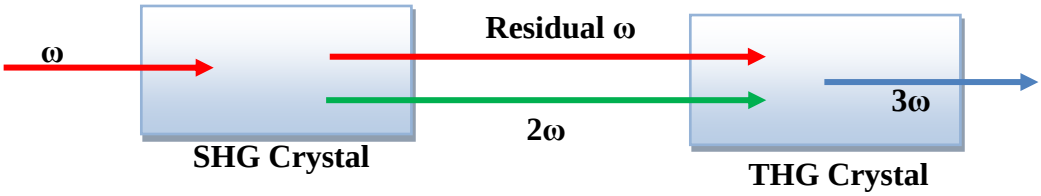

Figure 3.7. Schematic illustration of the SHG and THG processes.

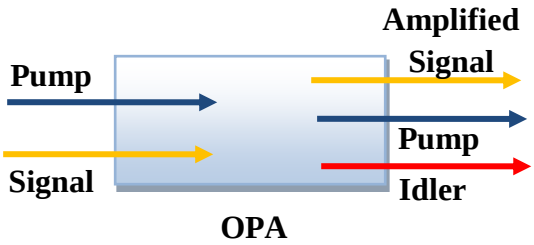

Figure 3.8. Illustration of OPA process.

3.5.5 White light generation

When an intense laser beam propagates in a nonlinear medium, the spectra of the initially monochromatic light can broaden rapidly in this medium, producing wavelengths from the ultraviolet to NIR region, this is called a WLC or supercontinuum [15]. A WLC can be generated in any transparent material within any phase of matter including sapphire, quartz and water, etc. To be able to produce WLC very high power laser pulses are required. In this regard femtosecond pulses with energy in the scale of a few mJ are sufficient to generate WLC as their peak power corresponds to 10s of megawatt. For example a femtosecond Ti:sapphire laser pulses at 800 nm wavelength with modest input energy can produce a broad WLC spectrum from 300 nm to 1500 nm with high spatial coherence which is difficult to achieve with picosecond pulses [6]. WLC generation has been explained by the self-focussing process (SFP), self-phase modulation (SPM) [15] and four wave mixing [16] and it is still the subject of intense research [17]. The threshold for self-focusing is equivalent to the power threshold of WLC and the critical pump power is determined from [15];

$$P_{crt} = \frac{3.77\lambda^2}{8\pi n_l n_k}, \quad (3.8)$$

where λ is the incident beam's wavelength and n_l and n_k denote the refractive indexes in the linear and nonlinear mediums, respectively. Femtosecond WLC has potential use in many applications. In particular the high spatial coherence and wide spectral bandwidth make it crucial for a TA experiment wherein the monitoring of intra-band and inter-band transitions are the main objective. A monochromator is used to pick one specific wavelength from the WLC corresponding to the monitored level in the electronic structure of the sample.

3.6 Visible ultrafast TA experiment

In this study a home built femtosecond TA experiment was used to monitor the exciton dynamics of QDs at the sample band gap. The experiment was originally built by Stuart Stubbs and Samantha Hardman and later modified by my colleague, Ali Al-Otaify, and me. The principle of this experiment is basically that the ultra-short pump beam excites electrons from the valance band to the conduction band and the subsequent probe pulse is tuned to the band edge of the sample to monitor the resultant exciton population. Figure 3.9 illustrates the layout of the femtosecond Vis-TA experiment.

The main light source in this experiment was a Spectra Physics Tsunami Mode-locked Ti:sapphire laser which was pumped by a Spectra Physics Millennia Pro laser. The Millennia Pro laser is a diode-pumped frequency-doubled CW laser producing an output beam of ~10 W at 532 nm. This laser employs neodymium-doped yttrium orthovanadete ($Nd:YVO_4$) and lithium triborate (LBO) crystals as the gain medium and SHG, respectively. The mode-locked Ti:sapphire laser produces 95 fs pulses at 800 nm with a repetition rate of 80 MHz and a pulse energy of about 15 nJ. The energy of these ultrafast pulses is not sufficient for WLC generation or optical parametric amplification [13]. Therefore, the output of the oscillator is used to feed a Spectra Physics Spitfire Ti:Sapphire regenerative amplifier to increase the energy of the ultrafast pulses.

The regenerative amplifier is pumped by a Spectra Physics Empower diode-pumped Nd:YLF laser which produces SHG pulses at 527 nm with an average power of 20 W. The mechanism of the amplifier used here operates as that demonstrated in Figure 3.6. Briefly, the ~15 nJ (~500 mW average power) femtosecond pulses enter into the regenerative amplifier and are directed only in the forward direction using the Faraday isolator. After that the orientated pulses undergo a stretcher process where the pulses widen in time to

prevent any damage to the crystal using a stretcher grating. Next, the first Pockels cell picks the stretched pulses and modifies the repetition rate, followed by the amplification of pulses in the resonator. The amplification process is completed after 20 passes of the pulse in the gain medium which is then let out by switching on the second Pockels cell whose timing is controlled by a computer. Then the amplified pulses are directed to a compressor grating to recompress the amplified pulse to its initial duration. After these procedures, the regenerative amplifier produces output pulses at 800 nm wavelength with a pulse energy of around 4 mJ (~4 W average power) with a 1 kHz repetition rate [19]. About 95% of the output of the regenerative amplifier is sent onto an OPA to produce pump wavelengths tunable over a broad spectrum range.

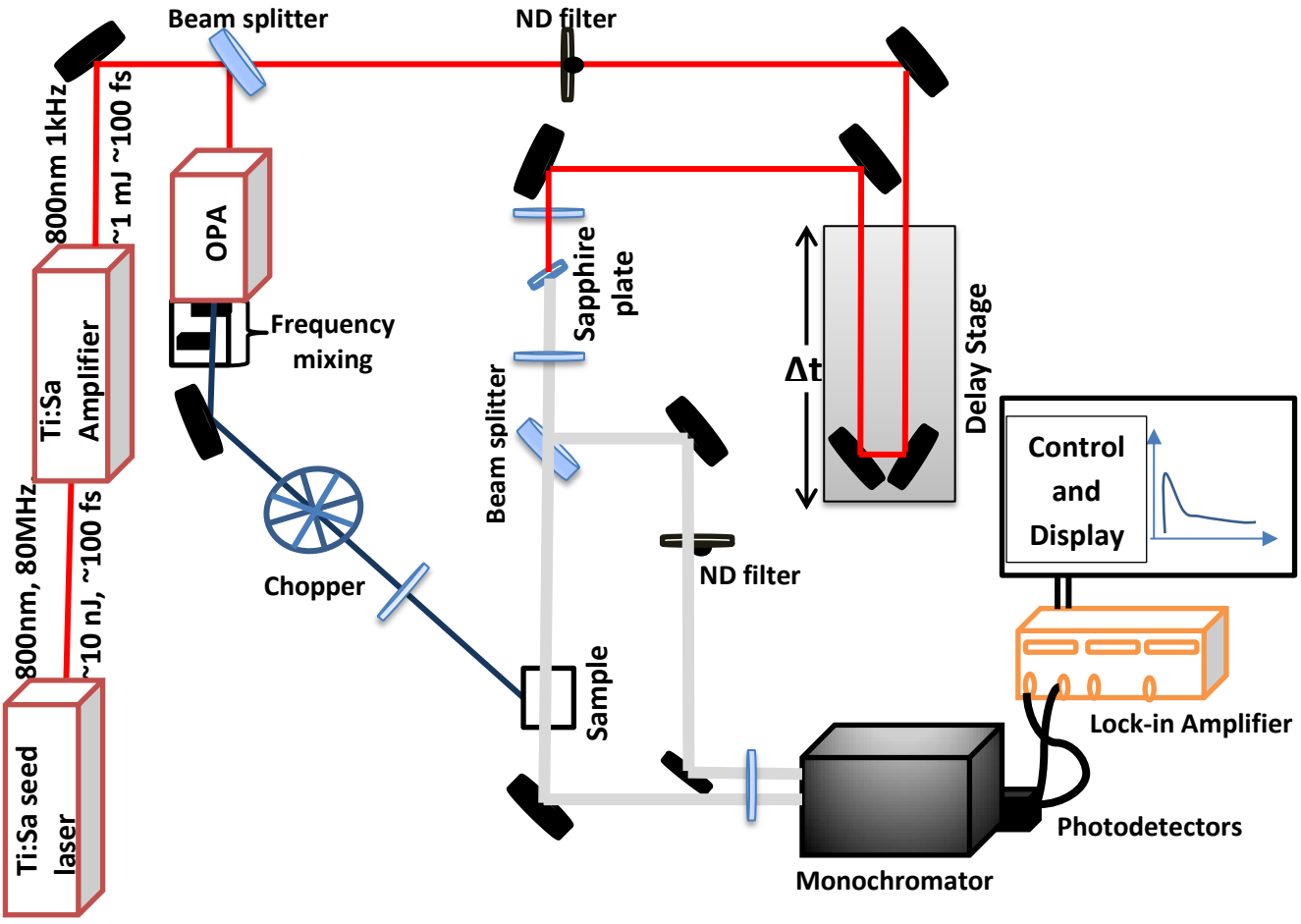

Figure 3.9. The Optical Outline of the Vis-TA experiment.

In this experiment a TOPAS–C (Light conversion) OPA is used to convert the ultrafast pulses at 800 nm wavelength with 1 kHz repetition rate into the desired pump wavelength. It is a collinear OPA using a WLC as the seed for the signal, combined with subsequent second and third harmonic generation mechanisms to produce pump wavelength between 189 nm and 2800 nm. In particular, pump wavelengths corresponding to the UV region are important in this project as the photon energy in these regions is several times the band gap of the samples used in this study. This requirement is necessary for investigating MEG. The OPA has an efficiency of ~33% at 1400 nm and can be tuned from 1200 nm to 2800 nm. The combination of second and third harmonic generation and sum frequency crystals allows one to produce the desired pump wavelengths. The stabilization of the pump beam is important for monitoring the ultrafast charge dynamics of QDs as each decay collection time is about 1 hour. In this context the OPA device is an ideal source since it offers less than 1% root mean square energy stability [20].

3.6.1 Optical bench

A small fraction of the amplified pulses at 800 nm wavelength is directly sent to the optical bench to generate WLC which is used as the probe beam. The beam is initially passed through a pre-fixed iris to be roughly aligned and a neutral density (ND) filter to control the average beam power for a stable WLC output. Then it is focused onto a 2 mm sapphire plate to generate WLC following reflection off a 200 nm Newport translation stage that controls the delay time between the pump and probe pulses' arrivals. The delay stage is a motorized device that includes a retro-reflector reflecting the incident beam parallel and in the opposite direction with respect to its original path. As stated earlier each step of the delay stage movement causes twice the change in the total path length of the probe beam because the probe pulses pass the delay stage two times. By this device it is possible to

adjust the incremental motion to down to 10 μm corresponding a time resolution of about 60 fs (This indicates that the time resolution of the system is only limited by the pulse duration). It is important to ensure that the incident beam is parallel to both delay stage and to the optical table. After passing the delay stage, an average of 1 mW pump power of the 800 nm pulses are focused onto a 2 mm thick sapphire plate to generate WCL. The stability of WLC output is crucial for a fixed probe beam corresponding to the sample's band edge. And thus the sapphire plate is slightly moved in the horizontal and vertical directions to get the optimum position. The output of the sapphire plate is shown in Figure 3.10 which was optimized for a probe wavelength of 650 nm, which is the nearest value to the band gap of most samples used here.

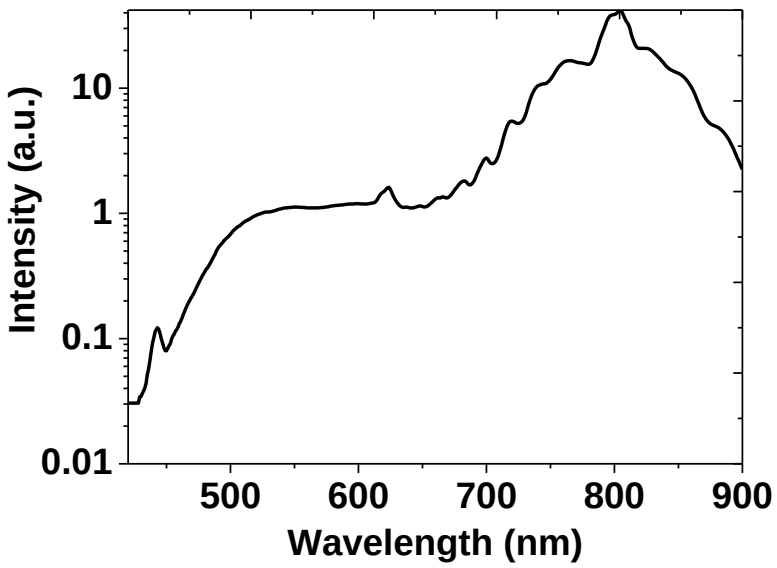

Figure 3.10. The spectral output of the employed sapphire plate when pumping with 800 nm ultrafast pulses at 1 mW power.

The generated WLC is divided into two parts using a beamsplitter. One of which is called sample beam and focused on the sample position so that the probe beam has a diameter of ~ 700 μm using two (500 mm and 250 nm focal length) achromatic doublet lenses. The other part of the WLC beam is called the reference beam and by-passes the sample before

being directed onto a Spectra Pro 2500i 0.5 metre imaging spectrometer. The reason for splitting the probe beam is that the absorption change in an excited QD is low enough to be confused with the contribution from the instruments. In a split beam system the difference between the sample and reference beams is considered and the contribution from the source or other instruments is cancelled out and sensitive absorbance measurements are achieved. The reference and the attenuated sample beams are balanced using a tunable ND filter. Both beams are sent onto the monochromator after passing through a 60 mm achromatic doublet lens to be focused on the spectrometer's entrance slit. The monochromator disperses the two beams before sending them onto a pair of Vishay Si PIN high speed photodiodes. The photodiodes transmit the detected signal to a Lock-in amplifier (Stanford Research Systems SR830) which is connected to the computer. A Lab View program was written to control the delay stage and to collect the output from the lock-in amplifier. On the other hand the output from the OPA is directed to the sample position after being modulated by a mechanical chopper which is phased-locked with the lock-in amplifier. The frequency of the chopper is set to 500 Hz meaning that every other pulse from the 1 kHz pump beam is blocked. Additionally the lock-in amplifier detects only the transmission changes due to pump beam excitation, ΔT, which is the transmittance difference between when the pump beam is on and off. This difference is then normalized by the transmission at the sample band edge, ΔT/T, which is proportional to the average number of excitons per QD, <N>, and expressed as;

$$\frac{\Delta T(t)}{T} = A\frac{<N>}{g}, \qquad (3.9)$$

where A and g are the absorbance at the band edge and the degeneracy of the sample, respectively. The angle between the directions of pump and probe beams at the sample

position is set to be less than 30^0 such that the active volume is not significantly reduced by beam walk-off.

3.7 High repetition infrared ultrafast TA experiment

The infrared (IR) femtosecond TA experiment is also a pump-probe experiment where the pump beam perturbs the system of the QDs and the following probe beam monitors the kinetics of electrons in the desired energy levels. In this experiment the photon energy of the probe beam is considerable less with respect to the visible TA experiment and thus usually the intra-band transition in the conduction band is monitored. The main difference between these two experiments comes from the instrumentation. For example, as well as using a high repetition rate amplifier, the IR TA experiment also detects the absorption change in signal with detectors that work at cryogenic temperatures. It is a valuable instrument for mapping out the ultrafast relaxation channels in QDs, particularly for investigation of MEG. Because this technique does not monitor the exciton dynamics at the band edge then there is no need to consider the effect of excited state emission on the ground state bleach [21]. In addition, in an IR TA experiment the probe beam can be tuned to the only optically allowed transition levels which gives a clear MEG signal [8]. On the other hand, high repetition rate pulses also contribute to a clear ultrafast exciton dynamic signal. Because when a system is pumped with low repetition rate femtosecond pulses then the data acquiring rate becomes slower which can be minimised by replacing high repetition rate sources. Taking into consideration these advantages we developed a high repetition IR TA technique to record the ultrafast exciton dynamics of QDs.

3.7.1 Laser system

This system employs several commercially available laser and detection systems. 150 fs

pulses are derived from a Coherent Mira-Optima 900-F seed laser. The oscillator is pumped by a diode-pumped Coherent Verdi laser producing 18 W of continuous wave radiation at 532 nm. The pump laser uses a Nd:YVO_4 crystal as the gain medium [22]. The seed laser is a mode-locked Ti:Sapphire laser that has a tuning range between 700 nm and 980 nm and produces pulses with duration of 150 fs and 76 MHz repetition rate. As explained earlier the ultrafast pulses are generated by applying the Kerr effect in the Ti:Sapphire gain medium [23]. The produced femtosecond pulses have energy in the order of 10s of nJ that is not sufficient to generate efficient WLC, and other nonlinear processes. Therefore a Ti:Sapphire regenerative amplifier is used to increase the pulse energy of the oscillator.

In this IR TA system, a CW-pumped Ti:Sapphire regenerative amplifier (Coherent RegA Model 9000) is used to amplify the energy of femtosecond pulses from the nJ scale to about 6 µJ with repetition rate of 250 kHz. About 14 W of output from the diode-pumped Verdi laser is used to pump the amplifier. Unlike the amplifier used for Vis-TA, this amplifier does not use a grating-based stretcher instead; it utilizes an AOM which uses tellurium dioxide (TeO_2) crystal. This crystal is highly dispersive, so that fs pulses stretch in time to permit a safe amplification process after about 20 round trips in the Ti:Sapphire crystal. The AOM also acts as a cavity dumper to control injected and ejected pulses in the amplification process and the time between these pulses. A Faraday isolator is used to prevent the feedback into the main oscillator and to permit unattenuated amplified pulses from the amplifier. The RegA 9000 produces output pulses at 800 nm with ~6 µJ with repetition rate between 10 kHz to 300 kHz and 1.4 W average power [24]. The extracted high energy compressed pulses are directed to an OPA to convert the femtosecond 800 nm pulses to higher frequencies.

To convert the 800 nm output from the amplifier to longer wavelengths a Coherent Model 9800 OPA is used, which is tunable from 1200 nm to 2400 nm. Approximately 25% of the 800 nm RegA output is diverted onto a sapphire plate to generate WLC in the spectral window between 460 - 1600 nm. The produced WLC is then combined with the remaining 75% of the RegA output for the first pass through β-barium borate (BBO) to produce a small amount of "signal" and "idler" beams. Next the signal and 800 nm beams are separated and reflected off two different adjustable optical delay stages. That is because of meeting the requirements for producing the remaining amount of the "signal" and "idler" beams whose frequency can be straightforwardly angle-tuned by a peripheral micrometer. Eventually the OPA produces signal (1200-1600 nm) and idler (1600- 2400 nm) beams with average output of about 150 mW at 250 kHz corresponding to a pulse energy of 0.6 µJ.

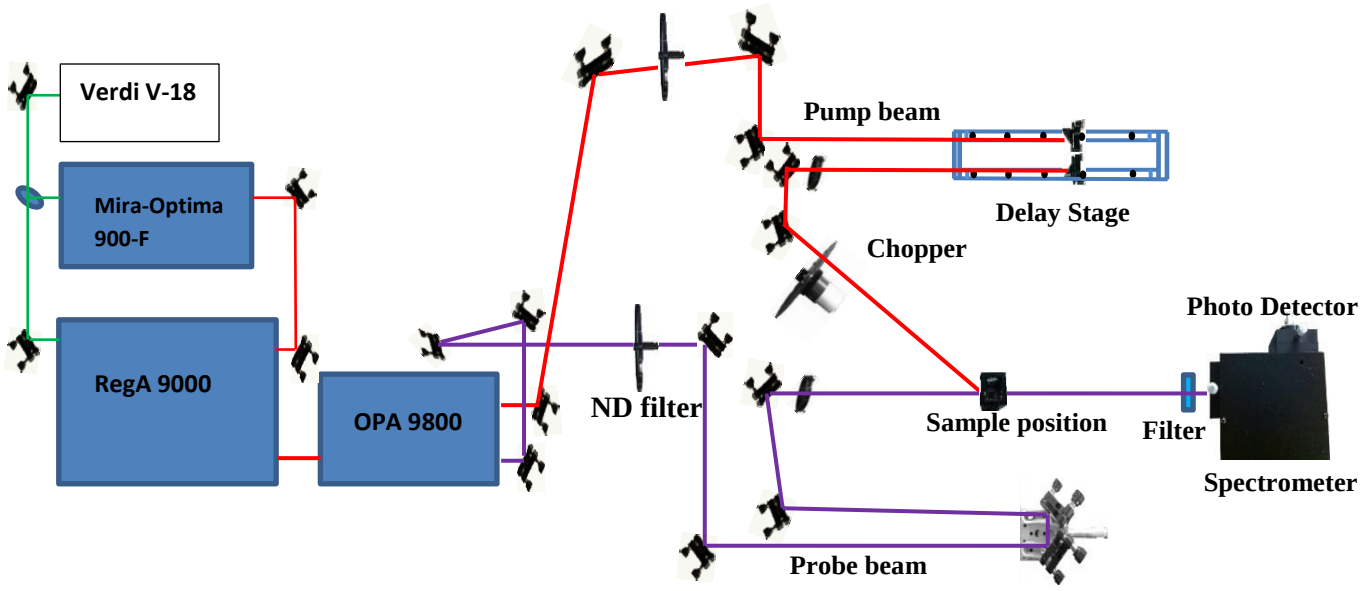

Figure 3.11. Schematic layout of the ultrafast IR TA experiment.

3.7.2 Optical bench

This experiment is two colour pump-probe IR TA spectroscopy where both beams emerge from the OPA and directed towards the sample on the optical bench, as shown in Figure 3.11. The pump beam derived from residual 800 nm pulses from the OPA is directed onto a Newport series delay line after passing through an ND filter. As stated earlier, the pump translation stage adjusts the delay time between the pump and probe beams. Here the key concern is that the travelled pump beam must be parallel to the translation stage to avoid any walk-off of the pump beam when the delay line moves. This is achieved by walking the beam in the far field by moving the delay line forth and back. A mechanical chopper is mounted in the pump beam path and synchronized to the amplifier frequency to block every other pulse. In that case, the lock-in amplifier (Stanford SR830) detects only the signals with 125 kHz. The pump beam waist at the sample is measured to be around 800 µm. On the other part, the probe beam is derived from the idler output of the OPA which is directed towards the sample using some optical components. A ND filter and iris are used to govern the intensity and the beam diameter, respectively. The pump and probe beams are focused on the sample with a narrow angle of about 20^0 to maximize the interaction area as much as possible. The probe beam size is measured to be about 700 µm, smaller than the pump beam waist, using an Ophir photonic beam profiler. The attenuated probe beam is then directed onto a long-pass filter to block the contribution from the 800 nm pump beam before passing through a spectrometer to be analyzed. A high speed InGaAs detector is used to detect the transmission difference signal and to send into the lock-in amplifier.

3.7.3 Test results

The experiment was verified by taking some initial ultrafast exciton dynamics of PbS QDs. Here the exciton population at the band gap of the sample is investigated rather than in intraband transmission. That is because the interband ultrafast exciton dynamics of PbS QDs has already been investigated which can be used as reference [25]. The PbS QDs were bought from Sigma Aldrich Company. The samples were dispersed in hexane solvent and kept in a 10 mm glass cuvette. The absorbance of the sample was adjusted to be around 0.12 at the band edge to well-observe the ultrafast dynamics of the QDs. Initially the steady state absorption spectrum of the sample was carried out using the lambda 1050 UV/Vis UV/Vis/NIR spectrometer, as shown in Figure 3.12. As it is clear from the figure that the band gap of the sample is about 1414 nm (~0.9 eV) which is within the limit of idler output of the OPA that is used as probe. Hence the probe beam can be tuned to the band edge of PbS QDs.

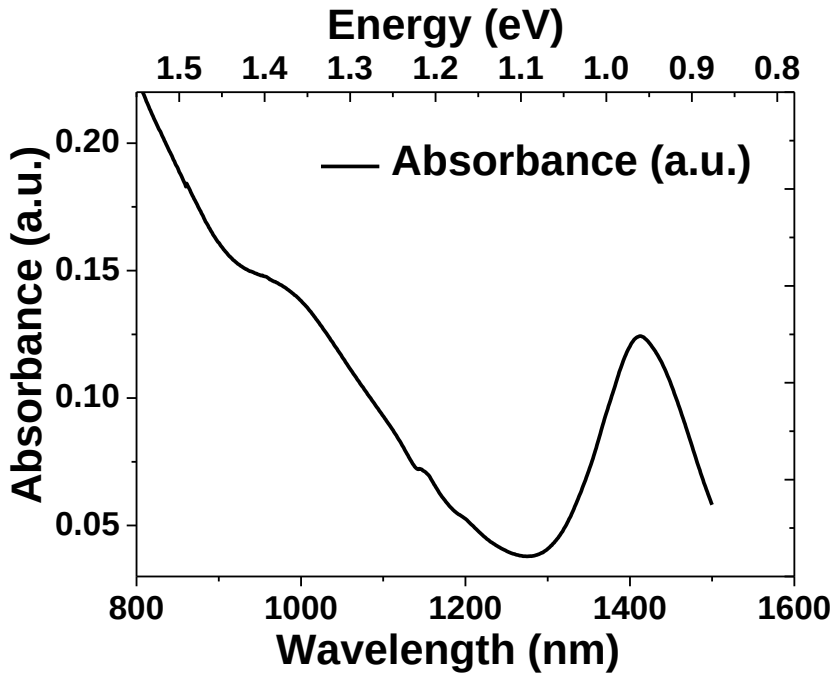

Figure 3.12. Steady state absorption spectra for PbS QDs.

The residual 800 nm (~1.8E_g) ultrafast pulses with an average power of 340 mW (~2.7 μJ/pulse) were used to pump the dots. Pump and probe beams are spatially and temporally overlapped on the sample position. The translation stage is fine tuned to ensure the pump beam does not displace as the stage moves. The small change in transmission, ΔT, due to pump beam is captured by phase locking the chopper with the lock-in amplifier. The transmission change is recorded as a function of time and is normalized by the transmittance, T, at the band edge to remove the spectral response of the instruments, as shown in Figure 3.13. The transient shown in the figure is the average of 10 consecutive scans.

As can be seen from the figure, a sharp rise emerges after about 150 ps indicating that pump and probe are spatially overlapped and hence electrons are excited across the band gap. Thereafter, the signal is a plateau demonstrating that only a long-lived exciton is formed. This single exciton has a lifetime of the order of 10s of ns which is well beyond the limit of this experiment. To confirm this result, Poisson statistics is used which estimates the possibility of a dot to absorb *N* photons during a pulse, P_N, and hence have N excitons just after excitation which is given by:

$$P_N = < N >^N \frac{e^{-<N>}}{N!} \qquad (3.10)$$

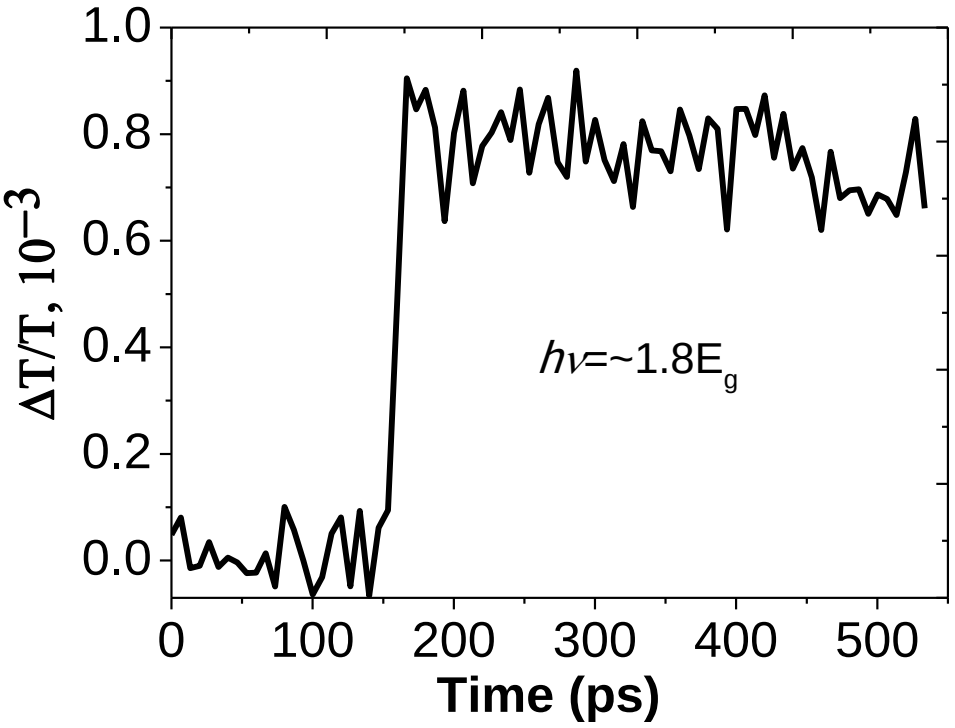

Figure 3.13. The first recorded fractional transmittance transient using the IR TA experiment.

Since PbS QDs are 8 fold degenerate and the absorbance was about 0.12 then from Eq.(3.9), <N> becomes about 0.066. Eq.(3.10) leads the probability of absorbing two photons per dot during a pulse, P_2, is about 2×10^{-3} which is less than 5% of P_1. Hence, according to the Poisson distribution only a single exciton is formed when the PbS QDs are pumped under the present circumstances, being consistent with the observed results. Biexciton or multi-exciton can be formed if the pump power is increased to certain levels where each dot absorbs more than one photon during a pulse.

3.8 Summary

Optical spectroscopy is the interaction between matter and light and does not destroy the materials' structure. Steady state PL and absorption spectroscopies reveal materials' structures by measuring the emitted and transmitted light through materials as a function of

wavelength, respectively. In this project, a Horiba Jobin Yvon Fluorolog-3 model FL3-22iHR spectrofluorometer and a Perkin Elmer Lambda 1050 UV/Vis/NIR spectrophotometer are used to record linear PL and absorption spectroscopies of the dots. In addition, a TCSPC experiment is used to measure the radiative recombination lifetimes of the dots. This method counts every single PL photon as a function of the delay time with respect to a reference pulse. The TA experiment is a pump-probe method in which the pump pulse excites the sample and the subsequent probe beams monitors the charge population at a desired energy level. In this work, a femtosecond TA experiment is used to investigate the ultrafast charge dynamics of the QDs. Furthermore, a high repetition rate IR TA experiment is built to measure the carrier dynamics of QDs by monitoring intra-band transitions in the CB of the dots.

3.9 References

1. Davis, C.C., *Lasers and Electro-optics: Fundamentals and Engineering*. 1996: Cambridge University Press.
2. Klimov, V., *Spectral and Dynamical Properties of Multiexcitons in Semiconductor Nanocrystals.* Annu. Rev. Phys. Chem., 2006. **58**: p. 635–73.
3. Crooker, S.A., et al., *Multiple temperature regimes of radiative decay in CdSe nanocrystal quantum dots: Intrinsic limits to the dark-exciton lifetime.* Applied Physics Letters, 2003. **82**(17): p. 2793-2795.
4. Gfroerer, T.H., *Photoluminescence in Analysis of Surfaces and Interfaces,* in *Encyclopedia of Analytical Chemistry*, R.A. Meyers, Editor 2000, John Wiley & Sons Ltd: Chichester.
5. Horiba, *Fluorolog-3 operation manual.* Jobin Yvon Inc., 2002.
6. V.Tkachenko, N., *Optical Spectroscopy Methods and Instrumentations*. 2006, Amsterdam: Elsevier.
7. Perkin Elmer, *Technical Specifications for the LAMBDA 1050 UV/Vis/NIR and LAMBDA 950 UV/Vis/NIR Spectrophotometers.* 2010.
8. N. McElroy, M.C., A. Al-Otaify, R. Page, D.J. Binks, *Quantum Dot Solar Cells*. Lecture Notes in Nanoscale, ed. J.W.a.Z.M. Wang. 2013, New York: Springer Science+Business Media.
9. Becker, W., *Advanced Time-Correlated Single Photon Counting Techniques*, W. Becker, Editor 2005, Springer: Verlag Berlin Heidelberg.
10. Binks, D.J., *Multiple exciton generation in nanocrystal quantum dots - controversy, current status and future prospects.* Physical Chemistry Chemical Physics. **13**(28): p. 12693-12704.
11. Beard, M.C. and R.J. Ellingson, *Multiple exciton generation in semiconductor nanocrystals: Toward efficient solar energy conversion.* Laser & Photonics Reviews, 2008. **2**(5): p. 377-399.
12. Rulli`ere, C., *Femtosecond Laser Pulses Principles and Experiments*, 2005, Springer: New York.
13. Spectra-Physics, *ed. User manual Tsunami mode locked Ti:sapphire laser.* 2006.
14. Hecht, E., *Optics*. 4 ed. 2002, San Francisco: Addison Wesley.
15. Brodeur, A. and S.L. Chin, *Ultrafast white-light continuum generation and self-focusing in transparent condensed media.* Journal of the Optical Society of America B, 1999. **16**(4): p. 637-650.
16. Alfano, R.R. and S.L. Shapiro, *Emission in the Region 4000 to 7000 Å Via Four-Photon Coupling in Glass.* Physical Review Letters, 1970. **24**(11): p. 584-587.
17. Nagura, C., et al., *Generation and Characterization of Ultrafast White-Light Continuum in Condensed Media.* Applied Optics, 2002. **41**(18): p. 3735-3742.
18. Stubbs, S., *Photo-physics and applications of collidal quatum dots* in *School of Physics and Astronomy*2010, The University of Manchester: Unpublished Phd Thesis. p. 98.
19. Spectra-Physics, *ed. User manual Spitfire Pro regenerative amplifier.* B ed., 2005.
20. Light Conversion, *TOPAS-C User's Manual.* 2009, Vilnius.
21. Ji, M., et al., *Efficient Multiple Exciton Generation Observed in Colloidal PbSe Quantum Dots with Temporally and Spectrally Resolved Intraband Excitation.* Nano Letters, 2009. **9**(3): p. 1217-1222.
22. Coherent inc., *Verdi Dual FAP Laser Operator's Manual. 2007*, Santa Clara,

23. Coherent Inc,, *Mira Optima 900-F Laser Operator's Manual,* 2004,Santa Clara.
24. Coherent Inc, *RegA 9000 Laser operator's Manual. 2009,* Santa Clara,
25. Ellingson, R.J., et al., *Highly Efficient Multiple Exciton Generation in Colloidal PbSe and PbS Quantum Dots*. Nano Letters, 2005. **5**(5): p. 865-871.

Chapter 4: Ultrafast exciton dynamics of colloidal ZnTe/ZnSe type-II QDs

4.1 Introduction

In this chapter, the ultrafast exciton dynamics of ZnTe/ZnSe type-II QDs will be described. Firstly steady state absorption and PL spectra characterization will be presented. This will be followed by a comprehensive investigation of charge relaxation and surface mediated trapping using ultrafast TA spectroscopy.

4.1.1 Motivation

As explained in chapter 2, type-II colloidal QDs have staggered band alignment wherein electron and holes reside in different volumes of the structure, while, in type-I structures both charges localise in the same volume, e.g core. Additionally, QDs can be also formed in quasi type-II structures where one of the charge localises in a certain section and the other can reside in any section in the whole structure. Therefore their electron and hole wavefunctions are easily modified by altering the core size and shell thickness during the synthesising process which regulates the basic optical properties of the structure. For instance, reducing the overlap of electron and hole wavefunctions results in an increase in the exciton lifetime [1, 2] and increases Δ_{XX} (either large red shift or large blue shift in the band edge spectrum) [3]. These characteristic features in type-II QDs put them in an advantageous position over their type-I counterparts in terms of application areas, such as lasers [4] and photovoltaics [5].

Many QDs contain heavy metals and hence are toxic and pollute the environment. The use of those toxic QDs can result in increase of heavy-metals in the subcellular region of

organisms as these organisms are easily decomposed [6-8]. Thus the use of toxic QDs is limited by the Restriction of Hazardous Substances Directive (RoHS) of the European Union [9]. However, zinc based QDs are environmentally friendly and are alternative semiconductor QDs to Pb [10], Cd [11], Hg [12], and As [13] based-QDs. Additionally, the particular reason for preferring ZnTe/ZnSe material is that the effective bandgap of these QDs are wider than that of those Cd based QDs making ZnTe/ZnSe type-II QDs attractive for application in the visible region of the spectrum [14]. The wide band gap type-II QDs are particularly important for lasing applications as the absorption at high energies are reduced and thus stimulated emission becomes dominant [15]. The lasing threshold in QDs is about one exciton per dot on average and thus depends on nonradiative Auger recombination [4]. Therefore, to understand optical gain dynamics it is critical to study sub-nanosecond exciton dynamics of QDs.

4.1.2 Sample information

In this study the ultrafast exciton dynamics of a series of type-II ZnTe/ZnSe core/shell quantum dots were investigated using ultrafast TA spectroscopy. All samples have an identical 4.1 nm ZnTe core surrounded with 1, 1.5 and 2 monolayer (ML) ZnSe shells. The unit ML corresponds to about 0.5 nm thickness. The samples were fabricated by Simon M. Fairclough at the University of Oxford using the synthesising method which is described in detail elsewhere [16].

ZnTe/ZnSe core/shell dots were dispersed in anhydrous hexane and kept in 10 mm path-length quartz cuvettes. The preparation of samples is conducted under nitrogen purging to avoid oxidation of the surface using a glove box in the Chemistry Department at the University of Manchester. The absorbance (natural logarithm of the ratio between the

incident and the transmitted beams) of samples at the band edge is adjusted to be between 0.2-0.4 to detect the ultrafast charge dynamics of the QDs more efficiently. All samples were vigorously stirred with a maximum speed of 1000 rpm during the TA experiment using a Thermo Scientific, Variog Mini stirrer (unless otherwise stated) to avoid the accumulation of photocharged QDs in the detection volume.

4.2 Photoluminescence and absorption spectroscopy

Primarily, the steady-state absorption and PL spectra experiments were performed by Simon M. Fairclough at the University of Oxford using a Varian Cary 5000 UV-visible-NIR spectrometer and a Varian Cary Eclipse fluorescence spectrophotometer, respectively. It is clear from Figure 4.1 a) that the 4.1 nm ZnTe core only sample exhibits a sharp absorption feature at around 450 nm (2.76 eV) which is a typical behaviour of a type-I structure. The distinctive ground state absorption feature indicates a strong electron-hole confinement in the ZnTe core. This well-defined peak is red shifted to 470 nm (~2.64 eV) with formation of a 1 ML ZnSe shell, which is then shifted further to 480 nm (~2.6 eV) and 490 nm (~2.53 eV) with increasing the shell thickness to 1.5 and 2 ML, respectively, as shown in Figure 4.1 b)-d). The first excitonic peaks for the samples with 1 and 1.5 ML ZnSe shells are still distinct (though less so in the latter case), suggestive of transition from type-I to quasi type-II structures. However, the 1S absorption feature is smeared with the addition of 2 ML ZnSe shell onto ZnTe core which is a characteristics of transition from type-I form to that of type-II wherein electrons and holes presumably are localised in the ZnSe shell and ZnTe core, respectively [14]. The formation of 2 ML ZnSe shell causes almost 40 nm red-shift in the absorption spectrum which is also another typical distinctiveness for transition from type-I to type-II structure. This is because as the shell

thickness increases the carrier wavefunction overlap decreases and hence the effective band gap between ZnTe core and ZnSe shell becomes smaller and the carriers are confined to a lesser degree. Figure 4.2 shows the schematic structure (top) and the energy band profiles (bottom) for ZnTe/ZnSe core/shell structures.

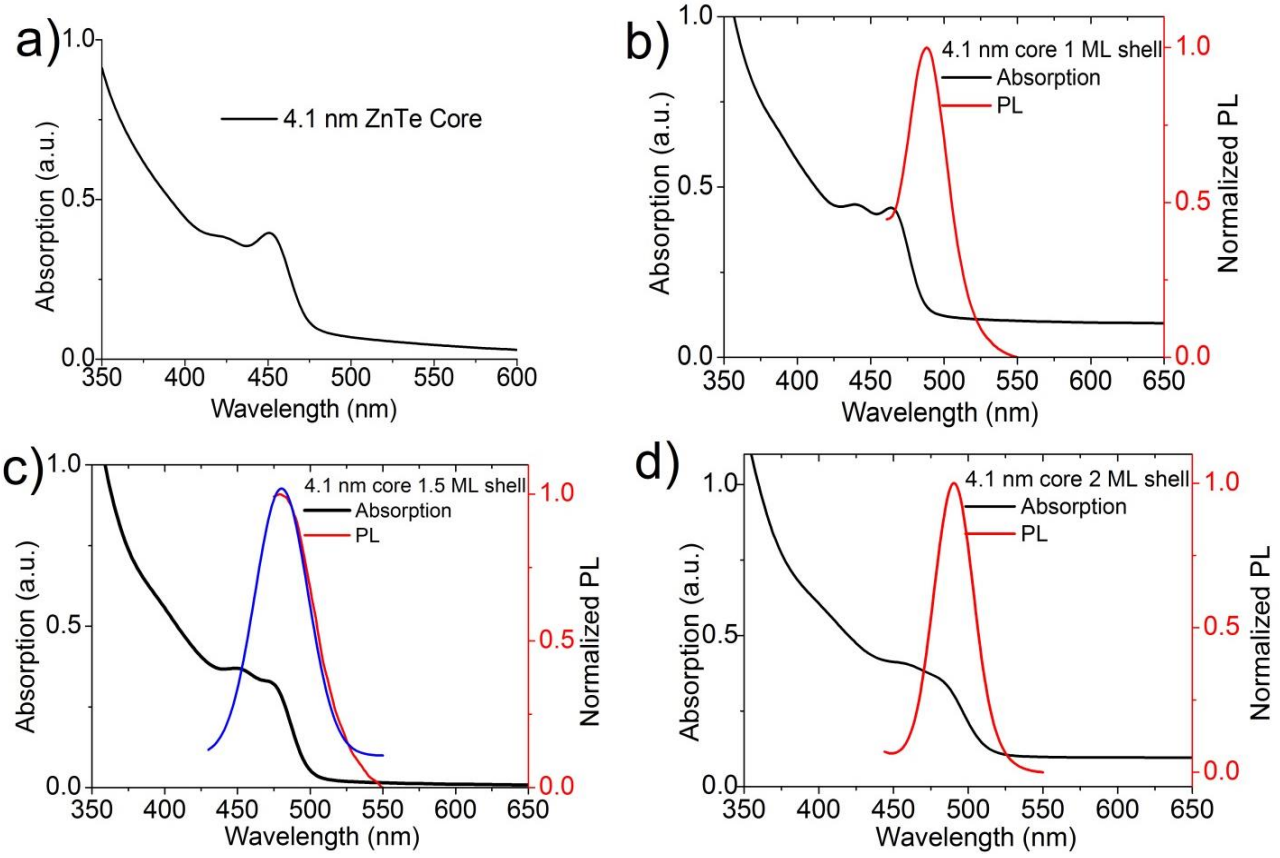

Figure 4.1. Absorption (black) and PL (red) spectra of ZnTe/ZnSe QDs at different steps which are a) 4.1 nm core only, b) core with 1ML shell, c) 1.5 ML shell and d) 2 ML shell. For clarity the photoluminescence spectrum of 1.5 ML ZnSe core is fitted with Gaussian fit shown in blue. This data is provided by Simon M. Fairclough, University of Oxford.

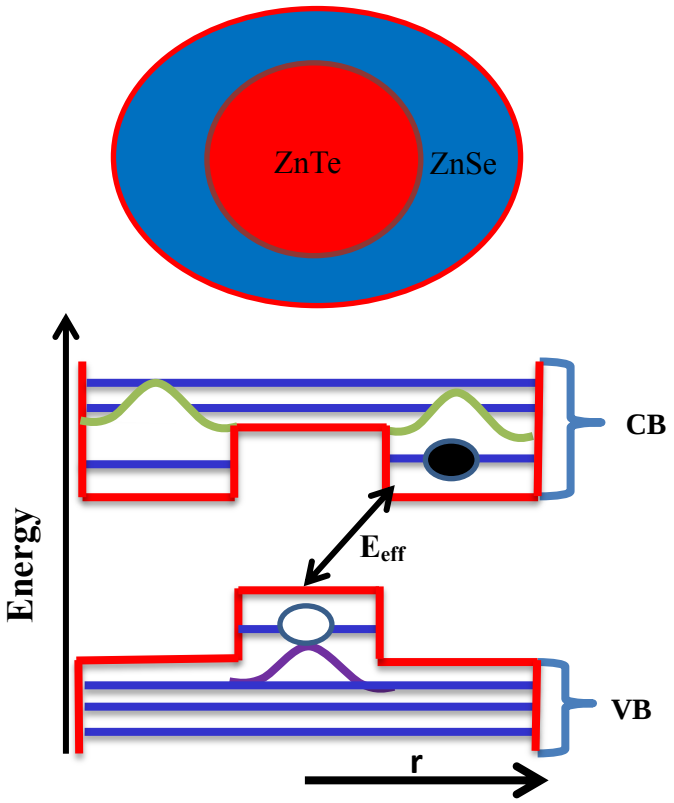

Figure 4.2. Schematic illustration of staggered band alignments for ZnTe/ZnSe type-II QDs in which electron and holes reside in different spatial regions leading to a decrease in the wavefunction overlap. The green and purple curves demonstrate the wavefunctions of the electrons and holes, respectively whereas r represents the radius of the spherical dot.

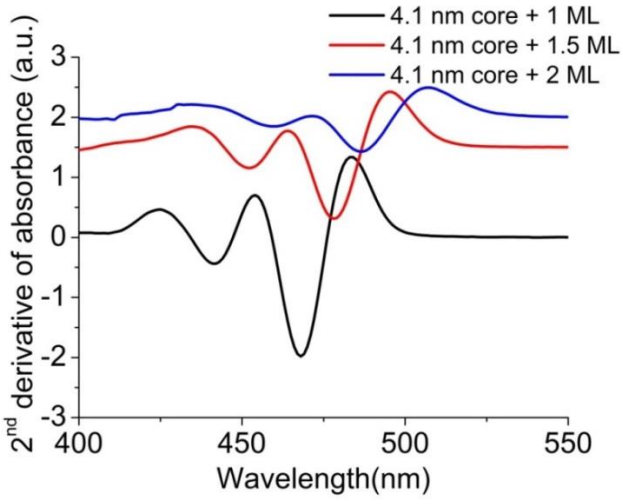

Figure 4.3. Second derivative of the absorption spectra for ZnTe/ZnSe QDs with 1ML (black), 1.5 ML (red) and 2 ML (blue) shell thicknesses.

In addition to the obvious 1S absorption features, the absorption spectra in Figure 4.1 also illustrate weak transition features at shorter wavelengths which are more clearly distinguishable from the 2nd derivative of the absorption spectra, $d^2A/d\lambda^2$, as shown in Figure 4.3. These transitions can be interpreted in light of the multi-band model which predicts the band structure of QDs more accurately than the single band approach [17]. Based on the core and shell thickness properties, this model also predicts the charge localizations in QDs. According to this model, in the samples used here electrons and holes accommodate in ZnSe shell and ZnTe core, respectively.

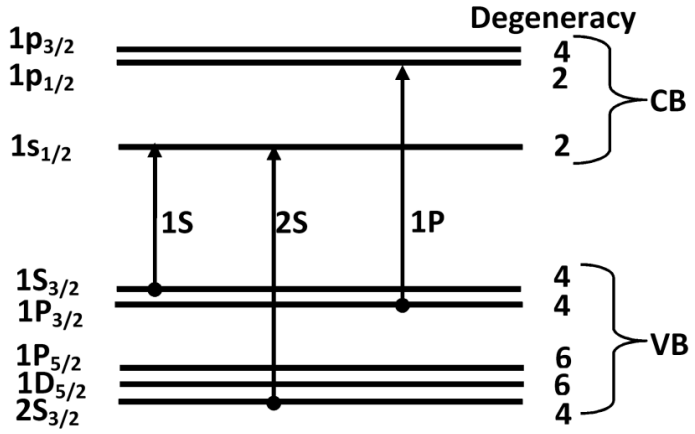

Figure 4.4. Energy levels based on the multi-band model and the transition observed in the steady state absorption spectra.

Figure 4.4 reveals the main energy states and three lowest energy transitions that contribute to the steady state absorption spectra. According to the multi-band model, the 1S transition corresponds to the transition from the $1S_{3/2}$ state in the valance band to the $1s_{1/2}$ in the conduction band and is the ground-state absorption feature. The next transition is 2S, which, in this case, corresponds to the transition to the $1s_{1/2}$ state in the conduction band from the $2S_{3/2}$ in the valence band. After this is the 1P transition from the $1P_{3/2}$ energy level in the valance band to the $1p_{1/2}$ energy level in the conduction band. Here electron

and hole states are respectively denoted as nq_j and nQ_j, where n is the number of level with a given symmetry, q (Q)= s,p,d…(S,P,D….) is the lowest value of envelope angular momentum and j is the total angular momentum. The degeneracy of the relevant energy states in Figure 4.3 are linked to the total angular momentum as 2j+1. From the second derivative graph in Figure 4.3, we can see that 2S absorption features for the samples with 1, 1.5 and 2 ML shells are around 440 nm (~2.82 eV), 452 nm (~2.75 eV) and 460 nm (2.7 eV), respectively.

The PL spectra are also red-shifted with increasing the ZnSe shell thickness, a symbolic of transition to type-II structure, as it is in the case of absorption spectra. The ZnTe core did not exhibit any sign of PL, which is suggested to be due to the existence of Te surface photocharging [16]. The ZnTe core with 1 ML ZnSe shell showed a PL maximum at 488 nm (~2.6 eV) whereas, the sample with 2 ML shell thickness showed a PL maximum position at 492 nm (~2.5 eV), as shown in Figure 4.1b) and d), respectively. The PL spectrum of the 1.5 ML sample is dominated by that of ligands which makes it difficult to distinguish the PL peak. Therefore, the PL spectrum for this sample is fitted with a Gaussian function to be identified clearly which shows the maximum PL position at about 485 nm (~2.6 eV), as shown in Figure 4.1 c). The full width at half maximum (FWHM) of these PL spectra is between 30-40 nm supporting a narrow size distribution of QDs.

4.3 Transient absorption spectroscopy

Since the exciton dynamics of QDs, such as Auger recombination, charge trapping, MEG, etc. can occur in the order of a few picoseconds time scale, an ultrafast technique is required to measure charge carrier dynamics of QDs. The time resolution of ultrafast laser

spectroscopy is principally limited by the laser pulse duration, typically ~100 fs. This laser pulse duration is at least 10 times shorter than that of the charge carrier dynamics of the QDs under study and thus a sufficient temporal resolution can be achieved when measuring exciton dynamics of QDs with such a laser system. Therefore, femtosecond TA spectroscopy was used to observe the ultrafast exciton dynamics of the type-II ZnTe/ZnSe QDs at the absorption edge. The instrumentation and working principle of the experiment is explained in detail in Chapter 3 section 4. Pump and probe beams are spatially overlapped on the sample position. The pump beam diameter was adjusted to be about 2.5 mm at 400 nm (3.11 eV) excitation wavelength, whereas, the probe diameter was measured to be around ~0.7 mm at the sample position.

4.3.1 Results and discussions

Figure 4.5 reveals pump induced fractional transmittance transients at the band edge of each of the core/shell samples at a moderate pump power. In order to reduce the noise as much as possible, each decay was averaged over at least 10 scans. The decay for the sample with 1.5 ML is fitted with a bi-exponential expression as this function yields the most reasonable decay parameters, such as time constants and errors:

$$\frac{\Delta T(t)}{T} = y_0 + A_1 \exp\left(-\frac{t}{\tau_1}\right) + A_2 \exp\left(-\frac{xt}{\tau_2}\right) \quad (4.1)$$

where, A_1 and A_2 are the amplitudes of transient components, and y_0 is the plateau, representing the signal of the single long-lived exciton. Time constants for this sample are found to be 40±13 ps and 114 ±3 ps. On the other hand, the decays for the samples with 1 ML and 2 ML are globally fitted with a mono-exponential decay with a long-lived exciton signal and the extracted time constants are found to be 17±1 ps and 43±5 ps, respectively. These fast decays could be due to multi-excitons to single decay, MEG, trion

recombination or hot and cold charge trapping on the sample surface. Now we attempt to analyse each possible mechanism one by one and determine which one is applicable to the recorded decays.

In a transmittance transient decay the ratio between the peak signal, $(\Delta T/T)_{MX}$ (before multi-exciton recombination), and plateau signal, $(\Delta T/T)_X$ (after multi-exciton recombination to single exciton), R, proportional to the average number of excitons produced by each absorbed pump photon. Figure 4.6 depicts the process of biexciton recombination in an excited QD. In this mechanism, multi-excitons are produced by absorption of more than one photon per QD which relax to the CBM within 5 ps. Next these excitons undergo nonradiative Auger recombination within 10s of ps, leaving behind only one exciton. The lifetime for this the long-lived single exciton lifetime is about 10 ns [12] which is well beyond the range of the TA experiment used in this work. To be able to determine the impact of multi-exciton recombination on the above decays, the average number of absorbed photons per QD needs to be evaluated. The Poisson statistic model predicts the probability of N photons absorbed by a QD [18] which is given by;

$$P_N = < N >^N \frac{e^{-<N>}}{N!} \qquad (4.2)$$

where, <N> is the average number of absorbed photons per QD which can be predicted, for small fractional transmittances, from ΔT/T, using Eq.(3.9). The degeneracy of the conduction band minimum of ZnTe/ZnSe dots is two-fold. The ΔT/T values for each sample are about 10^{-3} or less (see Figure 4.5). Likewise A values for all samples at 400 nm are about 0.6 or less, as shown in Figure 4.1 b)-d). If we substitute the obtained values of ΔT/T and A in Eq. (3.9), then <N> is found to be less than 10^{-3}. This value of <N> leads to the probability of absorbing two or more photons per QD to be around 10^{-5} or less which is

negligible.

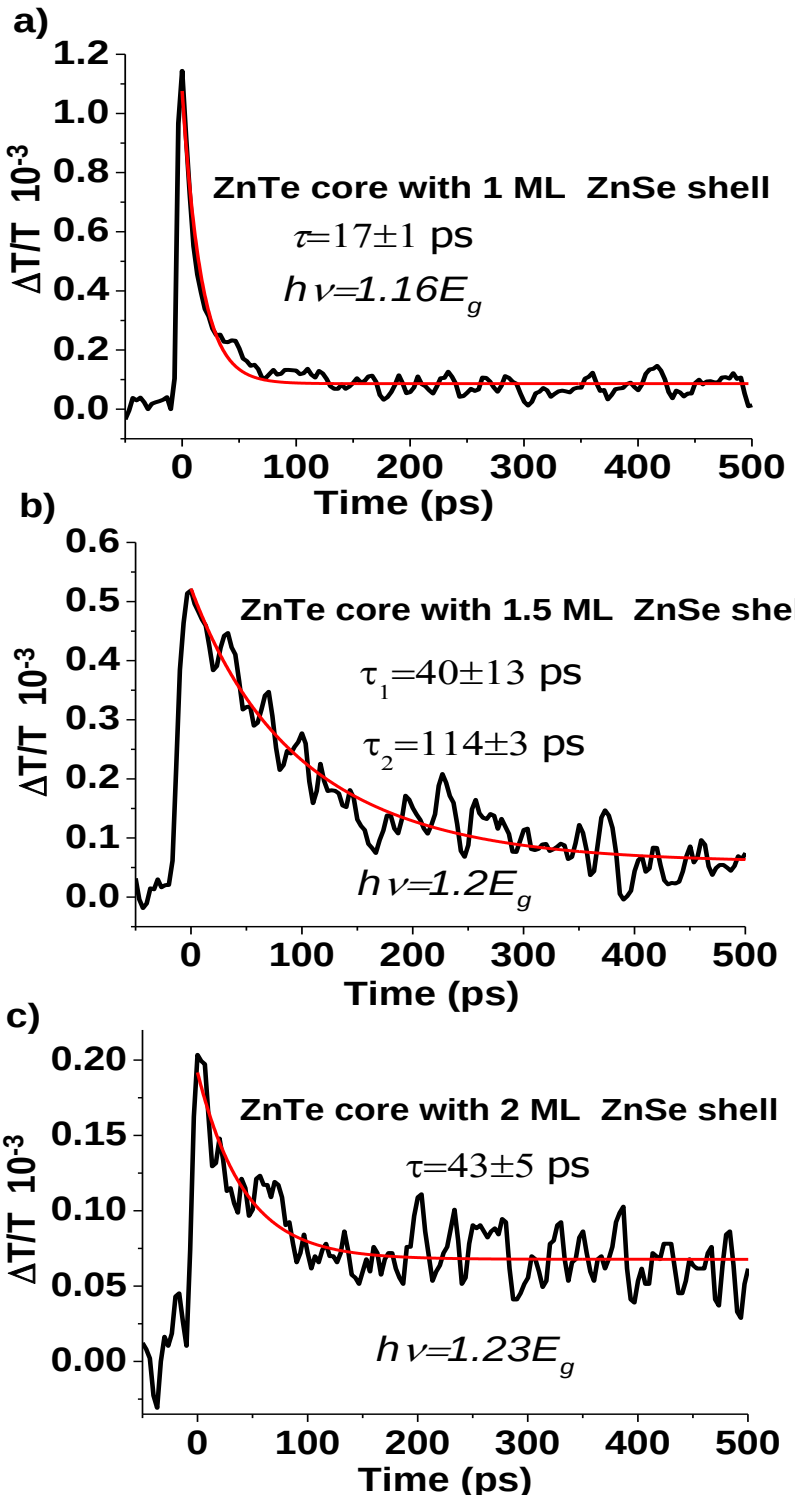

Figure 4.5. Fractional transmittance transients for ZnTe core with; a) 1 ML, b) 1.5 ML and c) 2 ML ZnSe shell excited with moderate pump fluence. The scans were recorded under an excitation wavelength of 400 nm (~3.11 eV).

These calculations confirm that only single excitons are formed rather than multi-excitons in each QD, meaning that multi-photon absorption cannot explain the greater than unity values for R observed. Therefore, the rapid decays in the pump-induced fractional transmittance change are not due to multi-excitons.

The second possible sub-nanosecond process that might affect the transients is the MEG mechanism where more than one exciton is produced by absorbing a single energetic photon [19]. However, the MEG effect cannot occur in the circumstances where the TA experiment was performed. That is because the MEG threshold for type-II ZnTe/ZnSe QDs is given by Eq. (2.7). Thus in order to generate MEG, the dots must be pumped with a photon energy of at least 2 times the sample's band gap. However, the pump beam used here was at 400 nm (~3.12 eV) corresponding to 1.2 times the band gap of the sample with the lowest band gap. Therefore, the MEG impact on above transients is not possible.

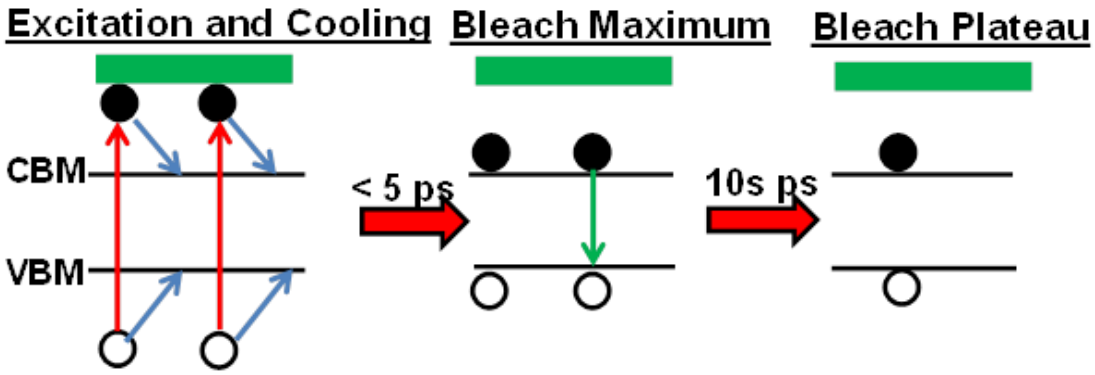

Figure 4.6. Schematic depiction of biexciton recombination process that undergoes Auger recombination and thus has potential to affect the transmittance transient decays. (VBM is valance band maximum)

Another physical process that causes R values to be larger than unity at low pump fluences is trion recombination. This process also involves Auger recombination and has a lifetime similar to that of biexciton decay, and thus can be confused with multi-exciton decays or MEG [20, 21]. In some circumstances, the photo-excited charges in the

conduction or valance band of a QD can become trapped on the surface of the QD for a time period longer than that between sequential pump pulses. In a study, Midgett *et al.*[22] reported that the life time of such trapped charges formed in PbSe QDs can last as long as 30 s which is well beyond the limit of this experiment. The formation of trions occurs when a single photon is absorbed by a QD already containing such a long-lived trapping charge, as shown in Figure 4.7.

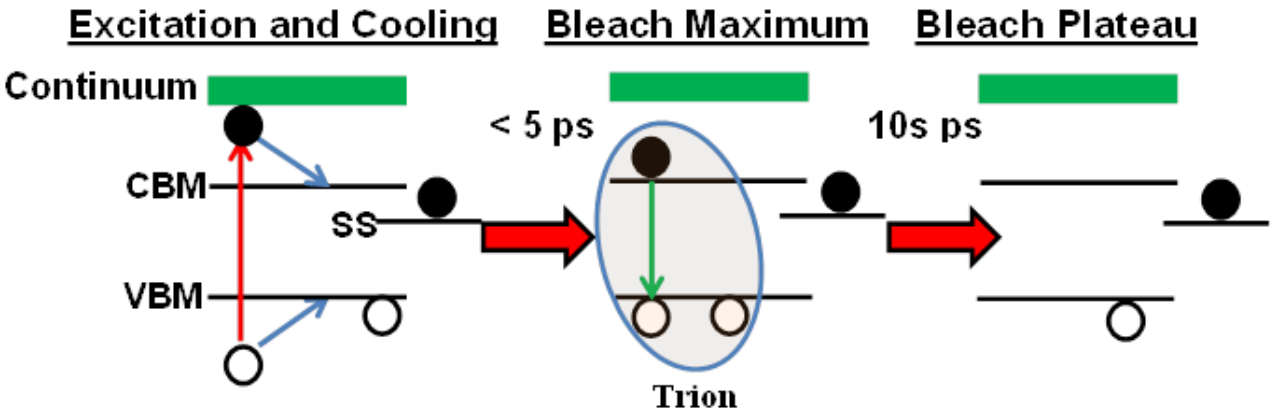

Figure 4.7. Schematic illustration of trion recombination that might account for large R values. (SS = surface state).

Multi-excitons decay to a single long-lived exciton whereas trions rapidly decay back to the state before the last pump pulse i.e. corresponding to the zero [20]. Since the samples used here are not passivated with a final shell whose band gap is larger than that of the core, electrons in ZnTe/ZnSe type-II samples are exposed to the surface and are thus prone to traps on the sample surface and thus give rise to large R values in the transient decays. Therefore, trion formation could account for the large R value in the transmittance transient of the samples. The significance of this process can be checked by comparing the decay results taken under stirring and static conditions. That is because the effect of trion formation on the R value is determined by stirring [23] or by flowing [24] the sample

because QDs containing trapped charges are swept away from the detection volume between subsequent pulses so that fresh QDs are excited. Thus to determine the impact of trions on the results taken in this study, TA experiment was conducted under stirring (1000 rpm) and static conditions with all other factors remaining the same. In the stirring case a 6 x 5 mm stirring bar was placed in the cuvette where the sample solution was kept and by means of a magnetic stirrer (Thermo Scientific, Variomag Mini) the sample was stirred throughout the experiment.

Figure 4.8 shows the transient transmittance results taken under stirred and static conditions. The stirred transient is well described by mono-exponential decay with a time constant of 13±0.6 ps. However, the transient taken under static conditions is a bi-exponential decay which yields time constants of 25±2 ps and 270±48 ps, now similar in form to the transient for the 1.5 ML sample. The second (longer) component is an order of magnitude larger than the first (fast) one (about 10 times greater than the fast component). We can say that the second time component is not due to biexciton decay to a single exciton as the value of $\Delta T/T$ is less than 10^{-3} where the formation of biexcitons is negligible. Therefore, the long time constant originates from trion recombination as the photocharged QDs remain in the detection volume.

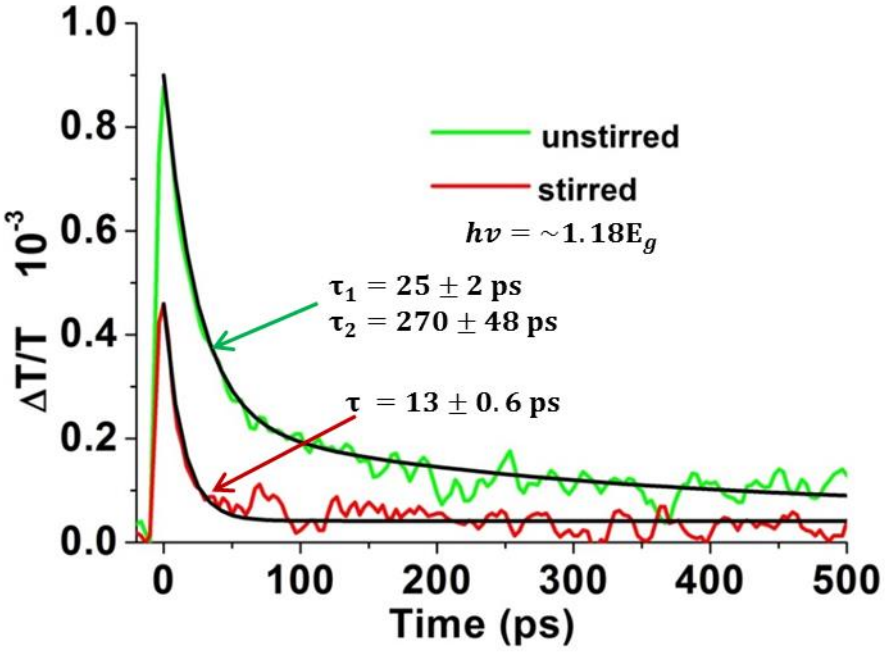

Figure 4.8. Comparison of fractional transmittance transients for the sample with 1 ML shell under stirred (red) and unstirred (green) circumstances with all other factors remaining the same. Black lines represent the mono- and bi- exponential curve fits to the stirred and unstirred decays, respectively.

These results suggest that trion formation occurs in the stirred sample with 1.5 ML shell whereas for the other samples trion formation is prevented by vigorously stirring the sample. Trion formation also depends on the pump fluence [20], as well as stirring the sample. That is due to the fact that, in some cases, the increased rate of trion formation at high pump powers means that stirring becomes insufficient to supress the effect [22]. Trion formation due to high pump fluence can be dominant when a substantial volume of charged QDs gather together in the probe volume. In addition, the rate of trion generation must be higher than that of loss by stirring and recombination. To address this aspect the TA experiment is repeated at average pump powers of 1.2 mW and 2.5 mW under stirring conditions with all other factors remaining the same. Results are shown in Figure 4.9. The transmittance transient obtained at low pump fluence shows a mono-exponential decay with a time constant of, τ, 22±1 ps. In contrast, the decay taken under high pump fluence

includes a further time constant, which is almost 8 times longer. Again here the possibility of absorbing two photons per QD is negligible and thus biexciton recombination is not significant as the values of ΔT/T is insufficient, being only about 10^{-3}. Therefore, the trion formation due to high pump fluence also suggests that the longer time constant in the transmittance transient of the sample with 1.5 ML shell is due to trion development.

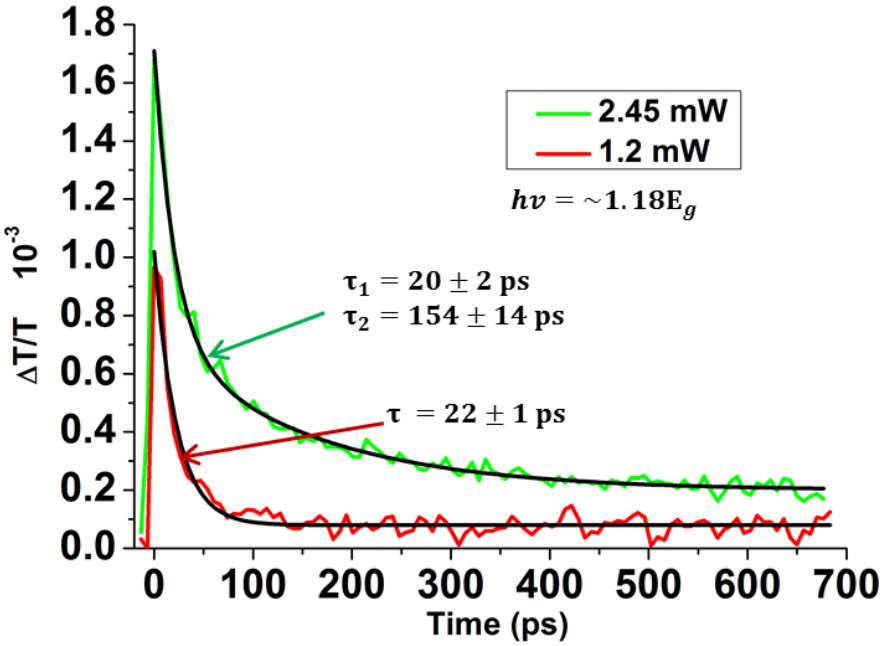

Figure 4.9. The comparison of the fractional transmittance transients for the sample with 1 ML shell conducted under high (green) and adequate (red) pump fluences with all other parameters remaining same.

Hitherto, biexciton decay, MEG and trion recombination mechanisms have been analysed in detail in this section and it is concluded that there is no significant effect of multi-exciton decay and MEG on these transients. However, we observed that the longer life time component in the decay for the sample with 1.5 ML is due to trion recombination. In order to explain the short life time components (~20-60 ps) shown in Figure 4.5 that causes large R values, an additional sub-nanosecond process is considered. In this regard, the first idea that comes to mind is that the photo-excited electrons become trapped on the

QD surface and thus depopulate the CBM, reducing the bleach on 20-60 ps time-scale but do not persist there long enough to enable trion formation. Tyagi *et.al* [25] reported hot and cooled electron trapping which has a significant effect on exciton dynamics in photo-treated CdSe QDs. Figure 4.10 a) and b) illustrate the mechanisms of cooled and hot electron trappings, respectively. In QDs the surface state lies between the CBM and VBM and slightly close to the conduction band [26]. The cooled electron trapping is the transition of electrons that are relaxed to the CBM to the surface state. Hot electron trapping is the transition of electrons from a high energy state (excited state) to the surface state that occurs straight after pump pulse excitation, and competes with relaxation to the band edge. Tyagi *et.al* [25] reports that the cold electron trapping life time in CdSe QDs is about 30 ps which is similar to that observed here. This result also suggests that the cooled electron trapping is responsible for large R values in singly excited and vigorously stirred QDs. In addition, the same study states that electron trapping affects the amplitude and position of the band edge bleach signal, by providing a photo-induced absorption (PA) that can overlap with the bleach spectrally.

Hence, differential transmission spectra of the bleach feature of the sample can help to explain the possible mechanisms that occur in a sub-nanosecond time scale in excited QDs. Bleach is the situation when all pump-created excitons relax to the band edge states before recombination, reducing the absorption. To understand the exciton dynamic of type-II ZnTe/ZnSe in further in detail, the TA spectra for these samples was obtained at the band edge region of the dots. The shape and sign of the bleach feature's signal can explain the depopulation of the CBM to the QDs' surface. Figure 4.11 reveals the fractional transient transmittance spectra for two samples at the time corresponding to the peak position of decays shown in Figure 4.5 where the excited electrons populate the CBM in

the system. In ideal cases, these spectra features should be due only to the state-filing process. In transient transmittance spectra the state-filling response is symmetrical and positive and has a width similar to that of 1S absorption and PL spectra. However, the spectral results shown in Figure 4.10 are not consistent with the characteristics of a state-filling only signal. The peak positions of these fractional bleaches are supposed to be the same as the corresponding positions of the minima of the 2nd derivative absorption spectra in Figure 4.3. Yet, the fractional bleaching deviates from the expected points to shorter wavelengths. There are two possible reasons for this blue shift, repulsive exciton-exciton interaction [27] and surface trapping [26].

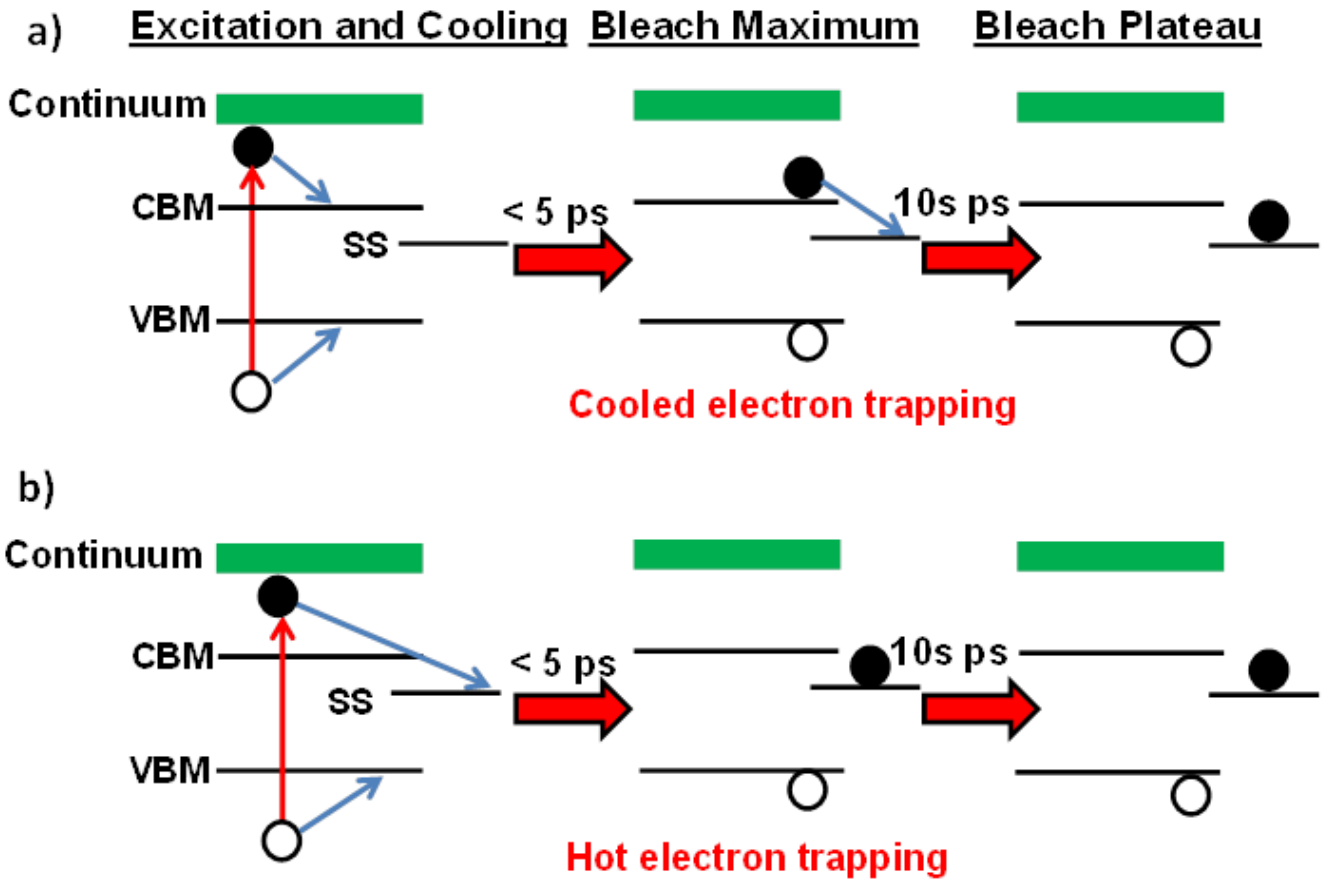

Figure 4.10. The diagram of a) cooled electron trapping and b) hot electron trapping processes that might occur when the samples are pumped with ultrafast pulse at 400 nm (~3.11 eV).

A broad PA that is due to surface trapping is observed at longer wavelength. This PA feature spectrally overlaps with the fractional bleaching and affects the shape, position and magnitude of the state-filling signal. Therefore, the observed blue shift in the peak of the transient bleach at the band-edge is largely due to carrier trapping on the QD surface. For example the broad PA for the sample with 2 ML has a significant effect so that the bleach at the band edge is almost entirely disappeared. It is expected that the Δ_{XX} can be an order of magnitude larger in Type II QD than in Type I. Values as large as 100 meV for CdS/ZnSe QDs have been reported [27], resulting in shifts of spectroscopic features that are significant in comparison with the linewidth of the band edge transition. However, the observed shift in Figure 4.11 is certainly too large and the wrong shape to be attributed just to the multi-exciton interactions in the dots.

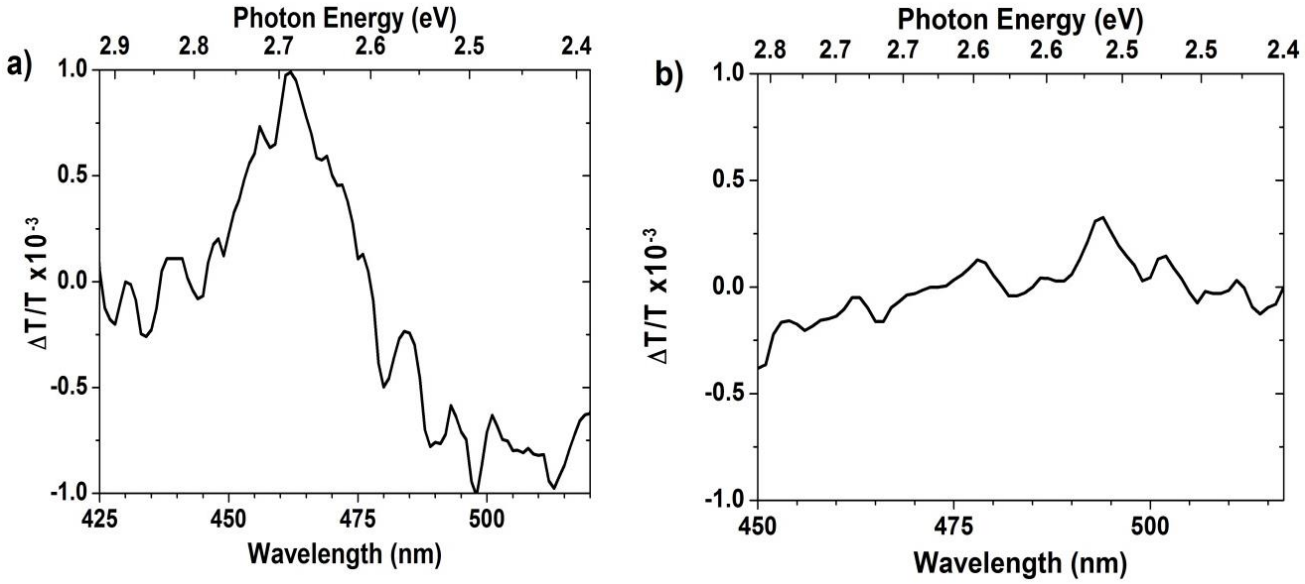

Figure 4.11. Differential TA spectra for 4.1 nm ZnTe core with a) 1 ML and b) 2 ML ZnSe shells. The spectra were recorded under 400 nm (~3.11 eV) excitation wavelength.

Tyagi *et.al* [25] proposed that excited state absorption (ESA) causes a negative broad PA feature. The ESA process occurs when the pump pulse generates an exciton and

the subsequent probe pulse excites the previous charge to the continuum of the CB which is an unexpected feature for ideal non-photocharged QDs [25]. In that case, due to trapping of an electron on the surface, the symmetry of the system is disturbed and thus the forbidden transitions, which are in this case ESA, are allowed. Therefore, this perturbation of symmetry and modifying of optical selection rules are responsible for the broad PA signal observed in the transmittance transient spectra in Figures 4.11.

The hot electron trapping mechanism also results in a broad PA signal which can be determined from the early stage of transmittance transients wherein the initial rise time corresponds to the relaxation time of the electrons. It has been suggested that Auger relaxation [28], phonon emission[29] and surface mediated relaxation [26, 30] contribute to the hot carrier relaxation process. Auger relaxation is proportional to the carrier wavefunction overlap and thus is more rapid for smaller NCs of type-I structures. However, the rate of phonon emission depends on the energy level separation and hence increases for large QDs. Figure 4.12 illustrates the initial stage of the decays of 1 and 2 ML samples recorded for the time resolution of about 3 ps, and the observed electron relaxation time is about 10 ps for both samples. However, the signature of the hot electron trapping is not detected in these decays. Therefore, the early stage of transmittance decays of the same samples were carried out by adjusting the step size of the delay stage to 0.1 mm corresponding to time resolution of ~ 0.7 ps that is regarded as high resolution time delays, as shown in Figure 4.13. In an ideal state filling process, the initial rise is expected to be monotonic starting from ground to the bleach maximum, meaning that hot electrons relax from excited states to the CBM, as it is for 2 ML sample curve. However, as it is clear that the initial rise for 1 ML starts from -15×10^{-4} value to the bleach maximum ($\sim 5 \times 10^{-4}$). The presence of negative signal in the small step transmission spectra shows that the

generated hot electrons relax not from the hot state but from the surface of the QDs indicating that there is significant hot electron trapping in these QDs.

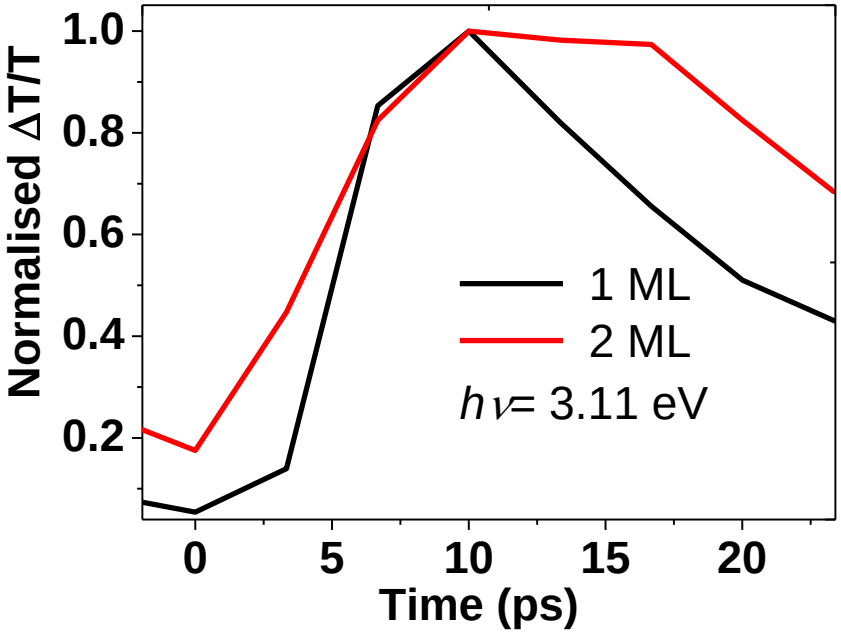

Figure 4.12. The normalised initial rise time for ZnTe/ZnSe samples with 1 ML (black) and 2 ML (red) recorded with time resolution of about 3 ps.

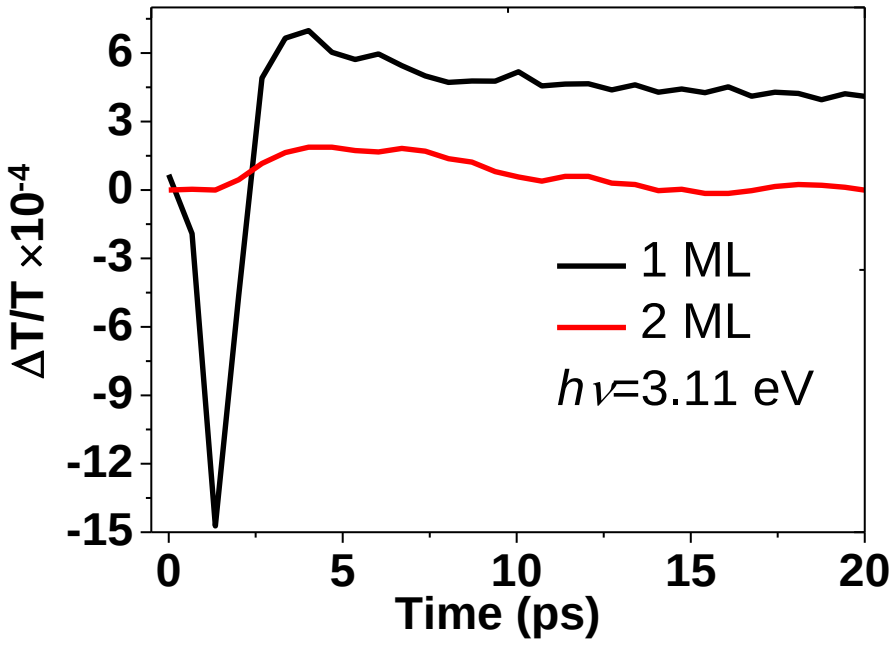

Figure 4.13. Small step fractional transmittance transients for the 4.1 nm core with 1 ML (black) and 2 ML (red) shell ZnTe/ZnSe QDs. The time resolution for this data is about 0.7 ps.

4.4 Summary

Ultrafast exciton dynamics of type-II ZnTe/ZnSe core/shell QDs has been investigated using a visible femtosecond TA experiment. It was found that hot and cold electron trapping take place which last for a time period of 10s of ps whose existence cannot be eliminated even with stirring the QD solution vigorously. A broad PA signal was observed that distorted and shifted the band edge bleach. The origin of the broad PA signal was found to be hot and cold electron trapping and ESA due to the presence of the surface state. Accumulation of charged QDs due to surface trapping was also detected in both cases when the samples were static at moderate pump powers and when the samples were stirred at high pump powers. This type of surface trapping resulted in bi-exponential transient decay with a second feature of about 10 times longer than the fast feature.

4.5 References

1. Jack Li, J., et al., *Wavefunction engineering: From quantum wells to near-infrared type-II colloidal quantum dots synthesized by layer-by-layer colloidal epitaxy*. Chemical Physics, 2005. **318**(1–2): p. 82-90.
2. Oron, D., M. Kazes, and U. Banin, *Multiexcitons in type-II colloidal semiconductor quantum dots.* Physical Review B, 2007. **75**(3): p. 035330.
3. Deutsch, Z., et al., *Energetics and dynamics of exciton-exciton interactions in compound colloidal semiconductor quantum dots.* Physical Chemistry Chemical Physics. **13**(8): p. 3210-3219.
4. Klimov, V.I., et al., *Optical Gain and Stimulated Emission in Nanocrystal Quantum Dots.* Science, 2000. **290**(5490): p. 314-317.
5. Schaller, R.D., J.M. Pietryga, and V.I. Klimov, *Carrier Multiplication in InAs Nanocrystal Quantum Dots with an Onset Defined by the Energy Conservation Limit.* Nano Letters, 2007. **7**(11): p. 3469-3476.
6. Chang, C.-C., et al., *Synthesis of Eco-Friendly CuInS2 Quantum Dot-Sensitized Solar Cells by a Combined Ex Situ/in Situ Growth Approach.* ACS Applied Materials & Interfaces, 2013. **5**(21): p. 11296-11306.
7. Derfus, A.M., W.C.W. Chan, and S.N. Bhatia, *Probing the Cytotoxicity of Semiconductor Quantum Dots.* Nano Letters, 2003. **4**(1): p. 11-18.
8. Tsoi, K.M., et al., *Are Quantum Dots Toxic? Exploring the Discrepancy Between Cell Culture and Animal Studies.* Accounts of Chemical Research, 2012. **46**(3): p. 662-671.
9. Commission, E. *Enterprise and Industry*. 2013 [cited 2013 12]; Available from: http://ec.europa.eu/enterprise/index_en.htm.
10. Zhang, R., et al., *Acute toxicity study of the interaction between titanium dioxide nanoparticles and lead acetate in mice.* Environmental Toxicology and Pharmacology, 2010. **30**(1): p. 52-60.
11. Wang, L., et al., *Toxicity of CdSe Nanoparticles in Caco-2 Cell Cultures.* Journal of Nanobiotechnology, 2008. **6**(1): p. 1-15.
12. Smith, A.M. and S. Nie, *Bright and Compact Alloyed Quantum Dots with Broadly Tunable Near-Infrared Absorption and Fluorescence Spectra through Mercury Cation Exchange.* Journal of the American Chemical Society, 2010. **133**(1): p. 24-26.
13. Tanaka, A., *Toxicity of indium arsenide, gallium arsenide, and aluminium gallium arsenide.* Toxicology and Applied Pharmacology, 2004. **198**(3): p. 405-411.
14. Bang, J., et al., *ZnTe/ZnSe (Core/Shell) Type-II Quantum Dots: Their Optical and Photovoltaic Properties.* Chemistry of Materials, 2009. **22**(1): p. 233-240.
15. Nanda, J., et al., *Light Amplification in the Single-Exciton Regime Using Excitonâ^'Exciton Repulsion in Type-II Nanocrystal Quantum Dots.* The Journal of Physical Chemistry C, 2007. **111**(42): p. 15382-15390.
16. Fairclough, S.M., et al., *Growth and Characterization of Strained and Alloyed Type-II ZnTe/ZnSe Core–Shell Nanocrystals.* The Journal of Physical Chemistry C, 2012. **116**(51): p. 26898-26907.
17. Tyrrell, E.J. and J.M. Smith, *Effective mass modeling of excitons in type-II quantum dot heterostructures.* Physical Review B. **84**(16): p. 165328.
18. Klimov, V.I., *Semiconductor and Metal Nanocrystals*. Marcel Dekker, ed. V.I. Klimov. Vol. 484. 2004, New York.
19. Schaller, R.D. and V.I. Klimov, *High Efficiency Carrier Multiplication in PbSe Nanocrystals: Implications for Solar Energy Conversion.* Physical Review Letters, 2004. **92**(18): p. 186601.
20. Binks, D.J., *Multiple exciton generation in nanocrystal quantum dots - controversy, current status and future prospects.* Physical Chemistry Chemical Physics. **13**(28): p. 12693-12704.
21. Smith, C. and D. Binks, *Multiple Exciton Generation in Colloidal Nanocrystals.*

Nanomaterials, 2013. **4**(1): p. 19-45.
22. Midgett, A.G., et al., *Flowing versus Static Conditions for Measuring Multiple Exciton Generation in PbSe Quantum Dots.* The Journal of Physical Chemistry C. **114**(41): p. 17486-17500.
23. McGuire, J.A., et al., *New Aspects of Carrier Multiplication in Semiconductor Nanocrystals.* Accounts of Chemical Research, 2008. **41**(12): p. 1810-1819.
24. McGuire, J.A., et al., *Apparent Versus True Carrier Multiplication Yields in Semiconductor Nanocrystals.* Nano Letters. **10**(6): p. 2049-2057.
25. Tyagi, P. and P. Kambhampati, *False multiple exciton recombination and multiple exciton generation signals in semiconductor quantum dots arise from surface charge trapping.* The Journal of Chemical Physics. **134**(9): p. 094706-10.
26. Kambhampati, P., *Hot Exciton Relaxation Dynamics in Semiconductor Quantum Dots: Radiationless Transitions on the Nanoscale.* The Journal of Physical Chemistry C. **115**(45): p. 22089-22109.
27. Klimov, V.I., et al., *Single-exciton optical gain in semiconductor nanocrystals.* Nature, 2007. **447**(7143): p. 441-446.
28. Klimov, V.I., et al., *Electron and hole relaxation pathways in semiconductor quantum dots.* Physical Review B, 1999. **60**(19): p. 13740-13749.
29. Stewart, J.T., et al., *Comparison of Carrier Multiplication Yields in PbS and PbSe Nanocrystals: The Role of Competing Energy-Loss Processes.* Nano Letters. **12**(2): p. 622-628.
30. Pandey, A. and P. Guyot-Sionnest, *Slow Electron Cooling in Colloidal Quantum Dots.* Science, 2008. **322**(5903): p. 929-932.

Chapter 5: Ultrafast charge dynamics in $CuInSe_2$ and $CuInS_2$ QDs

5.1 Introduction

In this chapter picosecond exciton dynamics of $CuInSe_2$ and $CuInS_2$ colloidal QDs will be investigated using an ultrafast TA experiment. Initially, the PL and absorption spectroscopies of the samples will be carried out. Next the ultrafast relaxation channels in these QDs will be revealed in detail by investigating charge dynamics of the sample.

5.1.1 Motivation

Recently, colloidal QDs of ternary semiconductors, such as $CuInSe_2$ and $CuInS_2$ (CIS in short), have drawn significant interest due to their unique characteristics. As well as being cheap to produce in large scale, these materials are also of engineered nanostructures which have size-tunable optical properties, making them attractive for numerous applications. In addition, like zinc-based materials, CIS QDs are also environmentally-friendly materials that have potential to be alternatives to toxic QDs [1, 2]. These QDs have a direct band gap so that they have potential to emit efficiently light in the visible and NIR region of the spectrum [3, 4]. Therefore, CIS QDs have a promising future for light emitting types of display electronics [5], NIR photodetectors [3], and in particular, in the biolabeling region (650-900 nm) [6] where the light absorption of water molecules is negligible. In addition, since CIS QDs have a direct low bandgap in the NIR region (up to 1.05 eV) , they are considered as a strong candidate for maximising the efficiency of the single junction solar cells where only one electron hole pair is produced per excited QD [3]. CIS QDs can also be used in the third generation photovoltaics, utilising MEG where the excess energy of the absorbed photon also contributes to the photocurrent, increasing the device efficiency as high as 44% [7].

Chapter 5 Ultrafast charge dynamics in $CuInSe_2$ and $CuInS_2$ QDs

The efficiency of the proposed optoelectronic devices depends on the employed QDs' quality and hence surface properties, such as surface trapping and non-radiative recombination which occur in the ps time scale [8-11]. It has been shown that the PL QY of NCs increases significantly with eliminating charge trapping on the surface [12]. Likewise, some recent reports have indicated that surface trapping restricts the MEG efficiency [13, 14], charge transfer in photovoltaics [15] and lasing [16]. To date ultrafast exciton dynamics of lead chalcogenide (PbX, X= S, Se, or Te) semiconductor QDs have been intensively investigated as they have a bandgap in the NIR spectral range, well-suited for photovoltaics and photodetectors. Further, some recent studies reported experimental ultrafast exciton dynamics of InAs [10], AlP [17] and CdS [9] NCs and theoretical explanation of trap-mediated processes on an ultrafast time-scale in InAs QDs [18]. Recently, $CuInS_2$ QDs have been used to measure the ultrafast electron transition time from excited donor materials into a TiO_2 substrate where the transfer rate was found to be 5.75×10^{11} s^{-1} [19]. In another study, the PL quantum efficiency of $CuInS_2$ QDs was significantly increased by growing CdS or ZnS monolayers around the material [20]. Similarly, the PL efficiency of $CuInSe_2$ QDs has been improved by ~60% using ZnSe and ZnS shells [21]. Despite these few initial studies, there is still limited knowledge about the ultrafast exciton dynamics of CIS colloidal QDs.

5.1.2 Sample information

In this study $CuInSe_2$ and $CuInS_2$ QDs with two different sizes from each material were obtained from Nanoco Group plc. Samples were dispersed either in anhydrous hexane or dry toluene. A glove box was used to prepare samples under nitrogen atmosphere to avoid oxidation that has a detrimental effect on the optical properties of the materials. The solutions were kept in 5 mm wide and 10 mm long quartz cuvettes during the study

process. The concentrations of solutions were adjusted so that the absorbance was between 0.2 and 0.4 to observe the ultrafast dynamics of QDs in a concentration free condition.

5.2 Initial sample characterization

Initially, the steady-state absorption and PL spectra of the samples were recorded to define the basic optical transition positions for the CIS samples using a Perkin Elmer Lambda 1050 spectrophotometer and a Horiba Jobin Yvon Fluorolog-3 model FL3-22iHR Spectrofluorometer, respectively. These machines are described in detail in Section 3 and 2 in Chapter 3, respectively. The excitation wavelength of the PL spectrofluorometer was tuned to 400 nm (~3.11 eV) to acquire the PL spectra. When recording absorption spectra, cuvettes of either anhydrous hexane or blank dry toluene were used in the reference arm. Figure 5.1 a) and b) depict the absorbance and PL spectra for two different $CuInSe_2$ samples. As seen from Figure 5.1 a), the absorption shoulder for the first sample is about 660 nm (~1.88 eV). However, it is hard from the largely featureless rise of the absorption spectrum of the second $CuInSe_2$ sample to decide the position of the absorption band gap. This is attributed to the large size distribution of the nanoparticles [4]. Therefore, the ground-state absorption feature for this sample was evaluated from the differential TA spectra where the hot electrons quickly occupy the available states in the minimum of the conduction band, resulting in bleach. Figure 5.2 shows the differential TA spectra, which confirms the absorption band edge to be about 770 nm (~1.61 eV) and the 2^{nd} derivative of the 1S absorption spectra for the second $CuInSe_2$ sample, $d^2A/d\lambda^2$. Based on the absorption band gap information of $CuInSe_2$ dots, their sizes are estimated from effective mass approximation calculations data for ternary chalcopyrite NCs provided in Ref.[5]. With reference to this approximation, 660 nm (~1.88 eV) and 770 nm (~1.61 eV) band

gaps correspond to diameters of 2.3 nm and 3.0 nm, respectively. The PL peak position for 2.3 nm dots is found to be about 766 nm (~1.62 eV) with a width of 101 nm. The broad PL width is attributed to large size and shape distribution of the dots [4]. There is about 106 nm global Stoke shift between PL and absorption spectra which originates from strong electron-phonon coupling, band edge exciton fine structure and inhomogeneous size dispersion [22-24]. Therefore, the PL maximum position for the 3.0 nm sample was expected to be about 950 nm. However, this is out of the spectral range of the PL machine and hence it is not shown here.

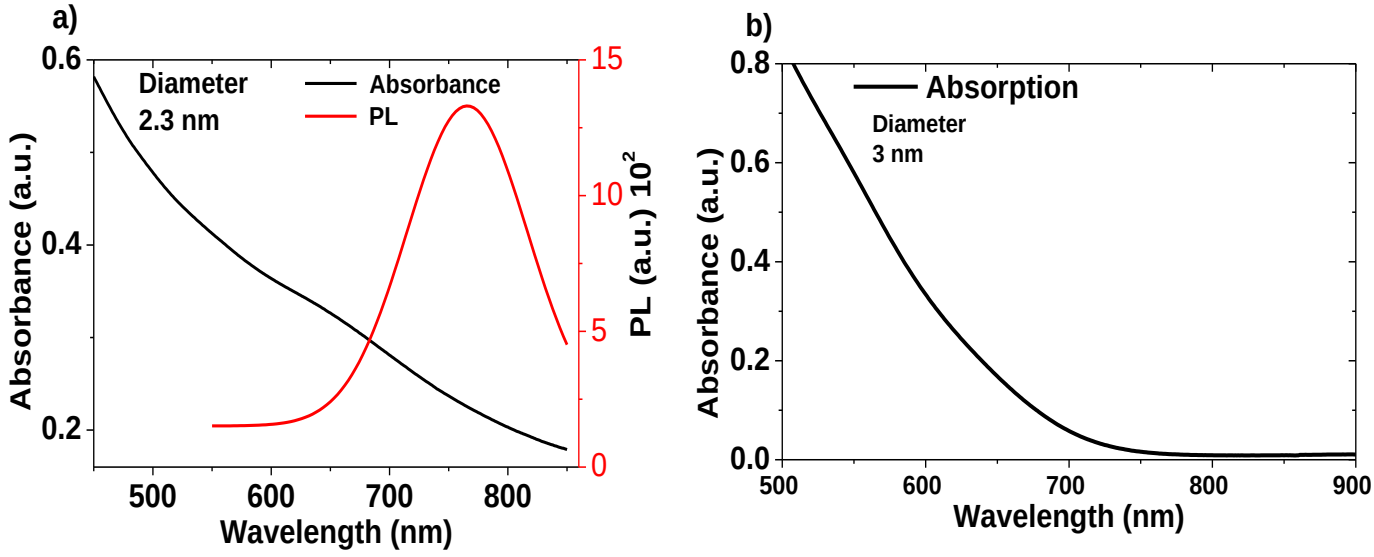

Figure 5.1. a) Linear absorption (black) and PL (red) spectra for $CuInSe_2$ QDs with 2.3 nm diameter and b) absorption spectra for $CuInSe_2$ QDs with 3.0 nm diameter.

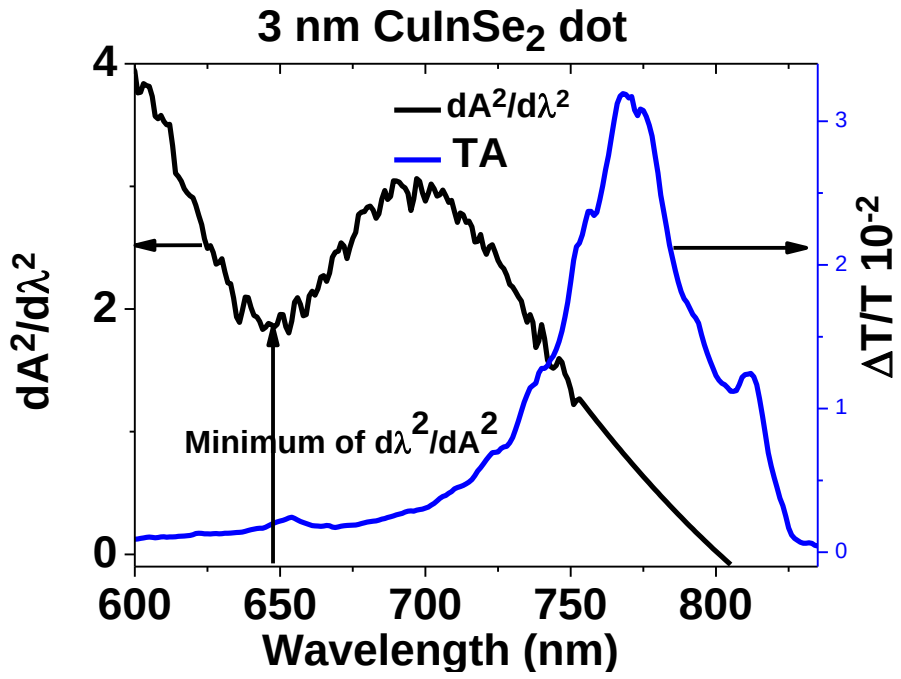

Figure 5.2. The comparison of the 2nd derivative of the 1S absorption spectra (black) and the fractional transmittance spectra (blue) for $CuInSe_2$ sample with 3.0 nm diameter.

Figure 5.3 illustrates the absorption and PL spectra of $CuInS_2$ samples. The 1S absorption spectra for each sample are found to be about 540 nm (2.3 eV) and 515 nm (~2.41 eV) as at these points the absorption spectra show smear features. Based on the absorption band edge data, the size estimation of $CuInS_2$ samples were predicted from effective mass approximation calculations for ternary chalcopyrite QDs [5] which let to diameters of roughly 2.4 nm and 2.1 nm, respectively. The PL peak energies occurred at 635 nm (~1.96eV) and at 745 nm (~1.67 eV) for the samples with sizes of 2.1 nm and of 2.4 nm, respectively. Liang *et al.*[20] also have estimated the empirical relationship between the PL peak energies and size information for $CuInS_2$ which agrees well with the sizes estimated for samples used here. From Figure 5.3 the full width at half maximum (FWHM) for 2.1 nm and 2.4 nm samples are found to be 99±1 nm and 105±1 nm, respectively. The wide width of PL spectra show the large size and shape distribution of the dots [4]. The size inhomogeneity for those samples are also confirmed from the mainly featureless profile of

absorption spectra of the samples [4].

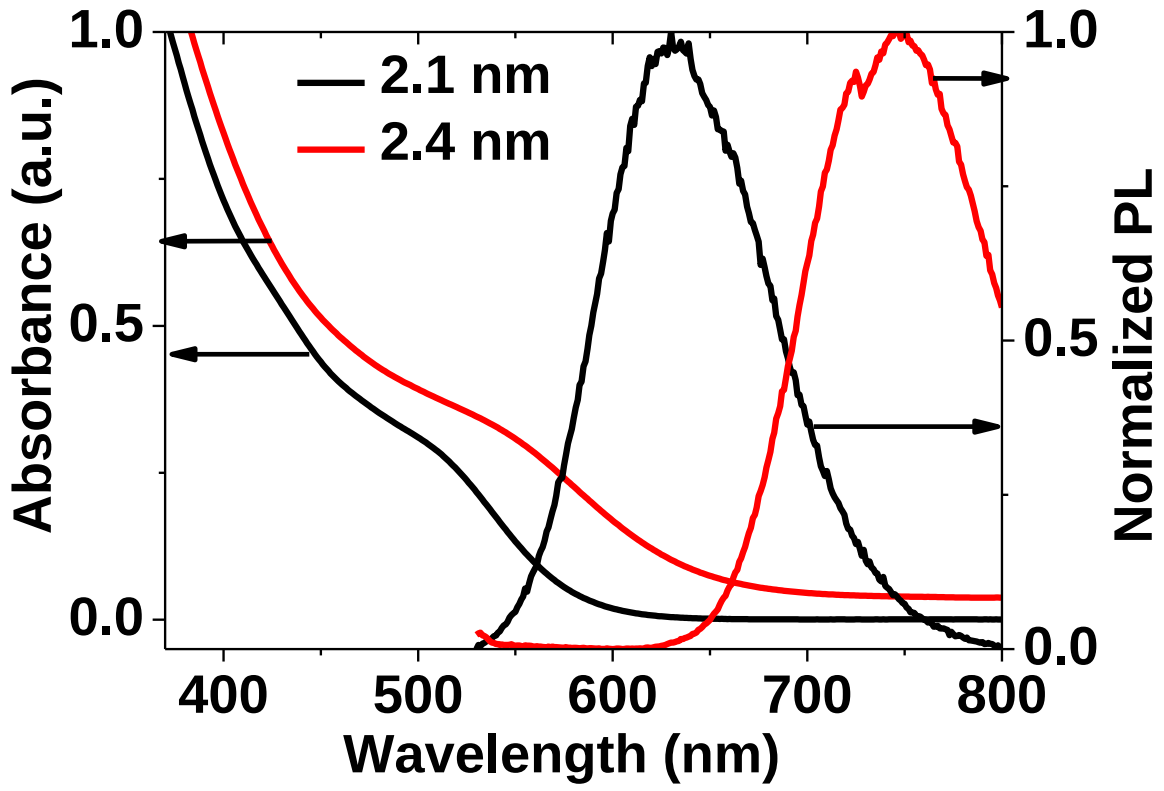

Figure 5.3. The absorption and PL spectra for $CuInS_2$ QDs with diameters of 2.1 nm (black) and 2.4 nm (red). The PL spectra were recorded at 400 nm (~3.11 eV) excitation wavelength.

5.3 Transient absorption spectroscopy

The femtosecond TA experiment used here is described in detail in Chapter 3 section 4. The excitation wavelengths were adjusted to be both 450 nm (2.76 eV) for $CuInS_2$ and 400nm (~3.11 eV) for $CuInSe_2$ dots. The probe wavelengths for the case of $CuInSe_2$ QDs were tuned to 660 nm (~1.88 eV) and 770 nm (~1.61 eV) for the dots with diameters of 2.3nm and 3.0 nm, respectively. Similarly, for the $CuInS_2$ case, the probe beam wavelength was adjusted to match the absorption edge i.e. 540 nm (2.3 eV) and 515 nm (~2.41 eV) for the dots with diameters of 2.4 nm and 2.1 nm, respectively. All other experimental

parameters remained the same as described in Chapter 3.

5.3.1 Results and discussions for $CuInSe_2$ QDs

Figure 5.4 a) and b) show the pump induced fractional transmittance transients for $CuInSe_2$ QDs at several different pump powers, when they were excited at 400 nm (~3.11eV) pump wavelength. This pump photon energy corresponds to about 1.65 and 1.9 times of the band gaps of the samples with sizes of 2.3 nm and 3.0 nm, respectively, i.e. too low to allow MEG to occur. Here the pump fluence was adjusted to be as low as possible to ensure the probability of absorbing more than one photon per dot is negligible. Hence, the incident pump power range was kept between 0.3 mW and 3 mW. The transients involve two phases; initial rise (~10 ps) and decay to plateau (10s -100s of ps). The former corresponds to the process of hot exciton relaxation from the higher states to the band edge where they fill states, reaching the absorption at the probe wavelength and increasing the transmittance [25]. The latter process is when the relaxed carriers undergo recombination or trapping [9]. The transients for the 2.3 nm sample are globally fitted with mono-exponential decay to a plateau. This plateau represents the long-lived single exciton whose lifetime is too long to be detected with the TA experiment used here. This fitting yields a time constant of 32.1±0.3 ps. On the other hand, the decay transients for the 3.0 nm sample are bi-exponential to a plateau, and a global fit yields rapid time constants of 32.8±0.5 ps and 497±4 ps.

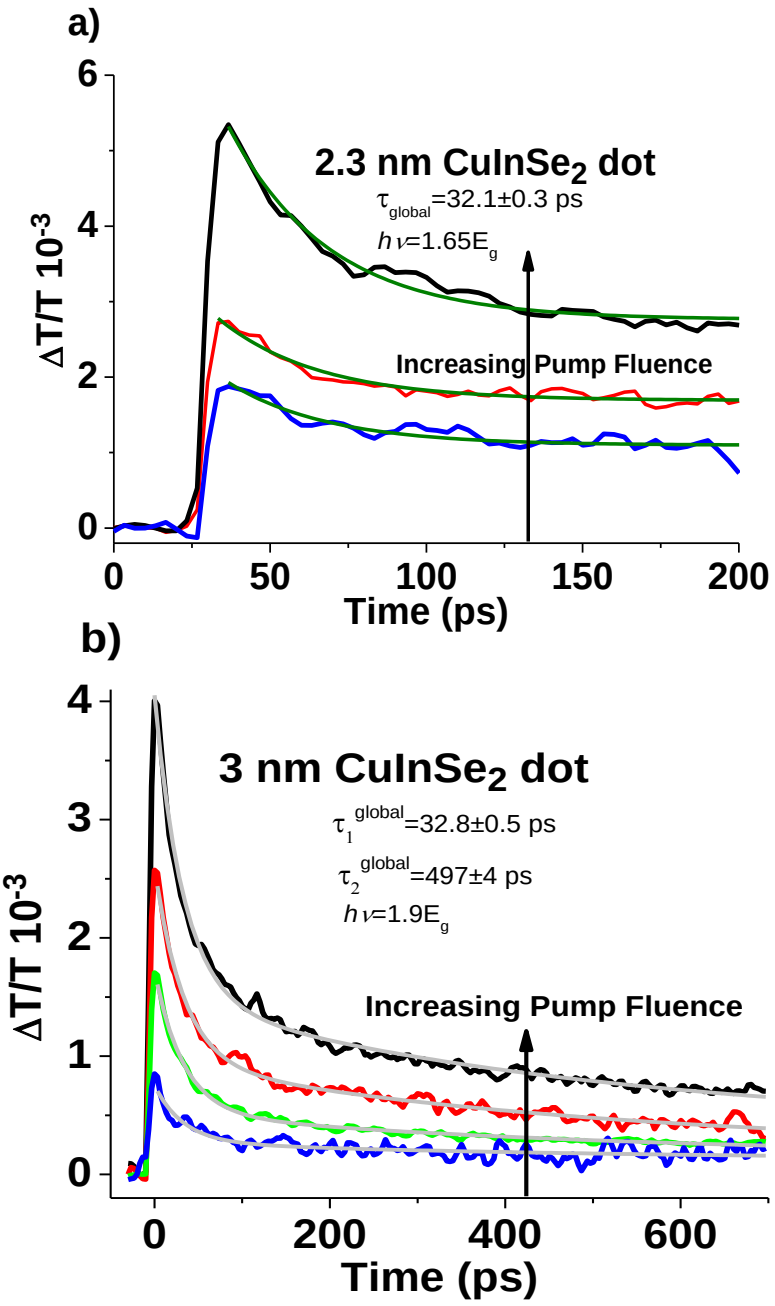

Figure 5.4. Pump-induced fractional transmittance transients for $CuInSe_2$ QDs with diameters of a) 2.3 nm and b) 3.0 nm for 400 nm (~3.11eV) excitation wavelength. Olive and Grey lines represent the mono-and bi-exponential fittings, respectively.

The observed ultrafast decay lifetimes are in the order of the picosecond time scale, consistent with Auger recombination of multi-excitons, generated either by multi-photon absorption, MEG, trion decay, or surface trapping [8, 9, 22, 26]. Now we will analyse these ultrafast processes one by one in detail and decide which one is dominant in the transient

decays shown in Figure 5.4 a) and b). As explained previously in Chapter 4, a process that might describe the decays is biexciton (or multi-exciton) decay to a single exciton via efficient Auger recombination. Multi-excitons can be produced at high pump fluences where the numbers of absorbed photons per dot per pulse are more than one. Hence, it is necessary to estimate the average number of absorbed photons per dot to determine the potential effect of biexciton recombination on the observed decays. Poisson statistics defines the possibility of a dot to absorb N photons during a pulse and hence have N excitons just after excitation which is given in Eq. (4.2). The average number of absorbed photons per QD, <N>, is expressed in Eq. (3.9). The maximum $\Delta T/T$ in Figure 5.4 a) is about 5×10^{-3} and the absorbance of the nanocrystal solution at the band edge is about 0.3. Then, from Eq. (3.9), the maximum value of <N> becomes 0.033. After substituting the calculated <N> value into Eq. (4.2), we obtain the probability of absorbing two photons per dot during a pump pulse, P_2, to be about 5.3×10^{-4} which is negligible compared with the probability of absorbing one photon per dot, P_1, which is about 0.032 for the same dots [10]. These results are not consistent with the mono-exponential decay fitting of the transients of 2.3 nm QDs as the transients consist of two decays; a ps non-radiative feature and a long-lived single exciton feature. Hence it is crucial to explain the origin of the ps non-radiative decay component. Similarly, if we apply the Poisson statistics to the transients of the 3.0 nm samples, the P_2 value for this sample becomes about 3.5×10^{-6}, which is negligible compared with the value of P_1 for the same dots which is about 2.7×10^{-3}. Thus it is concluded that the observed decays are not due to multi-exciton recombination where the multi-excitons are generated by the absorption of more than one photon per QD per pulse.

As stated above, the MEG mechanism is capable of producing more than one

exciton from a single absorbed photon. However, the MEG onset threshold depends on the effective masses of carriers and the bandgap of the material and whose expression is given in Eq.(2.7). Since the ratio between effective masses of electrons and holes, m_e^*/m_h^*, is about 0.12 for $CuInSe_2$ [27], then the MEG threshold becomes around $2.12E_g$. However, the transmittance transients for each sample were recorded for a pump wavelength of 400 nm, which is below the MEG threshold for both samples. Thus it is concluded that there is no effect of the MEG process on the observed transients.

Transmittance decay on the time scale of 10s and 100s of ps can also be a result of trion formation. The importance of this effect was recognised after a number of careful MEG studies [13, 14], as cartooned in Figure 4.7. The effect of trions is determined by comparing the transients conducted under stirring and static circumstances. In the former case, the accumulated QDs with long-lived trapping charges are swept out of the detection volume and fresh QDs are swept in, removing or reducing the effect of trions. Here, therefore, the fractional transmittance transients were recorded under stirring and static conditions for the sample with 2.3 nm diameter and the results are presented in Figure 5.5. Despite some noise in the stirred case, there is no significant difference between the two decays and they are both well-described by a global single exponential fit with a time constant of 33±1 ps. This suggests that there is no significant charge trapping that lasts longer than the time period between two laser pulses. However, in certain cases, the whole QDs in the solution can contain the long-lived charges and thus the stirring cannot suppress the effect of trions properly as there is no fresh QDs to be pumped. Therefore, a different approach is proposed to observe the trion formation in QDs which is the investigation of the transmittance change in the sample during a one-hour experiment [10]. In that case, the first, last and the average of 10 consecutive decays are compared and if there is a trion

formation, the decay dynamics will be changed to the gradual accumulation of trapped charges [10]. Figure 5.6 a) and b) compare the decays taken at the beginning of experiment and at the end of the experiment and the average of 10 consecutive scans taken during the experiment for the samples with sizes of 2.3 nm and 3.0 nm, respectively. In both cases, there is no visible difference between the first, second and the average decays, meaning that the samples do not change during the experiment. The decays for 2.3 nm dots are well-described with global single exponential fitting which yields a time constant of 34±2 ps, whereas, the decays for the 3.0 nm sample are globally fitted with a bi-exponential function with time constants of 36±2 ps and 500±9 ps. These findings indicate that there is no significant effect of trions for the transients observed for both 2.3 nm and 3.0 nm $CuInSe_2$ QDs, respectively.

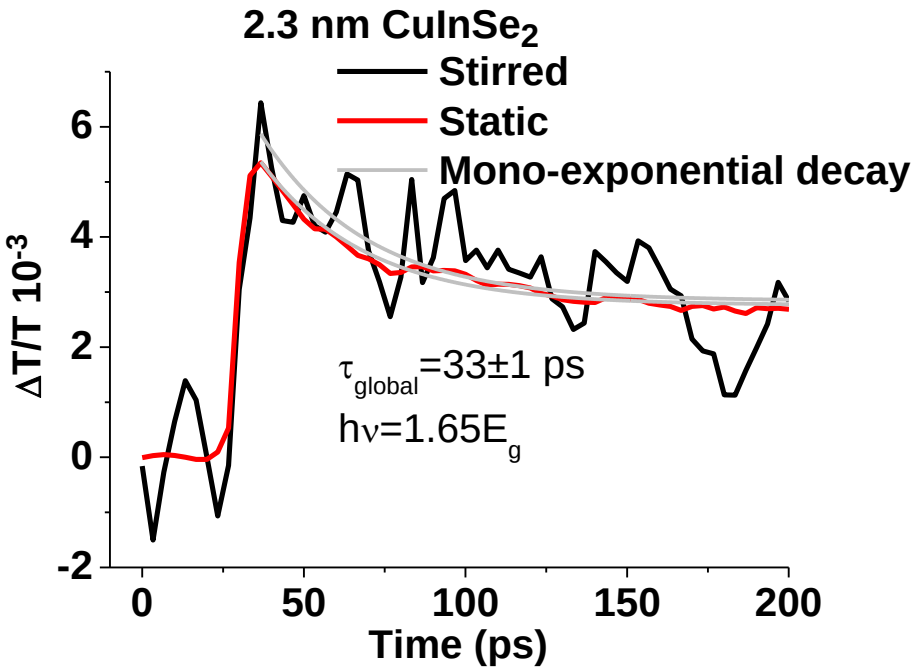

Figure 5.5. Fractional transmittance transients for the 2.3 nm $CuInSe_2$ QDs for stirred (black) and static (red) samples. The grey lines are single exponential fits for both transients.

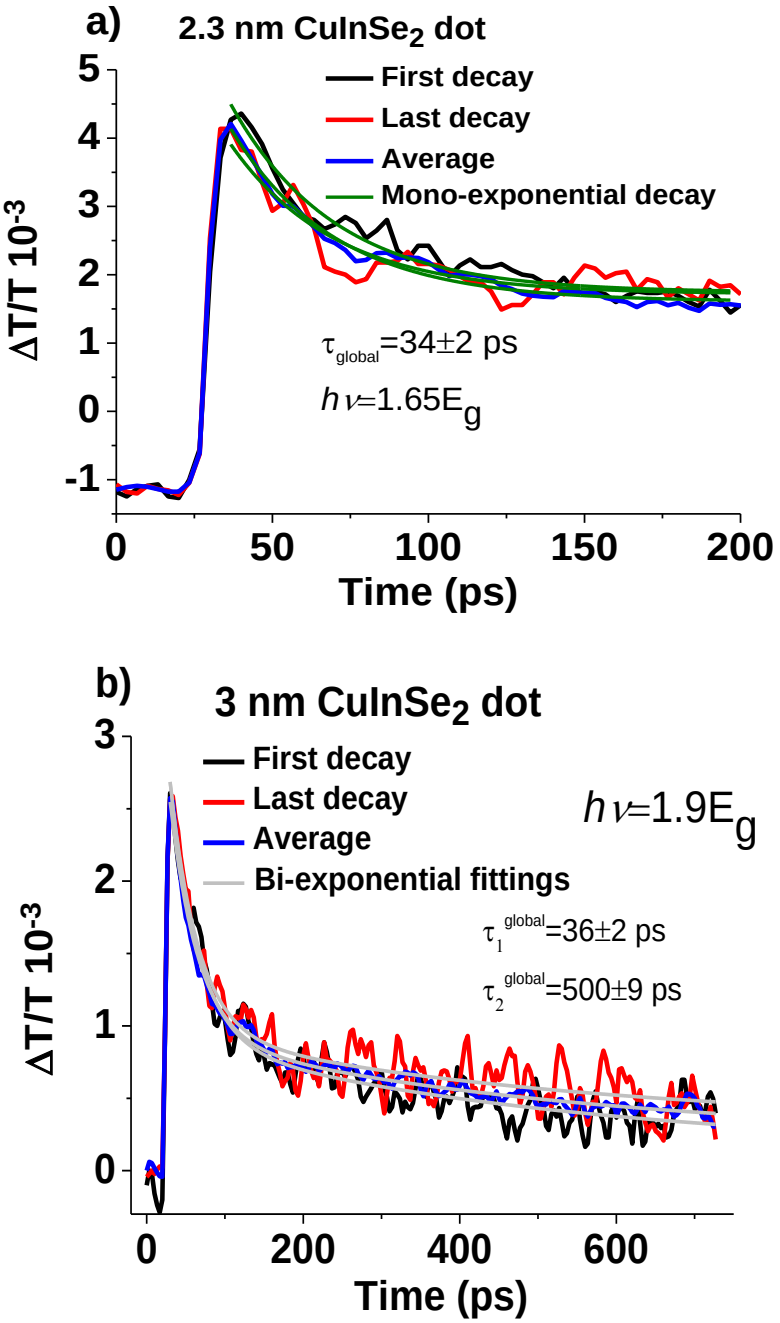

Figure 5.6. Fractional transmittance transients for the first (black), last (red) and average (blue) of 10 sequential scans for a) 2.3 nm and b) 3.0 nm $CuInSe_2$ samples. Olive and grey lines represent the mono-and bi-exponential fittings, respectively.

Electron trapping of the surface can depopulate the CBM; hence reversing the bleach, and previous studies on CdSe QDs have shown that this can occur on the timescale of 10s ps [8]. Similar features were also observed in ZnTe/ZnSe type-II QDs shown in Chapter 4. Thus, trapping could explain the observed decays even if short-lived compared to the pulse-to-pulse separation. Such trapping has been shown to result in PA in the region

of the band edge which changes to the shape and position of the bleach [9]. As seen in Figure 5.2, the transient transmittance spectrum for the 3.0 nm sample is positive over the scanned spectral region but has a narrower FWHM and is significantly red-shifted compared with the $d^2A/d\lambda^2$ curve, which shows strong evidence of electron trapping of the surface. Thus it is concluded that the short decay feature for the 3.0 nm sample is attributed to direct depopulation of carriers from the band edge.

Recently, it has been reported that a highly emissive channel with a lifetime of 190ns, less than the time period between consecutive laser pulses, was observed in $CuInS_2$ NCs [20]. As this feature could not be supressed with coating the bare $CuInS_2$ dots with a CdS shell, it is attributed to the recombination of the electrons in the CBM with the holes trapped in the internal states, being far from the surface states. Since the electronic structures of $CuInSe_2$ and $CuInS_2$ are very similar, then the long decay feature for the 3.0nm sample could be attributed to the recombination of the electrons with the internal trapped holes.

Figure 5.7 reveals the differential TA spectra at the band edge region for the 2.3 nm sample recorded at t= 12 ps, when all photogenerated excitons occupy the band edge. Clearly, there is no negative sign of the TA spectra over the scanned region. This suggests that the sample with diameter of 2.3 nm is free from surface trapped electrons. As explained in Chapter 4, $d^2A/d\lambda^2$ shows the location of the absorption band edge more clearly, which is plotted for 2.3 nm in Figure 5.7 to compare with the TA spectra. As it is apparent from the evaluation of two curves the minimum of $d^2A/d\lambda^2$ overlaps with the maximum of the TA spectra. This indicates that the TA spectrum is only due to the occupying of band edge states by hot carriers where the absorption is decreased at the probe wavelength. Thus, as it was for the 3.0 nm sample, we can conclude that the decay

feature with 32.1±0.3 ps for the 2.3 nm sample could be due to the hole trapping of the internal defect site which was observed for the first time in $CuInS_2$ QDs [20].

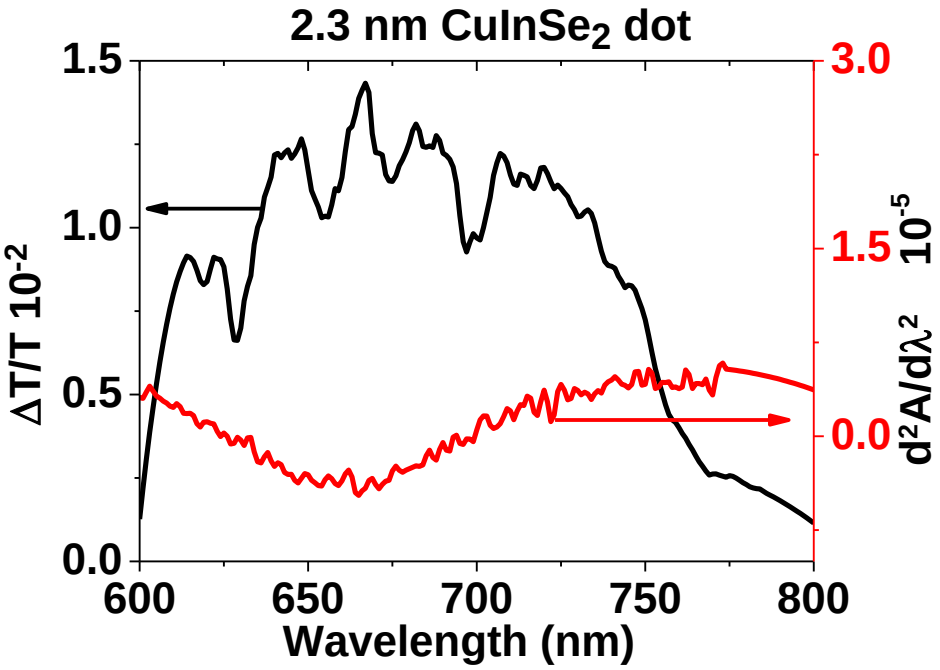

Figure 5.7. Comparison of the Savisky-Golay smoothed differential TA spectrum (black) and the 2nd derivative absorption spectrum (red) for 2.3 nm diameter $CuInSe_2$ QDs. An excitation energy of ~3.11 eV (1.65E_g) was used to record the TA spectrum.

5.3.2 Results and discussion for $CuInS_2$ QDs

Figure 5.8 a) and b) show the ΔT/T values as a function of delay time between the pump and probe pulses for 2.1 nm and 2.4 nm diameter $CuInS_2$ QDs for several average pump powers, respectively. An excitation wavelength of 450 nm (2.76 eV) was chosen which corresponds to about 1.14 and 1.2 times the absorption band gaps of 2.1 nm and 2.4 nm diameters samples, respectively, i.e. too weak to onset the MEG mechanism for the samples. Each decay is the average of 10 consecutive scans of the delay stage. It can be seen clearly from the figures that the pump induced changes in transmittance increases as the pump fluence increases. In addition, as the pump fluence increases the appearance of

the initial decay becomes clearer for both samples. The decays taken under absorbed pump powers of 0.3 mW, 0.4 mW and 0.5 mW for 2.1 nm dots are well-described with a global single exponential fitting which gives a time constant of 87±8 ps. However, the decay recorded under 1 mW absorbed pump power for the same sample is fitted with a bi-exponential decay that yields time constants of 24.4±0.9 ps and 88±1 ps. The emergence of the short life time at high pump fluence indicates that an extra ultrafast recombination or surface-mediated trapping takes place in 2.1 nm NCs. On the other hand, all decays for 2.4nm diameter samples are well explained by a global mono-exponential fit which yields a time constant of 117±10 ps. It is certain that the additional decay feature at 1 mW pump fluence for the 2.1 nm sample is not due to the MEG process. This is because, since the ratio between the effective masses of electrons and holes, m_e/m_h is about 0.12 in $CuInS_2$ QDs [27], then the MEG onset becomes $2.12E_g$ using Eq.(2.7). However, the pump wavelength used is $1.14E_g$ for the sample with 2.1 nm diameter.

Since the degeneracy of $CuInS_2$ QDs is 2 fold [20], the absorbance at the band edge is 0.3 and the maximum $\Delta T/T$ for the 2.1 nm sample is about 1.2×10^{-3}, then using Eq. (3.9) the maximum <N> value for the 2.1 nm QDs is calculated to be 8×10^{-3}. By substituting the <N> value into Eq.(4.2) we obtain the probability of absorbing two photons per QD during a pulse, P_2, for the 2.1 nm dots is about 3×10^{-5}. This value is insignificant compared with the P_1 value which is about 8×10^{-3}. This indicates that when 2.1 nm samples are pumped at pump fluence levels of 1 mW or less, only one photon per QD is absorbed, meaning that only the signal of the long-lived exciton ought to arise from the transient decays. However, as shown in Figure 5.8 a), there are two components that are not explained by Poisson statistics; the emerged fast decay feature when pumping with 1 mW absorbed pump power and the long decay component when pumping below 1 mW absorbed pump power.

Therefore, time constants of 24.4±0.9 ps and 88±1 ps are more likely to be due to either trion formation or surface trapping of carriers, or any other ultrafast process occurring in the sample.

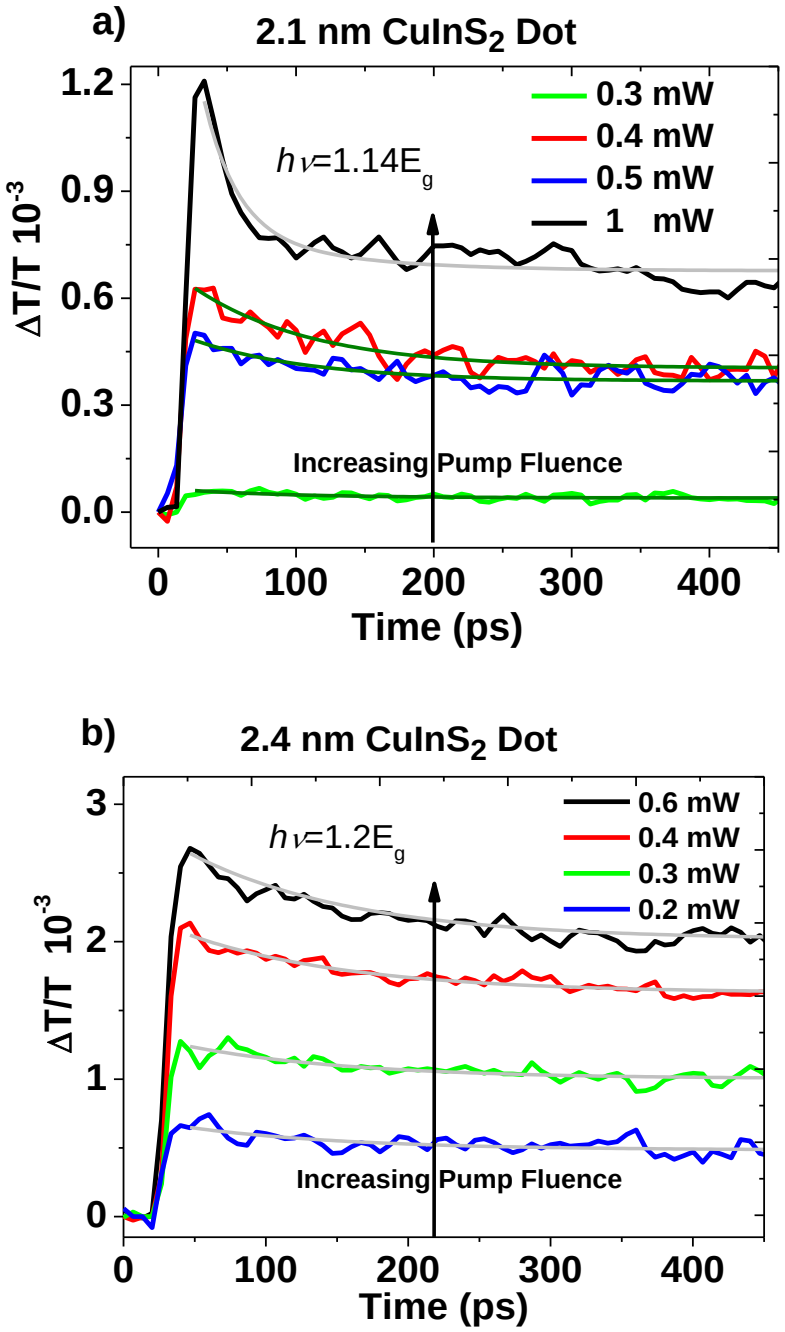

Figure 5.8. The pump induced fractional transmittance transients for a) 2.1 nm and b) 2.4 nm $CuInS_2$ QDs for an absorbed pump fluence alternating between 0.2 mW and 1 mW at 450 nm (2.76 eV) excitation wavelength. The olive and grey lines in a) represent mono- (τ=87±8 ps) and bi-exponential (τ_1=24.4±0.9 ps and τ_2=88±1 ps) fittings, respectively, whereas the grey lines in b) show the global single exponential fit to the decays with a time constant of 117±10 ps.

Similarly, if we consider the 2.4 nm diameter sample case, the maximum $\Delta T/T$ in Figure 5.8 b) is about 2.5×10^{-3} which yields the maximum <N> value of roughly 0.02 at the band edge absorbance of 0.3. Based on this calculation, P_1 and P_2 for 2.4 nm NCs are calculated to be $\sim2\times10^{-2}$ and $\sim2\times10^{-4}$, respectively. Hence, the value of P_2 is negligible in comparison with that of P_1. This suggests that at the excitation levels of 0.6 mW or less only one photon is absorbed per QD and hence the resultant decay must be in the form of a plateau. However, this conclusion is not consistent with the transient decays observed in Figure 5.8 b), as it is mono-exponential in form. Hence, it is necessary to determine the origin of the time constant of 117±10 ps extracted from Figure 5.8 b).

Figure 5.9 compares the differential TA spectra taken at t=0 ps and t=20 ps and the $d^2A/d\lambda^2$ for 2.4 nm diameter $CuInS_2$ QDs. The spectrum recorded at t=0 ps corresponds to the time when all photo-generated carriers relax to the sample band edge and hence $\Delta T/T$ is maximum, whereas, t=20 ps corresponds to the time when the relaxed excitons have started to leave the band edge states by recombination or trapping [9]. Since the minimum position of $d^2A/d\lambda^2$ corresponds to the absorption band edge of the dots, the maximum of the TA spectrum ought to be overlapped with the minimum of $d^2A/d\lambda^2$ spectrum. As it is clear from Figure 5.9 the pump induced transmittance change spectrum is positive over the scanned spectral region (470 nm – 600 nm) and its maximum position (~546 nm) matches well with the minimum of the $d^2A/d\lambda^2$ spectra. This feature is attributed to the fact that the pump induced bleach occurs when the carriers occupy the absorption band edge of the sample, reducing the absorption at the probe wavelength. In addition, the pump induced transmittance change spectrum is of similar shape and breadth to the linear absorption spectra which further supports that the observed differential TA spectrum is purely due to the relaxation of hot carriers from the higher states to the absorption band edge. The

broadness of the differential absorption spectra is attributed to the large size dispersion of $CuInS_2$ samples [4]. Therefore, it is concluded that direct surface trapping in 2.4 nm dots does not occur.

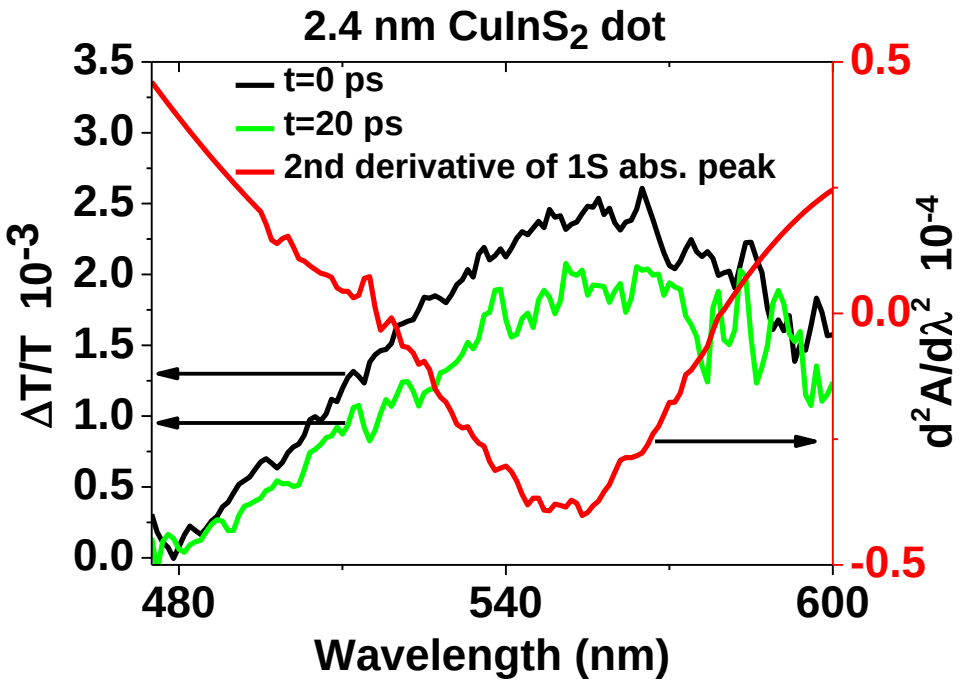

Figure 5.9. The comparison of the fractional differential TA spectra at t= 0 ps (black) and t=20 ps (green) and the Savisky-Golay smoothed second derivative absorption spectra (red) for 2.4 nm diameter sample. The pump energy was tuned to 2.76 eV ($1.2E_g$) when collecting the TA spectra data.

Figure 5.10 compares the first, last and the average scans of decay transients for the 2.4 nm sample to investigate the effect of trion formation. It is obvious from the decays there is no distinct difference between the three scans and they are all take a mono-exponential form with a global lifetime of 117±1 ps. This suggests that the 2.4 nm samples are not photo-damaged to build-up QDs with long-lived trapped charges. Up until now, MEG, absorption of multi-photons, direct surface trapping and trion formation have been introduced to the transient decays of 2.4 nm $CuInS_2$ dots, but none of these processes could explain the mono-exponential decay feature observed for this sample. Thus, it is concluded that the observed transient is consistent with the radiative recombination of trapped holes

in the internal defect states with the electron in the CBM, which occurs on the time scale of 100s of ns [20].

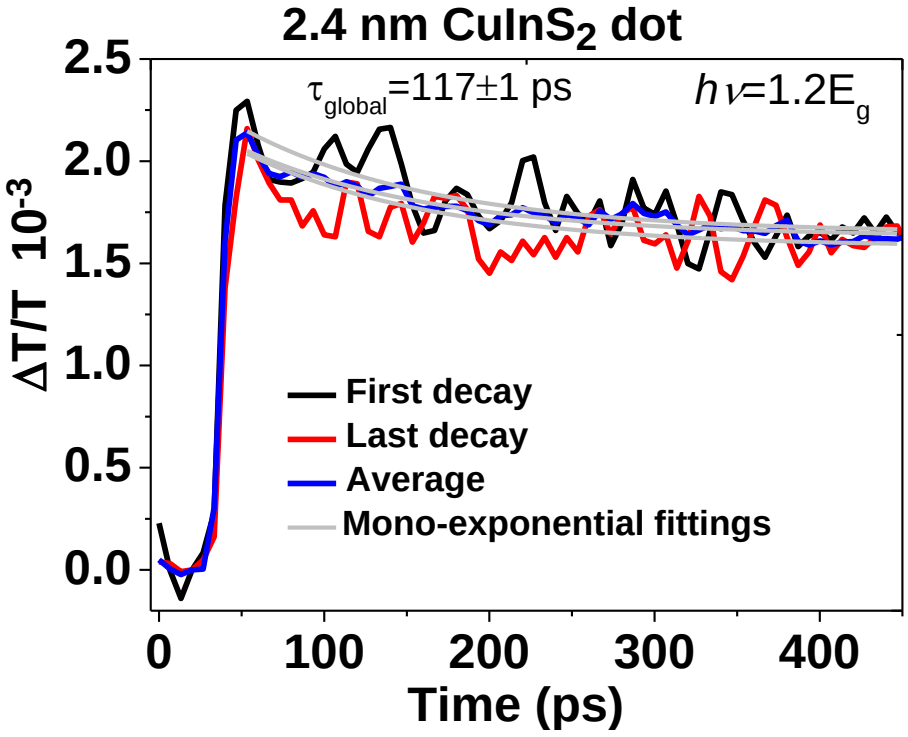

Figure 5.10. The comparison of the first, last and the average of cycles of 10 scans of the fractional transmittance transients for 2.4 nm dots. The grey lines denote the mono-exponential fittings.

Figure 5.11 compares the fractional transmittance transients for 2.1 nm dots recorded when the solution is vigorously stirred to when it was static for the excitation level of 1 mW absorbed power with all other parameters remaining the same. It is known that if there is the effect of trions on the TA decays of NCs, then this contribution is suppressed by stirring the sample strongly. However, it is apparent from the figure that there is no appreciable difference between the transients recorded under stirring and static circumstances at high power excitation levels. Both decays are well fitted with global bi-exponential decays which yield time constants of 24.4±0.4 ps and 122±6 ps, meaning that there is no build-up of the QDs containing the long-lived surface trapped charges. The first,

last and average transmittance decays were also compared to ensure that the trion formed QDs are not dispersed all over the sample solution where the stirring cannot defeat the effect of the trions accurately, as shown in Figure 5.12. Obviously, there is no noticeable difference between three the transient decays which are bi-exponential in form yielding global fit time constants of 24.4±0.4 ps and 122±1 ps, meaning that QDs with long-lived trapped charges are not spread in the solution. These two figures suggest that the effect of trion formation is not significant on the transient decays observed for the 2.1 nm QDs and hence the fast decay component in the same transient is not associated with the build-up of photo-excited carriers in long-lived surface traps.

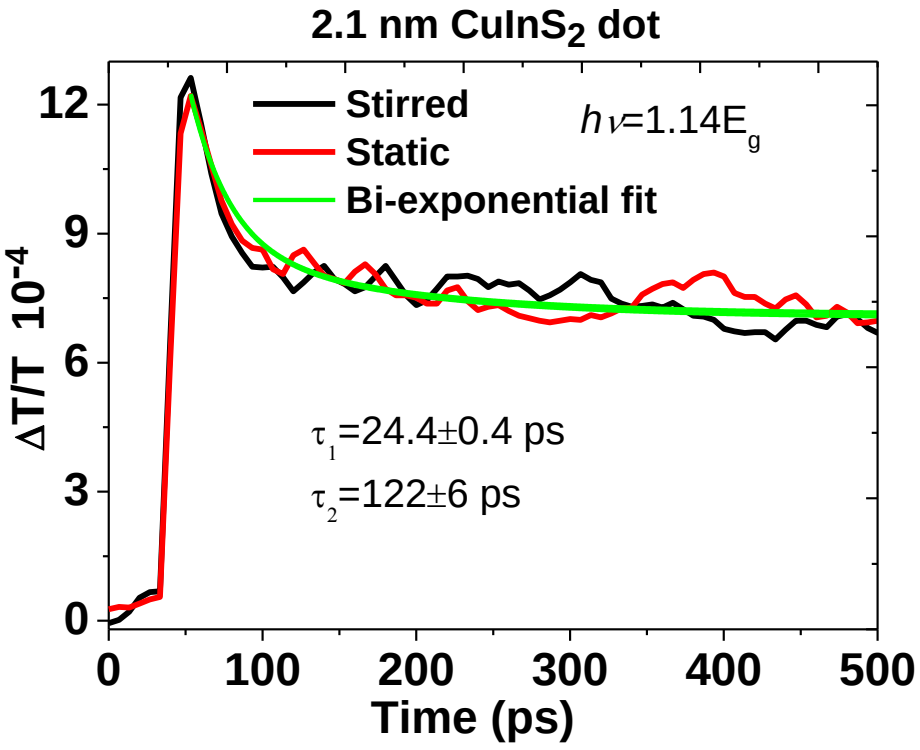

Figure 5.11. The fractional transmittance transients for 2.1 nm diameter $CuInS_2$ dots performed under stirring (black) and static (red) conditions. Green line represents bi-exponential fittings to the decays.

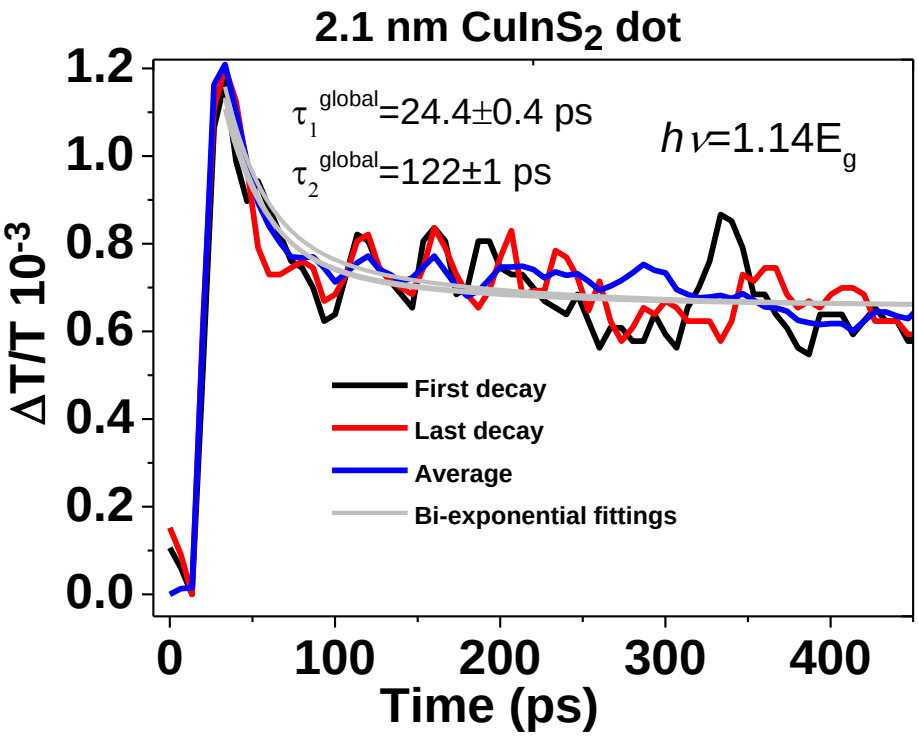

Figure 5.12. Fractional transmittance transient for the first, last and average decays of 10 consecutive scan for 2.1 nm $CuInS_2$ dots.

Figure 5.13 compares the fractional differential TA spectra at the band edge region taken at delay times between pump and probe beams equal to 0 ps and 650 ps and the $d^2A/d\lambda^2$ spectrum. At t=0 ps, all photo-generated excitons occupy the band edge states and the absorption is minimum at the probe frequency. However, at t=650 ps all pump created excitons thermalize to the band edge and any multi-excitons recombine and only one exciton remains in the lowest energy state of the dot, and hence the absorption at the probe wavelength is relatively high. It is clear from the figure that both TA spectra for the 2.1 nm sample is not coincident with the $d^2A/d\lambda^2$ spectrum. The maximum of the TA spectra occur at about 530 nm (~2.34 eV), whereas, the minimum of $d^2A/d\lambda^2$ arises at about 515 nm (~2.4 eV), corresponding to the absorption band edge of the sample. In addition, the differential TA spectra are not always positive over the scanned region (475 nm-600 nm). Except for the spectral region from 495 nm (~2.51 eV) to 561 nm (~2.21 eV), the sign of $\Delta T/T$ is negative over the scanned spectral window indicating that absorption is increasing.

This odd behaviour of the TA spectrum at the band edge region indicates that direct surface trapping occurs in 2.1 nm dots and hence the resultant TA spectrum is not solely due to a state filling effect but also due to the effect of PA. Thus it is concluded that the short decay feature observed in the transient decay recorded at 1 mW absorbed pump power is attributed to direct charge trapping at the surface which was observed in CdSe [9], InA [10] and ZnTe/ZnSe QDs in Chapter 4.

As explained above, Liang *et al.*[20] reported that the bleach decay in $CuInS_2$ QDs is affected by the electron recombination with a hole trapped in an internal defect state. According to the authors, the large shift between the PL and band edge absorption spectra is also due to the intra-gap hole trap states in the emission process. Therefore, we conclude that the observed long decay feature at low pump powers for the 2.1 nm sample is consistent with the intra-gap hole trap state formed when the sample is photo-damaged by pump pulses.

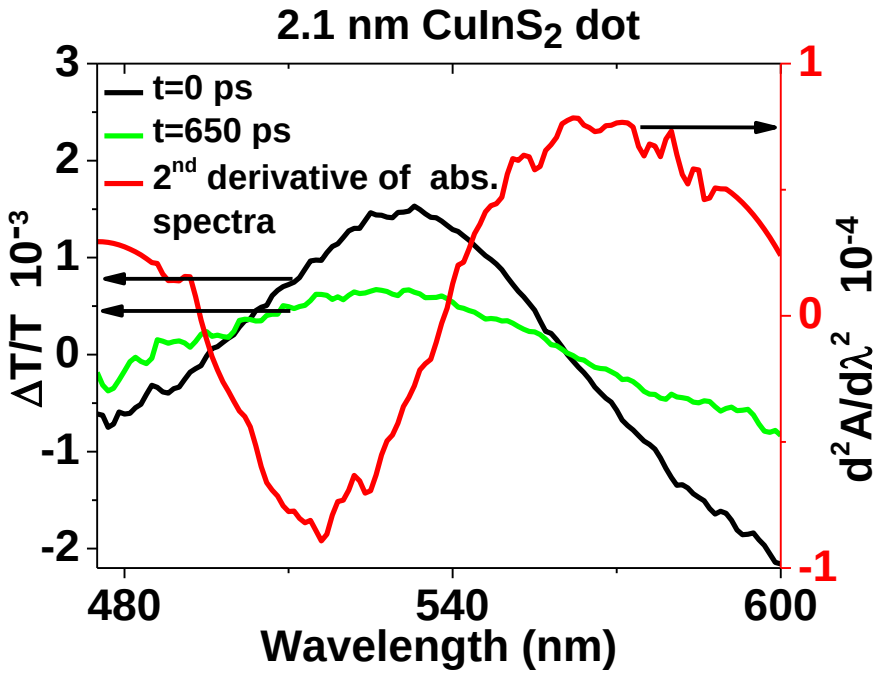

Figure 5.13. The fractional transmittance spectra for 2.1 nm sample at time t= 0 ps (black) and t= 650 ps after peak of transients at 1 mW absorbed pump power and the Savisky-Golay smoothed second derivative of the absorption spectra. The TA spectra were taken under a pump energy of 2.76 eV (1.14E_g).

5.4 Summary

Ultrafast exciton dynamics of ternary $CuInSe_2$ and $CuInS_2$ QDs has been studied using an ultrafast TA experiment. It was found that these QDs are free from the build-up of long-live charge trapping. However, direct surface trapping of charges was observed for both materials, which survive for 10s of ps. This type of charge trapping changed the position and shape of the TA spectra recorded. In addition, the trapping of holes on the internal defect states was observed for these materials. Such trapped holes last for about 100s of ps and radiatively recombine with the electrons occupying the CBM.

5.5 References

1. Chang, C.-C., et al., *Synthesis of Eco-Friendly CuInS2 Quantum Dot-Sensitized Solar Cells by a Combined Ex Situ/in Situ Growth Approach.* ACS Applied Materials & Interfaces, 2013. **5**(21): p. 11296-11306.
2. Pons, T., et al., *Cadmium-Free CuInS2/ZnS Quantum Dots for Sentinel Lymph Node Imaging with Reduced Toxicity.* ACS Nano, 2010. **4**(5): p. 2531-2538.
3. Kolny-Olesiak, J. and H. Weller, *Synthesis and Application of Colloidal CuInS2 Semiconductor Nanocrystals.* ACS Applied Materials & Interfaces, 2013. **5**(23): p. 12221-12237.
4. Xie, R., M. Rutherford, and X. Peng, *Formation of High-Quality I-III-VI Semiconductor Nanocrystals by Tuning Relative Reactivity of Cationic Precursors.* Journal of the American Chemical Society, 2009. **131**(15): p. 5691-5697.
5. Omata, T., K. Nose, and S. Otsuka-Yao-Matsuo, *Size dependent optical band gap of ternary I-III-VI[sub 2] semiconductor nanocrystals.* Journal of Applied Physics, 2009. **105**(7): p. 073106-5.
6. Li, L., et al., *Highly Luminescent CuInS2/ZnS Core/Shell Nanocrystals: Cadmium-Free Quantum Dots for In Vivo Imaging.* Chemistry of Materials, 2009. **21**(12): p. 2422-2429.
7. Hanna, M.C. and A.J. Nozik, *Solar conversion efficiency of photovoltaic and photoelectrolysis cells with carrier multiplication absorbers.* Journal of Applied Physics, 2006. **100**(7): p. 074510.
8. Kambhampati, P., *Hot Exciton Relaxation Dynamics in Semiconductor Quantum Dots: Radiationless Transitions on the Nanoscale.* The Journal of Physical Chemistry C. **115**(45): p. 22089-22109.
9. Tyagi, P. and P. Kambhampati, *False multiple exciton recombination and multiple exciton generation signals in semiconductor quantum dots arise from surface charge trapping.* The Journal of Chemical Physics. **134**(9): p. 094706-10.
10. Cadirci, M., et al., *Ultrafast exciton dynamics in InAs/ZnSe nanocrystal quantum dots.* Physical Chemistry Chemical Physics, 2012.**14**: p 15166-15172**.**
11. Al-Otaify, A., et al., *Multiple exciton generation and ultrafast exciton dynamics in HgTe colloidal quantum dots.* Physical Chemistry Chemical Physics, 2013. **15**(39): p. 16864-16873.
12. Aharoni, A., et al., *Synthesis of InAs/CdSe/ZnSe Core/Shell1/Shell2 Structures with Bright and Stable Near-Infrared Fluorescence.* Journal of the American Chemical Society, 2005. **128**(1): p. 257-264.
13. McGuire, J.A., et al., *New Aspects of Carrier Multiplication in Semiconductor Nanocrystals.* Accounts of Chemical Research, 2008. **41**(12): p. 1810-1819.
14. McGuire, J.A., et al., *Apparent Versus True Carrier Multiplication Yields in Semiconductor Nanocrystals.* Nano Letters. **10**(6): p. 2049-2057.
15. Kramer, I.J. and E.H. Sargent, *Colloidal Quantum Dot Photovoltaics: A Path Forward.* ACS Nano. **5**(11): p. 8506-8514.
16. Klimov, V.I., et al., *Optical Gain and Stimulated Emission in Nanocrystal Quantum Dots.* Science, 2000. **290**(5490): p. 314-317.
17. Busby, E., et al., *Ultrafast exciton dynamics in colloidal aluminum phosphide nanocrystals.* Chemical Physics Letters. **557**(0): p. 129-133.
18. Califano, M. and F.M. Gómez-Campos, *Universal Trapping Mechanism in Semiconductor Nanocrystals.* Nano Letters. **13**(5): p. 2047-2052.
19. Santra, P.K., et al., *CuInS2-Sensitized Quantum Dot Solar Cell. Electrophoretic Deposition, Excited-State Dynamics, and Photovoltaic Performance.* The Journal of Physical Chemistry Letters, 2013. **4**(5): p. 722-729.
20. Li, L., et al., *Efficient Synthesis of Highly Luminescent Copper Indium Sulfide-Based Core/Shell Nanocrystals with Surprisingly Long-Lived Emission.* Journal of the American Chemical Society, 2011. **133**(5): p. 1176-1179.

21. Yarema, O., et al., *Highly Luminescent, Size- and Shape-Tunable Copper Indium Selenide Based Colloidal Nanocrystals.* Chemistry of Materials, 2013. **25**(18): p. 3753-3757.
22. Klimov, V., *Spectral and Dynamical Properties of Multiexcitons in Semiconductor Nanocrystals.* Annu. Rev. Phys. Chem., 2006. **58**: p. 635–73.
23. Norris, D.J., et al., *Size dependence of exciton fine structure in CdSe quantum dots.* Physical Review B, 1996. **53**(24): p. 16347-16354.
24. Kuno, M., et al., *The band edge luminescence of surface modified CdSe nanocrystallites: Probing the luminescing state.* The Journal of Chemical Physics, 1997. **106**(23): p. 9869-9882.
25. Klimov, V.I., *Semiconductor and Metal Nanocrystals*. Marcel Dekker, ed. V.I. Klimov. Vol. 484. 2004, New York.
26. Binks, D.J., *Multiple exciton generation in nanocrystal quantum dots - controversy, current status and future prospects.* Physical Chemistry Chemical Physics. **13**(28): p. 12693-12704.
27. Rincón, C. and J. González, *Acoustic deformation potentials in $A^IB^{III}C_2^{vI}$ chalcopyrite semiconductors.* Physical Review B, 1989. **40**(12): p. 8552-8554.

Chapter 6: Tripled MEG efficiency in type-II QDs

6.1 Introduction

In this chapter, tripled MEG efficiency is demonstrated in CdSe/CdTe/CdS and CdTe/CdSe/CdS core/shell/shell and CdTe/CdS core/shell structures. The design of these structures reduced the rate of hot carrier cooling by both Auger cooling and the surface mediated trapping processes and thus increase the MEG yield. The samples are primarily characterized by linear absorption and PL spectra that were followed by lifetime measurements using TCSPC. Next we performed studies of MEG QY measurements using the ultrafast TA experiment.

6.1.1 Motivation

As explained in Chapter 2, the MEG process occurs when the excess energy of hot carriers is utilized to produce extra electron hole pairs in QDs (Figure 6.1a)). This process is still the subject of intensive study to understand its dynamics and generality. Beard *et.al* [1] indicated that in an ideal case after exceeding the threshold photon energy, MEG efficiency must increase by 100% for each increase of photon energy equivalent to E_g. Thus MEG efficiency is not best associated with only the photon energy but with the photon energy divided by E_g. Photocharging of QDs during excitation resulted in false MEG QYs in the earlier MEG reports [2-4]. After realization of charge trapping at the sample surface, which results in false MEG efficiencies, MEG has been reported in many materials, including InP [5], PbS [6], HgTe [7] and CdTe/CdSe core/shell structures [8]. However the MEG QY beyond the onset was found to be linear instead of being staircase and the rate of QY increase per E_g was about 40% [9]. Schaller *et.al*.[10] have reported 110%/E_g slope efficiency for CdSe QDs. However, that study was conducted before awareness of the

photocharging effect. On the other hand, two recent works have claimed that the observed MEG efficiencies in QDs to date is significantly less than the theoretical limit and too small to have substantial effect on the next generation photovoltaics [9]. This indicates that one or more ultrafast electron cooling process, such as Auger relaxation [11], surface mediated cooling [12, 13] or phonon emission [14] are competing with MEG in NCs. Phonon emission for electrons in QDs is reduced relative to bulk materials due to their discrete energy states where the separation of these states is at least three times wider than the phonon emission [9]. Multi-phonon scattering can still occur but is weak [15]. Therefore, MEG is dominant in comparison with phonon cooling in QDs [14].

Auger cooling is a mechanism by which the hot electron relaxes by transmitting its kinetic energy to its geminate hole which then cools via phonon emission, as shown in Figure 6.1c). That is because in QDs, the separation of states in the valance band is usually smaller than in the conduction band and thus the hole can relax via fast phonon emission [16]. Auger cooling typically occurs on a time scale of about 1 ps [17]. To decrease the Auger cooling rate, the QD structure must be engineered to reduce the electron and hole wavefunction overlap as much as possible [18]. Therefore, since type-II heterostructures increase charge separation, the Auger cooling mechanism in these structures is suppressed compared with their type-I counterparts.

Another process that has a detrimental effect on MEG yield is surface mediated relaxation, as shown in Figure 6.1 b). This can be reduced by adding a shell to the QD with a wide bandgap which acts as a barrier to both electrons and holes, reducing their interaction with the NC surface [5]. With all these in mind, as shown in Figure 6.1d), an unpassivated core only type-I QD is prone to surface mediated cooling (orange), fast Auger cooling (red), and MEG (purple) processes, reducing MEG QY. However, in a well

passivated type-II heterostructure surface-mediated and Auger cooling are suppressed and thus MEG QY will increase (Figure 6.1 e)).

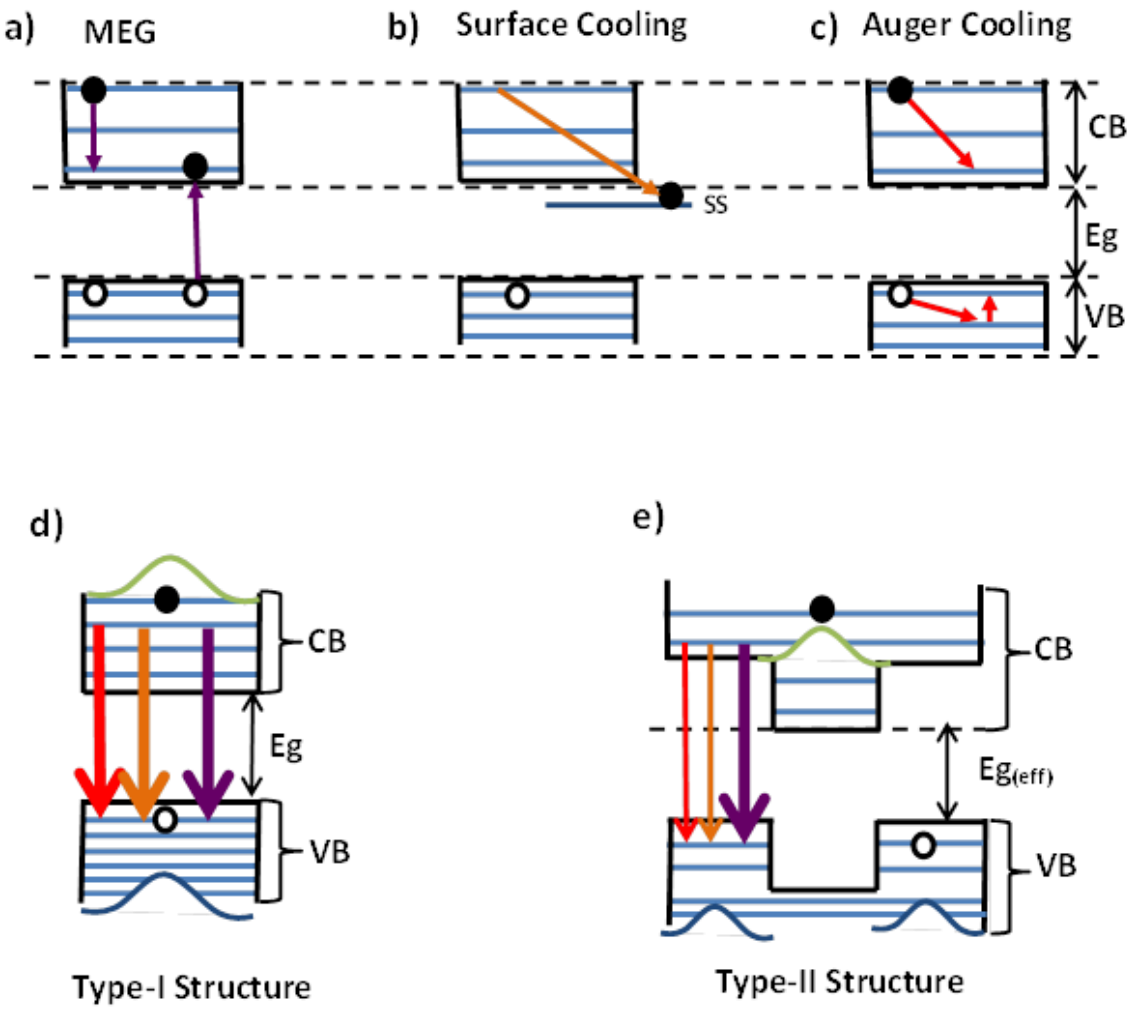

Figure 6.1. Schematic illustration of ultrafast cooling processes for hot electrons in a QD: a) MEG (purple), b) surface cooling (orange) and c) Auger cooling (red), and their relative rate comparison in a: d) type-I and e) core/shell type-II structure. (The arrow width indicates the probability of occurrence. SS= surface state. The green and dark blue lines show the wavefunctions of electron and hole, respectively.)

6.1.2 Sample preparation

In this study, three CdSe/CdTe/CdS and two CdTe/CdSe/CdS core/shell/shell structures and a CdTe/CdS core/shell structure were studied. In this chapter the samples will be labelled as CdSe/CdTe/CdS1, CdSe/CdTe/CdS2, CdSe/CdTe/CdS3, CdTe/CdSe/CdS1,

CdTe/CdSe/CdS2, and CdTe/CdSe. They were synthesised by Robert Page at the School of Chemistry of The University of Manchester using the hot-injection method described elsewhere [19]. The samples were prepared under a nitrogen atmosphere in a glove box and dispersed in anhydrous hexane. This solvent allows the TA of the dots to be conducted in a broad range of the electromagnetic spectrum *i.e.* from the IR to the UV range of the spectrum, as hexane transmits light down to the deep UV part of the spectrum. The concentrations of the solutions were adjusted so that the absorbance (natural logarithm of the ratio between the incident and the transmitted beams) was around 0.2 at wavelengths corresponding to the optical band gaps' of the samples. This is because that the absorbance window of 0.2-0.6 is the region where the picosecond exciton dynamics of QDs are effectively investigated. A 5 ml, 10 mm long rectangular quartz cuvette was used to keep the sample in during the experiment. Quartz material also does not absorb light down to the deep UV part of the spectrum, permitting the dots to be pumped within a broad range. The samples were vigorously stirred during the experiment to avoid any possible photocharging effect, unless otherwise stated.

6.2 Optical characterization

6.2.1 Absorption and PL spectra

Initially, the steady state absorption and PL spectra of the samples were recorded to characterize the basic optical transition positions in the samples using the Perkin Elmer Lambda 1050 UV/Vis/NIR spectrophotometer and the Horiba Jobin Yvon Fluorolog-3 model FL3-22iHR spectrofluorometer, respectively. Figure 6.2 illustrates the linear absorption and PL spectra of all NCs used in this study. It is apparent from Figure 6.2 a) that the CdSe core has a clear 1S feature at 553 nm (~2.3 eV) that is red-shifted to 721 nm

(~1.72 eV) with formation of the CdTe inner shell.

Similarly, the PL spectrum is red-shifted from 555 nm (~2.24 eV) to 728 nm (~1.7 eV) with addition of the CdTe shell. This is less than the bulk band gap of CdSe (~1.75 eV [20]) and indicates that the effective band gap corresponds to the energy difference between the valance band of the CdTe and the conduction band of CdSe. This is evidence that the formation of the CdTe inner shell transforms the structure from a type-I form to a type-II form [21] wherein the electrons and holes reside in the CdSe core and CdTe shells, respectively. The addition of the CdS outer shell also causes a slight red shift in both spectra, indicating some wavefunction penetration into the outer shell. Similar features were observed for other samples whose absorption and PL spectra of the final situation are presented in Figure 6.2 b)-f). In the case of the CdTe/CdSe core/shell structure, holes and electrons are confined in the core and shell, respectively. Finally, the CdTe/CdS core/shell has a type-II structure where the valance band of the CdTe core lies above the valance band of CdS and the conduction band of CdTe lies below that of the CdS material [22]. The FWHM for PL spectra of all samples is between 45-51 nm which is in the range of narrow size distribution, indicating that the size and shape of the QDs are well-controlled.

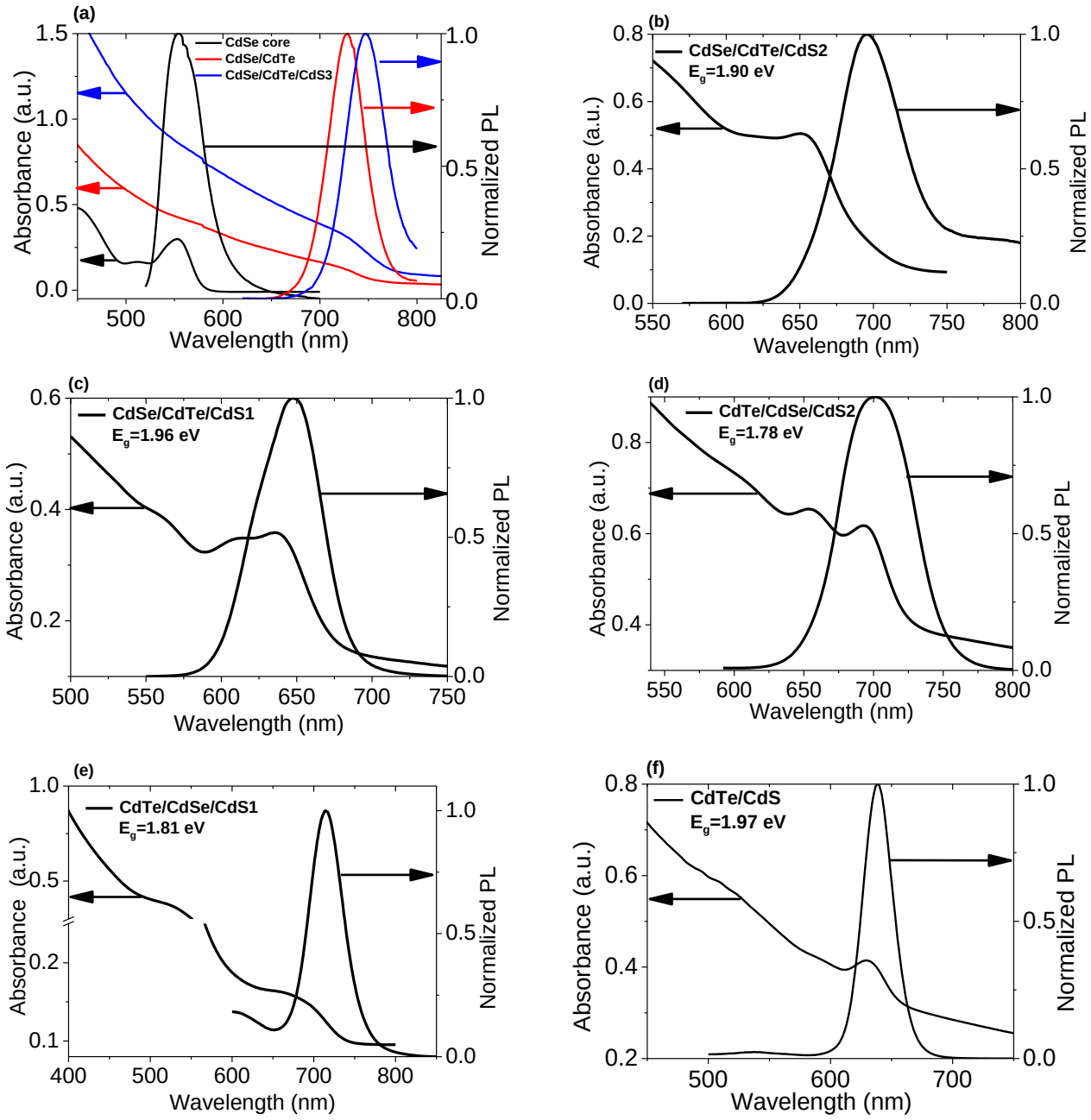

Figure 6.2. Absorption and PL spectra for; a) a typical CdSe core before and after addition of first a CdTe and then a CdS shell, b) and c) other two sets of CdSe/CdTe/CdS samples, d) and e) CdTe/CdSe/CdS samples and f) CdTe/CdS sample. For PL spectra, 400 nm (~3.11 eV) excitation pump wavelength was chosen. The absorption curves in the case of a) are vertically offset for simplicity. The PL peak wavelengths for CdSe core, CdSe/CdTe core/shell and CdSe/CdTe/CdS core/shell/shell structures in a) are 555 nm, 728 nm, and 743 nm, respectively. Similarly the PL peak wavelengths in the cases of b), c), d), e) and f) are 695 nm, 647 nm, 705 nm, 715 nm, and 638 nm, respectively.

6.2.2 Photoluminescence decay studies using TCSPC

To ascertain the radiative lifetime of each stage when developing the CdSe/CdTe/CdS core/shell/shell structure, a TCSPC experiment was employed. The set-up for this experiment is described in Chapter 3 in detail. However, in brief, femtosecond laser pulses at 400 nm were used to excite the samples and the emission decay traces were recorded at their peak wavelength using a Hamamatsu R3809U-5 multi-channel plate.

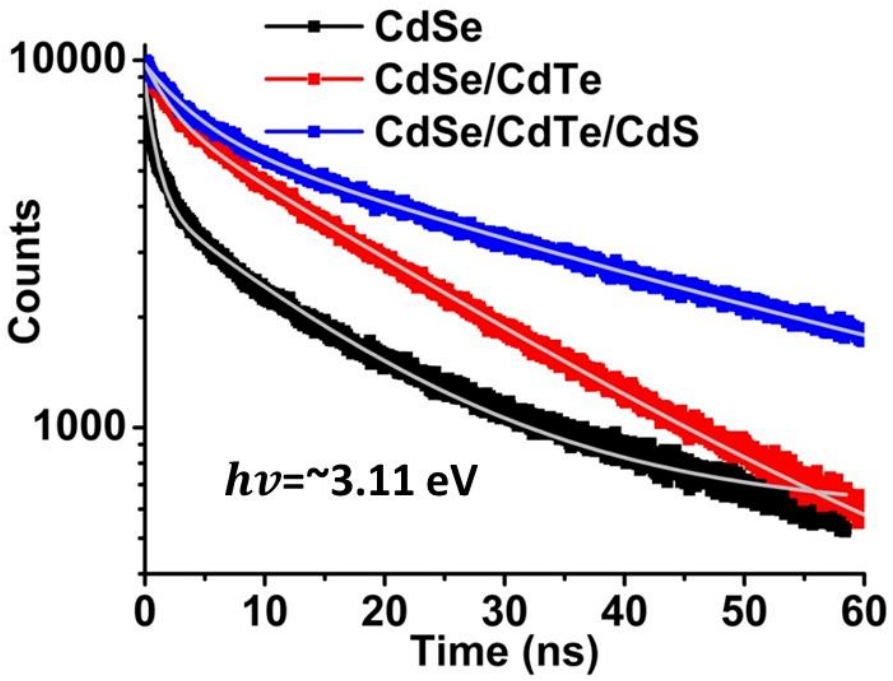

Figure 6.3. The PL decay transients for a CdSe core (black), CdSe/CdTe core/shell (red) and CdSe/CdTe/CdS core/shell/shell (blue) structures. Grey lines represent the bi- exponential curve fits to the decays.

Table 6.1. The extracted radiative time constants after fitting each PL decay transient with bi-exponential decay.

Sample	τ_1 (ns)	τ_2 (ns)
CdSe	0.90±0.01	14.80±0.10
CdSe/CdTe	2.22±0.03	21.30±0.05
CdSe/CdTe/CdS	4.32±0.04	39.72±0.21

The peak PL wavelengths for CdSe, CdSe/CdTe, and CdSe/CdTe/CdS structures were 567 nm (~2.2 eV), 665 nm (~1.87 eV) and 748 nm (~1.7 eV), respectively. Figure 6.3 illustrates the PL decay recorded at each stage of the CdSe/CdTe/CdS3 core/shell/shell structure. All decays are fitted biexponentially and the resultant time constants are presented in Table 6.1. With the formation of the inner and outer shell, the behaviour of decays varies considerably. The decay time constants of CdSe are increased significantly with the addition of a CdTe shell because the spatial separation of electrons and holes results in a reduced recombination rate. The recombination lifetimes further increase as the final CdS shell is grown around the CdSe/CdTe core/shell structure, which decreases surface-mediated recombination.

6.3 MEG studies of type-II structures using the TA experiment

The relaxation of electrons and subsequent nonradiative recombination processes were probed at the band edge using the ultrafast pump-probe experiment. The pump pulse creates hot electron hole pairs and the subsequent probe beam is tuned to the optical absorption edge to monitor the population of carriers at the band edge. Changes in the delay between the pump and probe pulses allows one to record the number of carriers in the CBM on a picosecond time scale.

The set-up of the TA experiment used in this study is explained in Chapter 3 in detail. Initially the pump beam wavelength was set to 450 nm (~2.8 eV) to measure ultrafast exciton dynamics without any MEG effect, as the excitation wavelength is below the MEG threshold. Above the MEG threshold, high energy pump beams of 260 nm (~4.78 eV), 250 nm (~4.97 eV) and 232 nm (~5.35 eV) were used. Each transient is the average of at least 10 consecutive scans. Unless otherwise stated, the transients were recorded under

the stirring condition of 1000 rpm. In all cases the fluence of the pump beam was kept as low as possible to avoid the absorption of more than one photon per dot.

6.3.1 Results and discussions

Figure 6.4 a) and b) show the pump induced fractional transmittance transients of the CdSe/CdTe/CdS3 and CdTe/CdSe/CdS2 samples for several different pump powers, below the MEG threshold, respectively. A fast decay becomes apparent as the pump fluence increases. All transients are globally fitted with a mono-exponential decay to a plateau. The plateau corresponds to a long-lived single exciton whose lifetime is too long to be detected with the TA experiment used here. The decay corresponds to a biexciton decay and the lifetime of which for the CdSe based NCs was measured to be 151±3 ps, whereas, it was 80±1 ps for the CdTe based NCs.

Since 2.76 eV lies below the MEG threshold, only a flat transient is expected at low pump fluences where the probability of absorbing more than one photon is negligible. The flat signal corresponds to a single exciton which recombines in the ns time-scale. However, if the fluence is increased then a second exciton is produced by absorbing two photons per dot, the decay of the resulting biexciton corresponds to a sub-nanosecond decay in the transmission transient. This decay is mono-exponential in form. Sometimes sub-ns transients are observed that are bi-exponential in form where the second sub-nanosecond decay component is attributed to the surface-mediated cooling system [20, 21]. However, as illustrated in Figure 6.4 a) and b), there is no the second picosecond decay component in the samples used in this study. This indicates that the CdS final shell acts as a proper barrier to stop the interaction between the hot carriers and the NC surface. And thus in these samples the rate of surface-related recombination is not significant and the

probability of efficient MEG is increased.

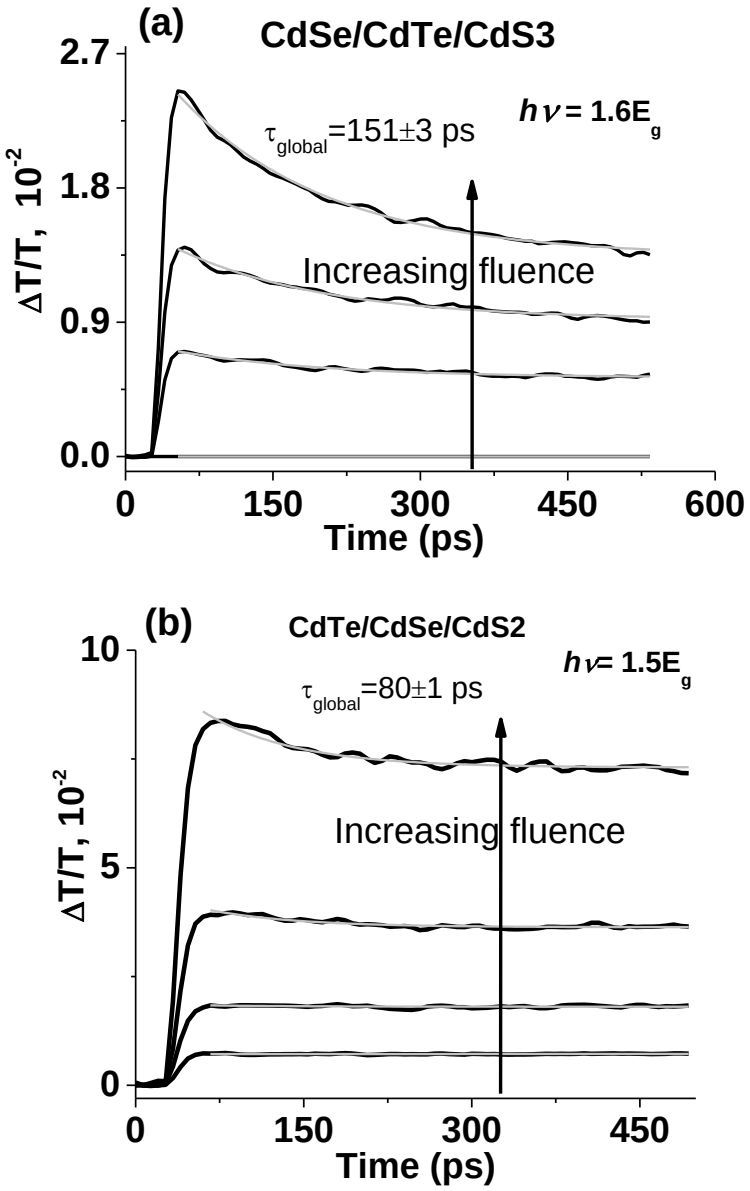

Figure 6.4. Transmittance transients taken on a) CdSe/CdTe/CdS3 and b) CdTe/CdSe/CdS2 samples for different pump fluences and at the photon energy of 2.76 eV. Grey lines represent the mono-exponential curve fits to transients.

In a transmittance transient at the bleach, the rise time indicates the relaxation time of hot carriers from the excited state to the CBM. Thus, the rise time of the CdSe/CdTe/CdS1 sample is compared to the corresponding samples of CdSe core only,

and CdSe/CdTe core/shell QDs, as shown in Figure 6.5. The relaxation time for CdSe core only type-I structure is about 5 ps that is consistent with the previously reported values for type-I PbSe and qausi type-II PbSe/PbS QDs [18]. The electron cooling time for the CdSe/CdTe core/shell structure is significantly increased to about 15 ps. This indicates that the formation of CdTe shell separates the electrons and holes from each other and consequently the Auger cooling rate is decreased. The addition of the final CdS shell extends the cooling time further to around 25 ps. This demonstrates that the CdS shell reduces the interaction between the hot carrier and the NC surface, decreasing the surface mediated cooling rate. These features further support that the MEG rate in the core/shell/shell samples is favoured over other ultrafast cooling processes.

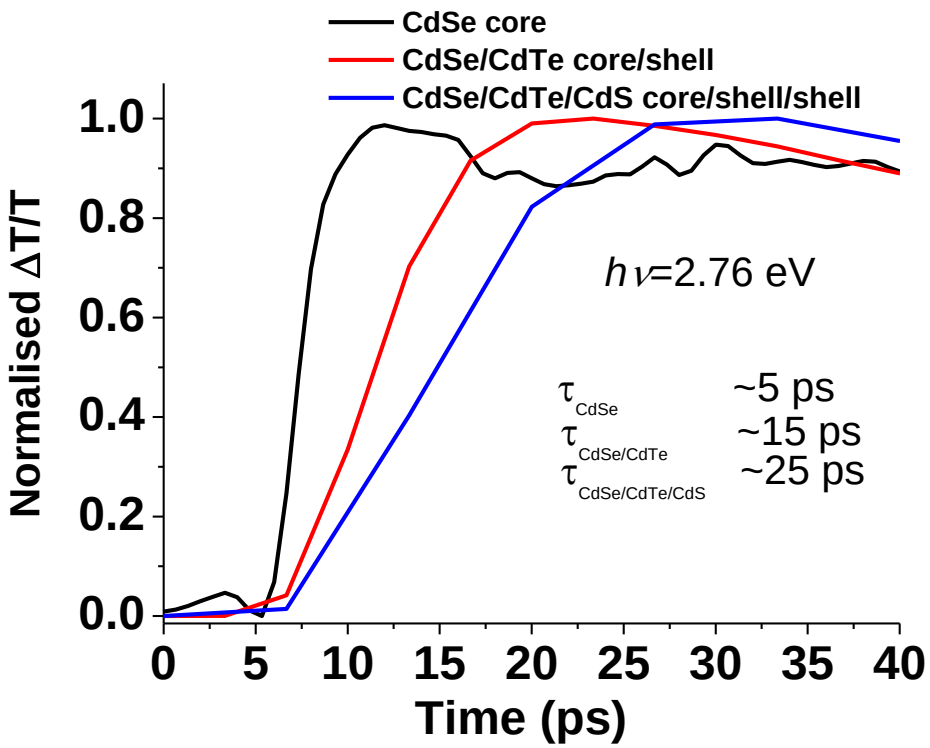

Figure 6.5. Initial bleach rise for standard CdSe QDs before and after the addition of the inner CdTe shell and outer CdS shell.

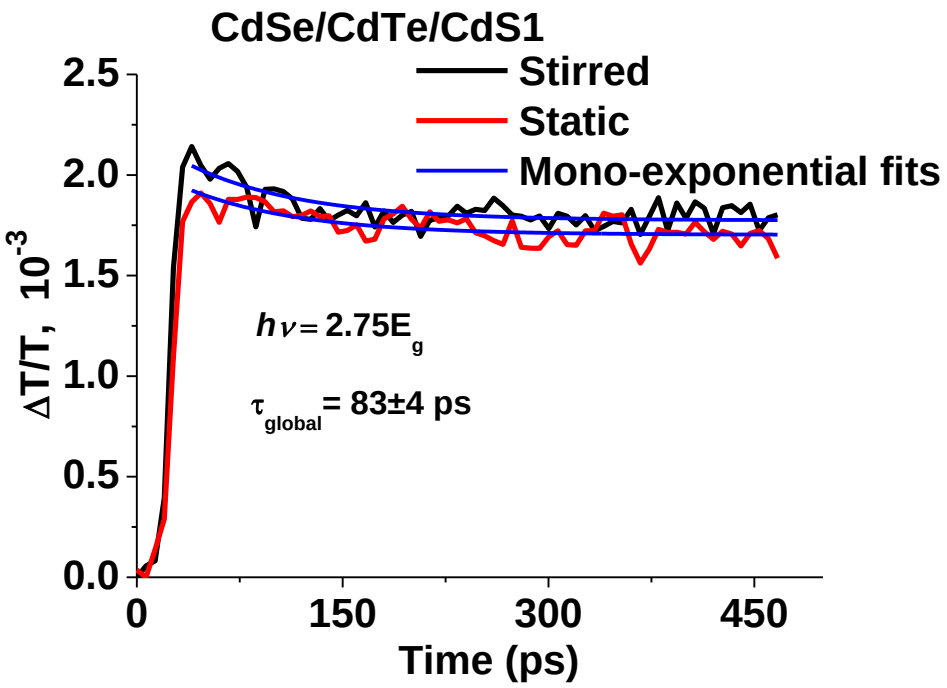

Figure 6.6. Transmittance transients for CdSe/CdTe/CdS1 for stirred (black) and static (grey) conditions.

Figure 6.6 illustrates the fractional transmittance transients for the CdSe/CdTe/CdS1 sample recorded under stirred and static conditions at a photon energy of ~5.36 eV (~2.75E_g). As explained in the previous chapter, the fast transmittance transients in the time scale of 10s and 100s of ps can be a result of photocharging of the sample [20, 21]. In this mechanism, a photo-generated charge is trapped on the surface for a time period longer than the time between two sequential pump pulses. Next, a subsequent pulse generates an exciton allowing trion formation instead of single exciton. The effect of trion decay is observed by comparing the transients conducted in stirring and static circumstances. In the former case, the accumulated charged QDs are swept out of the active zone and then fresh QDs are pumped. However, as is clearly seen from Figure 6.6, there is no observable difference between the stirred and static decays and both decays are fitted with a global single-exponential function with a time constant of 83±4 ps. This indicates that the samples are not susceptible to the photocharging.

It has been observed in ref.[21] that significant surface trapping may occur in some NC without accumulation of photocharged QDs and thus it is impossible to observe the surface charging effect by comparing the stirred and static decays. In this condition, the cooled electron directly moves to the NC surface in the timescale of 10s of ps. Electrons in the CBM are de-populated and thus the band-edge bleach is affected. Its spectral shape is distorted in a way that the bleach signal becomes broader and is distorted in shape. In addition, its sign is reversed in some cases [21, 22]. Figure 6.7 shows the differential transmission spectra for the CdSe/CdTe/CdS2 sample at the time where all hot electrons are cooled and before the recombination of pump-created multi-excitons started (maximum bleach). It is apparent from the figure that the spectrum shows a bleach feature corresponding to the 1S absorption feature of the sample. Overall, the shape is similar to the absorption edge and PL spectra. Its sign is not reversed at all. This indicates that the CdS outer shell accurately supresses the direct surface photocharging and the NCs used here are well-passivated structures.

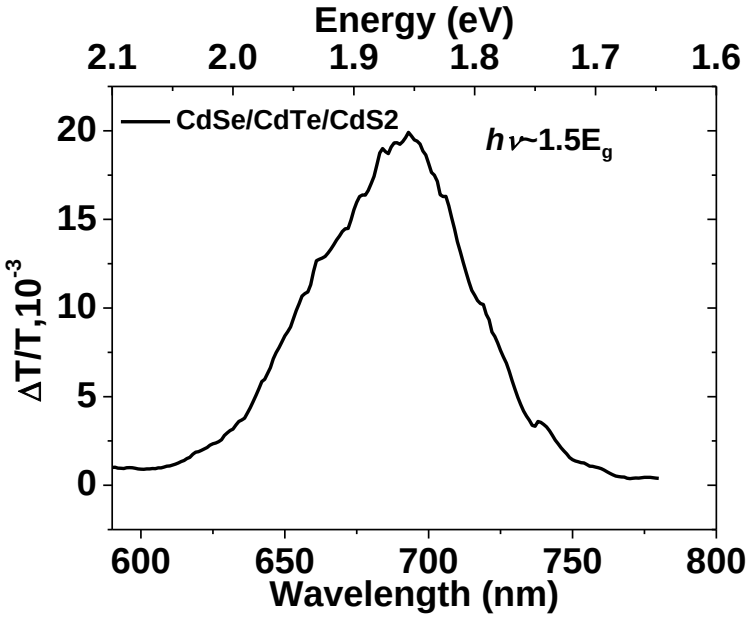

Figure 6.7. The TA spectrum in the band-edge region recorded at the delay time corresponding to the bleach maximum for CdSe/CdTe/CdS2.

As explained earlier, according to the energy conservation rule in order to create extra excitons by absorbing one photon per NC, the energy of the pump photon must be at least twice the band edge of the NC. Thus, here wavelengths of 260 nm (~4.78 eV), 250 nm (~4.97 eV) and 232 nm (~5.35 eV) were used to investigate the MEG signal in the QDs. Figure 6.8 compares the transients taken above (dash) and below (grey) the MEG threshold at similar levels of low fluences where the probability of absorbing more than one photon per dot per pulse is negligible for three samples. It is clear from the figure that with excitations corresponding to the above MEG threshold region, a fast decay feature emerges in the three cases. However, this fast decay component vanishes in the case of below MEG threshold excitations.

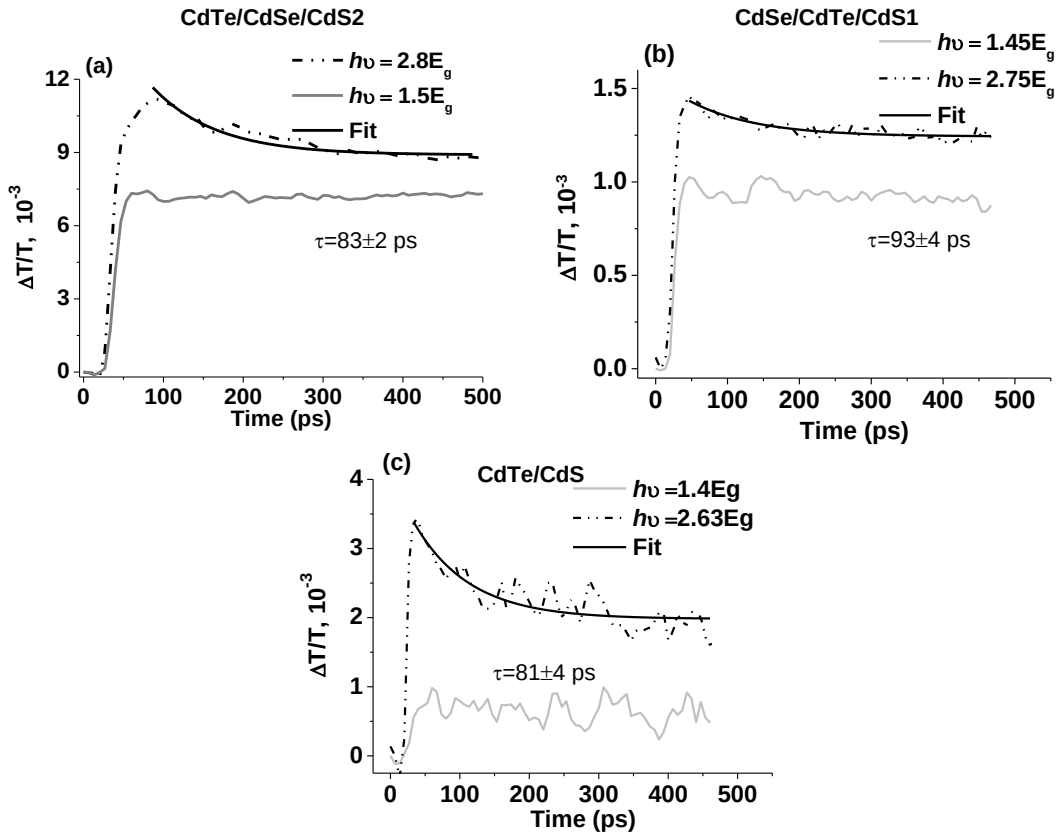

Figure 6.8. The comparison of the fractional change in transmission, ΔT/T, taken under high (dashed) and low (grey) excitation energies for a) CdTe/CdSe/CdS2, b) CdSe/CdTe/CdS1 and c) CdTe/CdS samples. Black lines represent the mono-exponential curve fits to the decays corresponding to above MEG threshold case.

The observed fast decay cannot be due to formation of a biexciton by absorbing of more than one photon per dot per pulse. That is because as explained in the previous chapter, the average number of photons absorbed per pulse, <n>, is related to the signal corresponding to the maximum bleach value in a transmittance TA decay, $\Delta T_{max}/T$, and is given by [23];

$$< n >= \frac{2}{A}\Delta T_{max}/T \ , \qquad (6.1)$$

where A is the absorbance of the solution at the band edge. The Poisson distribution governs the probability of a QD to absorb *n* photons during a pump pulse excitation as [23];

$$P_n =< n >^n \frac{e^{(-n)}}{n!}. \qquad (6.2)$$

The calculated probability of absorbing a biexciton due to absorbing two photons per pulse is less than 5% of the probability of forming a single exciton. As explained in ref.[20], this value indicates that formation of a biexciton due to absorbing more than one photon per pulse is negligible. Therefore, it is believed that the high energy pump photons used to pump the samples in this study create extra excitons in the QD system and the emerged fast decays in the case of above MEG threshold excitation in Figure 6.8 is due to MEG.

Figure 6.9 compares the rise times of transients for above and below MEG threshold excitation cases of the CdSe/CdTe/CdS3 sample. The initial rise time corresponds to the hot carrier relaxation time. In the case of high pump energy ($2.62E_g$), the electron relaxation is 5-10 ps faster than that of low pump energy ($1.46E_g$). This indicates that when MEG occurs, the hot carrier dissipates its energy to a carrier in the valance band and thus more quickly relaxes to the CBM. In other words, MEG increases

the overall carrier relaxation rate in these dots. This is further evidence for MEG manifestation in the investigated dots.

The change in the fractional transmittance at the bleach is a measure to quantify exciton population in the CBM of an excited QD. In the limit of vanishing fluence, the initial maximum signal in the fractional transmittance transient (after cooling is completed and before recombination is started), ΔT (0)/T, is equivalent to the biexciton (or multi-exciton) population produced by the pump pulse, while, the signal at the plateau corresponds to the population of QDs excited at the beginning. The ratio between them, R, in the limit of vanishing fluence, where each excited QD has absorbed only one photon, gives the average exciton population created by absorption of one photon per QD and thus the MEG QY [9].

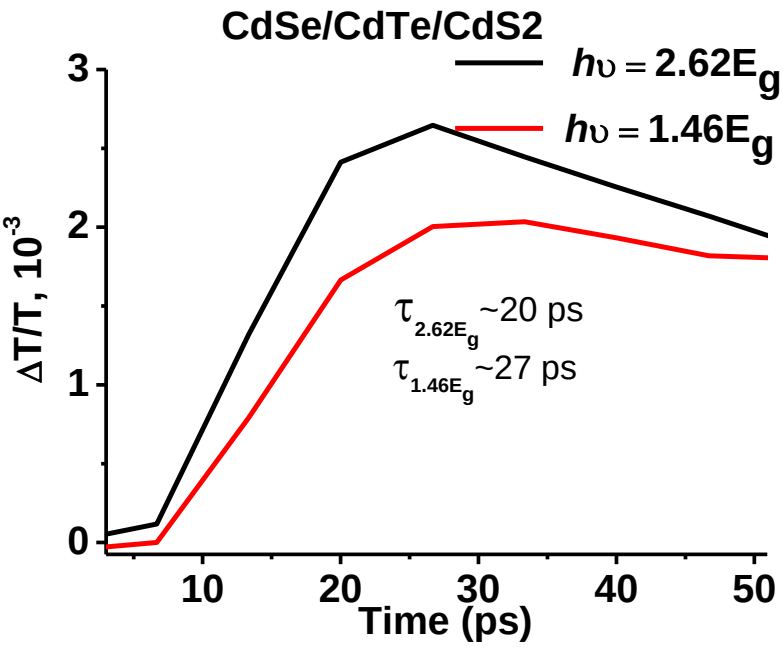

Figure 6.9. Initial bleach rises for above (black) and below (red) MEG threshold for CdSe/CdTe/CdS2.

Figure 6.10 shows the variation of R values as a function of pump fluence for

excitation energies above and below MEG threshold in all samples used in this study. Each curve is fitted with the following function [5];

$$R = k\frac{\Delta T(0)}{T}\left[1 - \exp(-\frac{k}{QY}\frac{\Delta T(0)}{T})\right]^{-1}, \qquad (6.3)$$

where, *k* is a constant whose formula for our sample is $2A^{-1}$. It is clear from Figure 6.10, the common trend is that R values increase with the pump fluence. In the limit of vanishing fluence, R values for all samples go to unity for below MEG threshold pumping. This indicates that the absorbed low energy photons do not produce extra excitons, limiting the QY to 100%. On the other hand, R values at low pump fluences for all samples are significantly greater than unity in the case of above MEG threshold. This shows that the absorbed energetic photon per pulse dissipates its additional energy to a third carrier in the valance band to produce extra excitons in the dot. In that case the QY becomes more than 100%. To give a few examples, the additional exciton yield per QD for the CdSe/CdTe/CdS3 sample for pump photon energies of $3.11E_g$ and $2.9E_g$ are observed to be 0.74±0.02 and 0.45±0.06, respectively. These values correspond to a QY of 174% at $3.11E_g$ and 145% at $2.9E_g$. The CdTe/CdS sample produces additional excitons of 0.21±0.08 per dot at $2.63E_g$ corresponding to a QY of 121% at $2.63E_g$.

Figure 6.11 a) shows the additional excitons created via MEG as a function of absolute incident photon energy for all NC designs used in this study with the indicated band gap energies. The data in the figure corresponding to above the MEG threshold is widely distributed. Beard *et al*.[24] showed that the right method of determining the MEG QY is plotting the QY versus the incident photon energy divided by E_g. Since for ideal MEG, efficiency is expected to be increased by 100% for each photon energy increment equivalent to the band gap, the MEG QY should be associated with the incident photon

energy normalised to E_g [1]. Therefore, in the present study, the generated extra excitons via MEG is plotted against pump energy normalised to the band gap energy, as shown in Figure 6.11 b).

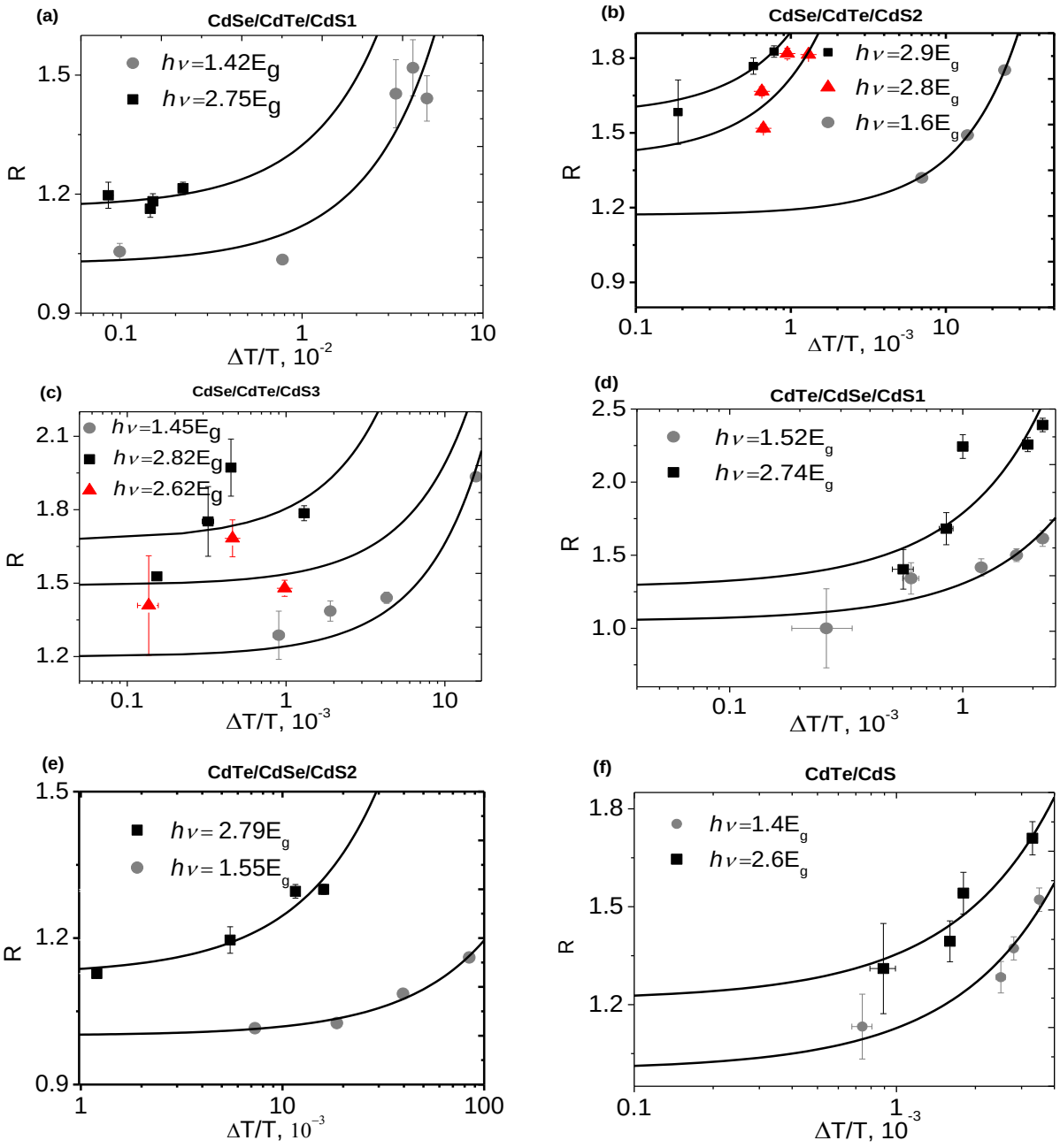

Figure 6.10. The comparison of average number of excitons created per absorbed photon per pulse for above and below MEG excitations for a)CdSe/CdTe/CdS1, b)CdSe/CdTe/CdS2, c)CdSe/CdTe/CdS3, d)CdTe/CdSe/CdS1, e)CdTe/CdSe/CdS2, and f)CdTe/CdS samples.

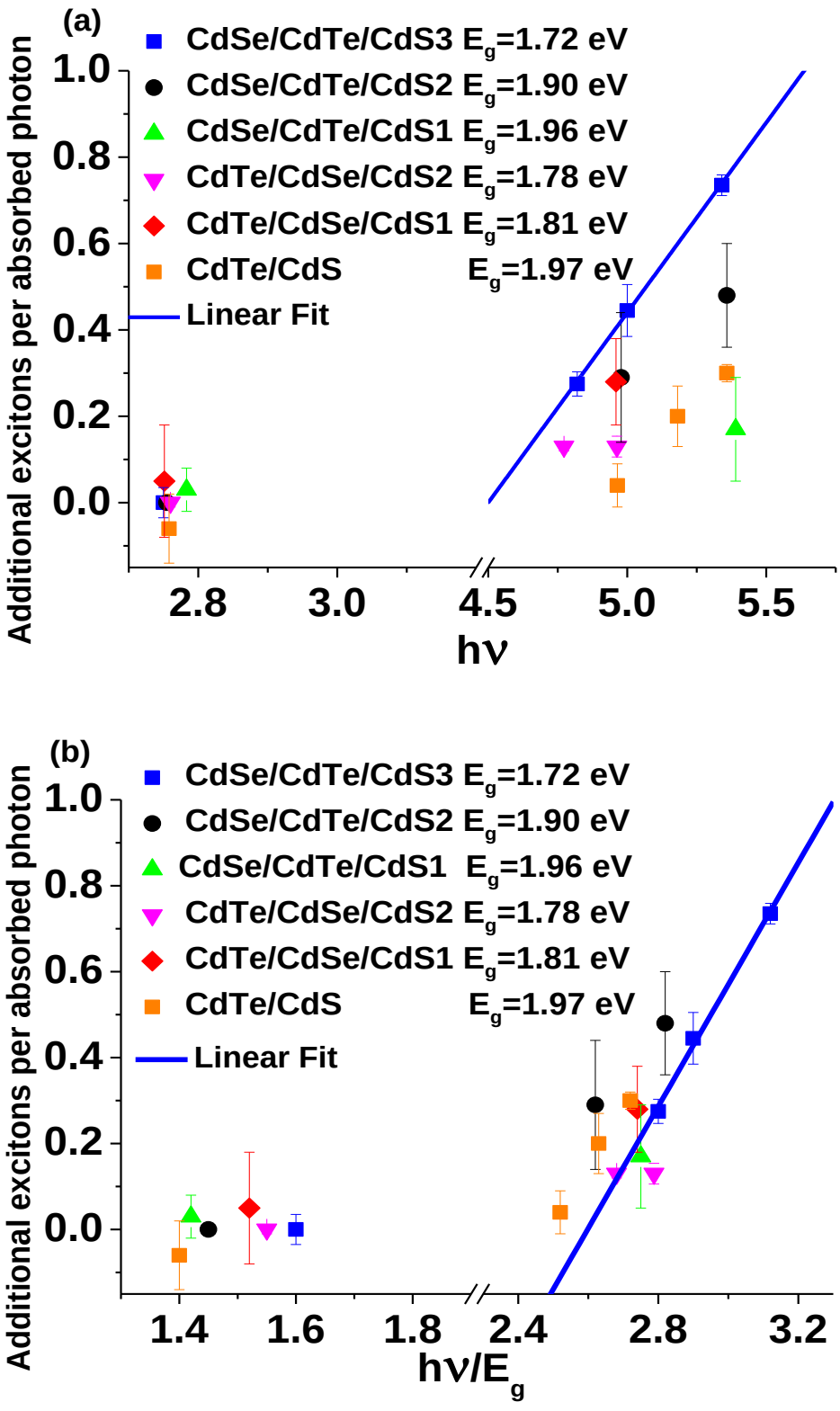

Figure 6.11. The number of additional excitons produced via MEG as a fuction of; a) absolute photon energy, hν, and b) absolute photon energy divide by band gap energy, hν/E_g.

The measurements clearly show that the data points are distributed narrowly rather than broadly as in the case of Figure 6.11 a). Overall the results agree well with the model predicted in ref.[24]. Since MEG only depends on the pump photon energy normalised to E_g [6, 24], the results presented in Figure 6.11 b) is due to MEG manifestation. As each sample has different design and thus properties, they can show different MEG efficiencies and thresholds. However, in general, each sample exhibits broadly similar MEG performance. A linear fit to those data above the 2.52 point yields a MEG threshold of (2.59±0.16) E_g. This value agrees well with the energy partition model which leads to a theoretical MEG threshold of $2.58E_g$ for the same materials calculated using Eq.(2.7). Moreover, the MEG threshold observed here is similar to that of previously investigated CdSe [10], CdTe [25] and CdSe/CdTe/CdS/ZnS [8] core/shell type-II QDs. The results are also in good agreement with the energy conservation which dictates that the MEG threshold in a QD must be at least twice band gap. As explained earlier, the slope efficiency of the linear fit corresponds to the MEG efficiency which is (142±9)%/E_g here. In other words, an average additional exciton of 1.42±0.09 is produced at each increment of the pump photon energy equivalent to the band gap of the QD.

As compiled in ref.[9], the slope efficiencies of type-I QDs observed so far lie between 30%/E_g and 40%/E_g. Gachet *et al.*[8] reported a MEG efficiency of 53%/E_g in CdTe/CdSe/CdS/ZnS type-II structures wherein ideally Auger cooling is expected to be suppressed. The observed MEG efficiency value in this study is about three times greater than that observed in ref.[8]. This indicates that the QDs used in this study are well-engineered and that not only Auger cooling is suppressed but also surface-related cooling is effectively controlled by growing a CdS outer shell around a type-II structure.

6.4 Summary

In this chapter, a significantly improved MEG efficiency has been demonstrated in type-II QDs using the TA experiment. Auger and surface-mediated cooling rates were suppressed to increase the MEG rate by well-engineering the electron and hole wavefunction overlap and carefully controlling the QDs' surface. The MEG QY was found to be proportional to the excitation photon energy normalized by the sample band gap energy. The MEG threshold for those type-II structures was observed to be $(2.59\pm0.16)E_g$, which is similar to the previously reported values for their type-I counterparts. However, a MEG QY slope efficiency of $(142\pm9)\%/E_g$ was observed for the type-II QDs used here. This value is about 3 times higher than previously reported for colloidal nanocrystals. Type-II QDs with well-passivated surfaces could improve the efficiency of PVs significantly if MEG is utilized properly.

6.5 References

1. Beard, M.C. and R.J. Ellingson, *Multiple exciton generation in semiconductor nanocrystals: Toward efficient solar energy conversion.* Laser & Photonics Reviews, 2008. **2**(5): p. 377-399.
2. Schaller, R.D. and V.I. Klimov, *High Efficiency Carrier Multiplication in PbSe Nanocrystals: Implications for Solar Energy Conversion.* Physical Review Letters, 2004. **92**(18): p. 186601.
3. Murphy, J.E., et al., *PbTe Colloidal Nanocrystals:â€‰ Synthesis, Characterization, and Multiple Exciton Generation.* Journal of the American Chemical Society, 2006. **128**(10): p. 3241-3247.
4. Richard, D.S., A.P. Melissa, and I.K. Victor, *Effect of electronic structure on carrier multiplication efficiency: Comparative study of PbSe and CdSe nanocrystals.* Applied Physics Letters, 2005. **87**(25): p. 253102.
5. Stubbs, S.K., et al., *Efficient carrier multiplication in InP nanoparticles.* Physical Review B, 2010. **81**(8): p. 081303.
6. Hardman, S.J.O., et al., *Electronic and surface properties of PbS nanoparticles exhibiting efficient multiple exciton generation.* Physical Chemistry Chemical Physics. **13**(45): p. 20275-20283.
7. Al-Otaify, A., et al., *Multiple exciton generation and ultrafast exciton dynamics in HgTe colloidal quantum dots.* Physical Chemistry Chemical Physics, 2013. **15**(39): p. 16864-16873.
8. Gachet, D., et al., *An Upper Bound to Carrier Multiplication Efficiency in Type II Colloidal Quantum Dots*, in *Nano Letters*2009, American Chemical Society. p. 164-170.
9. Binks, D.J., *Multiple exciton generation in nanocrystal quantum dots - controversy, current status and future prospects.* Physical Chemistry Chemical Physics. **13**(28): p. 12693-12704.
10. Schaller, R.D., et al., *High-Efficiency Carrier Multiplication and Ultrafast Charge Separation in Semiconductor Nanocrystals Studied via Time-Resolved Photoluminescenceâ€* The Journal of Physical Chemistry B, 2006. **110**(50): p. 25332-25338.
11. Klimov, V.I., et al., *Electron and hole relaxation pathways in semiconductor quantum dots.* Physical Review B, 1999. **60**(19): p. 13740-13749.
12. Pandey, A. and P. Guyot-Sionnest, *Slow Electron Cooling in Colloidal Quantum Dots.* Science, 2008. **322**(5903): p. 929-932.
13. Kambhampati, P., *Hot Exciton Relaxation Dynamics in Semiconductor Quantum Dots: Radiationless Transitions on the Nanoscale.* The Journal of Physical Chemistry C. **115**(45): p. 22089-22109.
14. Stewart, J.T., et al., *Comparison of Carrier Multiplication Yields in PbS and PbSe Nanocrystals: The Role of Competing Energy-Loss Processes.* Nano Letters. **12**(2): p. 622-628.
15. Li, X.-Q., H. Nakayama, and Y. Arakawa, *Phonon bottleneck in quantum dots: Role of lifetime of the confined optical phonons.* Physical Review B, 1999. **59**(7): p. 5069-5073.
16. Klimov, V.I., *Semiconductor and Metal Nanocrystals*. Marcel Dekker, ed. V.I. Klimov. Vol. 484. 2004, New York.
17. Hendry, E., et al., *Direct Observation of Electron-to-Hole Energy Transfer in CdSe Quantum Dots.* Physical Review Letters, 2006. **96**(5): p. 057408.
18. Trinh, M.T., et al., *Anomalous Independence of Multiple Exciton Generation on Different Group IV-VI Quantum Dot Architectures.* Nano Letters. **11**(4): p. 1623-1629.
19. McElroy, N., et al., *Comparison of solar cells sensitised by CdTe/CdSe and CdSe/CdTe core/shell colloidal quantum dots with and without a CdS outer layer.* Thin Solid Films, (0).
20. Cadirci, M., et al., *Ultrafast exciton dynamics in InAs/ZnSe nanocrystal quantum dots.*

Physical Chemistry Chemical Physics, 2012. **14**: p 15166-15172
21. Pooja, T. and K. Patanjali, *False multiple exciton recombination and multiple exciton generation signals in semiconductor quantum dots arise from surface charge trapping.* J. Chem. Phys., 2011. **134**(9): p. 094706.
22. Cadirci, M., et al., *Ultrafast exciton dynamics in Type II ZnTe-ZnSe colloidal quantum dots.* Physical Chemistry Chemical Physics. **14**(39): p. 13638-13645.
23. Klimov, I., *Semiconductor and Metal Nanocrystals*. V ed. 2004, New York: Marcel Dekker.
24. Beard, M.C., et al., *Comparing Multiple Exciton Generation in Quantum Dots To Impact Ionization in Bulk Semiconductors: Implications for Enhancement of Solar Energy Conversion.* Nano Letters, 2010. **10**(8): p. 3019-3027.
25. Kobayashi, Y., T. Udagawa, and N. Tamai, *Carrier Multiplication in CdTe Quantum Dots by Single-photon Timing Spectroscopy.* Chemistry Letters, 2009. **38**(8): p. 830-831.

Chapter 7: Attractive biexciton interaction energy in type-II QDs

7.1 Introduction

In this chapter, the femtosecond TA spectroscopy is used to study biexciton interactions in both CdSe/CdTe/CdS and CdTe/CdSe/CdS core/shell/shell and CdTe/CdS core/shell QDs. A procedure is used to ensure that only relaxed biexcitons contribute to the observed spectra. Each sample was initially characterized by steady-state absorption and PL spectroscopy. Analysis of the TA spectra of various samples yielded large attractive interaction energies of 30-60 meV. This is followed by studies of PL lifetimes and multi-exciton interactions using the TRPL spectroscopy previously used by others.

7.1.1 Motivation

To date, several studies have reported large repulsive exciton-exciton interaction energy ($\Delta_{XX}>0$) in type-II QDs using transient PL experiments. For instance, Klimov *et al*.[1] reported a repulsive Δ_{XX} value of ~100 meV in CdS/ZnSe type-II NCs based on features observed in the TRPL spectra. Similar values have been observed in CdS/ZnSe [2] and ZnTe /CdSe core/shell QDs [3] using the same method. These results are shown in Chapter 2 in detail. The authors claimed that the observed spectral shift is largely due to a repulsive Coulomb interaction between two excitons and the band gap of the material is increased by a magnitude corresponding to the magnitude of Δ_{XX}. Using an effective mass approach, modelling has been indicated, Δ_{XX} in type-II structures is always large and repulsive. Since the Δ_{XX} can have a magnitude greater than the emission linewidth and is positive then the absorption at the emission wavelengths can be decreased [3] which improve the efficiency of type –II QDs for lasers applications [4]. However, in these PL studies the authors

considered the QD system as two level which contains two electrons in the ground system before excitation and did not consider the contribution from the higher electronic states [1]. However, it has been shown that there are allowed transitions from high energy states, which are neglected in this two level approach [5]. These high energy transitions might affect the reported results, calling their interpretation into doubt. In addition, since the data in TRPL methods is collected straight after the excitation, then the resultant spectra can have contributions of higher-order multi-excitons.

On the other hand, it has been suggested that a large attractive Δ_{XX} (<0) in type-II QDs will decrease the material's band gap significantly [6]. In such case, the threshold for MEG will be reduced and thus the potential efficiency of a solar cell based on QDs would increase [6]. Such a threshold reduction would complement the MEG efficiency improvements found for type-II QDs in the work described in the previous chapter.

In support of the possibility that Δ_{XX} may be negative for type-II QDs, Avidan *et al.*[7] calculated Δ_{XX} in ZnSe/CdS type-II structures and found that the magnitude and sign of Δ_{XX} depends on the geometry of the structures. In addition, Stuart K. Stubbs and his colleagues reported attractive Δ_{XX} with a magnitude of -96±7 meV in quasi-type II CdSe/CdTe/CdS QDs using the TA experiment, as shown in Figure 7.1. This large attractive Δ_{XX} let to the band gap energy to be red-shifted by its magnitude. However, this measurement was done immediately after photo-excitation, and the contribution of higher-order multi-excitons could not be discounted.

The results obtained in the last two studies are impressive and promising as they imply that an accurate design of type-II structures might potentially increase significantly the efficiency of photovoltaics. However, clearly much work remains to be done to shed

light on this aspect of the applications of type-II QDs. To move further, in this study we devise a new experimental technique to investigate Δ_{XX} in type-II QDs. The experiment used here is an ultrafast TA experiment with a fixed delay time of 650 ps between pump and probe pulses which corresponds to the time when carrier cooling to the band edge and the recombination of pump-created multi-excitons are completed and only a single long-lived exciton remains in the system. This is confirmed by looking at the transient transmittance decay figures in this chapter as all figures show a plateau after about 200 ps delay that lasts beyond 800 ps delay time point. The second exciton is formed when the probe beam arrives after 650 ps. Hence the observed results are solely due to biexciton interactions.

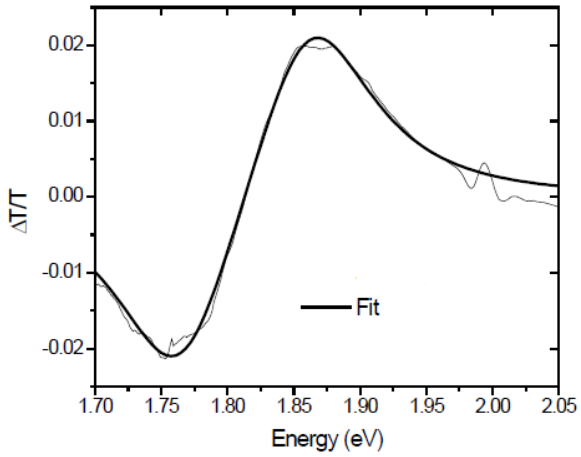

Figure 7.1. Differential transmission spectra for CdSe/CdTe/CdS QDs taken by Stuart K. Stubbs. Δ_{XX} is extracted from the fit to the spectra using Eq.(2.10)

7.2 Sample information

The samples used in this study were three different sets of CdSe/CdTe/CdS and two sets of CdTe/CdSe/CdS core/shell/shell and a CdTe/CdS core/shell type-II QDs. The samples were produced by Robert Page at the Department of Chemistry of The University of

Manchester using a hot-injection process. They were prepared under nitrogen purging to avoid oxidation and dispersed in dry toluene solvent. It has been experimentally proved that the ultrafast exciton dynamics of QDs can be effectively monitored when the absorbance at the band edge (the natural logarithm of the ratio between the incident and the transmitted beams) is between the values of 0.2 and 0.6 [8-11]. Therefore we adjusted the absorbance at the absorption shoulder between those values. The samples were preserved in a 5 ml wide and 10 mm long quartz cuvette. To prevent any sample photocharging, the samples are stirred at 1000 rpm using a magnetic stirrer during the TA experiment. All measruments were carried out under room temperature.

The localization of charges are determined from the band alignment of the samples using energy criteria explained in Chapter 2. Thus, electrons and holes are localised in the shell and core, respectively in CdTe/CdSe, and CdTe/CdS QDs, whilst, it is vice-versa in the case of CdSe/CdTe QDs. It has been shown that surface-mediated charge trapping will deteriorate the PL QY [12] and the MEG efficiency[13] in colloidal QDs. Therefore, CdSe/CdTe and CdTe/CdSe core/shell structures are passivated with CdS outer shell so that the hot carriers do not interact with the sample surface. The thickness of CdS is only a few monolayer and almost equall for all the samples. The core/shell and core/shell/shell structures used in this chapter are in the form of either quasi-type-II or type-II and will be called type-II structure throughout the thesis.

7.3 Optical characterization

7.3.1 Absorption and PL spectra

In order to characterise the QDs, we initially performed steady-state absorption and PL

spectra using a Perkin Elmer Lambda 1050 spectrophotometer and a Horiba Jobin Yvon Fluorolog-3 model FL3-22iHR Spectrofluorometer, respectively. The principle of these techniqies are shown in detail in Chapter 3. The PL spectra were recored for all the samples using a photon excitation wavelength of 400 nm (3.11 eV). Figures 7.2 a) and b) show the steady-state absorption and PL spectra developments of CdSe and CdTe core-based structures before and after addition of the inner shell and CdS shell, respectively. The curves of absorption spectra are vertically offset for clarity. The absorption and PL spectra for CdTe/CdS heterostructure are presented in Figure 6.2 f) in Chapter 6. Clearly from these figures 7.2 a) and b), the formation of the inner and outer shells results in a red shift for both materials. That proves that the material is transforming from a type-I to type-II structure where the overlap of electron and hole wavefunction is decreased.

In Figure 7.2 a), the CdSe core has a clear 1S absorption feature at 555 nm (~2.74 eV) that is red shifted to 630 nm (~1.97 eV) and then to 666 nm (~1.87 eV) with formation of a CdTe inner shell and a CdS outher shell, respectively (see also Table 7.2). In addition, the ground state absorption feature curves for the CdSe/CdTe core/shell and CdSe/CdTe/CdS core/shell/shell are smeared compared with that of the CdSe core. This is a further confirmation that the structures transformed from a type-I form to that of a type-II [14] wherein the electron and holes reside in the CdSe core and CdTe shells, respectively, reducing the oscillator strength of the band edge transitions. Similarly, the PL spectrum of CdSe was red shifted from 567 nm (~2.2 eV) to 670 nm (~1.85 eV) with addition of CdTe, and to 700 nm (~1.77 eV) with addition of the final CdS shell (see also Table 7.2). The 1S absorption and PL maximum values for the rest of the CdSe core-based samples are shown in Table 7.2. The bold digits at the end of each sample indicate the sample labelling. All samples show a global Stoke shift between the absorption-edge and the PL

maximum which for some samples goes up to 40 meV. The large shift between these spectra is explained by a strong electron-phonon interaction, size dispersion effect and band-edge exciton fine structure [15-17]. The absoprtion band gap energies for these nanoparticles are higher than that of the corresponded bulk crystals which indicates that quantum confinement is dominant in QDs.

Based on the band edge absorption spectra and transmission electron microscopy size measurements, Yu *et al*. [18] have developed new models to determine sizes of CdSe and CdTe QDs. These models are the most reliable sources to calculate the theoretical size information of the aforsaid QDs. Hence, the diameters D for the different CdSe core samples were calculated from;

$$D_{\mathrm{CdSe}} = (1.6122 \times 10^{-9})\lambda^4 - (2.6575 \times 10^{-6})\lambda^3 + (1.6242 \times 10^{-3})\lambda^2 - (0.4277)\lambda + (41.57) \quad (7.1)$$

and similarly, for the different CdTe core samples;

$$D_{\mathrm{CdTe}} = (9.8127 \times 10^{-7})\lambda^3 - (1.7147 \times 10^{-3})\lambda^2 + (1.0064)\lambda - (194.84) \quad (7.2)$$

where, λ is the ground state absorption of the material. Based on these expressions, the core diameters of CdSe QDs were found to be approximately 3.2, 3.6 and 4.2 nm; we label them as small, medium and large cores, respectively. Likewise, the CdTe QDs core diameters were found to be approximetly 3.7 and 3.9 nm, and they are labeled as small and large cores, respectively. The CdSe and CdTe core diameters presented in figures 7.2 a) and b) were that of 3.2 and 3.7 nm (regarded as small cores), respectively. The large CdTe core is used for the CdTe/CdS structure as it was used to obtain efficient MEG in Chapter 6. For CdSe core based QDs, the samples labelled as 1,2,3,4 and 5 have a core diameter of

4.2 nm, the samples labelled as 6 and 5 have a core diameter of 3.6 nm and the samples branded as 8,9,10,11,12,13 have a core diameter of 3.2 nm. Similarly, for CdTe core made QDs, the samples notated as 1,2,3,4 and 5 consist of a 3.7 nm diameter core, whereas, the sample 6 has a core diameter of 3.9 nm. A summary of the sample labelling is presented in Table 7.1.

Table 7.1. The labelling of the samples used in this Chapter. The bold digits at the end of each sample represent the sample number.

CdSe core based samples		
Large core (~4.2 nm)	**Medium core (~3.6 nm)**	**Small core (~3.2 nm)**
CdSe/CdTe/CdS**1**	CdSe/CdTe/CdS**6**	CdSe/CdTe**8**
CdSe/CdTe**2**	CdSe/CdTe/CdS**7**	CdSe/CdTe/CdS**9**
CdSe/CdTe/CdS**3**		CdSe/CdTe**10**
CdSe/CdTe**4**		CdSe/CdTe/CdS**11**
CdSe/CdTe/CdS**5**		CdSe/CdTe**12**
		CdSe/CdTe/CdS**13**
CdTe core based samples		
Small core (~3.7 nm)		**Large core (~3.9 nm)**
CdTe/CdSe**1**		CdTe/CdSe/CdS**6**
CdTe/CdSe/CdS**2**		
CdTe/CdSe**3**		
CdTe/CdSe/CdS**4**		
CdTe/CdSe/CdS**5**		

The linear absorption and PL spectra for the small CdTe core-based structure in Figure 7.2 b) also exhibits similar behaviours with that of the small CdSe core-based samples. The PL spectrum shown in Figure 7.2 b) was recorded by Robert Page at the School of Chemistry of The University of Manchester using a fluoroSENS (Gilden photonics) PL machine. The absorption band gap for the CdTe core is redshifted from 600nm (~2.07 eV) to 635 nm (~1.96 eV) with addition of the CdSe inner shell. This indicates that the 1S absorbtion feature becomes an effective band gap corresponding to the energy between the conduction band minimum of the CdSe shell and the valance band maximum of the CdTe core. In this stiuation, electrons and holes are confined to the core

and shell, respectively.

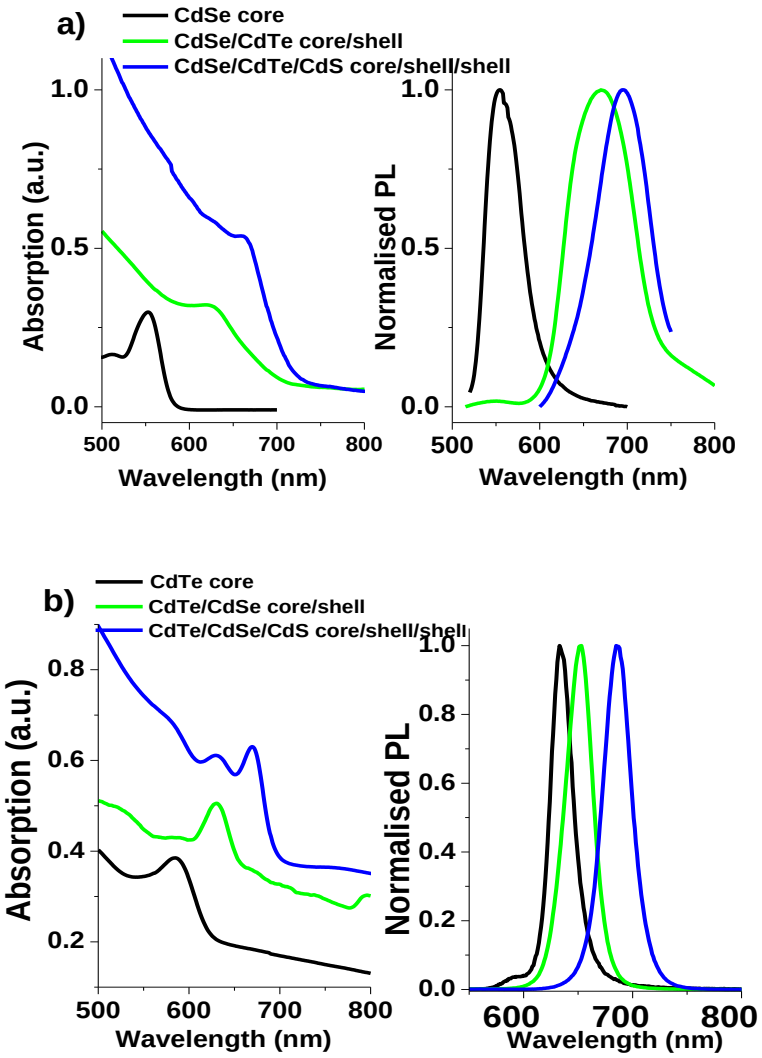

Figure 7.2. Absorption and PL spectra progress for a) CdSe and b) CdTe core-based structures before and after addition of the inner and outer shells. The PL excitation wavelength was chosen to be 400 nm (3.11 eV).

The resultant effective band gap is further shifted to 675 nm (~1.84eV) with formation of the final CdS shell. Similarly, the PL spectra for this set of sample designs is red-shifted with addition of the inner and outer shells. The small CdTe core has a PL peak at 630 nm (~2.00 eV) whereas, this value is shifted to 655 nm (~1.91 eV) and 685 nm (~1.81 eV) with addition of the CdSe and CdS shells, respectively. This is again another

proof of transformation from type-I form to that of a type-II. The first steady-state absorption and PL peak values for all CdTe core-based QDs are provided in Table 7.3. Similar to that of the CdSe core-commisioned samples, these samples also show a Stoke shift up to 30 meV between the PL maximum and the 1S absorption feature.

Table 7.2. The summary of the ground state absorption and PL maximum values for CdSe core-based samples.

Sample	*1S Absorption (nm)*	*PL (nm)*
Large CdSe core (~4.2 nm)	590	608
CdSe/CdTe/CdS**1**	658	691
CdSe/CdTe**2**	638	664
CdSe/CdTe/CdS**3**	670	692
CdSe/CdTe**4**	650	669
CdSe/CdTe/CdS**5**	672	675
Medium CdSe core (~3.6 nm)	572	603
CdSe/CdTe/CdS**6**	637	647
CdSe/CdTe/CdS**7**	655	664
Small CdSe core (~3.2 nm)	555	567
CdSe/CdTe**8**	630	671
CdSe/CdTe/CdS**9**	666	700
CdSe/CdTe**10**	713	728
CdSe/CdTe/CdS**11**	723	748
CdSe/CdTe**12**	622	669
CdSe/CdTe/CdS**13**	655	695

Table 7.3. The compilation of band edge absorption and maximum PL wavelengths values for CdTe core-based samples.

Sample	*1S Absorption (nm)*	*PL (nm)*
Small CdTe core (~3.7nm)	600	614
CdTe/CdSe**1**	635	642
CdTe/CdSe/CdS**2**	690	705
CdTe/CdSe**3**	659	666
CdTe/CdSe/CdS**4**	675	679
CdTe/CdSe/CdS**5**	715	718
Large CdTe core (~3.9 nm)	621	629
CdTe/CdSe/CdS**6**	685	715

7.4 Results and discussions

7.4.1 Biexciton interaction energy measurements using TA experiment

An ultrafast TA experiment was used to monitor X-X interaction in the lowest conduction band level of the QDs. This method is a pump-probe experiment wherein the pump beam excites the system and the subsequent probe beam monitors the exciton population at the desired energy levels. The ultrafast TA experiment is explained in Chapter 3 (see section 3.4.) in detail. The pump beam was set to 450 nm (~2.8 eV) which lies below the MEG threshold of the samples. The differential transmittance spectra for fixed Δt (650 ps for our samples), the time between the arrivals of pump and probe beams, was recorded using the monochromator over the wavelength range of the sample band gap.

The Eq.(2.9) is used to fit the recorded differential transmittance spectra to extract the magnitude and sign of the Δ_{XX}. This equation is used when carrier relaxation is completed and only one exciton remains at the band edge of the QD [15]. The second exciton is formed by the absorption of probe pulse. As explained in Chapter 2, depending on the magnitude and sign of the Δ_{XX}, three scenarios can take place in QDs; small and attractive Δ_{XX}, large and repulsive Δ_{XX}, and large and attactive Δ_{XX}. The shape of the differential transmission spectra is altered at each situation, as shown in Figure 7.3. In the case of small and attarctive Δ_{XX} which occurs in type-I QDs, the spectrum is almost symmetrical as there is no any significant force from neither side of the spectrum. However, if large and repulsive Δ_{XX} takes place then the observed differential transmission spectra is skewed to the blue. In the third scenario, if Δ_{XX} is large and attractive then the recorded spectra is skewed to the red. Fitting Eq.(2.9) enables the sign and magnitude to be extracted from the TA spectrum.

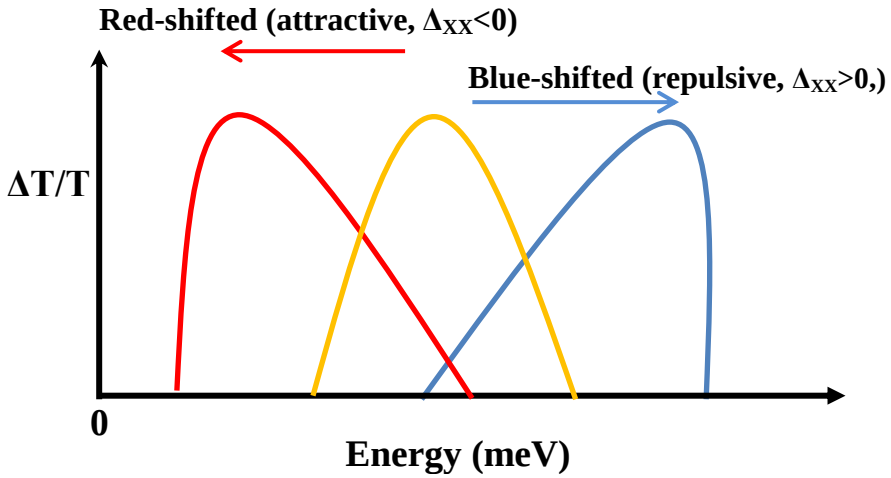

Figure 7.3. Three possible consequence of Δ_{XX} arising in QDs. The orange spectrum represents the small attractive Δ_{XX} occurring in type-I QDs. The blue spectra corresponds to large repulsive Δ_{XX} which is skewed to high energy side.. The red spectrum is attributed to large and attractive Δ_{XX} in type-II QDs which is skewed to low energy side.

Transient transmittance decays for the samples were obtained to observe the biexciton decay constants and the effects of any photocharging on the ultrafast dynamics of the dots. Then the differential transmittance spectra of these dots were recorded to investigate Δ_{XX} in type-II structures. Figure 7.4 a) and b) provide example pump induced fractional transmittance transients obtained for different pump fluences for CdSe/CdTe/CdS**13** and CdTe/CdSe/CdS**5** samples at excitation pump wavelength of 450nm (~2.76 eV), respectively. The pump energy lies below the MEG threshold of the sample and thus there is no MEG contribution in the obtained transients. Both figures are well-described with global mono-exponential decays to plateau. The time constants for CdSe/CdTe/CdS**13** and CdTe/CdSe/CdS**5** were found to 80±1 ps and 108±1 ps, respectively. The flat signals beyond the mono-exponential decays indicate the existence of the long-lived single exciton whose lifetime is too long to be identified with the ultrafast TA experiment. The radiative lifetime of the single exciton for CdSe core-based samples is found to be in the order of 10s of ns, as shown in the previous section. The radiative single

exciton lifetimes for CdTe/CdSe [19] and CdTe/CdS [20] have been reported to be in the order of 10s of ns. This shows that the employed ultrafast TA experiment is not capable of measuring the single exciton lifetimes of the samples used here. The observed transients also show that there is no surface mediated-relaxation due to use of the final CdS shell. Because, researchers have shown that in some cases, despite expecting decays in mono-exponential form, they could be bi-exponential or tri-exponential in form due to surface trapping [9, 21]. However, as expected from the used excitation power levels, the transients in Figure 7.4 fitted with a mono-exponential decay.

Figure 7.5 shows the fractional transmittance transients for the CdSe/CdTe/CdS**3** sample obtained under stirring and static conditions, with all other parameters remaining same. Both decays are globally fitted with a single exponential decay with a characteristic time constant of 117±9 ps. It is apparent from the figure that both decays are nearly identical. This confirms that there is no formation of trions which occurs when a geminate partner of a charge traps on the sample surface for a time period more than the time between two consecutive pulses [22]. This is further evidence since the addition of the final CdS shell around the core/shell structures reduces charge interaction with the sample surface.

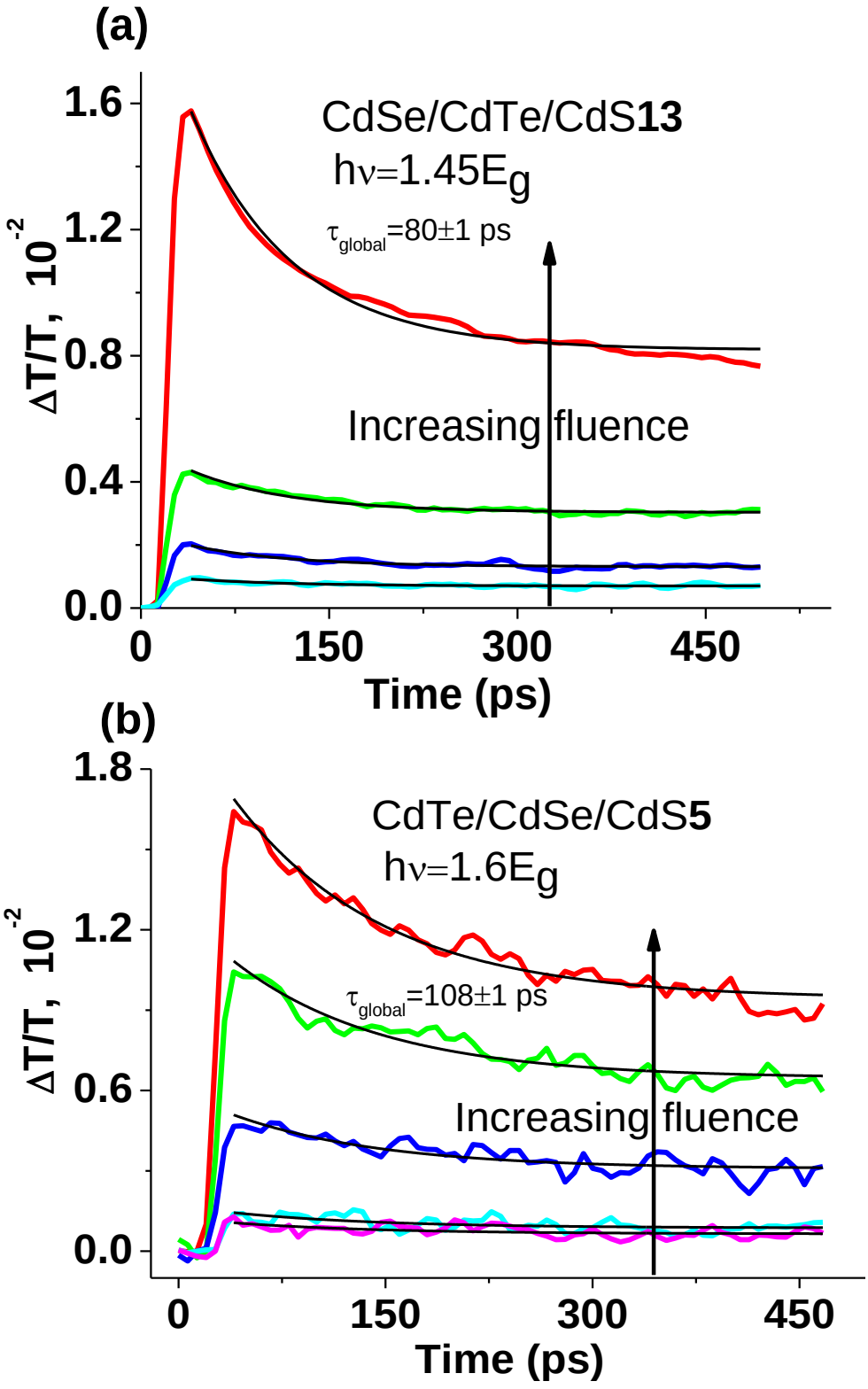

Figure 7.4. The variation of the fractional transmittance transients of a) CdSe/CdTe/CdS13 and b) CdTe/CdSe/CdS5 core/shell shell samples with different pump fluences for the photon energy of 2.76 eV. The black lines indicate mono-exponential fit.

Similarly, the bleach transients (monitoring carrier population at the band edge) for the CdTe/CdSe/CdS**6** sample recorded under stirring and static conditions, with all other experimental parameters remaining the same, shown in Figure 7.6. The decays are globally fitted with a single exponential function which yields a time constant of 105±1 ps. There is no significant difference between stirring and static conditions. This also proves that the CdS shell acts as a proper barrier between the sample surface and charges and thus photocharging is not an obstacle for these samples.

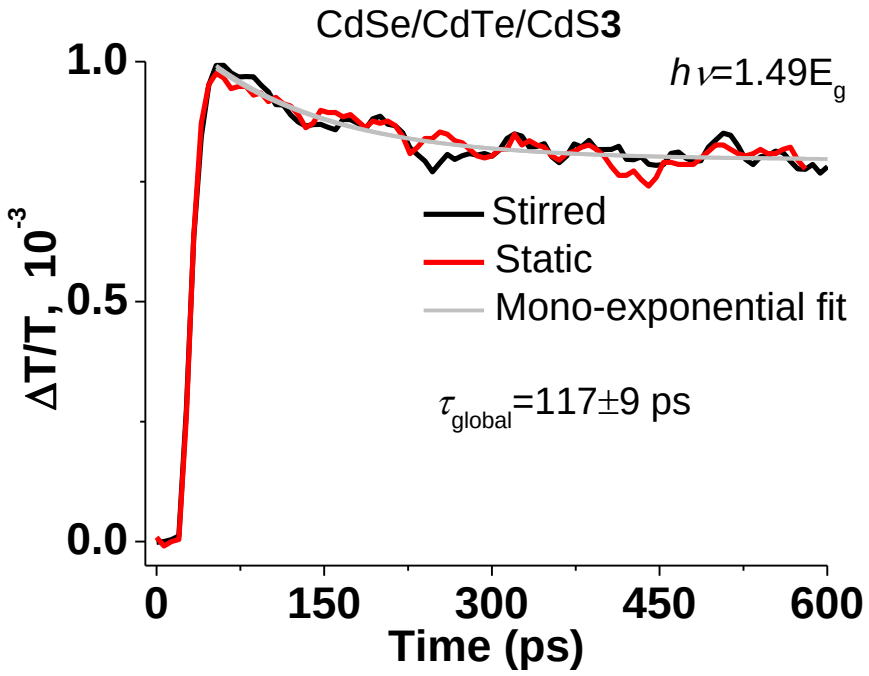

Figure 7.5. The comparison of the fractional transmittance transients of CdSe/CdTe/CdS3 sample monitored when the sample is stirred at 1000 rpm (black) and when it is statics (red). The sample is excited with a photon energy of 2.76 eV, corresponding to 1.49 times of the sample band gap.

Figure 7.7 a) and b) illustrate the initial high resolution fractional transmittance transients at 450 nm (2.76 eV) pump wavelength for the CdSe/CdTe/CdS**9** and CdTe/CdSe/CdS**4** samples, respectively. The delay stage step size for these transients was adjust to be 0.1 mm which corresponds to a delay time of 667 fs that is considered to be a high resolution delay time between pump and probe pulses. Research has shown that the

hot electrons from the higher energy states of the conduction band directly move to the sample surface, resulting in direct surface trapping [23, 24]. One of the significant sign of direct surface trapping is that the initial rise in the bleach transient starts at somewhere below zero; this is explained in detail in Chapter 4. However, as clearly seen from the initial growth of the fractional transmittance transients, there is a monotonic initial rise starting from zero to the bleach maximum. This indicates that the hot electrons relax to the CBM instead of trapping on the surface. Hence, it can be concluded that the outer CdS shell acts as an efficient block to stop the charge interaction with the sample surface.

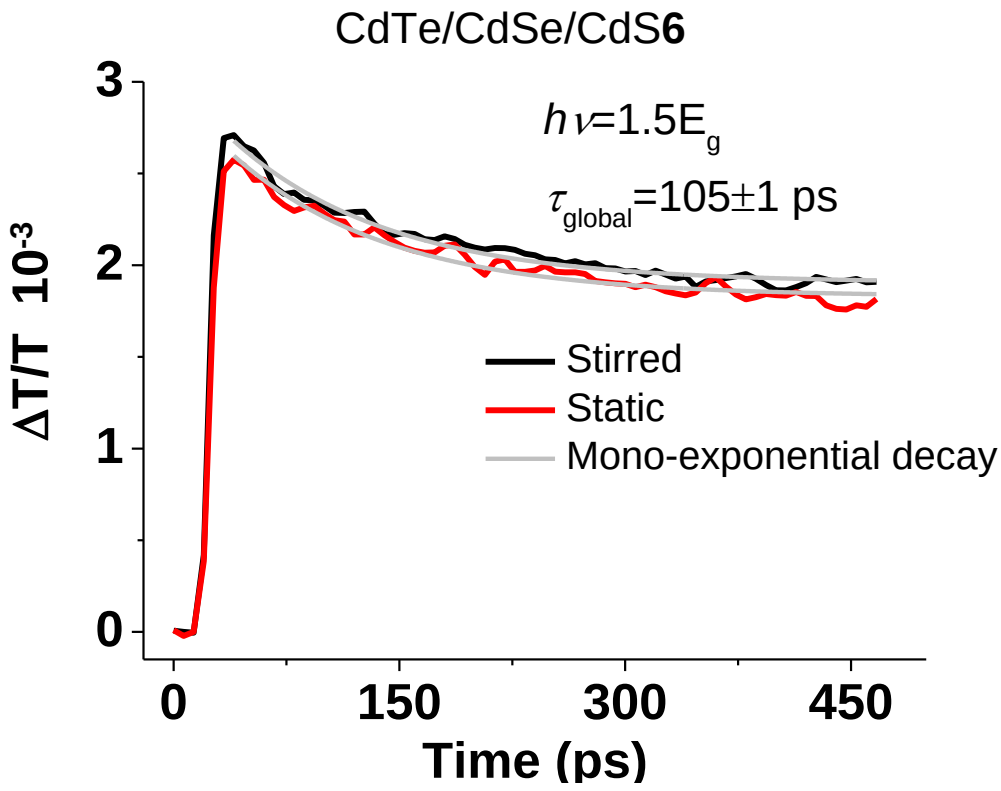

Figure 7.6. The fractional transmittance transients for CdTe/CdSe/CdS6 sample under stirring (black) and static (red) conditions at 2.76 eV excitation energy, corresponding to about 1.5 times of the sample band gap.

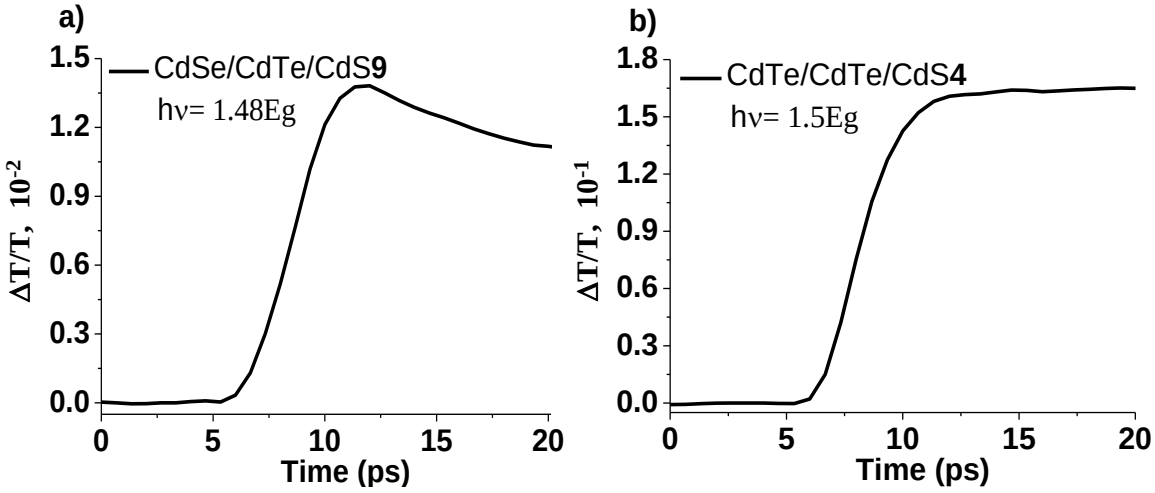

Figure 7.7. The initial bleach rise for a) CdSe/CdTe/CdS9 and b) CdTe/CdSe/CdS4 core/shell/shell structures with pump energy of 2.76 eV.

The differential transmission spectra known as TA spectra at the anticipated wavelength range is recorded by fixing the delay time, Δt, corresponding to the time between arrivals of pump and probe beams. In this work, the delay time is fixed to 650 ps, by which time all hot excitons are cooled to the band edge and the pump created multi-excitons are recombined; before recombination of the long-lived single exciton. This can be confirmed from the above transmittance transient decays as 650 ps in those transients corresponds to the plateau, indicating the presence of only a long-lived exciton. The second exciton is created with the probe beam and hence the resultant interaction between excitons is purely due to the interaction between two excitons, and not more.

Figure 7.8 a) presents the differential transmission spectra of the large CdSe core-based CdSe/CdTe/CdS**5** core/shell/shell QDs. Eq.(2.9) is fitted to the spectrum and it is deconvoluted into two components; one at ~1.81 eV and another at ~1.94 eV, corresponding the linear 1S and 2S absorption spectra, respectively, as shown in Figure 7.9. The derived differential transmittance spectra corresponding to the 1S absorption feature is of similar shape and breadth to the ground state absorption edge of the

CdSe/CdTe/CdS**5** core/shell/shell sample, as shown in Figure 7.8 b). However, the peak position of the TA spectra is slightly red-shifted with respect to the ground state absorption spectrum. The magnitude of the redshift is extracted to be -25.10±1.70 meV from the fitting function. This indicates that the interaction between the two excitons (one from the pump pulse and the other from probe pulse) in the dot results in a decrease of about 25 meV in the dot band gap. The additional evidence for the red-shift of the band gap is that the peak is skewed to the lower energies, which is consistent with the explanation of Figure 7.3. The primary aim here was to investigate the effect of Δ_{XX} on the material's band gap and thus we focused on the change in the differential spectra corresponded to the sample band gap. The observed 2S and higher order pump-induced absorption spectra do not contribute to the dots' absorption band gaps. The position of the observed pump-induced 2S transitions are compared with the theoretical calculated estimations using the multi-band model [5]. For example, the theoretical calculated 2S transition occurs at about 1.88 eV for the CdSe/CdTe/CdS**5** core/shell/shell QD, which is slightly different than the experimental pump-induced 2S.

Figure 7.10 a) and b) compare the TA spectrum and the ground state absorption spectrum of the small core CdSe/CdTe/CdS**13** type-II structure. The TA spectrum is recorded at 650 ps after the arrival of pump pulse which assures that only the long-lived single exciton exists. Eq. (2.9) is used to fit the differential transmittance spectra which is deconvoluted into two bands; corresponding to the signals of 1S and 2S absorption features. The derived peaks are found to be at 1.77±0.02 eV and 1.85±0.01eV for 1S and 2S features, respectively. The recorded TA spectrum is skewed to the low energy side, indicative of an attractive interaction between excitons. The spectral shape and breadth of the first pump-induced absorption feature is similar to the band edge spectra. The FWHM

of the 1S differential spectra is found to about 91.8±2.0 meV.

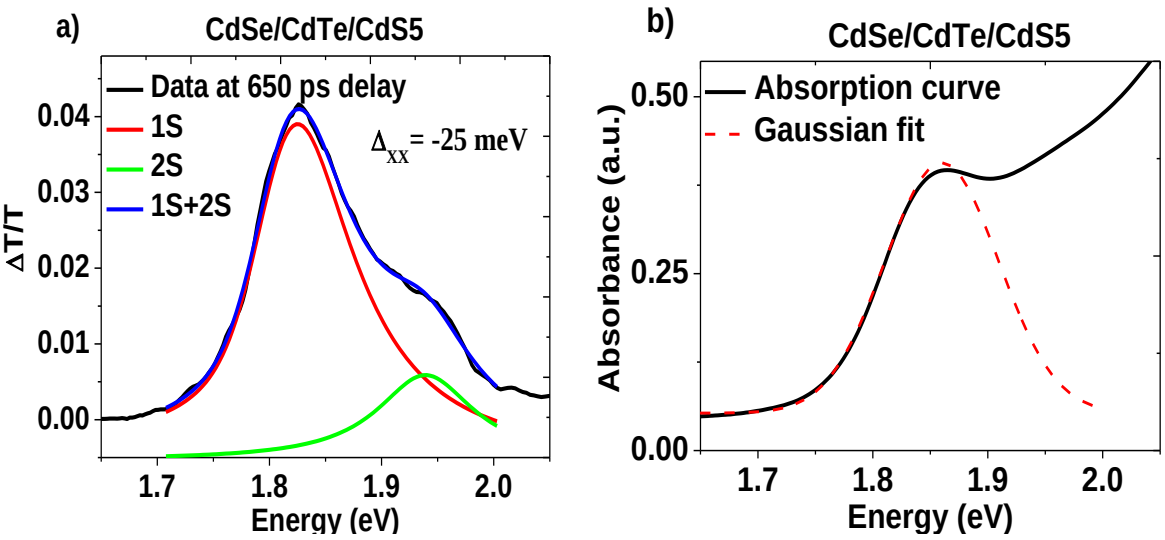

Figure 7.8. a) The TA spectra of large core CdSe/CdTe/CdS5 core/shell/shell sample for 650 ps time delay between the pump and probe pulses. The red band relates to the sample bandgap, whereas, the green band represents the 2S absorption feature. b) The ground state absorption spectra of CdSe/CdTe/CdS5 sample. The red dashed line shows a Gaussian fit to the 1S absorption spectra.

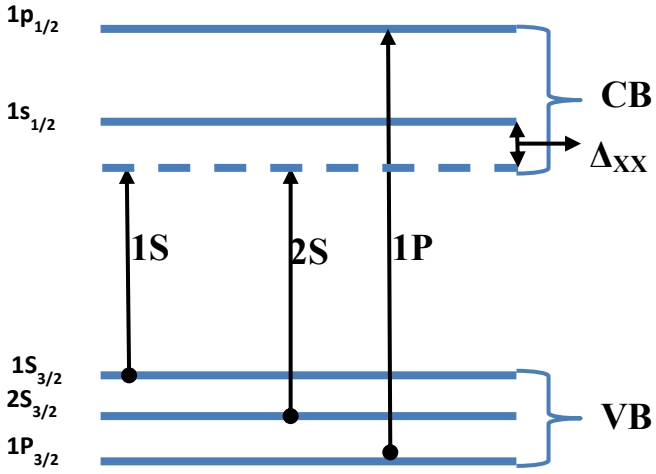

Figure 7.9. Illustration of the absorption transitions that can be observed from the differential TA spectra.

The magnitude and shape of the obtained TA spectra is also consistent with previously reported type-I CdSe QDs [15, 25]. The attractive biexciton interaction energy is measured to be -59±2 meV, indicating that the band gap of the CdSe/CdTe/CdS**13** type-II QDs is decreased by that amount of energy. The position of the 2S transition for the

CdSe/CdTe/CdS**13** sample is estimated from the theoretical calculation [5] to be about 1.88 eV which is less than 100 meV different than the experimentally observed pump-induced 2S transition [5].

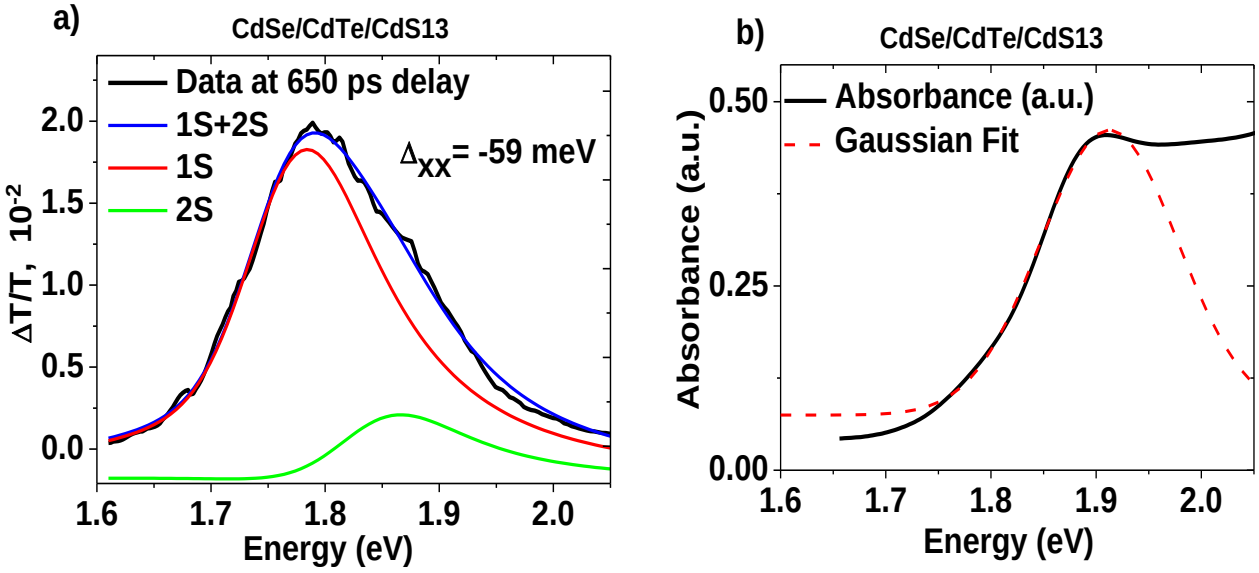

Figure 7.10. Comparison of a) the transient absorption and b) first absorption edge of the small core CdSe/CdTe/CdS13 QDs. The transient absorption spectra consists of contribution from pump-induced 1S (red) and 2S (green) absorption spectra. The blue line is the fit of eq.(2.13) to the data taken at 650 ps after the arrival of pump beam. Gaussian fit is done to the ground state absorption spectra (red dashed line).

Δ_{XX} was measured for all the CdSe core-based samples and the results are presented in Table 7.4. All type-II samples showed attractive biexciton interaction energies with magnitude between about -25 meV and -60 meV. CdSe core only samples have a type-I design and thus they showed a Δ_{XX} value of as low as -16 meV.

Typical TA spectra for CdTe core-based CdTe/CdSe/Cd**5** and CdTe/CdS samples are provided in Figure 7.11 a) and b) and the corresponding first steady-state absorption features are shown in Figure 7.11 c) and d), respectively. Eq.(2.9) is used to fit the TA spectra and the 1S ground state absorption spectra is fitted with a Gaussian function to derive the peak parameters accurately. First and second pump-induced absorption features occur at 1.73±0.02 eV and 1.83±0.01 eV for the CdTe/CdSe/CdS**5** sample, respectively

and at 1.93±0.03 eV and 1.96±0.02 eV for CdTe/CdS QDs, respectively. The first pump-induced absorption features for both samples agree well with their steady state band edge absorption features regarding the breadth. For example, the transition line width for the 1S TA spectra of CdTe/CdSe/CdS**5** is measured to be 0.07±0.01 eV which is consistent with 0.06±0.01 eV measured for the corresponded 1S linear absorption spectra of the same sample. The 1S TA spectrum features in Figure 7.11 a) and b) are similar to those reported for CdTe/CdSe [19] and CdTe/CdS [20] type-II QDs, respectively. However, in these studies, it was observed that photocharging of the samples was significant. In comparison, the dots used here are well-passivated with the final CdS shell to avoid any PA features associated with surface-mediated cooling. The estimated theoretical 2S transition for CdTe/CdSe/CdS**5** was found to be about 1.81 eV which is almost consistent with the observed value.

Table 7.4. The summary of biexciton interaction energy values for CdSe core based samples.

Sample	Δ_{XX} (meV)
CdSe/CdTe/CdS**1**	-34.00±1.54
CdSe/CdTe**2**	-27.00±1.00
CdSe/CdTe**4**	-50.00±0.50
CdSe/CdTe/CdS**5**	-25.10±1.70
Medium CdSe core (~3.6 nm)	-16.10±6.11
CdSe/CdTe/CdS**6**	-28.02±4.04
CdSe/CdTe/CdS**7**	-60.00±7.21
Small CdSe core (~3.2 nm)	-17.00±2.03
CdSe/CdTe**8**	-46.01±7.01
CdSe/CdTe/CdS**9**	-36.10±2.21
CdSe/CdTe**10**	-34.10±1.50
CdSe/CdTe/CdS**13**	-59.10 ±2.30

The analysis of the TA spectra for the rest of the CdTe core-structured samples yielded attractive biexciton interaction energies between -11 meV and -59 meV. The

summary of all CdTe core based samples are shown in Table 7.5. The smallest Δ_{XX} value is observed in the CdTe core only sample which is an expected value for type-I structures [15] wherein the hole and electron wavefunctions are completely overlapped. However, the magnitude of Δ_{XX} is significantly higher for the core/shell and core/shell/shell structures. This is a typical behaviour of type-II and quasi-type-II structures [26], wherein the carrier wavefuntions overlap is reduced. Therefore, the large attractive biexciton interaction energy in type-II QDs can increase the efficiency of solar cells by decreasing the MEG threshold.

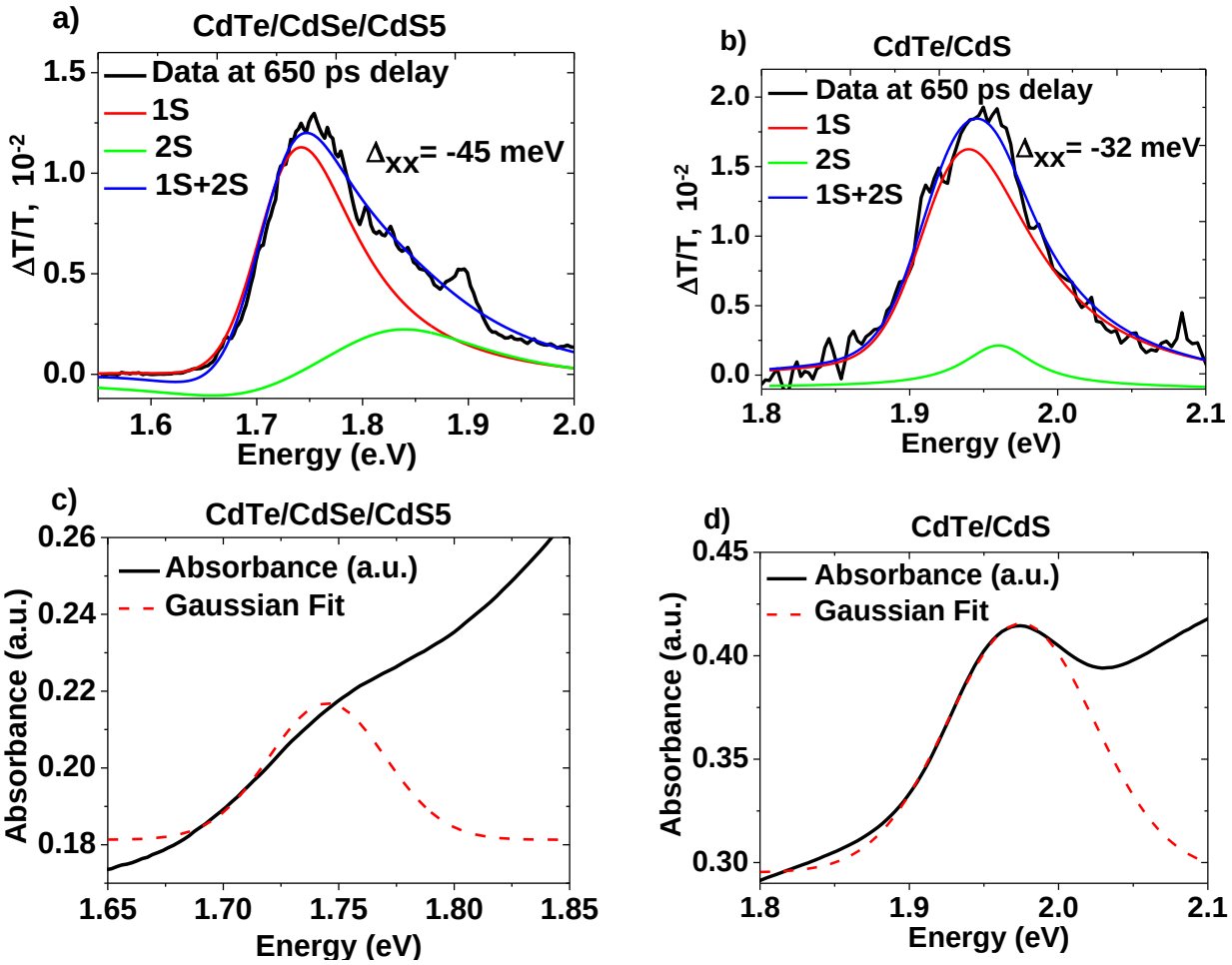

Figure 7.11. The differential transmission transients for a) CdTe/CdSe/CdS5 and b) CdTe/CdS and the corresponded first linear absorption peaks for c) CdTe/CdSe/CdS5 and d) CdTe/CdS samples. The transient absorption spectra are recorded for 650 ps delay between the pump and probe pulses. They are deconvoluted into 1S (red lines) and 2S (green lines) transient absorption bands. The first linear absorption band edge features are fitted with Gaussian function (dashed red lines).

Table 7.5. The values of the observed attractive biexciton interaction energies in CdTe core based samples.

Sample	Δ_{XX} (meV)
Small CdTe core (~3.7 nm)	-11.22±0.41
CdTe/CdSe**1**	-16.10±0.31
CdTe/CdSe/CdS**2**	-59.20±1.72
CdTe/CdSe**3**	-27.22±0.64
CdTe/CdSe/CdS**4**	-49.30±1.40
CdTe/CdSe/CdS**5**	-45.00±1.23
CdTe/CdSe/CdS**6**	-51.40±0.33

7.4.2 Photoluminescence time decay measurements

In order to further understand the effect of growing CdTe and CdS shells on the CdSe core we performed PL time decay measurements on the CdSe core-based samples before and after addition of CdTe and CdS shells. The TCSPC method used is explained in detail in Chapter 3 (see section 3.4). Figure 7.12 shows the typical change in PL decay dynamics of a series of CdSe core-based samples as the shells are added. The detection wavelengths for the experiment were set at the PL peak of the samples; these were 567 nm (~2.19 eV), 728nm (~1.71 eV) and 748 nm (~1.66 eV) for small CdSe core, CdSe/CdTe**10** and CdSe/CdTe/CdS**11**, respectively. Comparing the different cases, clearly the PL lifetimes increase when going from the single CdSe core (black line) to the type II CdSe/CdTe (red line) and CdSe/CdTe/CdS (blue line) systems with the single and double shell cases, respectively. Also shown (see Figure 7.12) are the biexponential decay function global fittings (grey line). The extracted emission life times are summarized in Table 7.6. These values further rise with the formation of a CdS outer shell, which is used as a barrier to eliminate surface-mediated recombination in the samples. This is typical evidence - and as expected from their absorption and PL behaviours (see Figure 7.2) - of converting from type-I design to type-II design as the spatial separation of electrons and holes results in a

longer charge recombination lifetime [27]. As expected, the observed radiative lifetimes are much longer than the duration of the TA experiment shown above, confirming that single exciton recombination does not interfere with the X-X interaction measurements.

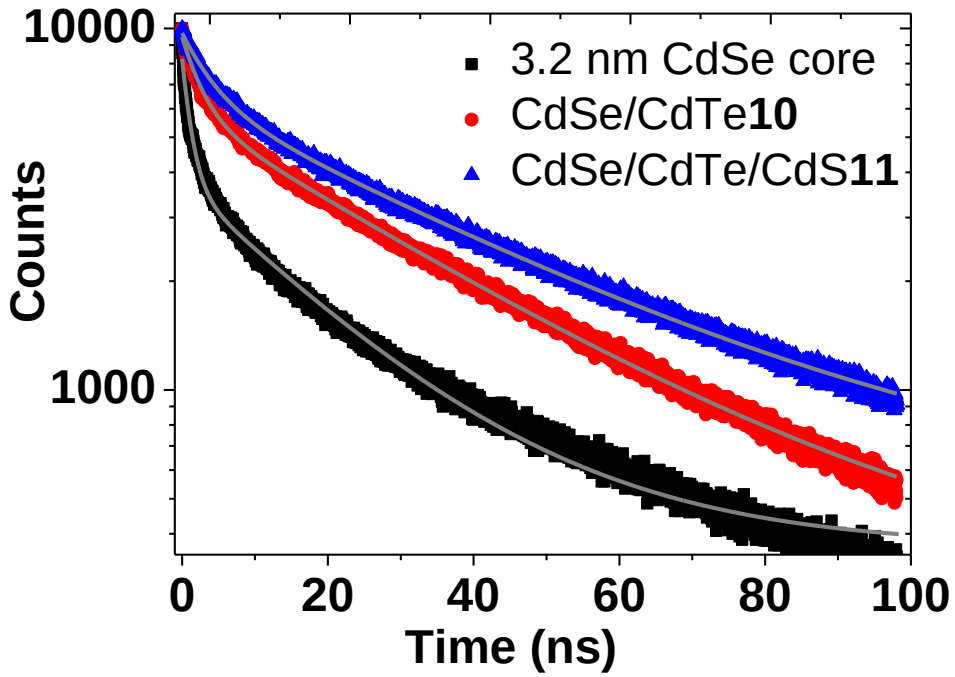

Figure 7.12. The time-resolved emission decays of CdSe core (black), CdSe/CdTe10 (red), and CdSe/CdTe/CdS11 (blue) samples. The curves are globally fitted with a biexponential function (grey lines).

Table 7.6. The summary of radiative exciton lifetimes obtained from PL decays of small CdSe core-based samples. It is clear that the emission lifetimes increase with addition of CdTe inner shell. Errors shown are statistical uncertainties calculated by the fitting software.

Sample	τ_1 (ns)	τ_2 (ns)
3.15 nm CdSe core	1.28±0.01	20.96±0.10
CdSe/CdTe**10**	2.78±0.02	34.00±0.14
CdSe/CdTe/CdS**11**	4.32±0.04	39.72±0.22

Figure 7.13 shows the PL decay transients for large CdSe core-based samples. The only difference between CdSe/CdTe/CdS**1** and CdSe/CdTe/CdS**3** is the thickness of CdTe

inner shell (the latter is thicker), all other parameters are identical. Similarly the CdSe core and the CdS final shell are identical in both cases. The PL emission was recorded for each sample at 687 nm (~1.81 eV), 664 nm (~1.87 eV), and 692 nm (~1.80 eV) for CdSe/CdTe/CdS**1,** CdSe/CdTe**2**, and CdSe/CdTe/CdS**3** samples, respectively. The decays are fitted with global biexponential functions. The derived emission lifetimes are presented in Table 7.7. As expected, the PL lifetime increases considerably with the addition of the CdS final shell. In addition, increasing the thickness of the CdTe shell increases the PL emission lifetime.

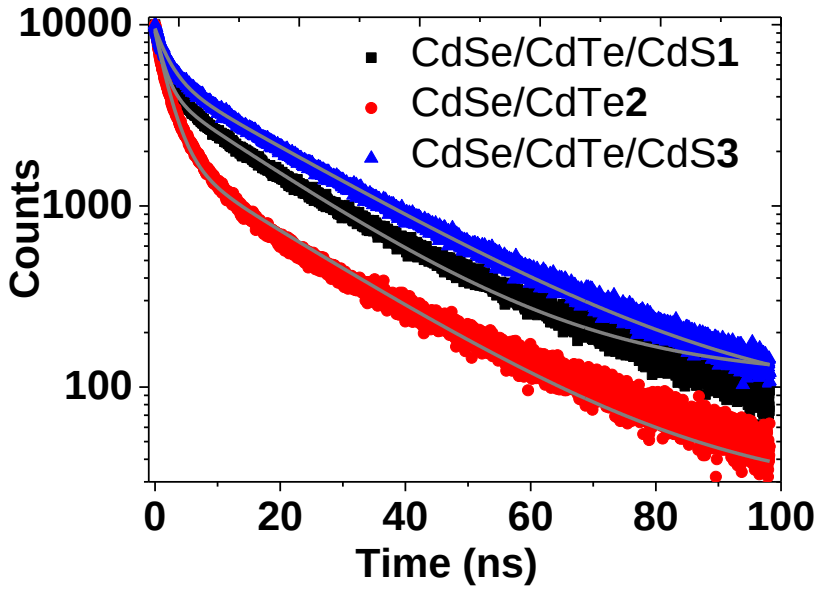

Figure 7.13. PL decay curves of CdSe/CdTe and CdSe/CdTe/ CdS samples with 4.2 nm core. The grey lines represent a global bi-exponential fit.

Table 7.7. PL emission lifetimes of the core/shell and core/shell/shell samples with 4.2 nm core.

Sample	τ_1 (ns)	τ_2 (ns)
CdSe/CdTe/CdS**1**	1.56±0.01	18.40±0.06
CdSe/CdTe**2**	2.19±0.01	20.00±0.00
CdSe/CdTe/CdS**3**	2.35±0.01	22.00±0.00

7.4.3 Multi-exciton interaction energy studies using the TRPL method

In order to understand why we observe X-X attraction whilst others have reported repulsive interaction, we followed the steps of previous experimental reports [2, 3] using TRPL. In this method, the TRPL spectrum is recorded at early and late times at high excitation levels to determine the shift between these two spectra. It has been suggested that the early-time spectra is due to biexciton interactions and thus the displacement between the early- and late-time spectra is interpreted as the biexciton interaction energy [2, 3]. In the present study the obtained results are compared with the Δ_{XX} results taken by the ultrafast TA experiment. The TRPL were derived from the TCSPC results explained in the previous section. The PL decays were recorded for all CdSe core-based samples at the PL peak wavelength. The process was repeated for the spectral range spanning from 40 nm below to 40 nm above the wavelength of the PL peak with 4 nm intervals for CdSe core-based samples. The average power of 400 nm and ~90 fs pulses with 8 MHz repetition rate was about 1.5 mW at the sample position. A microscope objective lens was used to focus the beam so that the beam has a diameter of about 0.7 mm on the sample. In that case the increased pump fluence will allow us to access the multi-exciton regime [2]. The absorbance of samples was adjusted to be between 0.2 and 0.5 at the wavelength corresponding to the sample band gap.

Figure 7.14 illustrates the normalised PL spectrum of the CdSe/CdTe/CdS**9** sample at time delays of 0 ns and 2 ns. The 2 ns time delay corresponds to the PL spectra when all multi-excitons are recombined and only one long-lived exciton remains in the system. This is confirmed with the fact that the long-lived spectrum is of similar shape with the steady-state PL spectrum of the CdSe/CdTe/CdS**9** sample and they both have a coincidence peak at about 700 nm (~1.8 eV). In contrast, the t=0 ns spectrum has a contribution from all

multi-exciton emissions and is blue-shifted with respect to the t=2 ns spectra. Therefore, the t= 0 ns PL spectrum is deconvoluted into two bands: one of which (black) corresponds to single exciton recombination and the other (grey) represents the multi-exciton emission spectra. The single exciton spectrum deconvoluted from the early PL spectrum is similar with the long-lived single exciton spectrum. However, the emission spectrum for the multi-exciton is about 40 meV blue shifted with respect to the single exciton emission spectrum. Further, the grey spectrum is broader than the black spectrum. Likewise, the short-lived PL curve (t=0 ns) is broader than the long-lived curve.

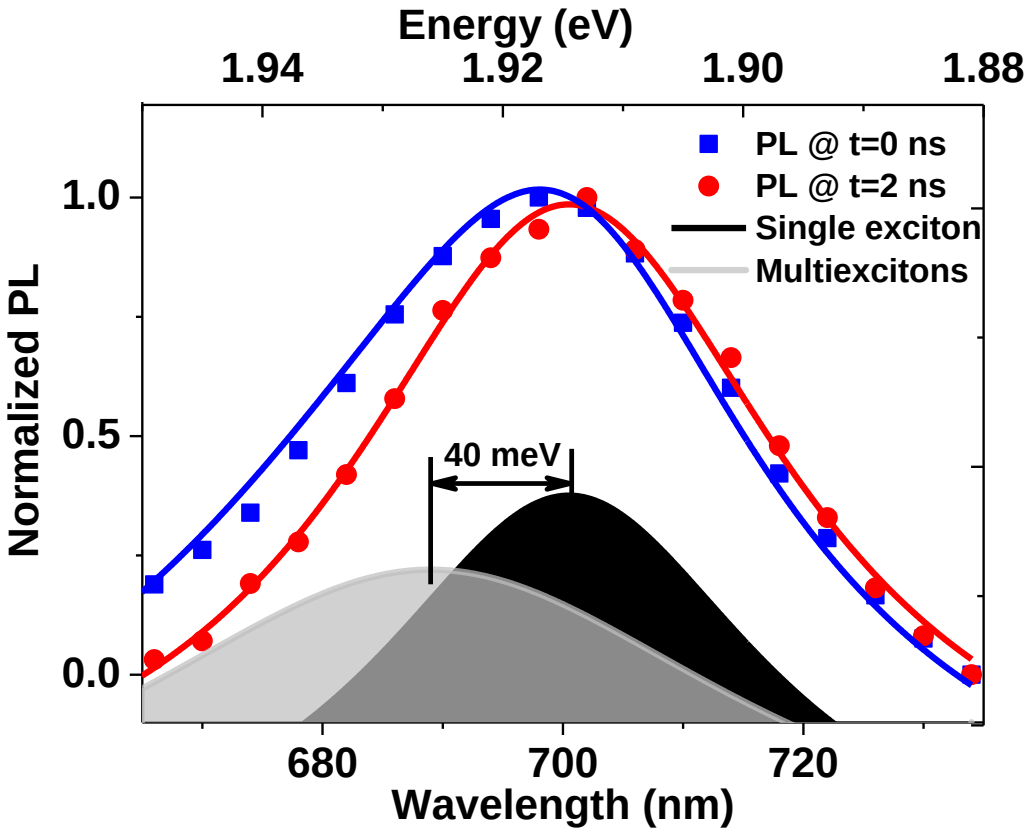

Figure 7.14. The normalized PL spectrum of CdSe/CdTe/CdS9 recorded at t= 0 ns (blue square) and t= 2 ns (red circles). The short-lived spectrum is deconvoluted into two parts: single exciton spectra (black) and multi-exciton spectra (grey).

Similarly, the same procedure is applied to the CdSe/CdTe/CdS**1** sample which has a CdSe core diameter of about 4.2 nm, regarded as large core. Figure 7.15 compares the long-lived (red circle) and short-lived (blue square) PL spectra for the CdSe/CdTe/CdS**1** sample. The short-lived emission spectrum is recorded straight after the excitation with ~90 fs pulses at 400 nm (~3.11 eV), whereas the long-lived spectrum is monitored 2 ns after the excitation. As expected, the peak wavelength of the t=2 ns spectra is about 691nm (~1.80 eV) which is the same as the peak wavelength of the steady state PL spectra of the same sample shown in Table 7.2. Therefore, the long-lived spectrum is due to single exciton emission. On the other hand, the t=0 ns spectrum is shifted to shorter wavelengths with regard to the t=2 ns spectrum. Additionally, this spectrum is broader than the single exciton emission. Thus, it is believed that the short-lived spectra consist of contributions from both single exciton emission and multi-exciton emissions. And hence to see the effect of contributions from multi-exciton emissions, the short-lived emission curve is divided into two components; the single exciton emission part (black) and multi-exciton emission part (grey), as shown in Figure 7.15. The peak position of the single exciton PL curve is the same as that of the long-lived PL curve. However, the multi-exciton emission component appears to be broader than the single exciton PL component. In addition, it is blue-shifted with respect to the single exciton emission spectra. The spacing between these two components is found to be about 20 meV.

The TRPL spectra of two series of CdSe core-based samples (small and large cores) were also recorded. The effect of multi-exciton emission is observed for only some of them, for the others no shift was seen. The peak wavelengths of the long-lived emission spectra and of the components of the short-lived emission spectra and the corresponding blue shift values between two components are given in Table 7.8. The values show that the

blue shift between the single-and multi-exciton emission spectra varies for the different samples, with a value being between 0 meV and 40 meV.

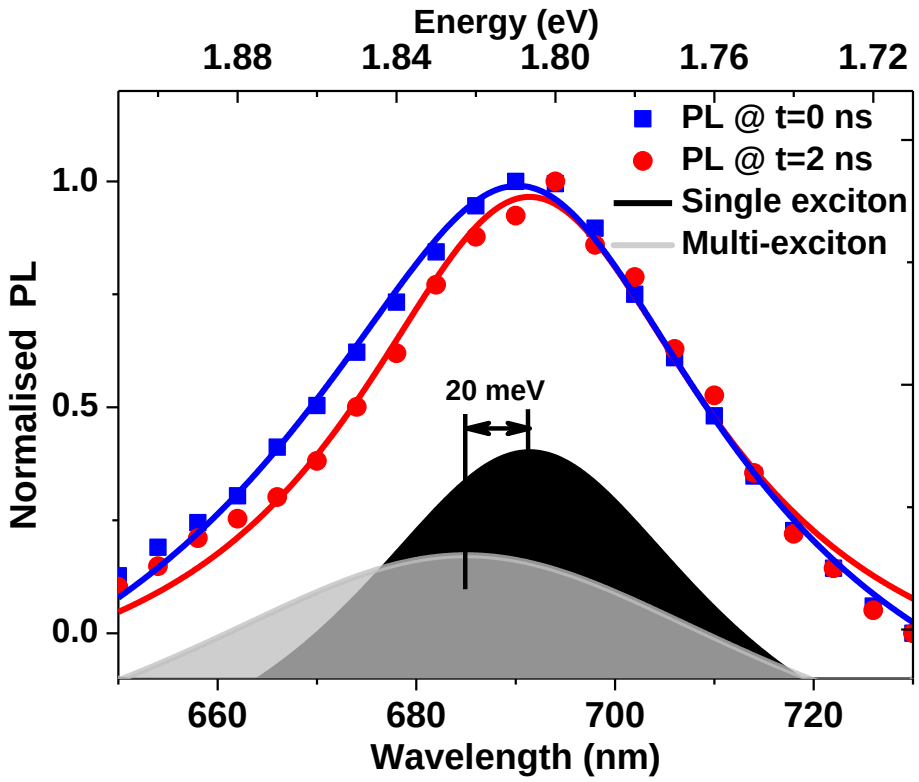

Figure 7.15. The normalised emission spectra recorded at early (blue squares) and late (red circles) times for CdSe/CdTe/CdS1. Both spectra are fitted with Lorentz function. The late-time PL spectrum is deconvoluted into single exciton component (black) and multi-exciton component (grey).

Table 7.8. The summary of blue shift between the single and multi exciton emission spectra for CdSe core-structured samples.

Sample	Blue shift (meV)
CdSe/CdTe/CdS**1**	20
CdSe/CdTe/CdS**3**	10
CdSe/CdTe**4**	0
Small CdSe core (~3.15 nm)	10
CdSe/CdTe**8**	0
CdSe/CdTe/CdS**9**	40
CdSe/CdTe**10**	0
CdSe/CdTe/CdS**11**	0
CdSe/CdTe**12**	10
CdSe/CdTe/CdS**13**	10

Similar features have been observed in CdS/ZnSe [1, 2] and ZnTe /CdSe core/shell QDs [3] using the same method. The authors of these reports claimed that the long-lived emission spectra occur in the single exciton regime and are identical with the steady state PL spectra and hence this emission is due to single exciton emission. However, the short-lived emission is a result of both single-and biexciton emission spectra. Therefore, the spacing between two components of the short-lived emission curve is considered as due to the repulsive X-X interaction. And thus, to the authors' perspective, the material band gap is increased by the value corresponding to the shift between two constituents of the short-lived spectra. According to the model used in these studies, in the biexciton regime, same-sign charges confine in the same volume of the QDs and the Coulomb repulsion between them will extend the material band gap. Hence, as a result of the widening of the band gap, the biexciton emission occurs at shorter wavelengths regarding the single exciton emission.

An effective mass model suggests that biexciton interaction in type–II QDs is a result of two main factors. Firstly, direct Coulomb repulsion between same sign charges confined in the same volume of dot, which is large and repulsive [26]. Secondly, polarization at the core/shell interface is another component that affects the magnitude and sign of the X-X interaction. This component is related to the dielectric constant change and its sign is negative (attractive) if the dielectric constant of the core is smaller than that of the shell [26]. The interface polarization component has an effect of about 30 % on the total biexciton interaction energy in type-II heterostructures. Therefore, the biexciton interaction energy in type-II is always positive. However, Professor Stanko Tomić at the University of Salford is currently developing a model to explain Δ_{XX} in type-II QDs. It is based on an atomistic model that includes Coulomb repulsion, interface polarization and configuration interactions between electrons which varies with shell thickness and is

usually attractive in type-II QDs. Initial X-X interaction calculations based on this model agree well (see next) with results obtained here using the TA experiment.

The CdTe shell thicknesses of CdSe/CdTe**2**, CdSe/CdTe**4**, CdSe/CdTe**8** and CdSe/CdTe**10** core/shell samples were estimated by comparing absorption edge measurement theoretical results available in the literature [5]. The shell thicknesses were found to be about 0.2 nm, 0.5 nm, 1 nm and 2 nm, respectively. Figure 7.16 compares the experimental and theoretical Δ_{XX} values. The calculated X-X interaction in CdSe/CdTe type-II structures is attractive which is consistent with the experimental results. Clearly the Δ_{XX} is minimum when the CdTe shell thickness is about 0.5 nm and then goes towards zero as the thickness increases. Finally, if the CdTe shell thickness is equal or bigger than 1.75 nm, then X-X interaction becomes repulsive in CdSe/CdTe type-II QDs. The Δ_{XX} value for the CdSe/CdTe**10** sample slightly diverges from the theoretical trend line. Nevertheless, the other three experimentally observed Δ_{XX} values are perfectly in line with the theoretical results.

Clearly, there is a discrepancy between the measured attractive Δ_{XX} using the TA experiment and the blue-shift in the early TRPL spectra since the latter is considered to be due to the repulsive X-X interaction in the literature [1, 3, 26]. Hence, it is necessary to compare the results and methods side-by-side to resolve the conflict between the results. To start with the TRPL method, the PL signals are collected straight after the excitation with 400 nm (~3.12 eV) ultrafast pulses. Since the biexcitons are created here with a probability described by the Poisson distribution, a significant population of biexcitons mean that there will also be a comparable population of tri-excitons, which will also contribute to the PL. Further, emission from hot states has also been reported which

produces a short-lived, blue-shifted component to the PL spectra [28].

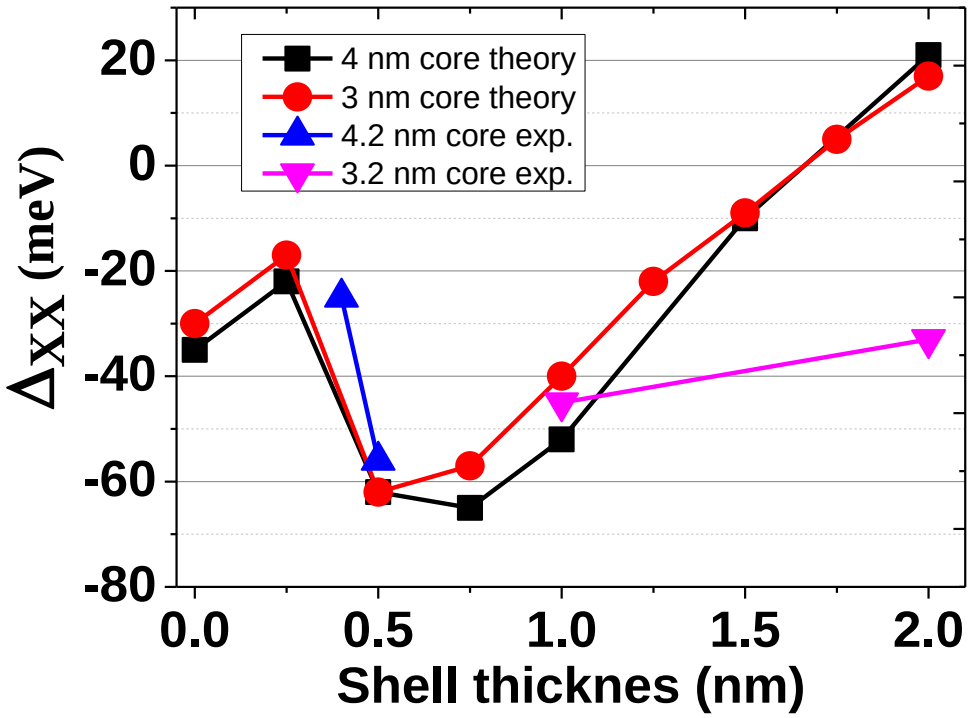

Figure 7.16. The theoretically calculated Δ_{XX} values as a function of shell thickness for a 4 nm core diameter (black) and 3 nm core diameter (red) CdSe/CdTe core/shell QDs and experimentally measured Δ_{XX} values as a function of shell thickness for 4.2 nm (blue) core and 3.2 nm (pink) core diameters CdSe/CdTe core/shell structures. The theoretical results are provided by Professor Stanko Tomić at the University of Salford.

The authors assumed that the single exciton is perfectly relaxed to the sample band edge and the system is considered as a single-band model. However, it is worth mentioning that it has been shown that the single-band model does not recognize the second and third absorption features clearly [5]. Furthermore, recent work has shown that the presence of hot carriers perturb the electronic structure of a QD, increasing the optical transition strength of forbidden transitions [29].

However, when investigating exciton interactions with the ultrafast TA experiment, the resultant spectrum is free from these effects. In our case, the spectra were recorded 650

ps after the arrival of the pump pulse. By that time, the entire pump produced excitons decay to the QD band edge and any multi-excitons have recombined; only one exciton now remains in the band edge of the structure. This can be confirmed from the transmittance transient decays in the figures 7.7 a) and b), where the 650 ps region corresponds to the plateau which is the signal of the long-lived exciton. The second exciton is created at the band edge by the probe pulse after 650 ps. Hence, the observed shift in the TA spectra is purely due to X-X interaction in the QDs.

7.5 Summary

In this chapter, spectral properties of multi-excitons have been investigated in a set of CdSe/CdTe/CdS and CdTe/CdSe/CdS core/shell/shell and CdTe/CdS core/shell type-II QDs using both the TA and the TRPL experiments. Large attractive Δ_{XX} up to ~-60 meV was observed using the TA method. The delay time between pump and probe was set to 650 ps to ensure that the obtained spectra are only due to the interaction between two excitons. However, a blue-shift up to 30 meV was observed using the TRPL method. This is attributed to the interaction between more than two excitons and emission from higher order states as PL photons are collected straight after excitation by this method. Hence the TA experiment is the most reliable tool to measure Δ_{XX} in QDs. A large attractive Δ_{XX} will decrease the MEG threshold in QDs and thus increase the efficiency of PVs.

7.6 References

1. Klimov, V.I., et al., *Single-exciton optical gain in semiconductor nanocrystals.* Nature, 2007. 447(7143): p. 441-446.

2. Ivanov, S.A. and M. Achermann, *Spectral and Dynamic Properties of Excitons and Biexcitons in Type-II Semiconductor Nanocrystals.* ACS Nano. 4(10): p. 5994-6000.

3. Nanda, J., et al., *Light Amplification in the Single-Exciton Regime Using Excitonâ^'Exciton Repulsion in Type-II Nanocrystal Quantum Dots.* The Journal of Physical Chemistry C, 2007. 111(42): p. 15382-15390.

4. Ivanov, S.A., et al., *Light Amplification Using Inverted Core/Shell Nanocrystals: Towards Lasing in the Single-Exciton Regime.* The Journal of Physical Chemistry B, 2004. 108(30): p. 10625-10630.

5. Tyrrell, E.J. and J.M. Smith, *Effective mass modeling of excitons in type-II quantum dot heterostructures.* Physical Review B. 84(16): p. 165328.

6. Schaller, R.D., J.M. Pietryga, and V.I. Klimov, *Carrier Multiplication in InAs Nanocrystal Quantum Dots with an Onset Defined by the Energy Conservation Limit.* Nano Letters, 2007. 7(11): p. 3469-3476.

7. Avidan, A., Z. Deutsch, and D. Oron, *Interactions of bound excitons in doped core/shell quantum dot heterostructures.* Physical Review B, 2010. 82(16): p. 165332.

8. Hardman, S.J.O., et al., *Electronic and surface properties of PbS nanoparticles exhibiting efficient multiple exciton generation.* Physical Chemistry Chemical Physics. 13(45): p. 20275-20283.

9. Cadirci, M., et al., *Ultrafast exciton dynamics in InAs/ZnSe nanocrystal quantum dots.* Physical Chemistry Chemical Physics, 2012. **14**: p 15166-15172

10. Al-Otaify, A., et al., *Multiple exciton generation and ultrafast exciton dynamics in HgTe colloidal quantum dots.* Physical Chemistry Chemical Physics, 2013. 15(39): p. 16864-16873.

11. Midgett, A.G., et al., *Flowing versus Static Conditions for Measuring Multiple Exciton Generation in PbSe Quantum Dots.* The Journal of Physical Chemistry C. 114(41): p. 17486-17500.

12. Aharoni, A., et al., *Synthesis of InAs/CdSe/ZnSe Core/Shell1/Shell2 Structures with Bright and Stable Near-Infrared Fluorescence.* Journal of the American Chemical Society, 2005. 128(1): p. 257-264.

13. McGuire, J.A., et al., *New Aspects of Carrier Multiplication in Semiconductor Nanocrystals.* Accounts of Chemical Research, 2008. 41(12): p. 1810-1819.

14. Nanda, J., et al., *Absorption cross sections and Auger recombination lifetimes in inverted core-shell nanocrystals: Implications for lasing performance.* Journal of Applied Physics, 2006. 99(3): p. 034309-7.

15. Klimov, V., *Spectral and Dynamical Properties of Multiexcitons in Semiconductor Nanocrystals.* Annu. Rev. Phys. Chem., 2006. 58: p. 635–73.

16. Norris, D.J., et al., *Size dependence of exciton fine structure in CdSe quantum dots.*

Physical Review B, 1996. 53(24): p. 16347-16354.

17. Kuno, M., et al., *The band edge luminescence of surface modified CdSe nanocrystallites: Probing the luminescing state.* The Journal of Chemical Physics, 1997. 106(23): p. 9869-9882.

18. Yu, W.W., et al., *Experimental Determination of the Extinction Coefficient of CdTe, CdSe, and CdS Nanocrystals.* Chemistry of Materials, 2003. 15(14): p. 2854-2860.

19. Rawalekar, S., et al., *Surface-State-Mediated Charge-Transfer Dynamics in CdTe/CdSe Core–Shell Quantum Dots.* ChemPhysChem, 2011. 12(9): p. 1729-1735.

20. Rawalekar, S., et al., *Ultrafast Charge Carrier Relaxation and Charge Transfer Dynamics of CdTe/CdS Coreâ^'Shell Quantum Dots as Studied by Femtosecond Transient Absorption Spectroscopy.* The Journal of Physical Chemistry C, 2009. 114(3): p. 1460-1466.

21. Pooja, T. and K. Patanjali, *False multiple exciton recombination and multiple exciton generation signals in semiconductor quantum dots arise from surface charge trapping.* J. Chem. Phys., 2011. 134(9): p. 094706.

22. Binks, D.J., *Multiple exciton generation in nanocrystal quantum dots - controversy, current status and future prospects.* Physical Chemistry Chemical Physics. 13(28): p. 12693-12704.

23. Kambhampati, P., *Hot Exciton Relaxation Dynamics in Semiconductor Quantum Dots: Radiationless Transitions on the Nanoscale.* The Journal of Physical Chemistry C. 115(45): p. 22089-22109.

24. Cadirci, M., et al., *Ultrafast exciton dynamics in Type II ZnTe-ZnSe colloidal quantum dots.* Physical Chemistry Chemical Physics. 14(39): p. 13638-13645.

25. Klimov, V., S. Hunsche, and H. Kurz, *Biexciton effects in femtosecond nonlinear transmission of semiconductor quantum dots.* Physical Review B, 1994. 50(11): p. 8110-8113.

26. Piryatinski, A., et al., *Effect of Quantum and Dielectric Confinement on the Exciton−Exciton Interaction Energy in Type II Core/Shell Semiconductor Nanocrystals.* Nano Letters, 2006. 7(1): p. 108-115.

27. Chin, P.T.K., et al., *Highly Luminescent CdTe/CdSe Colloidal Heteronanocrystals with Temperature-Dependent Emission Color.* Journal of the American Chemical Society, 2007. 129(48): p. 14880-14886.

28. Moreels, I., et al., *Band-Edge Exciton Fine Structure of Small, Nearly Spherical Colloidal CdSe/ZnS Quantum Dots.* ACS Nano, 2011. 5(10): p. 8033-8039.

29. Trinh, M.T., et al., *A Hot Electron–Hole Pair Breaks the Symmetry of a Semiconductor Quantum Dot.* Nano Letters, 2013. 13(12): p. 6091-6097.

Chapter 8: Conclusions and further work

Colloidal QDs are nanoscale semiconducting materials that have size-dependant band gaps. Owing to strong quantum confinement in QDs, they exhibit quasi-discrete energy level structures which are of interest to researchers as they result in characteristics useful for numerous applications. MEG is one such feature of QDs, and is predicted to increase the efficiency of next generation solar cells significantly. The main motivation of this thesis is to investigate the ultrafast charge dynamics, in particular MEG, of several different types of colloidal QDs using a number of different optical spectroscopies. This chapter summarizes the work detailed in this thesis and highlights the possible future work upon the finding obtained here.

Primarily steady-state absorption and PL spectroscopies were used in order to gain insight into the electronic structure of the studied NCs. A TCSPC experiment was used to measure fluorescent lifetimes of the QDs down to a few 10s of picoseconds. With the use of the TRPL method, we studied the multi-exciton interactions for both CdSe/CdTe core/shell and CdSe/CdTe/CdS core/shell/shell QDs. Ultrafast TA is an effective tool to investigate MEG and to determine the MEG QY in these materials. In this thesis a visible femtosecond TA experiment was employed to investigate carrier dynamics of the QDs on the femtosecond time scale. In addition a high repetition rate IR ultrafast TA experiment was designed and built to observe intraband exciton relaxation in QDs with a high accuracy. The ultrafast IR system was tested using the well-known and previously investigated PbS QDs. The results obtained were in good agreement with previous reports. Due to the low energy per pulse, only long-lived single excitons formed. This experiment could be further developed to monitor intraband exciton dynamics of QDs. For example, a

difference frequency generator (DFG) could be employed to access wavelengths in the deeper IR region which can be used as the probe beam. Given an increased energy per pulse, a second and third harmonic generator unit could be used to access the pump beam in the visible and UV region of the spectrum.

The sub-nanosecond carrier dynamics of ZnTe/ZnSe core/shell type-II NCs at the band edge were investigated at an excitation photon energy of ~3.1 eV and under different experimental conditions of stirred and static or high and moderate powers. These type-II QD structures are promising candidates for developing new efficient and environmentally friendly optoelectronic devices. The analysis of the picosecond transient transmission decays yielded two decay features (a slow and fast) for the static and high power cases. The slower component was found to be 10 times longer than the other decay component. This was attributed to the formation of trions which occur when the excited electron traps on the sample surface, leaving its geminate partner un-recombined for a time period longer then the time between two subsequent pump pulses. The observed trion formation is in strong agreement with the literature [1, 2], emphasising the importance of stirring the sample and of modest pump power. On the other hand, substantial hot and cold electron trapping on the surface was also observed in these nano-structures. A broad PA absorption spectrum was observed mainly at energies corresponding to the blue side of the band edge. This feature was attributed to the occurrence of surface-mediated electron cooling in the ZnTe/ZnSe core/shell QDs as similar results had been previously observed in CdSe QDs [3]. The hot electron trapping life time was determined and found to be a few tens of ps (19.2±0.5 ps). Since the surface-mediated cooling reverses and broadens the TA spectrum which spectrally overlaps with the band edge bleach, cancellation and alteration occurred in the observed band edge bleach. Hot electron trapping was confirmed by observing the

initial rise time of the fractional transmittance transient which initially corresponded to a PA, indicating that hot electron relaxation can be directly to the sample surface. The observed hot and cold electron trapping features for ZnTe/ZnSe core/shell QDs were consistent with the previous reports [3, 4]. The results obtained for ZnTe/ZnSe core/shell QDs were published in the journal of *Physical Chemistry Chemical Physics* [5].

Surface-mediated cooling is detrimental for both MEG QY [1, 7] and PL QY [8]. The effective method to eliminate this issue is to over-coat the QD with a material that has wider band gap which acts as a barrier to prevent the charge interaction with the sample surface [8, 9]. Hence, the studied ZnTe/ZnSe core/shell QDs could be passivated by over-coating the structure with a higher band gap material, such as CdS [9, 10], or ZnS [11], to obtain better results. In addition, since ZnTe/ZnSe core/shell QDs have a wide band gap, optical gain studies can be carried out on these materials which could inspire the development of the QD-based lasers and amplifiers.

The ultrafast exciton dynamics of $CuInSe_2$ and $CuInS_2$ colloidal NCs have also been investigated at excitation energies of ~3.11 eV and 2.76 eV, respectively, using the visible ultrafast TA set-up. The reason for choosing these materials is twofold: first, $CuInSe_2$ and $CuInS_2$ QDs are less toxic, being alternatives to the toxic QDs, such as Pb and Cd. Second, these nanostructures can emit light in the spectrum spanning from the visible and NIR region, making them promising materials for a number of electro-optics devices, in particular for next generation solar cells utilizing MEG. The fractional transmittance transient decays for two different sizes of $CuInSe_2$ QDs were recorded: the first sample yielded a single life time of 32.1±0.3 ps, whereas, two decay features with lifetimes of 32.8±0.5 ps and 497±4 ps were extracted from the second sample. Decays for different dot sizes were found to be not consistent with the Poissonian distribution. Since the TA

spectrum did not changed and there was no discernable difference between stirred and static cases for the first sample, then the observed decay feature was attributed to the radiative recombination of holes which are trapped in an internal defect site. As the TA spectrum of the second $CuInSe_2$ dot was shifted and altered, the fast decay feature observed for this sample was attributed to surface-mediated cooling which arises when charges directly depopulate the CBM. The about 10 times slower time constant was attributed to radiative trapped hole recombination, in agreement with the literature [12].

The transient decays of one of the $CuInS_2$ samples were fitted with single exponential function with a time constant of 117±10 ps, which was not consistent with the Poissonian statistics. The transients recorded under static and stirring conditions and the observed TA spectra for the same samples were also not in line with Poissonian statistics. Similarly, in the case of the second $CuInS_2$ sample, the transient decays at moderate pump power yielded a single time constant with time constant of 86.5±8.4 ps. In contrast, the decay recorded at high pump power yielded a second feature which was about 10 times faster than the first decay constant. The effect of the faster decay component was also confirmed from the differential TA spectra recorded at the band edge region wherein the position of the bleach peak was shifted and reversed. This was attributed to the formation of direct surface trapping which is consistent with the literature [3, 13]. However, the long decay feature for both sample sizes was attributed to the intra-gap hole trap state due to photo-damage of the QDs which was previously reported for the same material [12].

Enhanced engineering of the $CuInSe_2$ and $CuInS_2$ QDs by better controlling their size, shape and surface quality will result in improved characteristics. For example, a large size of these QDs can have a direct band gap in the NIR where the utilization of solar radiation is maximum. In addition, the sub-nanosecond relaxation channels that compete

with MEG can be supressed by passivating the sample with CdS or ZnS [12] to increase both PL QY as well as MEG efficiency. Furthermore, since these materials are eco-friendly, their type-II counterparts could be synthesised to gain more control over the QDs' properties. Ultrafast exciton dynamics in QDs of other novel, narrow-band gap materials like Ge, SiGe, and InSb could be investigated [14] and their suitability for solar cells can be discussed. Finally, both experimental and theoretical studies are undoubtedly required to shed light on the mechanisms that are detrimental to MEG efficiency.

It has been shown that the MEG efficiency in QDs can be significantly improved by carefully controlling the surface and structure of the QD. Auger relaxation, surface mediated cooling, and phonon emission mechanisms compete with MEG and were successfully suppressed, resulting in tripled MEG efficiency in CdSe/CdTe/CdS and CdTe/CdSe/CdS and CdTe/CdS core/shell/shell and core/shell structures. The thin layer of CdS was effectively used to prevent the charge interaction with the sample surface. An overall MEG threshold for these materials was observed to be (2.59±0.16) E_g which is slightly improved in comparison with the value of about 2.65E_g that was previously observed in CdTe/CdSe/CdS/ZnS QDs [15] and consistent with other reported results of type-I structures [16, 17]. The average MEG efficiency for the QDs used here was found to be about (142±9)%/E_g. This value is at least three times higher than that of previously reported results [15-17]. Finally, the spectral properties of excitons and biexcitons in type-II QDs were investigated and large attractive biexciton interaction energies up to about -60meV were observed in a set of CdSe/CdTe/CdS and CdTe/CdSe/CdS core/shell/shell and CdTe/CdS core/shell QDs. The delay time between pump and probe experiment was set to 650 ps which confirms that the resultant interaction is only due to biexciton interaction. The results show that the solar cells performance could be considerably

increased as an attractive large interaction energy would decrease MEG threshold.

The results show that, if optimised, MEG in type-II QDs could significantly enhance the efficiency of solar cells. These results are not restricted to the Cd-based QDs used here. Different types of materials, in particular environment friendly ones, could be used for efficient MEG. In addition, it is also interesting to investigate how MEG QY varies with the materials' morphology [18]. Another key challenge is the extraction of charges from the QD before recombination, wherein the MEG effect could be directly measured from photocurrent. Despite a successful attempt of enhancing photocurrent via MEG [19], clearly much work is required to extract MEG generated excitons efficiently. The work of attractive X-X interaction in type-II QDs could be implemented in different materials to gain a complete depiction of working dots which is crucial regarding designing next generation PV devices.

8.1 References

1. McGuire, J.A., et al., *New Aspects of Carrier Multiplication in Semiconductor Nanocrystals.* Accounts of Chemical Research, 2008. **41**(12): p. 1810-1819.
2. Midgett, A.G., et al., *Flowing versus Static Conditions for Measuring Multiple Exciton Generation in PbSe Quantum Dots.* The Journal of Physical Chemistry C. **114**(41): p. 17486-17500.
3. Tyagi, P. and P. Kambhampati, *False multiple exciton recombination and multiple exciton generation signals in semiconductor quantum dots arise from surface charge trapping.* The Journal of Chemical Physics. **134**(9): p. 094706-10.
4. Kambhampati, P., *Hot Exciton Relaxation Dynamics in Semiconductor Quantum Dots: Radiationless Transitions on the Nanoscale.* The Journal of Physical Chemistry C. **115**(45): p. 22089-22109.
5. Cadirci, M., et al., *Ultrafast exciton dynamics in Type II ZnTe-ZnSe colloidal quantum dots.* Physical Chemistry Chemical Physics. **14**(39): p. 13638-13645.
6. Hanna, M.C. and A.J. Nozik, *Solar conversion efficiency of photovoltaic and photoelectrolysis cells with carrier multiplication absorbers.* Journal of Applied Physics, 2006. **100**(7): p. 074510.
7. McGuire, J.A., et al., *Apparent Versus True Carrier Multiplication Yields in Semiconductor Nanocrystals.* Nano Letters. **10**(6): p. 2049-2057.
8. Aharoni, A., et al., *Synthesis of InAs/CdSe/ZnSe Core/Shell1/Shell2 Structures with Bright and Stable Near-Infrared Fluorescence.* Journal of the American Chemical Society, 2005. **128**(1): p. 257-264.
9. McElroy, N., et al., *Comparison of solar cells sensitised by CdTe/CdSe and CdSe/CdTe core/shell colloidal quantum dots with and without a CdS outer layer.* Thin Solid Films, (0).
10. Ning, Z., et al., *Solar cells sensitized with type-II ZnSe-CdS core/shell colloidal quantum dots.* Chemical Communications, 2011. **47**(5): p. 1536-1538.
11. Jung, S.W., et al., *ZnS overlayer on in situ chemical bath deposited CdS quantum dot-assembled TiO2 films for quantum dot-sensitized solar cells.* Current Applied Physics, 2012. **12**(6): p. 1459-1464.
12. Li, L., et al., *Efficient Synthesis of Highly Luminescent Copper Indium Sulfide-Based Core/Shell Nanocrystals with Surprisingly Long-Lived Emission.* Journal of the American Chemical Society, 2011. **133**(5): p. 1176-1179.
13. Cadirci, M., et al., *Ultrafast exciton dynamics in InAs/ZnSe nanocrystal quantum dots.* Physical Chemistry Chemical Physics, 2012.
14. Beard, M.C. and R.J. Ellingson, *Multiple exciton generation in semiconductor nanocrystals: Toward efficient solar energy conversion.* Laser & Photonics Reviews, 2008. **2**(5): p. 377-399.
15. Gachet, D., et al., *An Upper Bound to Carrier Multiplication Efficiency in Type II Colloidal Quantum Dots*, in *Nano Letters*2009, American Chemical Society. p. 164-170.
16. Schaller, R.D., et al., *High-Efficiency Carrier Multiplication and Ultrafast Charge Separation in Semiconductor Nanocrystals Studied via Time-Resolved Photoluminescenceâ€* The Journal of Physical Chemistry B, 2006. **110**(50): p. 25332-25338.
17. Kobayashi, Y., T. Udagawa, and N. Tamai, *Carrier Multiplication in CdTe Quantum Dots*

by Single-photon Timing Spectroscopy. Chemistry Letters, 2009. **38**(8): p. 830-831.
18. Beard, M.C., *Multiple Exciton Generation in Semiconductor Quantum Dots.* The Journal of Physical Chemistry Letters. **2**(11): p. 1282-1288.
19. Sambur, J.B., T. Novet, and B.A. Parkinson, *Multiple Exciton Collection in a Sensitized Photovoltaic System.* Science. **330**(6000): p. 63-66.